GAS BUBBLE EMISSIONS AT CONTINENTAL MARGINS
Detection, mapping, and quantification

Dissertation

Zur Erlangung des
Doktorgrades der Naturwissenschaften (Dr. rer. nat.)

Im Fachbereich der Geowissenschaften
der Universität Bremen

vorgelegt von

Miriam Römer

Gutachter: 1. Prof. Dr. Gerhard Bohrmann
2. Prof. Dr. Heinrich Villinger

Datum der Einreichung: 27.10.2011
Datum der Verteidigung: 21.12.2011

This PhD thesis was written at the Department of Geosciences at the University of Bremen in Germany and funded through 'MARUM – Center for Marine Environmental Sciences'. The work has been carried out from November 2008 until October 2011. The data analyzed in this thesis were retrieved in the Black Sea, in the Arabian Sea offshore Pakistan, and in the Eastern Mediterranean Sea during the R/V METEOR cruises M72/3, M84/2, M74 Legs 2 and 3 and R/V Maria S. MERIAN cruises MSM15/2 and MSM13 Legs 3 and 4.

The thesis comprises seven chapters including three research papers in order to give a better understanding of the role of gas bubble emissions in various deep-sea environments. The introduction focuses first on methane gas emissions in general, beginning with the hydrocarbon formation in the sediments and the role of gas hydrate formation within the sediment deposits. This is followed by the description of gas migration processes to the sediment surface and the presence of cold seep systems, which are places where the hydrocarbon gases come very close to the sediment-seawater boundary. The processes affecting the fate of gas bubbles when released into the water column closes the first part of Chapter I. The introduction further focuses on the significance of gas bubble emissions as part of the global carbon cycle and their contribution to the global atmospheric methane inventory as well as the relevance for past and future climate changes. The second chapter expresses the motivation and main objectives of this study and general open questions driving this work. In the frame of this PhD three case studies have been performed located at three different continental margins, which are shortly introduced in Chapter 3. Previous knowledge about evidence for gas seepage areas in the frame of their geological settings is described and the objectives for the conducted cruises based on this information are specified. The main part of this work is represented by the three manuscripts itself (Chapters 4 - 6). Each paper is focusing on gas bubble emissions detected in one of the three areas in relation to their geological setting, their role within the seep areas and their fate after escaping the seafloor. The thesis closes with a chapter pointing out the main conclusions and presenting future perspectives. Besides a description of the most important new findings, also a critical examination on techniques and methods used to achieve the presented results and their limitations are described and required improvements are proposed in this chapter.

Table of contents

Abbreviations

Table 1: Abbreviations used in this work

GH	Gas hydrate
GHSZ	Gas hydrate stability zone
BGHSZ	Base of the GHSZ
AOM	Anaerobic oxidation of methane
OMZ	Oxygen minimum zone
mbsf	Meter below seafloor
mbsl	Meter below sea level
BSR	Bottom simulating reflector
MV	Mud volcano
GC / GC-T	Gravity corer / GC equipped with temperature loggers
ROV	Remotely operated vehicle
AUV	Autonomous underwater vehicle
TV-MUC	Multicorer equipped with a video-data telemetry
GBS	Gas bubble sampler
MTL	Miniaturized temperature logger
BS	Backscatter
MBES	Multibeam echosounder
PS	PARASOUND (single beam echosounder)
P / T	Pressure / Temperature
r_e	Bubble equivalent spherical radius

C_1 or CH_4	Methane
C_{2+}	Hydrocarbons higher than methane
$\delta^{13}C$	Stable carbon isotope ratio
δD or δ^2H	Stable hydrogen isotope ratio
V-PDB	Vienna Pee Dee Belemnite standard
SMOW	Standard mean ocean water (Vienna standard)
wt-%	Weight percent
s / min/ h / yr	Second/ minute/ hour /year
mL	Milliliter
mol	Unit for the amount of a chemical substance
g	Gram (unit of mass)
Tg or 10^{12} g	Teragram
Gt or 10^{15} g	Gigatonne
SD	Standard deviation
kHz	Kilohertz
PHF	Primary high frequency (of single beam echosounder)
SLF	Secondary low frequency (of single beam echosounder)
SiBu-GUI	Single bubble dissolution model
MCM	Makran continental margin
NDSF	Nile Deep Sea Fan

Definitions

Table 2: Definition of expressions related to gas emissions

Expression	Definition
Seep site / seep area	The entire site / area where hydrocarbons in gas bubbles or dissolved in pore water come close to the seafloor and potentially emanate into the water column
Gas bubble emission	A site or area where gas bubbles emanate from the seafloor into the water column
Gas bubble stream	Gas bubbles emanating from the seafloor from a distinct orifice or crack in the sediments forming an individual stream
Bubble emission site (BES)	A site at the seafloor influenced by gas bubble escape, regardless of currently observed gas bubble streams
Flare	Flame-shaped hydroacoustic anomaly in the water column caused by uprising gas bubbles
Flare area	The area estimated by hydroacoustic observations, where a gas bubble emission is located
High-backscatter anomaly	Area in multibeam echosounder backscatter maps characterized by elevated backscatter values
Carbonate slab	Carbonate-paved area at the seafloor

Abstract

The significance of gas bubble emissions at deep-water hydrocarbon seeps on the global carbon cycle is poorly constrained. Methane is, however, an important component regarding past and future climate change scenarios since it acts as a strong greenhouse gas. One of the main motivations of this study was to obtain a better understanding of the sources and transport pathways of gas bubbles in order to evaluate their input to the atmospheric methane inventory.

To appraise the importance of deep-water gas emissions, a combination of several approaches to investigate these sites were applied including hydroacoustic surveys for detection and localization, and visual observations during ROV-dives for seep inspection and characterization as well as quantification of individual gas bubble streams. For this study, three areas were investigated, which are located in different geological settings, representing a variety of fluid flow systems and physico-chemical controlling factors.

Gas emissions detected at the Makran continental margin are related to accreted sediment sequences in a subduction zone. In the accretionary wedge, compression leads to fluid migration and accumulation of hydrocarbons within anticlines. Gas bubbles escape into the water column at several sites, where they have been found through a systematic hydroacoustic survey in water depths between 575 and 2870 mbsl. Although the quantification indicates that significant amounts of methane are released through bubbles at the seafloor, it was shown that the bubbles dissolve within the water column. However, they could be traced while rising up to ~2000 m through the water column using hydroacoustics. The enormous rising heights result from the formation of a hydrate skin around the bubbles, which significantly enhance their lifetime. But, as soon as the bubbles reach the upper limit of the gas hydrate stability zone (GHSZ), they finally dissolve.

The second case study focuses on the Don-Kuban paleo-fan located in the north-eastern Black Sea. Numerous gas emissions were detected in water depths shallower than the upper limit of the GHSZ while only few gas escapes occur within the GHSZ. This pattern is explained as a result of 'gas hydrate sealing', which precludes the migration of free gas to the seafloor. Nevertheless, a vigorous gas bubble emission area (the Kerch seep area) was detected within the GHSZ in 890 mbsl. Due to elevated temperatures as a consequence of upward fluid flow, the base of the GHSZ is shifted towards the seafloor allowing free gas to migrate through the sediments. Part of the gas bubbles form hydrate deposits in the subsurface, which leads to several meters high elevations that are characterized by high backscatter as revealed by ship- and AUV-based multibeam data. The other part of the gas bubbles escape into the water column and may contribute, as an additional type of hydrocarbon seep, to the Black Sea anoxic basin methane inventory.

A particular type of seafloor manifestation of fluid seepage was investigated at the Nile Deep Sea Fan in the Eastern Mediterranean Sea. More than 150 areas with distinctively higher backscatter were identified in the study area using multibeam. Visual seafloor observations confirmed that carbonate slabs (tens to a few hundred meters in size) cause the high-backscatter anomalies. A systematic hydroacoustic survey revealed evidence for bubble emissions at ~8% of the carbonate slabs but it could be shown again, that all of the methane remains in the ocean interior and does not even reach the mixed surface layer. The volume of carbonate slabs protruding the generally smooth seafloor was quantified based on AUV-based high-resolution multibeam data. The amount of carbon in the carbonate slabs was calculated and illustrate, together with the quantification of the bubble flux, that only a small fraction of carbon is deposited as carbonates via the pathway of anaerobic oxidation of methane in the sediments near the seafloor while the major part is emitted as methane bubbles into the water column.

Summing up, gas emissions were found in all three study areas, indicating that this is a common phenomenon at different types of hydrocarbon

seeps at continental margins also in deep-water environments. The case studies show that the gas bubble emissions represent an effective pathway to transport methane into the water column bypassing the benthic filter. Furthermore, the fate of the gas bubbles while rising through the water column is strongly influenced by hydrate formation around the bubbles, which hampers gas exchange processes. Nevertheless, it was generally observed that the emitted gas bubbles ultimately remain in the ocean interior and thus do not contribute to the atmospheric methane inventory. Furthermore, gas bubbles rising through the sediments have a significant influence on the manifestation of cold seeps at the seafloor. For instance, gas bubbles are essential for the formation of shallow gas hydrate deposits, which can constantly fuel and stabilize the seep environments and their colonization by chemoautotroph living organisms.

Kurzfassung

Über die Bedeutung von Gasblasenaustritten an Kohlenwasserstoff-Austritten in der Tiefsee für den globalen Kohlenstoff Kreislauf ist bisher nur sehr wenig bekannt. Dabei spielt Methan eine wichtige Rolle in Bezug auf vergangene oder zukünftige Klimaänderungen, da es sich um ein starkes Treibhausgas handelt. Einer der übergeordneten Beweggründe für diese Arbeit ist daher, ein besseres Verständnis über die Prozesse an solchen Methan-Austrittstellen am Meeresboden zu erhalten. Ziel ist, den Einfluss des Methans, das in Form von Gasblasen durch die Sedimente und die Wassersäule transportiert wird, zum atmosphärischen Budget abzuschätzen.

Um die Bedeutung der Gasaustritte einschätzen zu können, wurden verschiedene Methoden zur Untersuchung dieser Gebiete eingesetzt. Zum Auffinden und genauen Lokalisieren wurden hydroakustische Systeme genutzt und visuelle Eindrücke wurden während Unterwasser-Tauchgängen mit dem Tauchroboter gewonnen. Anhand dieser Videoaufnahmen konnten die Gebiete in der Umgebung von Gasaustrittstellen beschrieben und charakterisiert, sowie die einzelnen Gasblasenströme quantifiziert werden. Während dieser Doktorarbeit wurden drei Regionen unterschiedlicher geologischer Gegebenheiten untersucht, die verschiedene Systeme der Fluidmigration ausgebildet haben und somit auch von verschiedenen physikalisch und chemisch kontrollierten Prozessen und Faktoren gekennzeichnet sind.

Die Gasaustritte, die am Makran Kontinentalrand gefunden wurden, sind an akkretionäre Sedimentakkumulationen einer Subduktionszone gebunden. Die Kompression innerhalb des Akkretionskeils führt hier zur Fluidmigration und zur Ansammlung von Kohlenwasserstoffen in den Antiklinalstrukturen. Während einer großräumigen Suche mit Hilfe hydroakustischer Systeme wurden an mehreren Stellen in Wassertiefen zwischen 575 und 2870 m Austritte von Gasblasen in die Wassersäule gefunden. Obwohl die Quantifizierung zeigte, dass hier erhebliche Mengen an Methan in Gasblasen vom Meeresboden entweichen, zeigte sich zudem, dass sich alle Gasblasen innerhalb der Wassersäule auflösen. Mit hydroakustischen Methoden konnten einige Gasblasenaustritte jedoch bis zu ~2000 m durch die Wassersäule verfolgt werden. Diese enormen Aufstiegshöhen werden erreicht, da sich Gashydrathüllen um die Blasen herum bilden, wodurch ihre Auflösung wesentlich verlangsamt wird. Sobald die Blasen die obere Grenze der Gashydrat-Stabilitätszone (GHSZ) erreichen, lösen sie sich schnell auf.

Die zweite Fallstudie konzentriert sich auf den Don-Kuban Paläo-Fächer im nordöstlichen Schwarzen Meer. In diesem Gebiet wurden zahlreiche Gasaustritte aus Sedimenten in flachen Wassertiefen oberhalb der GHSZ gefunden, während nur sehr wenige Austritte innerhalb der GHSZ vorkommen. Diese Verteilung erklärt sich daraus, dass durch das Vorhandensein der GHSZ die Gasmigration unterbunden wird und diese somit den Meeresboden für den Aufstieg von freiem Gas versiegelt. Trotz dessen wurde ein Gebiet mit intensiven Gasblasenaustritten innerhalb der GHSZ in 890 m Wassertiefe gefunden (Kerch seep area). Aufgrund aufsteigender Fluide, die Wärme mit transportieren, wird in diesem Gebiet die untere Grenze der GHSZ hin zu sehr flachen Sedimenttiefen verschoben, so dass freies Gas aufsteigen kann ohne in Gashydrate umgewandelt zu werden. Ein Teil der Gasblasen kristallisiert in oberflächennahen Sedimenten zu Hydraten um und bildet dort lokale Gashydrat-Ablagerungen, was zur Ausbildung von bis zu mehreren Metern hohe morphologische Strukturen an der Meeresbodenoberfläche führt. In Fächerecholot-Daten (aus Schiffs- und AUV-basierten Datensätzen) sind diese nicht nur morphologisch, sondern auch durch verstärkte Rückstreu-Intensitäten charakterisiert. Der andere Teil der Gasblasen strömt in die Wassersäule und trägt somit zum Methan Reservoir der anoxischen Schicht des Schwarzen Meeres bei.

Eine besondere Ausprägung von Fluidaustritten am Meeresboden wurde am Nil Tiefseefächer im östlichen Mittelmeer untersucht. Mehr als 150

Gebiete mit deutlich höheren Rückstreu-Intensitäten wurden im Untersuchungsgebiet mit Hilfe von Fächerecholotkartierungen festgestellt. Visuelle Meeresbodenbeobachtungen haben bestätigt, dass diese Anomalien von Karbonatplatten (von Zehnern bin Hundertern Meter Durchmesser) am Meeresboden verursacht werden. Eine systematische Kartierung ergab, dass an ~8% dieser Karbonatflächen Gasblasenaustritte vorkommen, wobei sich die Gasblasen innerhalb der Wassersäule auflösen und das Methan somit im Ozean verbleibt. Die Karbonatflächen erheben sich über den generell sehr flachen Meeresboden und mit Hilfe der sehr detaillierten AUV basierten Fächerecholotdaten wurde deren Volumen vermessen. Die Menge Kohlenstoff in diesen Karbonatflächen wurde berechnet und zeigt im Vergleich zur Menge an Methan austretend in Gasblasen, dass nur ein geringer Anteil des Kohlenstoffs in Karbonat gebunden wird, während der größere Anteil in Gasblasen in die Wassersäule gelangt.

Zusammenfassend wurden in allen drei Arbeitsgebieten Gasblasenaustritte gefunden, was verdeutlicht, dass dies eine verbreitete Erscheinung entlang der Kontinentalränder auch in größeren Wassertiefen ist. Die Fallstudien zeigen, dass Gasblasen einen effektiven Transportmechanismus darstellen, mit dem Methan in die Wassersäule gelangen kann - im Gegensatz zu im Porenwasser gelösten Methan, das zum größten Teil durch den sogenannten benthischen Filter noch im Sediment anaerob oxidiert wird. Der weitere Verbleib der Gasblasen während ihres Aufstiegs in der Wassersäule ist stark von der Gashydratbildung abhängig, da eine Hydratumhüllung den Gausaustausch verlangsamt. Trotz dessen lösen sich die in den Fallstudien untersuchten Gasblasen letztendlich innerhalb der Wassersäule auf und tragen somit nicht zum atmosphärischen Methanreservoir bei. Die Gasblasen im Sediment haben jedoch einen erheblichen Einfluss auf die Ausbildung von kalten Quellen am Meeresboden, da sie beispielsweise für die Bildung von flachen Gashydrat Ablagerungen verantwortlich sind, was wiederum zur konstanten Energielieferung und damit Stabilisierung dieser Gebiete und deren Besiedelung durch chemoautotrophe Organismen beiträgt.

1 Introduction

1.1 Natural gas emissions in the marine environment

Natural emissions of free gas associated to cold seeps in the marine environment are increasingly documented by marine scientists (Judd and Hovland 2007). The fluids emanating at cold seeps transport hydrocarbon gases, oil, and water and can contain remineralized nutrients, hydrogen sulfide and other constituents. In most cases, however, gas emissions at those sites are predominantly composed of methane. Together with water vapor and carbon dioxide, methane is one of the most abundant greenhouse gases in the atmosphere and their possible impact on climate change is therefore of high interest.

At many cold seeps methane is emitted as gas bubbles generating bubble streams, which sometimes reach high up into the water column and in particular settings up to the sea surface. The indirect detection of numerous gas emissions worldwide has been achieved by using hydroacoustic records, in which the gas emissions appear as backscatter anomalies. As these anomalies in the water column are often flame-shaped, they are commonly called flares (Greinert et al. 2006).

Gas emissions in shallow waters (e.g. Coal Oil Point, NW Black Sea shelf, Santa Barbara Basin, Tommeliten) are comparably well studied and several sites have been also quantified (Hovland et al. 1993; Hornafius et al. 1999; Artemov et al. 2007; Schneider von Deimling et al. 2011). In contrast, little is known about deep-water gas bubble emissions. Very little documentation of these sites exist and only four papers that quantified gas emissions had been published prior to this work. Two publications were related to the Håkon Mosby (Sauter et al. 2006) and the Vodyanitskii (Sahling et al. 2009) mud volcanoes and further two studies were presented for seep sites in the Gulf of Mexico (GC185; Leifer and MacDonald 2003) and offshore Oregon (Hydrate Ridge; Torres et al. 2002).

1.1.1 Origin of light hydrocarbons

Two principal sources of light hydrocarbons are known: thermogenic and biogenic processes. Thermogenic methane (as well as higher hydrocarbons) is generated by catagenesis in deep anoxic sediments (Tissot and Welte 1984). Organic matter is cracked at temperatures of ~75 and 200°C and low-molecular weight hydrocarbons are produced (depending on the local geotherm this takes place at sediment depths exceeding 2 km). Biogenic methane is produced by microbes through organic matter degradation just after deposition, which is called the biologically-mediated methanogenesis (Whiticar et al. 1986; Whiticar 1999). Significant amounts of natural hydrocarbons in the earth's crust are known to be of microbial origin (Rice and Claypool 1981; Claypool and Kvenvolden 1983). Methanogenic archaea utilize fermentative end products such as CO_2 along with hydrogen (Equation 1-1) or acetate (Equation 1-2).

$$CO_2 + 4\,H_2 \rightarrow CH_4 + 2\,H_2O \qquad \text{(Eq. 1-1)}$$

$$CH_3COOH \rightarrow CH_4 + CO_2 \qquad \text{(Eq. 1-2)}$$

Geological conditions favoring microbial hydrocarbon formation and accumulation in sedimentary rocks include high sedimentation rates promoting the presence of sufficient sedimentary organic matter, an anoxic and sulfate-deficient environment, and temperatures below about 75°C (Rice and Claypool 1981).

The molecular ratio of methane (C_1) to higher hydrocarbons (C_{2+}) allows for an identification of the major hydrocarbon source. Both, biogenic and thermogenic hydrocarbons are usually dominated by methane, however, biogenic hydrocarbons mostly consist of methane reflected by a C_1/C_{2+} ratio higher than about 1000, whereas thermogenic hydrocarbons are characterized by lower ratios, i.e. by higher proportions of higher hydrocarbons (Fig. 1-1a; Bernard et al. 1976). In addition, the extent of fractionation of stable isotopes can be used to distinguish between biogenic and thermogenic methane. Microbes preferentially take up molecules depleted in the more heavy isotopes. In contrast, thermogenic methane as the end product of unselective hydrocarbon cracking is

not associated with significant isotope effects. Thus, biogenic hydrocarbons are dominantly composed of methane which is depleted in the more heavy isotope ^{13}C due to kinetic fractionation relative its thermogenic counterpart (Whiticar 1999). Therefore, it is generally accepted that $\delta^{13}C$ values less than –50‰ (V-PDB) are diagnostic for biogenic methane while values higher than about –50‰ point to a thermogenic methane origin (Fig. 1-1a; Claypool and Kvenvolden 1983; Schoell 1980).

The stable hydrogen isotope ratio (D/H) provides additional information on the principal metabolic process used for methane production. Hydrogen isotopes of methane originating from acetate fermentation are characterized by δD values lower than about –250‰ (SMOW), whereas carbonate fermentation typically leads to δD values between –250 and –150‰ (Fig. 1-1b; Whiticar et al. 1986).

Secondary, post-diagenetic processes, such as migration, microbial oxidation (biodegradation), or mixing, may complicate the identification of the principal hydrocarbon origin as they can modify the primary diagnostic signatures (Whiticar 1999). For instance, Vandré et al. (2007) proposed the presence of biodegraded thermogenic hydrocarbons (secondary biogenic hydrocarbons) in addition to a co-existence or rather mixing with microbial hydrocarbons in sediments of the eastern Nile Deep Sea Fan. Similarly, Stadnitskaia et al. (2008) reported about secondary microbial hydrocarbons as alteration products of thermogenic hydrocarbons expelled from mud volcanoes in the Sorokin Trough (Black Sea) and in the Gulf of Cadiz. Results from compositional studies on oil reservoirs in the Gulf of Mexico lead to the assumption that biodegradation can take place at temperatures exceeding about 80°C and, thus, is most probably carried out by hyperthermophilic methanogens (Milkov and Dzou 2007). The alteration effects on hydrocarbons occurring during migration through the sediment and accumulation in different gas reservoirs in the shallow subsurface within the gas hydrate stability field (free gas, dissolved gas, and hydrate-bound gas) might be even more complex.

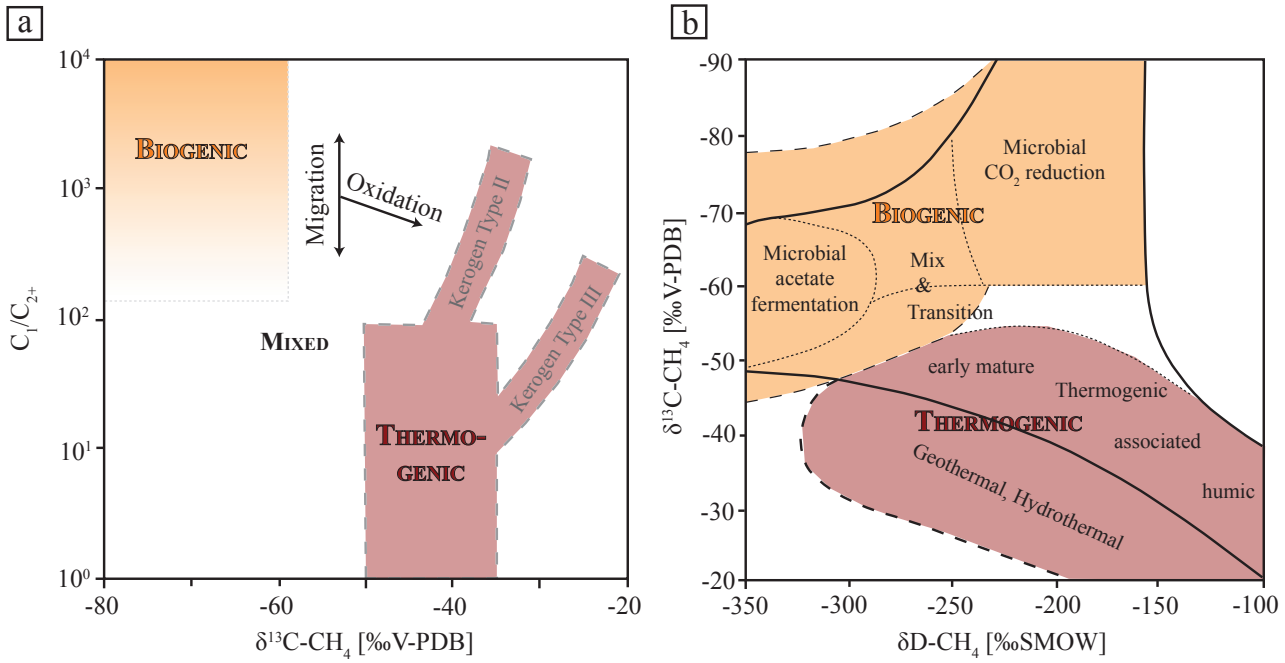

Fig. 1-1: a) Bernard diagram' (modified after Whiticar, 1990) to plot $\delta^{13}C$ values of methane versus molecular hydrocarbon ratios indicating the biogenic or thermogenic origin or mixing of both. The arrows indicate the relative compositional effects of migration or oxidation. b) Cross plot of $\delta^{13}C$ and δD values of methane illustrating the classification of thermogenic and biogenic generated methane and for the latter also an explicit differentiation between carbonate or acetate fermentation products (after Whiticar et al. 1999).

By evaluating the physico-chemical properties of individual gas types (Pape et al. 2010) proposed a conceptual model for gas in shallow deposits of the Batumi seep area (Black Sea), where multiple processes affect the partitioning and alteration of light hydrocarbons.

1.1.2 Gas hydrates

Gas hydrates are naturally occurring ice-like crystalline compounds (also called clathrates), in which water molecules form cage structures enclosing low molecular weight gases as guest molecules (Fig. 1-2 left). The first discovery of clathrates was by Sir Humphrey Davy in 1810 (Davy 1811). Nevertheless, there was a long time without intense interest in its investigation, but during the last ~30 years research about gas hydrates has been quite popular due to the fact that it might represent an important future energy resource and because of its large volume on earth. Additionally, the possible role in global processes like the carbon cycle, impact on climate change, and contribution on seafloor stability as well as related geohazards resulted in the strong interest in better understanding all aspects of gas hydrates (Bohrmann and Torres 2006).

Gas hydrates can contain different types of gas molecules, which are fitting into five types of water cages depending on its molecular diameter (Fig. 1-2 right). By combining those five cage types, three different crystal structures occur: structure I, II, and H. Structure I gas hydrate, which is composed of the smallest cage types can enclose only gas molecules smaller than propane. Since methane is the most dominate gas in marine sediments, structure I is most frequently observed (Bohrmann and Torres 2006).

The formation of gas hydrates depends on several factors, of which the most important parameters are the temperature and pressure conditions as well as the gas composition and saturation and the presence of dissolved ions in the pore water (or surrounding medium) (Sloan 1998). In Fig. 1-3a the P/T conditions for pure methane hydrate stability at normal seawater salinity is illustrated. The presence of higher hydrocarbons, CO_2 or H_2S would shift the stability curve to the right (hence increasing the stability field), whereas an increase in salinity (or other ions) would shift the phase boundary to the left (and decreases the stability field).

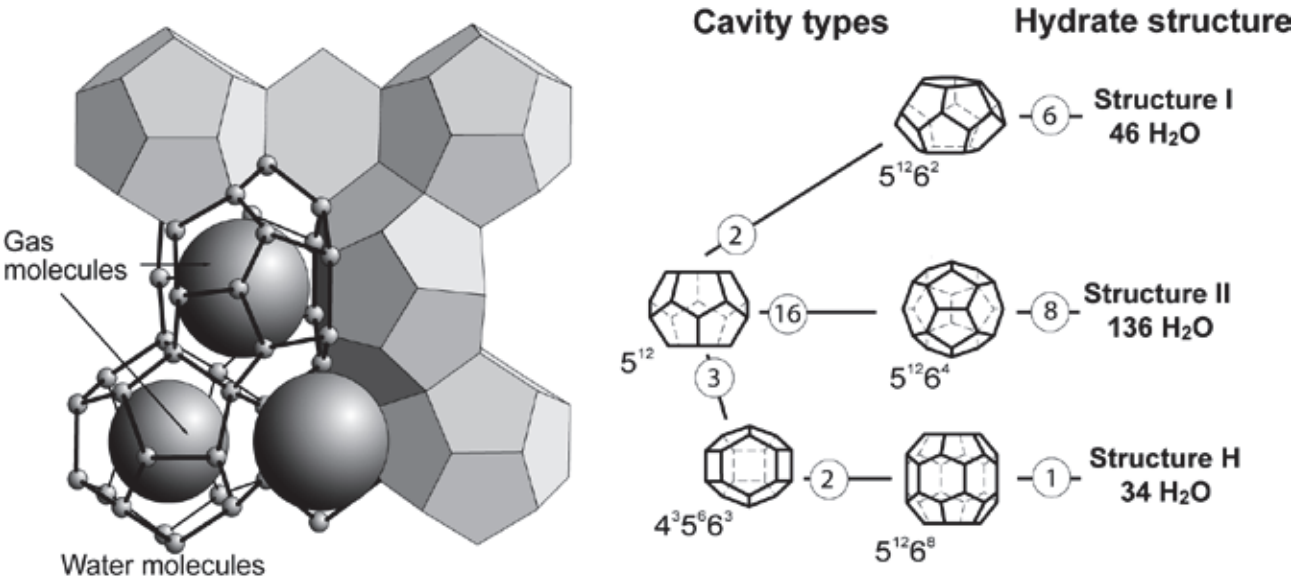

Fig. 1-2: Left: The clathrate structure consists of large gas molecules enclosed in cages of water molecules, which interact through van der Waals forces. Right: Five types of cage structures of different sizes for compatible guest molecules forming the three known hydrate structures (Bohrmann and Torres 2006).

Gas hydrates therefore occur on the one hand in permafrost regions, where huge amounts of methane are available and temperatures are low enough that hydrates are stable in relatively shallow depths close to the surface. On the other hand, they are widely distributed along the marine continental margins (Fig. 1-3b) and also in very deep lakes with cold water (e.g. Lake Baikal), where organic matter accumulates rapidly enough to support methane production (Kvenvolden 1988). The upper boundary of the gas hydrate stability zone (GHSZ) is defined by the local temperature distribution within the water column and the base of the GHSZ is controlled through the local geothermal gradient in the sediments (Kvenvolden 1993). As pressure increases with increasing water depths, the base of the GHSZ (BGSHZ) extends further below the seafloor, thickening the GHSZ. The BGHSZ can be imaged in seismic records as a pronounced reflection (called the bottom simulating reflector or BSR), when free gas is accumulated below a gas hydrate layer (Shipley et al. 1979). The GHSZ should not be regarded as an area where necessarily gas hydrate deposits occur as also the other parameters (gas occurrence and saturation) play an important role. In deep-ocean basins hydrate formation is usually inhibited as methane concentration are below saturation (Claypool and Kaplan 1974).

In areas with high methane fluxes, gas hydrates can form in shallow sediment depth and gas hydrate samples have been retrieved by different sampling tools at numerous sites worldwide. Typical fabrics of hydrates range between hydrates interlayering the sediments to massive and pure hydrate layers. Hydrates often show a porous framework (Figs. 1-4a and b). This globular fabric seems to result from frozen gas bubbles, which have been trapped and accumulated under an impermeable layer while they became incased by a hydrate skin (Fig. 4c; Bohrmann et al. 1998; Suess et al. 2001).

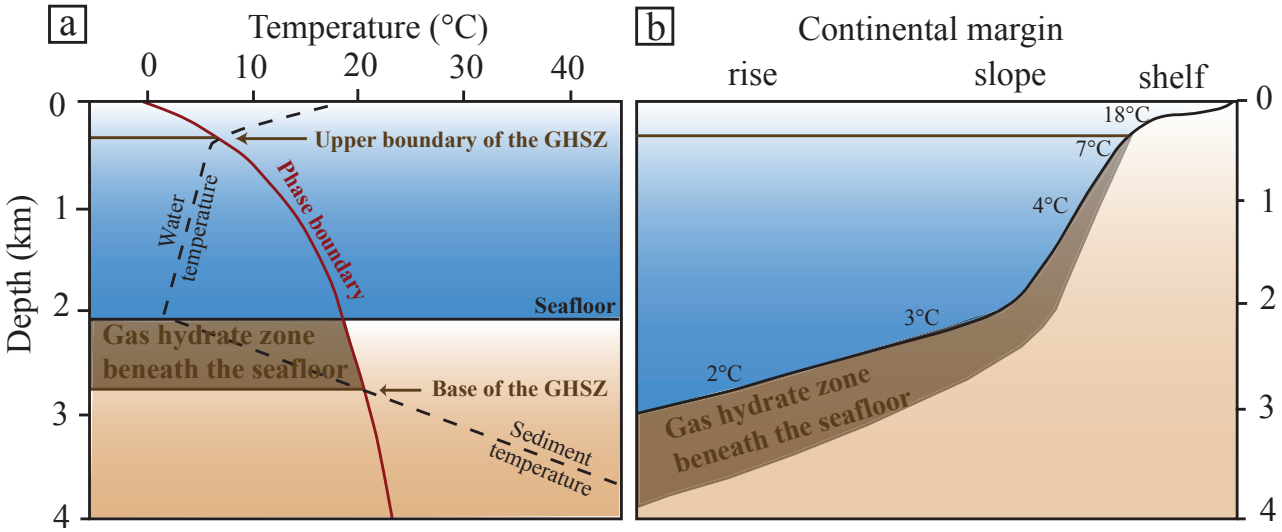

Fig. 1-3: a) Phase diagram of methane as hydrate opposed to free gas and water at normal seawater salinity, defined by temperature and pressure conditions. Intersections of the temperature profiles (stippled lines) with the phase boundary (red line) define the area of the gas hydrate stability zone (GHSZ). b) Inferred thickness of the GHSZ in sediments at a schematic continental margin assuming a typical geothermal gradient (28°C km^{-1}). Typical bottom water temperatures are marked, and range from 18°C on shallow shelf regions to 2°C at the bottom of the continental rise (adopted from Bohrmann and Torres 2006).

The determination of the global gas hydrate quantities still contains large uncertainties. Several studies using different approaches exist and the wide range of estimations indicate the difficulties and illustrate the restricted knowledge about this parameter. The earlier rough estimations were achieved by estimating the global volume of the GHSZ along the continental margins and assuming an average gas hydrate content of about 1 – 10%, implying that between 1,000 and 22,000 Gt of carbon is stored in gas hydrates (Dickens 2001; Dickens 2003) and a generally 'consensus estimation' of 10,000 Gt was established (Kvenvolden 2002). These very uncertain estimations were improved by implementing direct measurements of methane concentrations obtained during ODP Leg 204 at Hydrate Ridge and more realistic volumes for the GHSZ as well as the specification of the portion which may contain gas hydrates and the new estimate published by Milkov et al. (2004) is in the range of 500 – 2,500 Gt. A considerably higher amount has been published by Klauda and Sandler (2005) of 74,400 Gt, which is however considered to be an overestimation (Archer 2007). Another approach has been made by modeling the global gas hydrate inventory: While Buffett and Archer (2004) yield a global estimate of 3,000 Gt of carbon in hydrates and 2,000 Gt in methane bubbles and some years later, Archer (2007) published, that the gas hydrate system contains 500 – 3,000 Gt of carbon stored in gas hydrate and a similar amount of free gas below the gas hydrates. More recently published values of 4 – 995 Gt carbon stored in hydrates were obtained by Burwicz et al. (2011) as well through modeling, which was largely improved by adjusted input parameter but has been criticized to fail by comparing with field observations (Dickens 2011). The model was further improved by considering upward fluid flow induced by tectonic overpressuring at continental margins resulting in a best estimate of ~3,000 Gt (Wallmann et al. 2011). Generally, the large range of published values indicates clearly ongoing uncertainty about the global inventory of gas hydrates and improvements will definitely continue to better evaluate this important parameter.

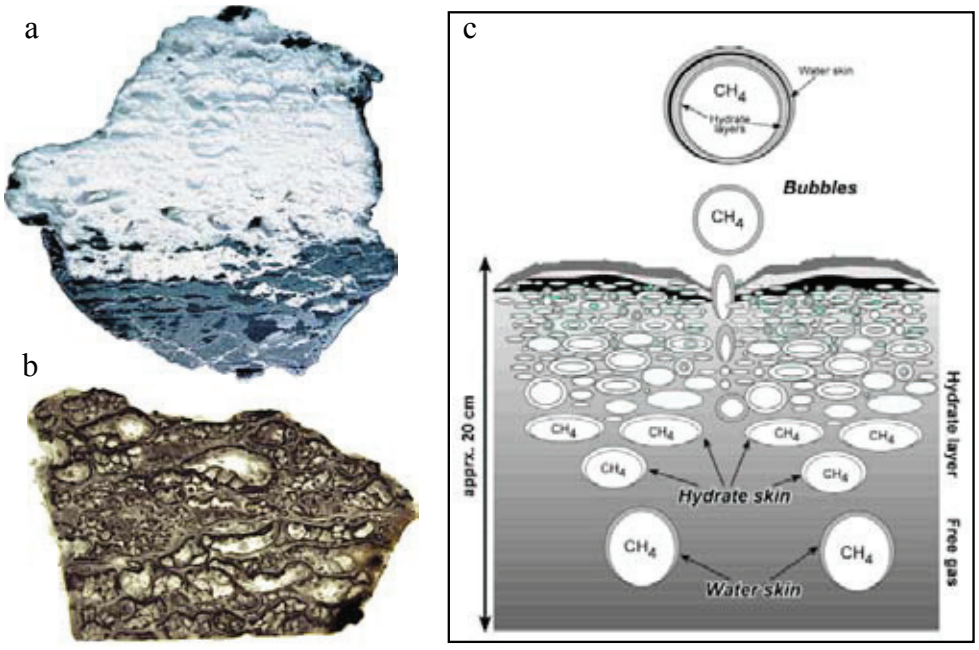

Fig. 1-4: a) Image of a massive gas hydrate layer sampled at Hydrate Ridge and b) thin-section illustrating the globular structure outlining former gas bubbles (a and b from Bohrmann et al. 1998). Schematic illustration of the development of sub-seafloor hydrate layers as a product of rising gas bubbles trapped below the surface and converted to hydrate (Suess et al. 2001).

1.1.3 Gas migration through the sediments

Diffusion and advection of methane in solution in pore water are two possible transport pathways of methane. If methane however, occurs in concentrations above solubility, it exists as free gas and the buoyancy is the dominant force driving methane gas bubbles towards the surface (Matthews 1996). The amount of dissolved methane that can be transported by advection is limited by the low level of methane saturation in the pore water and the amount of methane transported by diffusion is limited by small concentration differences. Those migration pathways are therefore very inefficient (Clennell et al. 2000). Far more methane can be transported through free gas migration, which is strongly buoyant and additional overpressure, for instance as a consequence of unbalanced compaction, drive the migration upwards. A fluid or gas must overcome the capillary resistance to move through a rock or sediment (Clennell et al. 2000). Fluid flow through either the normal pore spaces (called invasion percolation) or discontinuities as open faults or fractures (Judd and Hovland 2007). The fluids squeeze through conduits or generate their own migration pathway by hydrofracturing using efficient force to fail the sediment (Judd and Hovland 2007). If faults or fractures are present, they often dominate the flow pattern. Boudreau et al. (2005) have shown by X-ray computed tomography imaging of mud sediments during bubble injection, that disk-shaped bubbles form which grow either by fracturing or by reopening preexisting fractures. Although several studies have been published assuming faults and fractures to act as seals, they represent at least temporally efficient migration pathways. In several areas of the Atlantic margins (Norway, Congo deep-sea fan) widespread polygonal fault systems are proposed to enable hydro-carbon gas to migrate upwards (Gay et al. 2006; Hustoft et al. 2007). Additionally, diapirism is a mechanism often occurring in fine grained sediments, which may induce gas migration by pushing sediments closer to the seafloor (Clennell et al. 2000). Low permeability together with high gravitational load and/or strong fluid sources may result in fluidized sediments flowing upwards. Mud volcanoes are formed when fluidized muds reach the surface through localized narrow conduits.

Gas migration is most often not a steady process but occurs episodic and may reflect external forcing through tidal pumping or seismic activity (Boles et al. 2001; Leifer et al. 2004; Leifer and Boles 2005). The hydrostatic pressure changes during the tidal cycle and gas bubbles expand and contract simultaneously, which is coupled with the poroelastic properties of gassy sediments (Clennell et al. 2000). The permeability and compressibility of the sediments and the tide itself control the oscillation amplitude. Tidally-driven influence on flow oscillation was described by Tryon et al. (2002) for the seepage at Hydrate Ridge as one important factor of a complex hydrological process in a dynamic system. Earthquakes are supposed to have also an influence on abrupt gas migration as a consequence of pore pressure build-up. A relation between seismic activity and mud volcano eruptions shortly after nearby earthquakes as well as pockmark formation and enhanced gas emission activity at seep sites has been reported (Hovland and Judd 1988; Manga et al. 2009). The trigger mechanisms are probably liquefaction, an increased hydraulic permeability or removing hydraulic barriers leading to an opening of fractures but also bubble formation and gas hydrate dissociation through pulses of warm fluid have been postulated to possibly play an additional role (Manga et al. 2009).

The potential formation of gas hydrates in the sediments is an important factor for the presence of gas emission to the water column. Naudts et al. (2006) observed that the abundant gas seepage at the Dnepr paleo-delta seem to be restricted to water depths shallower than 725 m, which is approximately the upper boundary of the GHSZ and suggests in sediments of deeper water depths a sealing mechanism of gas hydrate bearing sediments for gas migration to the seafloor (Fig. 1-5). Free gas seems to be trapped below the GHSZ and crystallizes usually to gas hydrates within

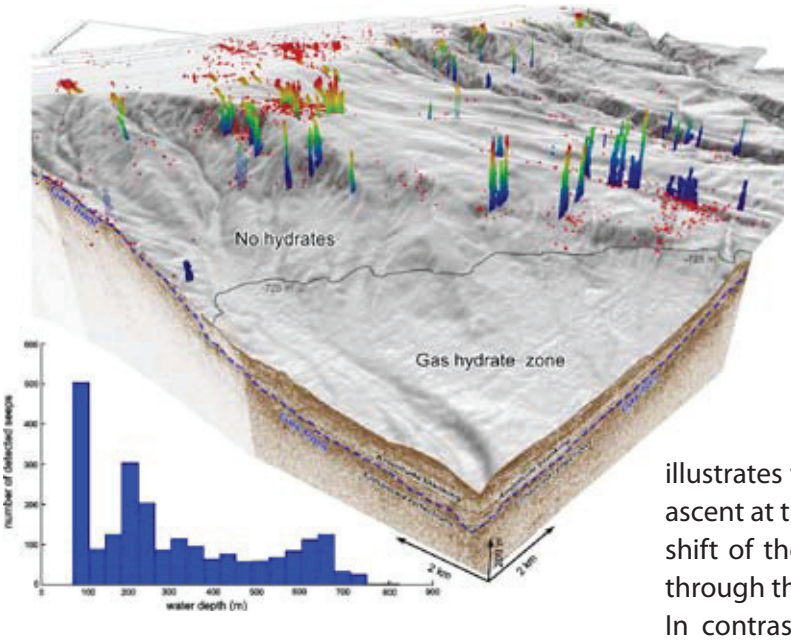

Fig. 1-5: Numerous gas emissions at the Dnepr paleo-fan in the north-western Black Sea are distributed in water depths shallower than 725 m, which is the regional boundary of the GHSZ, indicating the sealing character of the GHSZ (Naudts et al. 2006).

the stability field when it gets in contact to water molecules (White 1979; Hovland 2002).

Nevertheless, gas seepage does exist in areas located within the GHSZ as well (Suess et al. 1999). Methane escape as free gas was observed for instance from mud volcanoes, which are located within the GHSZ. At Dvurechenskii mud volcano (Black Sea) warm, saline fluids and mud ascend from greater depth resulting in elevated sediment temperatures (Bohrmann et al. 2003), which explains the migration of gas bubbles through the sediments into the water column (Greinert et al. 2006). Fig 1-6 illustrates the gas hydrate distribution and free gas ascent at the Håkon Mosby mud volcano due to the shift of the GHSZ as a result of warm fluid ascent through the conduit.

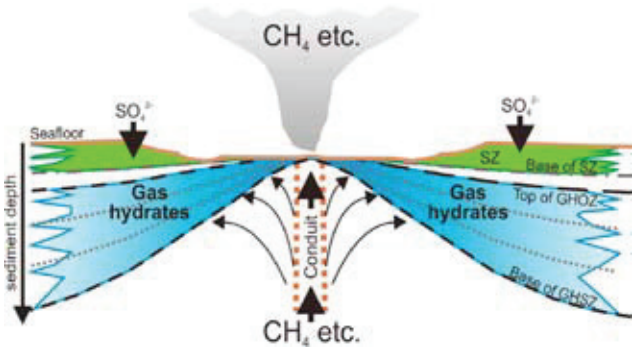

Fig. 1-6: Cross section illustrating the gas hydrate distribution in shallow deposits at the Håkon Mosby mud volcano. Free gas ascent through the central conduit where elevated temperatures impede the formation of gas hydrates and emanate into the water column forming methane plumes (Pape et al. 2011b).

In contrast to that, the Batumi seep area in the Black Sea is not connected to mud volcanism, but also located within the GHSZ. The presence of gas hydrates in shallow sediments has been confirmed but no explanation is given for the migration of free gas through the GHSZ at this seep site (Klaucke et al. 2006).

Another setting permitting gas migration within the regional GHSZ is above salt diapirs, where salt-rich fluids may migrate and form brines at the seafloor and simultaneously inhibit gas hydrate formation due to very high chloride content. This has been documented in the Gulf of Mexico (Ruppel et al. 2005). Additionally, Milkov et al. (2004) and Liu and Flemings (2006) predict a model of a co-existence of gas hydrate, free gas and brine within the GHSZ at Hydrate Ridge. Salt enrichment was produced by very rapid hydrate formation (Torres et al. 2004) whereupon freshwater gets consumed leading to the enrichment of salinity in the rest of the pore water. And the low permeability of the fine-grained sediments does not allow diluting the salt-enriched pore water by diffusion (Haeckel et al. 2004). As available water is essential for the hydrate formation, in those low-permeable sediments gas may exist beside hydrates especially when additionally high gas saturation exist at the base of the GHSZ (Tréhu et al. 2004).

1.1.4 Cold seep systems

Cold seeps or vents are sites at the seafloor where fluids are transported close to the sediment-seawater interface and eventually come in contact with the water body. Cold seep systems are generally considered as being not related to hydrothermal circulation and therefore distinguished from hydrothermal vents. The fluids transport hydrocarbon gases, oil or freshwater and contain remineralized nutrients and hydrogen sulfide, however, most sites are dominated by methane. Most continental margins are composed of thick sedimentary sequences and contain enough methane so that the gas is moving upwards either dissolved or as free gas. When entering the GHSZ gases are crystallizing to hydrates or when reaching different levels of the sediments close to the seafloor, methane or methane hydrates are fueling the cold seep systems (Suess 2010). Cold seeps have been described at a variety of sites worldwide along the continental margins (Fig. 1-7) and can be related to many different geological settings which facilitate fluid migration. At a high number of the detected cold seep environments, gas escape into the water column has been observed and described (Fig. 1-7) and every year the number of findings is still increasing.

Cold seeps have been described along active and passive continental margins as well as at margins, which are in the influence of transform plate boundaries (Suess 2010). Most studied seeps, however, occur at convergent plate boundaries, where oceanic plates are subducting beneath the continents and lateral compression results in dewatering of sediments and fluid expulsions at the seafloor (Suess 2010). Two different types of subduction zone exist: (a) accretionary subduction zones form when the sediments covering the subducted oceanic crust get off-scraped and generate an accretionary wedge with ridges perpendicular to the subduction movement and sedimentary basins in between these ridges; (b) at erosional subduction zones the sediment load gets subducted together with the oceanic plate and additionally sometime also material from the overriding plate gets removed (von Huene and Scholl 1991). Both types are characterized by over-

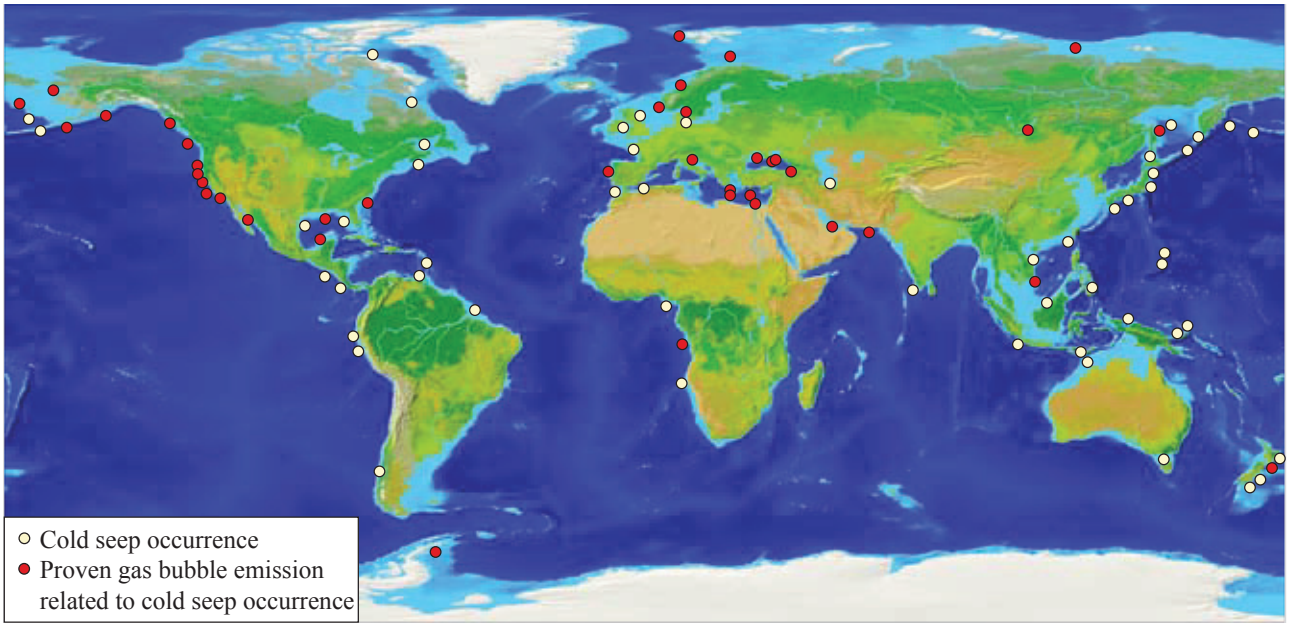

Fig. 1-7: Global distribution of hydrocarbon seeps and related gas bubble emissions, either detected as hydroacoustic anomaly in the water column or by visual observations. Data compilation of Campbell 2006, Judd and Hovland 2007, Suess 2010, with additional findings by Domack et al. 2005, Granin et al. 2010, Shakova et al. 2010.

pressuring and fluid generation through mineral-bound water dehydration and also the formation of fault systems facilitating their upward migration (Suess 2010). In addition, a lot of cold seeps have been found at passive margins, related to a variety of different geological settings, including deep-sea fans, buried canyons, salt and shale diapirs, as well as marginal seas with high sedimentation or an anoxic environment. The main factors driving fluid flow in these settings are the sediment load, differential compaction, overpressure, and facies change (Suess 2010) and the tectonic setting has again great influence on the generation of fluid pathways. In Fig. 1-8 a schematic three dimensional block diagram presented by Gay et al. (2007) based on the research results performed at seeps of the Lower Congo Basin is illustrating various fluid-escape structures at a passive continental margin. Seabed fluid escape is often related to recent and former canyon developments, diapirs, faults as well as the pinch-out zone of the base of the GHSZ. It is assumed, that the GHSZ tends to hinder vertical migration, whereas a polygonal fault system may facilitate gas migration to the seabed (Gay et al. 2007).

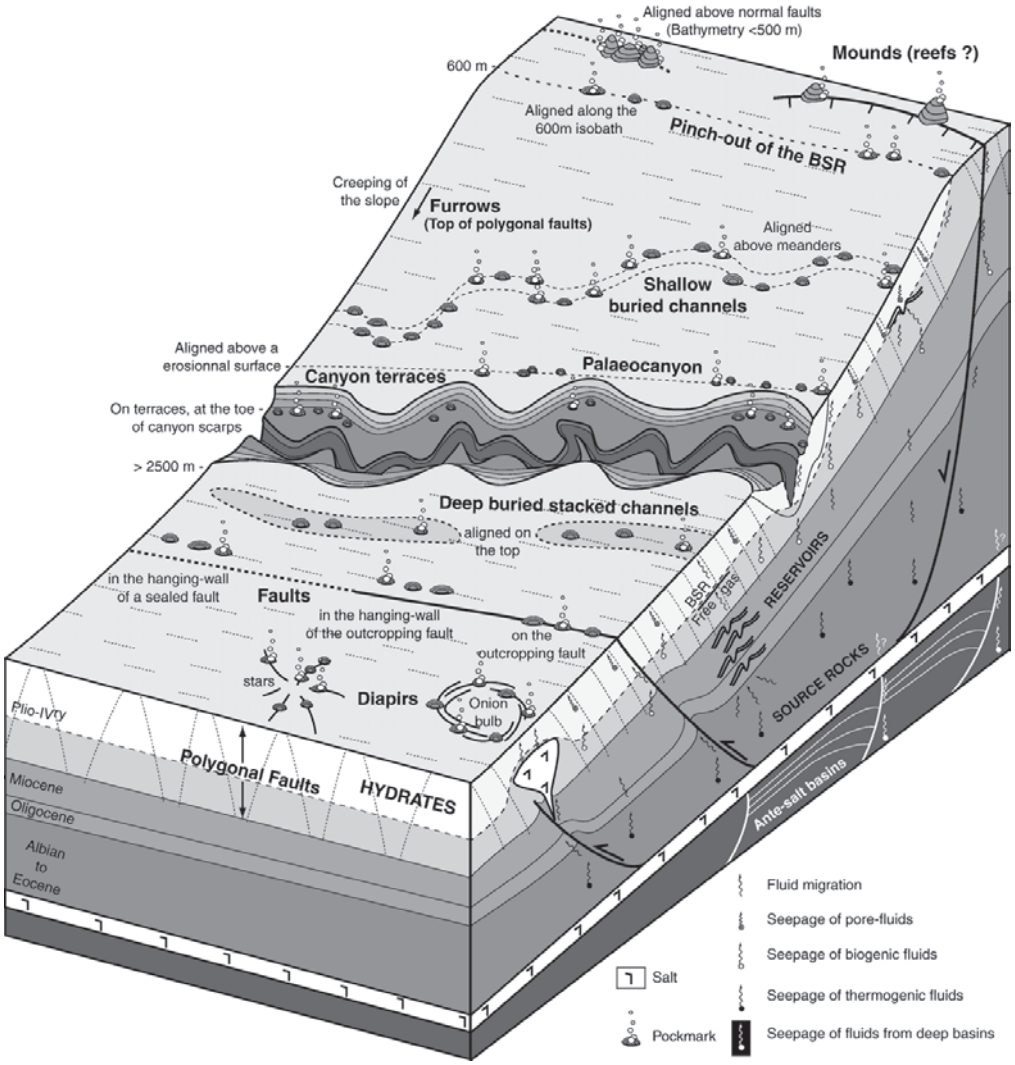

Fig. 1-8: Three dimensional block diagram of a passive continental margin illustrating the different occurrences of gas emissions connected to several possible migration pathways depending on the existing sedimentological and tectonical setting (Gay et al. 2007).

Seafloor expressions related to cold seep activities can be very different. If fluid transport is accompanied with sediment movement, morphologically positive structures may evolve at the seafloor, forming mud volcanoes. Viscosity and density of the extruded material as well as the duration of eruption are the main factors determining the shape of mud volcanoes, which can strongly vary (Kopf 2002). In contrast, seeping fluids may produce as well negative morphological features, which are called pockmarks (Judd and Hovland 2007). Pockmarks are indicators for fluid seepage but the formation process is still discussed. They might be the result of explosive events releasing overpressured fluids and the sediments are ejected into the water column and transported away (Judd and Hovland 2007). Alternatively they might form slowly as gas bubbles only remove small amounts of sediments at a given time. The continuous action then leads to the formation of composite (large) pockmarks (Sahling et al. 2008). Some cold seeps, however, were described which lack striking morphology, which in contrast to the first two mentioned types inhibit a simple detection in bathymetric maps.

The anaerobic oxidation of methane (AOM) coupled with sulfate reduction (Equation 1-3) is a dominant microbial process at cold seeps. A consortium of methanotrophic archaea and sulfate-reducing bacteria have been identified to mediate AOM (Boetius et al. 2000).

$$CH_4 + SO_4^{2-} \rightarrow HS^- + HCO_3^- + H_2O \qquad \text{(Eq. 1-3)}$$

The formation of hydrogen sulfide represents an energy source for chemoautotrophic organisms living on the seafloor and the available amount controls the individual colonization with e.g. bacterial mats or macrofauna such as clams, mussels and tubeworms (Fig. 1-9; Sahling et al. 2002).

The AOM by microorganisms is a significant process in the global carbon cycle as it represents an important sink for methane and limits the transfer into the water column. This process is observed as a benthic filter which represents a type of

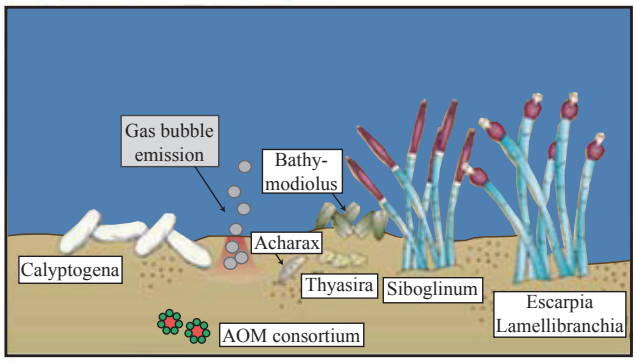

Fig. 1-9: Overview of the typical organisms living in a deep-water cold seep environment (modified after Dubilier et al. 2008).

natural sealing (Hovland 2002; Sommer et al. 2006). However, the benthic filter plays only a significant role for the methane dissolved in pore water, whereas methane transported through gas bubbles mostly bypass the benthic filter and represent therefore an effective pathway for methane to enter the hydrosphere (Fig. 1-10).

The microbial activity at seep sites leads also to the formation of carbonates, which are typical manifestations of active and passive fluid emanation sites. The bicarbonate ions produced by AOM (Equation 1-3) increase the carbonate alkalinity and, together with Ca and, to minor accounts Mg, leads to the precipitation of authigenic carbonates at the seafloor within the sediment (Fig. 1-10; Berner 1980). Carbonates have been found in various cold seep systems (e.g. Ritger et al. 1987; Bohrmann et al. 1998; Aloisi et al. 2000; Naehr et al. 2000; Aloisi et al. 2002; Greinert et al. 2002; Han et al. 2004; Teichert et al. 2005a; Teichert et al. 2005b; Mazzini et al. 2008; Bahr et al. 2009; Bahr et al. 2010) and Hovland (2002) propose that carbonate cemented sediments represent another form of natural sealing in cold seep systems. Authigenic carbonates occur as chimneys protruding the seafloor (Michaelis et al. 2002), chemohermes (Teichert et al. 2005b) or most typically as crust pavements and concretions at the seafloor or in very shallow depth in the sediment (Luff et al. 2004; Gontharet et al. 2007; Bayon et al. 2009a). The time needed for the formation of such a carbonate crust is poorly constrained but Luff

et al. (2004) showed by numerical modeling that a few centimeter thick carbonate crust could be formed within a few hundred years. The presence of carbonates at cold seeps enables the detection by using hydroacoustic systems, as the backscatter signal is modified due to different sediment properties (Anderson and Bryant 1990; Orange et al. 2002; Sager et al. 2003; Loncke et al. 2004; Zitter et al. 2005; Klaucke et al. 2006; Klaucke et al. 2008). The relation between backscatter intensity and seep evolution and expression at the seafloor was unraveled by Gay et al., (2007) (Fig. 1-11). Highest backscatter values were reached when the cold seep is within the most active phase,

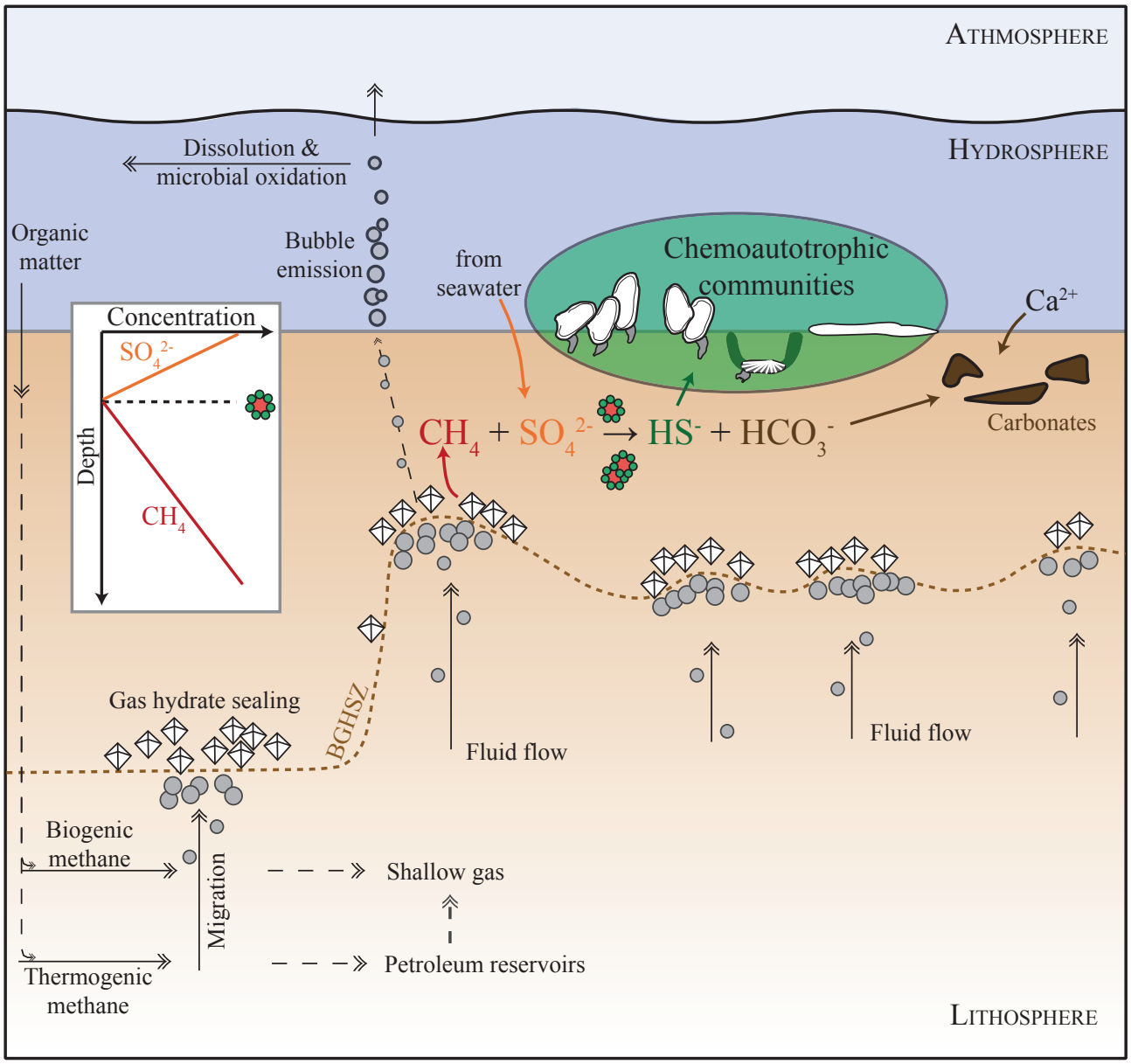

Fig. 1-10: Schematic overview of the processes in the shallow sediments at cold seep systems. The principle cycle from the sources to the fate of methane is adopted from Judd (2004) and extended with the chemical processes leading to the consumption of dissolved methane by AOM, which further fuels the chemoautotrophic communities and induce carbonate precipitations.

when carbonates have precipitated and organisms are settled. Nevertheless, backscatter values are still very intense when the seep further becomes inactive and is getting buried below few meters of sediments.

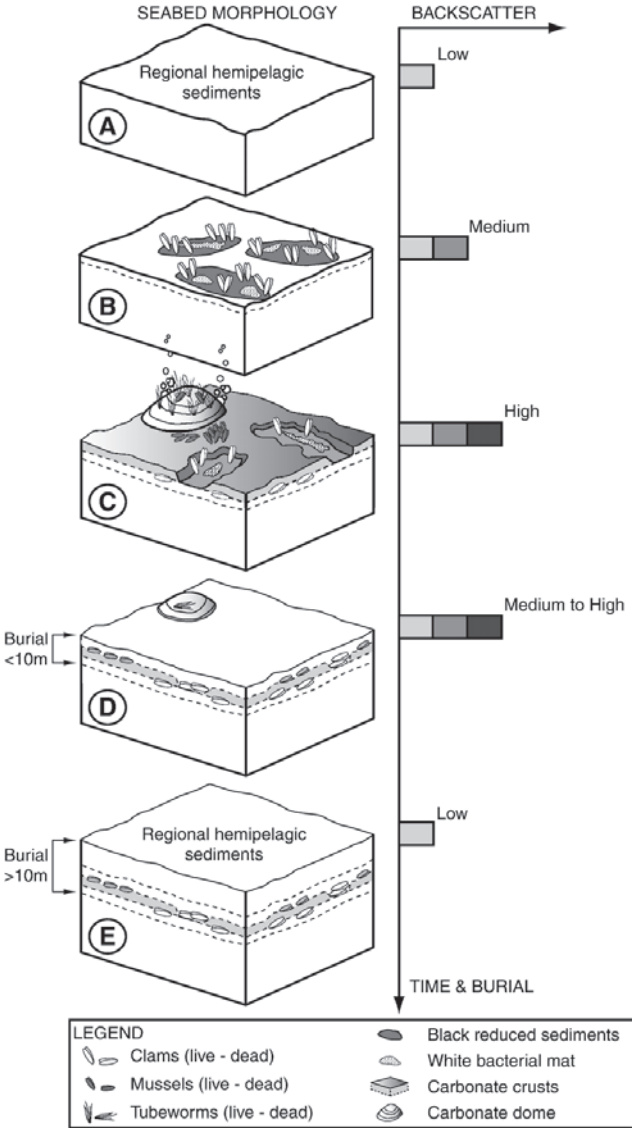

Fig. 1-11: The relation between backscatter intensity and the evolution of a cold seep environment at the seafloor (Gay et al. 2007).

1.1.5 Processes affecting gas bubbles in the water column

In recent years the acoustic surveys and also direct visual observations of seep sites documented the emanation of gas as bubbles in various sites. Since the bubbles are positive buoyant in the water column they are rising upwards. The fate of bubbles rising through the water column has been studied by several authors (e.g. Leifer and Patro 2002; Patro et al. 2002; McGinnis et al. 2006). The main parameters controlling the destiny of a gas bubble are the initial water depth of the gas release, the bubble size and rising velocity, the aqueous methane concentration, as well as the presence of upwelling flows (Leifer and Judd 2002), and surface active substances (Leifer and Patro 2002). Furthermore, the balance between two general processes affects a methane bubble and determines if and in which rate it dissolves (Fig. 1-12): On the one hand, expansion occurs in the course of ascent due to the decreasing hydrostatic pressure as the bubble rises (Leifer et al. 2000; Leifer and Judd 2002) but on the other hand gas exchange processes between the gas bubble and the ambient water take place resulting in a fast decrease of methane content inside the bubbles. As the bubble is highly supersaturated in methane with respect to the surrounding sea water, the gas rapidly diffuses out of the bubble due to the concentration difference, where it gets oxidized by microbes (De Angelis et al. 1991; Valentine et al. 2001). In the opposite direction dissolved air (i.e. nitrogen and oxygen) enters the bubble. This process is also responsible that the bubbles reaching shallower depths or even the sea surface often do not contain methane anymore (McGinnis et al. 2006).

As mentioned before, the bubble size is crucial for the fate of the gas contained, because larger bubbles transport more methane and potentially a greater fraction of the initial methane amount to shallow water depth compared to their smaller counterparts (MacDonald et al. 2002). To predict the fate of gas emissions at cold seeps, it is therefore essential to know the bubble size distribution and the rising velocities. So far, the only two bubble

size distributions from deep-sea settings including the average bubble size and rising velocities are published by Leifer and MacDonald (2003) and Sahling et al. (2009).

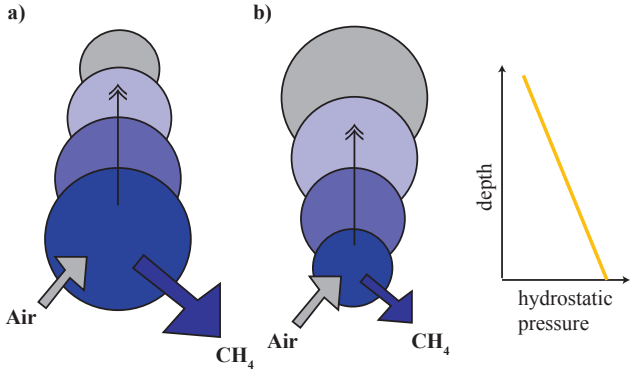

Fig. 1-12: Schematic drawing illustrating the processes affecting a gas bubbles. a) Methane outflow is much greater than air inflow and the bubble size decreases. b) When air inflow and methane outflow are similar, the bubble size increases due to pressure decrease as the bubble rises. (Adopted from Leifer and Judd (2002).

It was shown that the bubble size distribution depends on the sediment characteristics (such as grain size, porosity, density, adhesiveness, elasticity) and the orifice geometry (Leifer et al. 2010). A clear correlation exist as well between bubble size distribution and flow rate, where low fluxes show a narrow size distribution and high fluxes a much broader distribution (Leifer and Culling 2010). Gas emissions with low fluxes depend only on the sediment parameters and an increase of flux would increase the amount of emitted bubbles but not their size (Leifer and Culling 2010). Gas emissions with high flow rates produce larger bubbles but due to fragmentation also a wide range of bubble sizes is produced in these plumes (Leifer et al. 2004). Furthermore, surfactant contamination is an important parameter modifying bubble size distribution, especially when higher hydrocarbons are present and bubbles become oil coated. The bubble size distribution of oil-coated bubbles is broad and non-Gaussian shaped (Leifer and MacDonald 2003). Other surfactants in and on bubbles are primary organic matter such as polysaccharides produced by phytoplankton, protein and lipid substances but also ionic surfactants as salt (Patro et al. 2002), but have primarily an influence on the rising velocity of the bubbles (Leifer and Patro 2002).

The rising speed of a bubble mainly depends on its size. In general, rising speeds for "clean" (without surfactants) bubbles increase with bubble radius up to a size of approximately 0.7 mm r_e (Leifer et al. 1995). The flow around those small bubbles is laminar and does not influence the ascent but the larger the bubbles become, they begin to oscillate and deformation appears within the bubbles, which causes wakes (Leifer and Judd 2002). Bubbles with radii greater than ~0.7 mm not only oscillate in shape but also in their pathways what decreases their rising velocity. Still larger bubbles are influenced by stronger wake instabilities and have higher modal oscillations. Perpendicular oscillations decrease therefore and the rising velocity become faster again (Leifer et al. 1995). In contrast, surfactants (as oil or gas hydrates) strongly decrease the rising velocity of bubbles larger than ~0.6 mm, resulting from the reduction of the interfacial mobility, the so-called Maragoni effect (Patro et al. 2002). An generally increase of the rising velocity could be caused by upwelling effects when high flux rates in a plume or strongly pulsing emissions accelerate the surrounding water (Leifer and MacDonald 2003). An upwelling flow could therefore decrease the time for bubbles to reach the mixed layer or even the sea surface (Leifer et al. 2004). This phenomenon has been observed first at seeps in the Santa Barbara Channel in 20 – 70 m water depth by inducing dye clouds into the bubble streams (Leifer et al. 2000) and Leifer and MacDonald (2003) calculated upwelling flows for bubble streams in the Gulf of Mexico in 550 m deep seeps of up to 20 cm s^{-1} for high flow vents.

A useful method to reveal information about the fate of gas bubbles emanating from the seafloor is by using hydroacoustic systems, because in addition to localization of bubble emission sites at the seafloor, this technique is also suitable to

follow the bubbles rising in the water column. Gas bubbles in the water column can be recorded by echosounder as acoustic anomalies (flares) and it was shown that bubbles emitted from sites at water depths of several hundred meters below sealevel (mbsl) usually dissolve in the water column (Fig. 1-13; Merewether et al. 1985; Zonenshayn et al. 1987; Heeschen et al. 2003; Schmale et al. 2005; Greinert et al. 2006; McGinnis et al. 2006; Sauter et al. 2006; Nikolovska et al. 2008; Sahling et al. 2009).

Enhanced bubble lifetime is provided when the gas exchange process is hampered. Within the gas hydrate stability zone (GHSZ) gas hydrate rims form around methane bubbles (Maini and Bishnoi 1981), hence, preventing them from dissolution (Rehder et al. 2002). When passing the upper limit of the GHSZ, however, the hydrate rims and therefore as well the entire bubbles rapidly dissolve (Heeschen et al. 2003; Greinert et al. 2006; Sauter et al. 2006). Recent investigations showed that the coating with oil seeping from the seafloor probably also hampers bubble dissolution and may be responsible for increased methane concentrations at the sea surface (Solomon et al. 2009). Thus, the presence or absence of an oil coating significantly influences the bubble lifetime (MacDonald et al. 2002; De Beukelaer et al. 2003) and might represent an important criterion allowing methane within gas bubbles to reach the atmosphere.

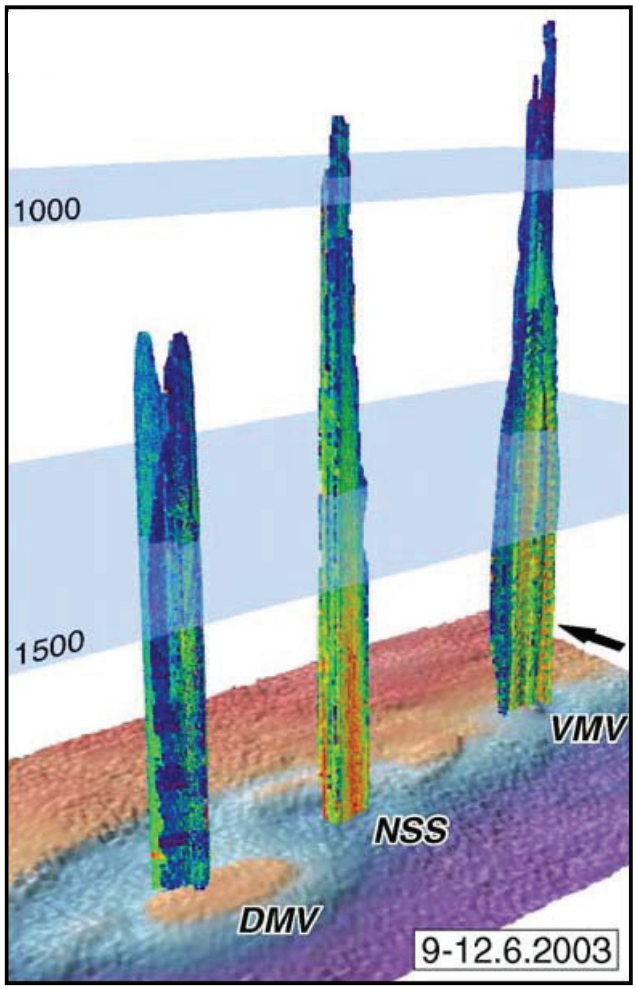

Fig. 1-13: Three strong gas emissions related to mud volcanoes in the Sorokin Trough in the Black Sea recorded by singlebeam echosounder showing that deep-water bubble emissions can reach heights up to 1300 m, but nevertheless dissolve within the water column (Greinert et al. 2006).

1.2 Relevance of the marine methane emissions

Following water vapor and carbon dioxide, methane is the most abundant greenhouse gas in the troposphere. In addition, methane is actually much more effective as greenhouse gas than CO_2 (Wuebbles and Hayhoe 2002). The contribution of marine emissions to the atmospheric inventory and their possible impact on climate change is therefore of high interest.

1.2.1 Contribution to the atmospheric methane inventory

The input of methane into the atmosphere from marine hydrocarbon seeps is discussed controversial in the current literature. The general view about the sources for methane emitted into the atmosphere differentiates between anthropogenic and natural emissions. Methane emitted from anthropogenic sources including rice cultivation, ruminant animals, biomass burning, waste disposal and fossil fuel exploitation represents the main contribution of the atmospheric methane inventory today accounting for at least more than 60% of the total global budget (Fig. 1-14; IPCC 2007; Wuebbles and Hayhoe 2002; Kvenvolden and Rogers 2005; Kroeger et al. 2011). Natural methane arises from wetlands, oceans, forests, fire, termites and geological sources; whereas the by far largest sources of those are the wetlands (IPCC 2007; Wuebbles and Hayhoe 2002). The global methane emission of 500 – 600 Tg yr^{-1} (IPCC 2007; Dlugokencky et al. 2011) is nearly balanced by terrestrial uptake through biological oxidation in dry soils, tropospheric reactions with oxidizing radicals (OH) and loss to the stratosphere (IPCC 2007; Kroeger et al. 2011). A minor sink is probably the oxidation by chlorine within the marine atmospheric boundary layer (IPCC 2007; Platt et al. 2004). Dlugokencky et al. (2011) also mentioned the importance of the methanotrophic bacteria in soils as an important sink by oxidizing methane and their significance within the ocean water as an uptake before reaching the atmosphere if increasing methane emissions in the ocean may take place, for instance due to gas hydrate dicomposition.

While the total global emissions are constrained reasonably well, estimates by source sector vary considerably (Dlugokencky et al. 2011). In particular, global estimations of methane fluxes from geological sources in the marine realm such as natural gas seeps and mud volcanoes are highly uncertain due to a very small data base. They have

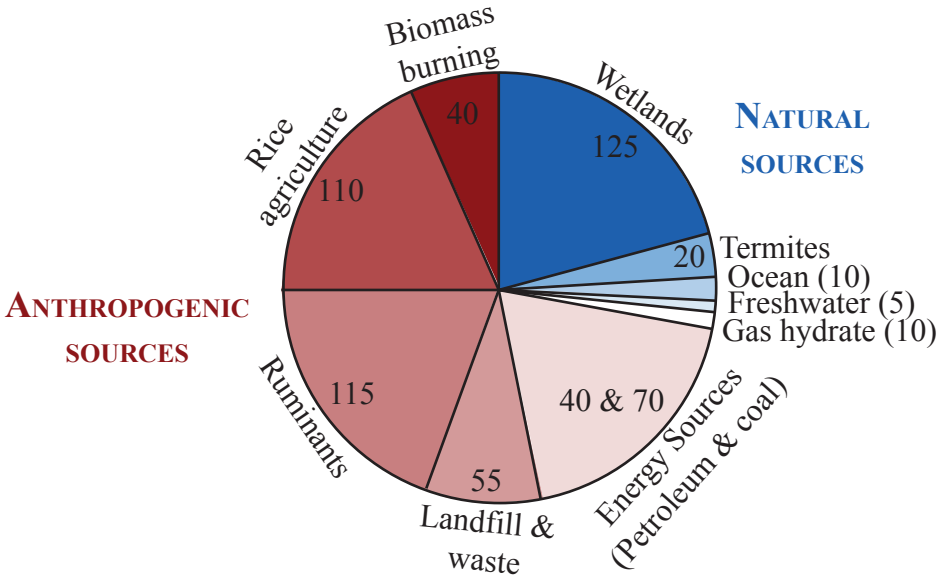

Fig. 1-14: Diagram of different methane sources and their relative portions contributing to the atmospheric budget. Numbers are in Tg yr^{-1}. Anthropogenic sources have a clearly higher input than natural sources and within the natural emissions gas hydrates represent as well only a minor part (adopted from Kvenvolden and Rogers 2005).

not been included in the estimation of the sources presented in the IPCC report 2007, but it was mentioned that they could be as large as 40 – 60 Tg yr^{-1}, which are numbers that were roughly estimated by Kvenvolden and Rogers (2005) and Etiope and Klusman (2002). Nevertheless, individual values for methane emissions related to the different geological settings show very high uncertainties and vary in orders of magnitude, complicating the estimation of the total input into the atmosphere. Already the gas emission into the hydrosphere is challenging and becomes even more difficult regarding the deep-water environment. Prior to the study presented here, the gas bubble emissions at only four geological structures in deep-water settings have been quantified. Two estimations exist for marine mud volcanoes, where the fluxes range between 14.4×10^6 g yr^{-1} at the Vodyanitskii mud volcano located in the Black Sea (Sahling et al. 2009) and ~100×10^6 g yr^{-1} at the Håkon Mosby mud volcano in the Barents Sea (Sauter et al. 2006). Another quantified gas emission related to a small area is a seep site in the Gulf of Mexico, GC 185, which emits about 31.4×10^6 g yr^{-1} (Leifer and MacDonald 2003). These three estimations were achieved by visual analyzes of gas bubble streams, in addition, a larger seep area at Hydrate Ridge was quantified by gas sample analyzes resulting in a methane flux through gas bubbles of 350×10^6 g yr^{-1} (Torres et al. 2002) and similar values for the same site were estimated by Heeschen et al. (2005) through water column methane budgeting.

1.2.2 Implication on climate change

Paleoclimatic records show strong coupling of climate and atmospheric methane abundance (Nisbet and Chappellaz 2009; Dlugokencky et al. 2011). Because of the enormous amount of methane stored in gas hydrates and as free gas below the gas hydrates, the growth or decay of this reservoir has been intensively discussed to have a direct influence on changes of the climate in the past and in the future. With rising temperatures, the methane hydrates could become destabilized and release large amounts of methane into the atmosphere and increase global warming. Most studies, however, agree upon the improbability that gas hydrate directly triggered changes from glacial to warm periods (Kroeger et al. 2011). Nevertheless, gas hydrate might dicompose as an effect of initialized warming resulting in a positive feedback and therefore contribute to further warming. The determination of the global gas hydrate quantities is crucial to predict future impact but as described in chapter 1.1.2, the estimation of this methane reservoir still contains very large uncertainties.

During the Paleocene-Eocene thermal maximum (PETM) the bottom water temperature rapidly rose by ~5°C and together with numerous findings of peculiar negative $\delta^{13}C$ values of seafloor carbonates, Dickens et al. (1995) hypothesize a massive release of methane related to this period (Fig. 1-15). As the methane from the gas hydrates is strongly depleted in ^{12}C, relatively low amounts of methane emissions (~2000 Gt) could explain the $\delta^{13}C$-excursion (Dickens et al. 1995; Katz et al. 1999; Dickens 2001). Nevertheless, there are different publications arguing against the theory of gas hydrate decomposition associated with the PETM and Dickens (2011) recently published a study explicitly discussing arguments in favor and against this relation.

Luyendyk et al. (2005) additionally propose that natural marine hydrocarbon seeps at continental margins today play a minor role in the global atmospheric inventory, but have been probably more importance during glacial times when the sealevel was lowered. This hypothesis is in accordance with the observation of increased rates of seep-carbonate precipitations during glacial times with low sea level (Teichert et al. 2005b; Kiel 2009).

Different particular scenarios leading to enhanced gas emissions and eventually also to an increased methane flux into the atmosphere are discussed in the literature. Landslide triggered massive eruptions (Paull et al. 2003; Zhang 2003; Davy et al. 2010) or liberation of vast amounts of methane through

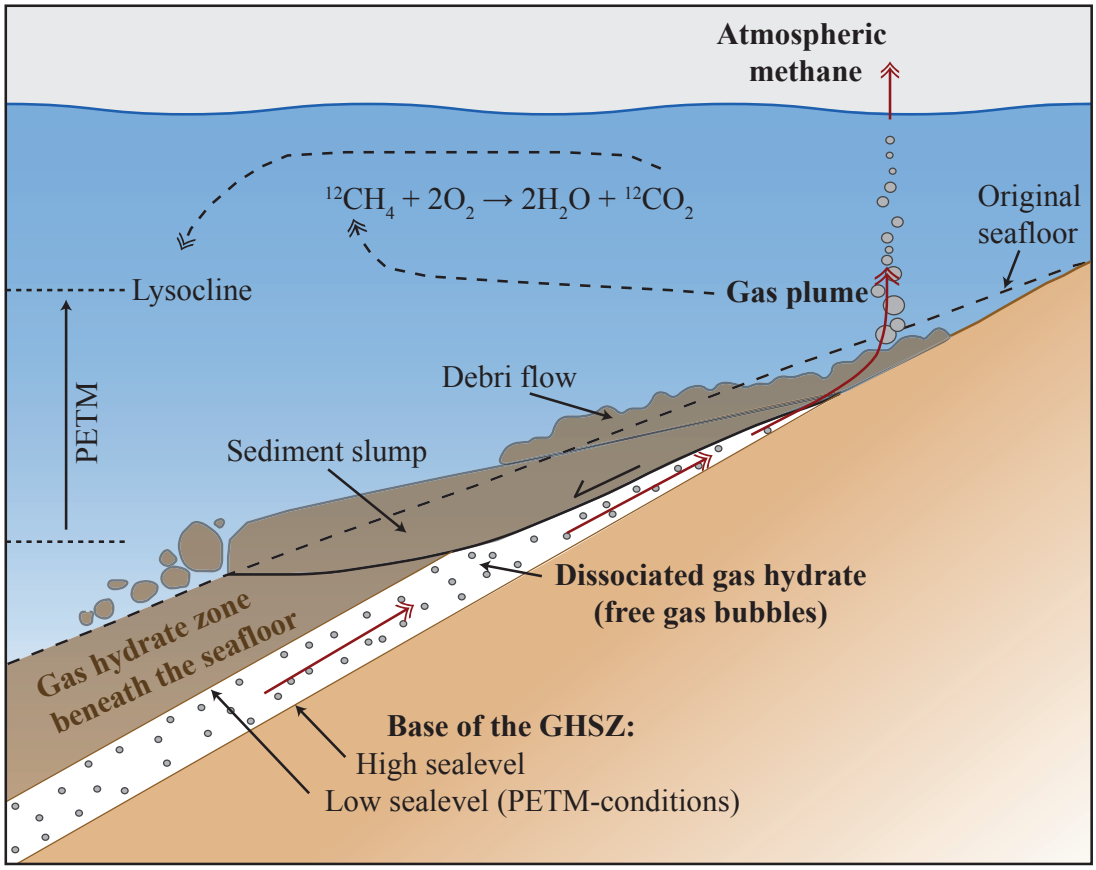

Fig. 1-15: The hypothetic scenario for the PETM (modified after Dickens et al. 1995; Katz et al. 1999; Maslin et al. 2010) suggests that a shift of the GHSZ resulted in the decomposition of huge amounts of gas hydrates. The release of methane into the ocean water leads to enhanced CO_2 content which further shifted the lysocline.

seafloor erosion were postulated, as suggested for instance at the continental margin of Japan by (Bangs et al. 2010). Hornbach et al. (2004) pointed out, that vast amounts of free gas bubbles trapped below the GHSZ are highly sensitive to changes in ambient conditions and could be released through faults as the result of critical pressure build-up. A sudden release of bubbles would rise collectively forming a bubbly water plume, providing a rapid pathway to enter the atmosphere (Zhang 2003). Another important process is gas hydrate rafting, which was first assumed by Suess (Suess et al. 2001) and was recently proposed to account for the rough morphology observed at the Batumi seep area (Pape et al. 2011a). Suess et al. (2001) described floating gas hydrate chunks of up to 1 m at the seasurface above Hydrate Ridge where they slowly decomposed and discharged methane into the atmosphere. Brewer et al. (2002) confirmed by controlled experiments that already small pieces of initially ~0.1 m size easily reached the surface after rising through a 780 m water column. In addition, it was already earlier suggested by Paull et al. (2003), that slumping events may liberate large gas hydrate pieces to float up and reach the seafloor as well.

Other important facts on rapid gas hydrate decomposition were brought up by Pecher (2002) arguing that high amounts of gas hydrate lenses exist in shallow areas, which are much faster effected during bottom water warming than deeply buried deposits. These gas hydrate lenses form because the BGHSZ is not as often schematized a strait plain within the sediment column, but has numerous intrusions with upward flow of warmer

fluids which increases the area where gas hydrates may be present (Wood et al. 2002) and lenses in shallow sediment depth may have developed.
Future global warming is discussed in the scientific community as there are first evidences for methane release caused by warming of the bottom water (Biastoch et al. 2011). Buffett and Archer (2004) estimated by modeling that the predicted methane inventory would decrease by 85% as the response to a bottom-water warming of 3°C, but revised this in the publication of 2009 (Archer et al. 2009) to probably 50%. Worldwide, the most rapid response to global warming is in the Arctic and a spatially inhomogeneous warming of Arctic bottom water temperatures have been postulated by modeling (Biastoch et al. 2011) and past temperature reconstruction of planktonic foraminifers (Spielhagen et al. 2011). Biastoch et al. (2011) stated that the resulting methane release on global warming is substantial but limited in the next century, nevertheless could enhance ocean acidification and oxygen depletion in the water column. Enhanced gas emissions at the West Spitsbergen continental margin were reported by Westbrook et al. (2009), probably as a result of destabilizing gas hydrates (Fig. 1-16). They propose a down slope shift of the GHSZ due to a 1°C increase in temperature of the northward flowing West Spitsbergen current over the last thirty years. Reagan and Moridis (2009) support this hypothesis by simulating the response of warmer conditions on the dissociation of shallow gas hydrates.
It is generally accepted that future climate change has a major impact on high-latitude wetlands and permafrost areas leading to large positive greenhouse feedbacks on global warming. High amounts of gas hydrates are stored in permafrost acting as a shallow methane reservoir and affected first in the cause of global warming and the released methane additionally further contributes to global warming. The findings by Shakova et al. (2010) at the East Siberian Arctic Shelf point to the susceptibility of a large sub-sea permafrost reservoirs besides permafrost structures on land as

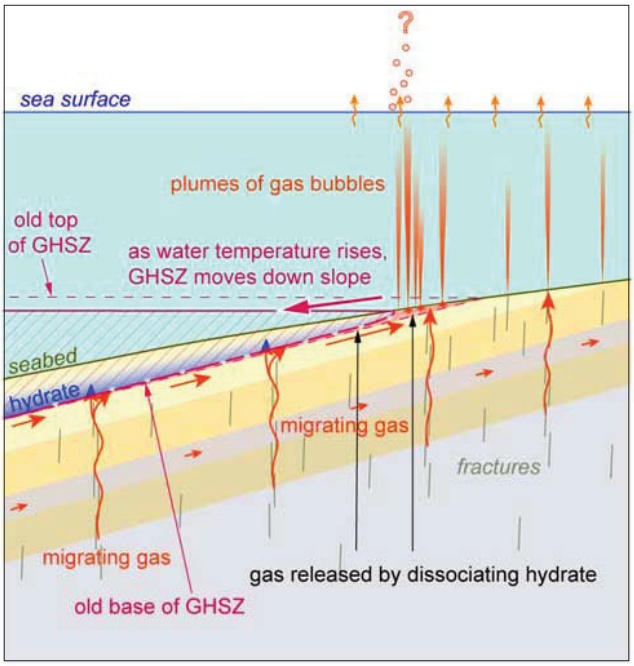

Fig. 1-16: Schematic illustration of the enhanced gas emissions resulting from the shift of the GHSZ due to recent bottom water warming at the West Spitsbergen continental margin (Westbrook et al. 2009).

they are as well very temperature sensitive (Kroeger et al. 2011). Huge amounts of methane are already escaping to the atmosphere (Shakova et al. 2010) (Fig. 1-17), which is in the same order of magnitude as previous estimates of methane venting from the global ocean (IPCC 2007; Reeburgh 2007).

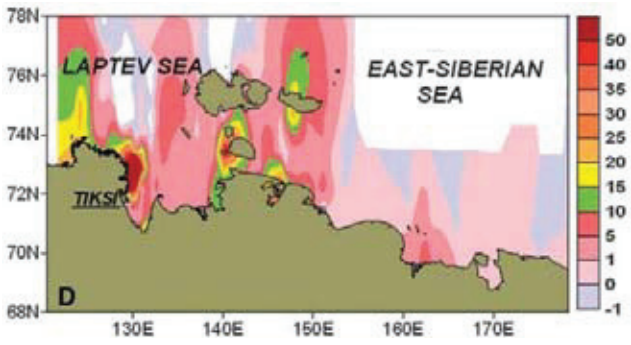

Fig. 1-17: Methane fluxes into the atmosphere over the East Siberian Arctic Shelf (Shakova et al., 2010).

Kroeger et al. (2011) noted that also negative feedbacks do exist and have to be considered. They argue with the relation that a sealevel rise related to melting of ice caps will reduce the methane release from the seafloor as the gas hydrate stability increases in correspondence to the pressure increase. And they also emphasize that part of the methane seepage is not reaching the atmosphere, but remains in the ocean water, where it might have also an indirect impact on global warming. The additional carbon input from seeps into shallow waters and thus increasing carbon saturation in the oceans may lead to a hampered capability of atmospheric carbon uptake and therefore increasing global warming effect.

2 Motivation and objectives of this study

Gas bubble emissions at cold seep systems on the seafloor:

One overarching objective of this study is to investigate the significance of gas bubble emissions at hydrocarbon seeps qualitatively by providing detailed description of the seafloor manifestation in hydrocarbon seep areas using visual observation during ROV-dives. Several issues have been considered while describing the gas emissions within a seep area:

- Do gas bubble emissions generally occur?
- Where are the bubble streams located within the seep area?
- How many individual bubble streams are distributed within the seep area? If there is more than one, do they show differences in intensity?
- How many bubbles are emitted within the individual bubble streams? Are they steadily escaping as bubble trains or irregularly in form of bubble pulses?
- Do the bubble streams show spatial or temporal variability?
- What is the bubble size distribution? What are the rising velocities?

Furthermore, the significance of gas bubbles related to the manifestation of hydrocarbon seepage close to the seafloor has been in focus during this study. This issue is particularly highlighted in the second manuscript (Chapter 5) regarding a seep area in the Black Sea, where shallow gas hydrate accumulate due to focused gas bubble flux.

Gas bubble emissions as a methane transport pathway:

The second overarching objective of this study is to answer the question weather or not deep-water gas emissions matter for the methane inventory of the atmosphere. Although previous studies have shown that natural submarine gas emissions seem to play a minor role for the atmospheric inventory, the estimations especially for geological sources are poorly constrained. In particular, high uncertainties concern the role of deep-water gas emissions, as this source is not well constrained so far.
This objective primarily implicates the quantification of the methane flux through gas bubbles. This is important to be able to present absolute values of methane flux as contribution to the global methane cycle. Furthermore, methane flux as gas bubbles may be viewed as efficient transport pathway of methane bypassing the benthic filter, which can only remove methane dissolved in advecting pore water. In order to achieve a quantification of methane fluxes as gas bubbles, areas with evidence of present gas emissions were mapped by echosounder to first detect and localize the gas emissions and to get an overview about the extent of the area influenced by gas emissions. Furthermore, variability and localized intensity differences can be roughly determined. With this information ROV dives can be planned and conducted to rapidly discover the areas of major gas emissions and afterwards obtain high-definition videos, which can be used for characterization and quantification of the bubble streams.
Another very important objective within this issue is the fate of the methane emitted from these deep-water seep areas in the water column. The rising height of bubble streams can be determined by using echosounder systems, revealing an evaluation about the bubble lifetime and their possible viability to the sea surface.

Gas bubble emissions at different geological settings:

In order to study the significance of the bubble transport pathways in different geological settings, three different hydrocarbon seep systems have been subject of this investigation located at tectonically active as well as passive continental margins. The first case study is located at the Makran continental margin, which is an active margin and gas bubble emissions are connected to the anticlines within an extensive accretionary wedge. The other two case studies are located at passive continental margins, related to deltaic deposits. One is situated in the Black Sea, which is known as a large anoxic basin. The other study area is located in the Eastern Mediterranean Sea at the Nile Deep Sea Fan. The comparison of the seep areas connected to the three different settings may provide differences as well as similarities of manifestations of seepage at the seafloor, their controlling factors and the fate of bubbles in the water column.

3 Study areas

Natural gas bubble emissions have been investigated in three areas during this work (Fig. 3-1). Each area is characterized by specific geological settings, fluid flow mechanisms and the evolution of cold seep environments as well as their local gas bubble escape at the seafloor.

The Makran continental margin was investigated during M74 Legs 2 and 3 in 2007. Results regarding the detected gas bubble emissions, a rough estimation of the methane flux and an evaluation of the gas bubble fate are presented in the first manuscript (Chapter 4).

The Black Sea seepage has been intensively studied already before beginning of this PhD work. New data achieved during three cruises (M72/3, MSM15/2 and M84/2) in 2007, 2010 and 2011 were combined within the second manuscript (Chapter 5).

Several sites in the Eastern Mediterranean Sea were surveyed during MSM13 Legs 3 and 4 in 2009 and part of the results from the Nile Deep Sea Fan are presented in the third manuscript (Chapter 6).

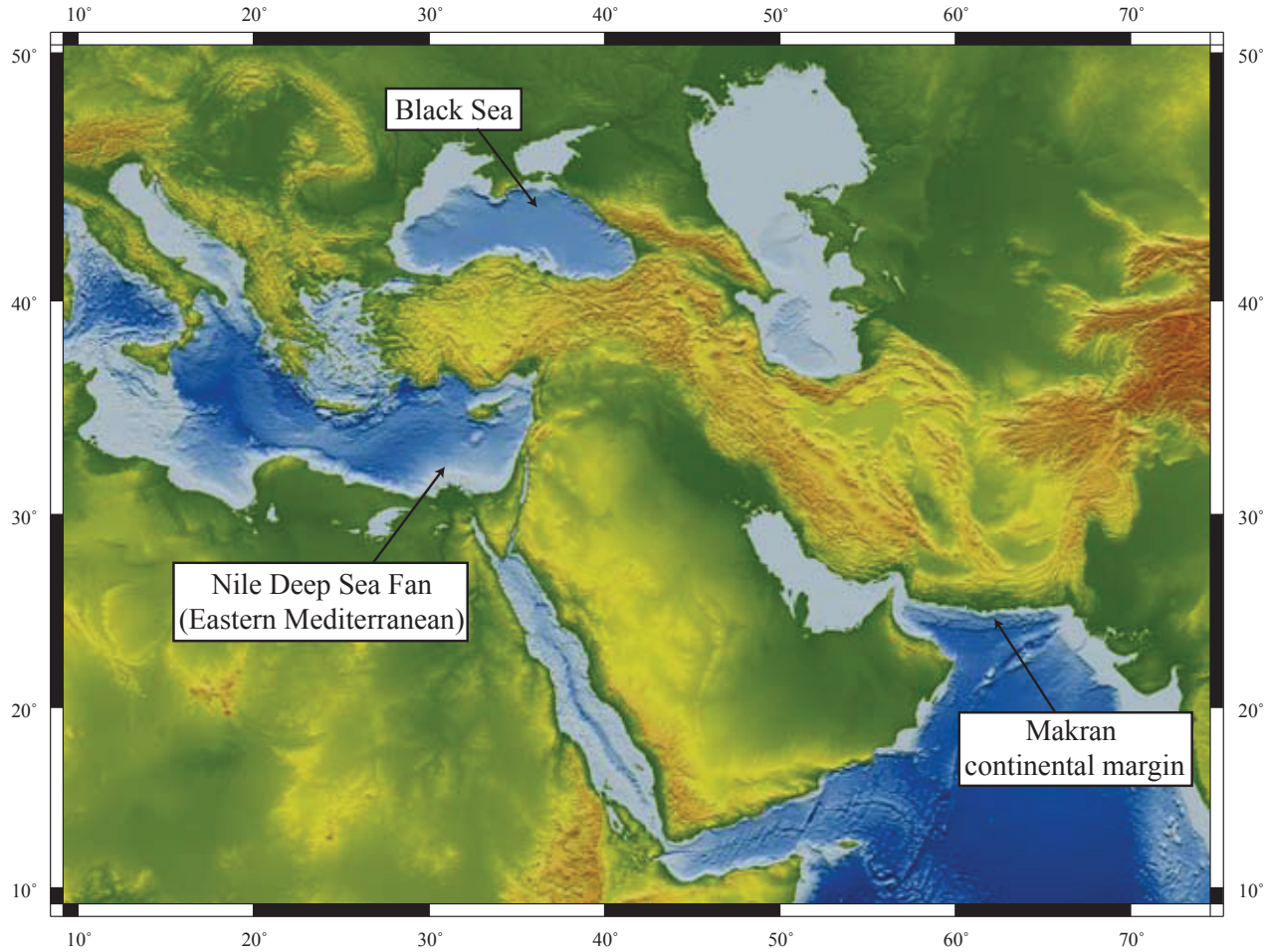

Fig. 3-1: Overview map (based on the Gebco bathymetric data set; Smith and Sandwell 1997) showing the locations of the three case studies presented in the manuscript in Chapters 4 to 6.

3.1 Makran continental margin

The Makran continental margin (MCM) is the submarine part of an accretionary wedge, which has formed due to the subduction of the Arabian Plate under the Eurasian Plate. The wedge is considered as one of the most extensive worldwide (Clift and Vannucchi 2004), extending about 1000 km from W to E and 400-500 km from N to S. A remarkably thick sediment pile of up to 7 km enters the subduction zone (Fig. 3-3). Approximately the upper 4 km of the incoming sediment section deposited on the subducting plate becomes offscraped and incorporated in the accretionary wedge, while the lower portion of about 3 km thickness is underthrusted and, at least partly, underplated further towards the hinterland (Platt et al. 1985; Kopp et al. 2000).

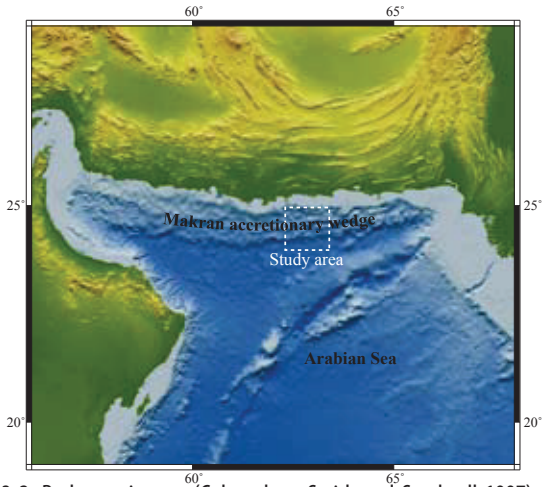

Fig. 3-2: Bathymetric map (Gebco-data; Smith and Sandwell 1997) of the the northern Arabian Sea with the Makran accretionary wedge as a result of plate convergence.

First evidences for high gas concentrations in the sediments at the MCM were obtained during seismic investigations as so-called "bright spots" (White 1977). Seismic studies further indicated a bottom simulating reflector (BSR) occurring throughout the continental slope (Minshull and White 1989), suggesting the presence of free gas below the gas hydrates stability zone (GHSZ). However, first direct evidence for fluid seepage was obtained in the 1990's by discovering typical seep-associated features, such as methane anomalies in the water column, seep-related authigenic carbonate precipitation, and chemosynthetic clams (von Rad et al. 1996; von Rad et al. 2000). Despite the findings of seeps, their occurrence was limited to water depths shallower than 850 mbsl, which lead to the hypothesis that gas hydrates may act as a cap rock preventing the seepage of methane through the sediments (von Rad et al. 2000; Delisle and Berner 2002). In addition to the seeps at the continental slope, mud volcanoes have been described at the shelf close to the coast (Delisle 2004), on land (Ellouz-Zimmermann, 2008), as well as seaward of the first accretionary ridge (Wiedicke et al. 2001) (Fig. 3-3). However, the mud volcanoes on the abyssal plain appear inactive (Wiedicke et al. 2001).

In 2007 the Meteor cruises M74 Legs 2 and 3 were conducted at the MCM (white box in Fig. 3-2) in order to better evaluate the distribution and characteristics of cold seeps and related gas emissions (Bohrmann et al. 2008). Therefore, a systematic search by using hydroacoustic systems was conducted and followed by visual inspections of several detected seep sites.

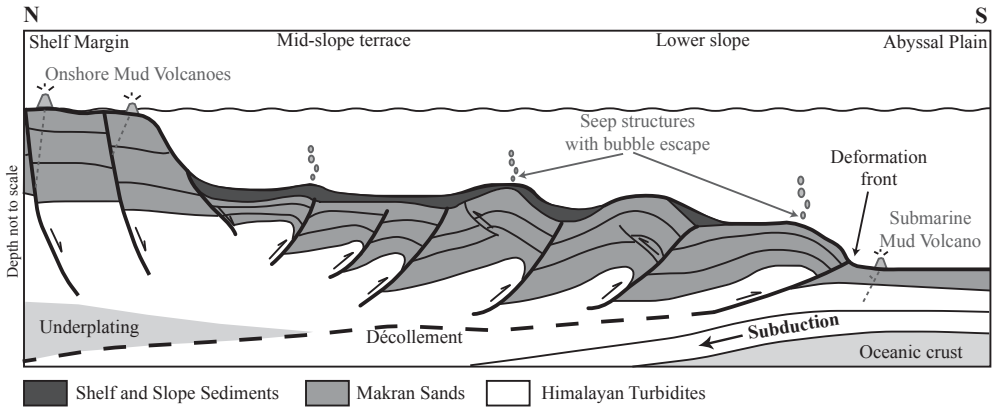

Fig. 3-3: Schematic profile through the accretionary wedge (modified after Grando and McClay 2007).

3.2 Black Sea

The Black Sea is a marginal sea with maximum water depth of 2.2 km, which is separated into a Western and Eastern basin. The basins are underlain by oceanic or thinned continental crust with a sediment cover of 10-19 km in thickness (Tugolesov et al. 1985). The Black Sea is interpreted as a back-arc basin which evolved during late Cretaceous times (Nikishin et al. 2003), as the Tethys was subducted northwards under the volcanic arc of the Balkanides and Pontenides. Stress field observations show that the Black Sea region is still in a dominantly compressional environment (Reilinger et al. 1997). The tectonic evolution of the basin is nevertheless characterized by alternations of extensional and compressional phases and by different stages of subsidence (Nikishin et al. 2003).

As numerous gas emission sites in the Black Sea are well-known, the intention of the last cruises was to determine methane emission fluxes in selected regions and to better evaluate the presence of near-surface gas hydrate deposits as they are potentially associated with free gas. One of the working areas is located at the Don-Kuban paleo-fan (southwest of the Kerch Strait, which is the connection between the Black Sea and the Sea of Azov). The large fan represents the paleo-delta of the Don and Kuban rivers (Barg 2007; Starostenko et al. 2010). Shale diapirs have been described in this area that are associated with folds of Oligocene-Miocene age and have probably undergone compaction processes since then (Meisner et al. 2009). Earlier studies report on the existence of gas emissions in this area (Egorov et al. 2003; Starostenko et al. 2010), but a thorough investigation of this region has not been performed prior to our cruises.

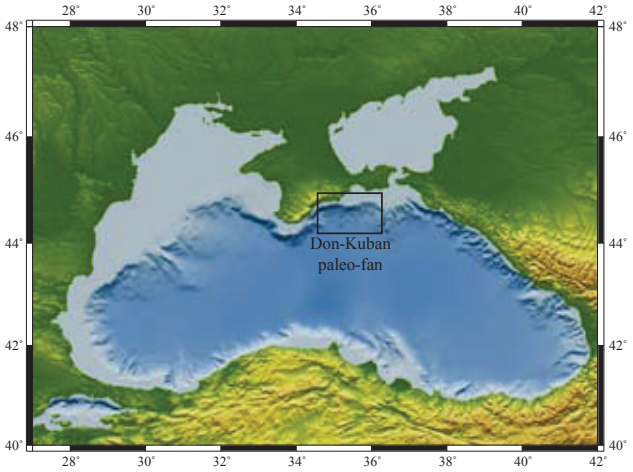

Fig. 3-4: Section of the bathymetric map (Gebco-data) focusing on the Black Sea. The three boxes indicate three of the working areas which have been investigated during the last cruises.

During M72/3, MSM15/2 and M84/2, the distribution of gas emissions was investigated by using hydroacoustic methods (Bohrmann 2007; Bohrmann 2011b; Bohrmann 2011a). The focus of the study presented in this work was laid on a newly discovered gas emission area, called the Kerch seep area, located at about 890 m water depth. AUV-based high-resolution bathymetric and backscatter data in combination with visual seafloor inspections and sampling during ROV dives were planned to provide a better understanding of this seep system.

3.3 The Nile Deep Sea Fan in the Eastern Mediterranean Sea

The Nile deep Sea Fan (NDSF) in the Eastern Mediterranean Sea is a thick sedimentary wedge formed since the late Miocene and the sedimentary sequence is mainly composed of terrigeneous sediments delivered from the Nile River (Salem 1976) and partly underlain by evaporitic layers deposited during the Messinian salinity crisis (Hsu et al. 1977; Ryan 1978) and salt-related tectonic deformations in the overburden sediments developed later. The interaction between salt tectonics and various sedimentary distribution processes, such as turbidites, slumps or debris flows, control the morphology and fluid-releasing structures at the NDSF (Gaullier et al. 2000; Mascle et al. 2000; Loncke et al. 2002; Loncke et al. 2004; Loncke et al. 2006; Loncke et al. 2009).

At the NDSF the existence of gas emissions at the seafloor and the distribution within the different provinces at the NDSF was already known prior to the cruise MSM13 Legs 3 and 4 conducted in 2009 (Loncke et al. 2004; Dupré et al. 2007; Bayon et al. 2009b; Dupré et al. 2010). Different fluid-releasing structures at the NDSF have been observed comprising pockmark structures and mud volcanoes, which occur either as mud cones <1 km in diameter or flat but huge mud pies (gas chimneys) with diameters up to 5 km (Fig. 3-6; Loncke et al. 2004).

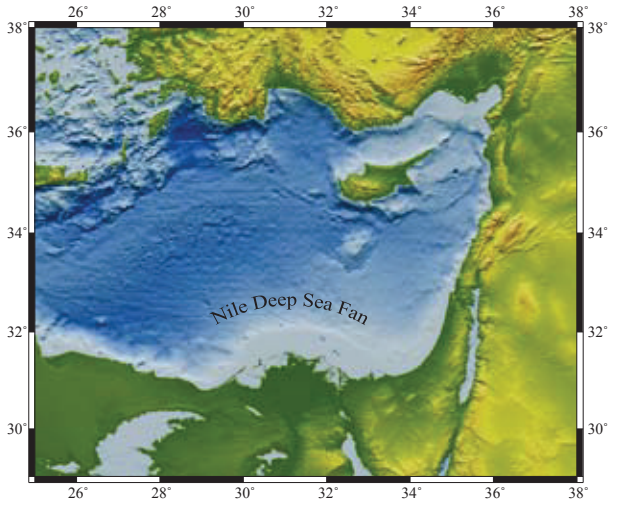

Fig. 3-5: Bathymetric map (Gebco-data; Smith and Sandwell 1997) in the Eastern Mediterranean Sea, where Maria S. Merian cruise MSM13 Legs 3 and 4 took place. A major focus was laid on the detection of gas emissions at the Nile Deep Sea Fan (NDSF).

In the central province at the NDSF, numerous areas of high backscatter at the seafloor imaged by multibeam systems have been interpreted as manifestation of fluid seepage, because visual observations showed that methane-derived authigenic carbonates are causing the high backscatter (Loncke et al. 2004; Zitter et al. 2005; Dupré et al. 2010). During MSM13 Legs 3 and 4 the gas bubble emissions located in the central province were investigated systematically by hydroacoustic surveys and visual seafloor observation with ROV and TV-MUC dives regarding their relation to carbonate-paved areas (carbonate slabs) and evaluation of the fate of bubbles in the water column.

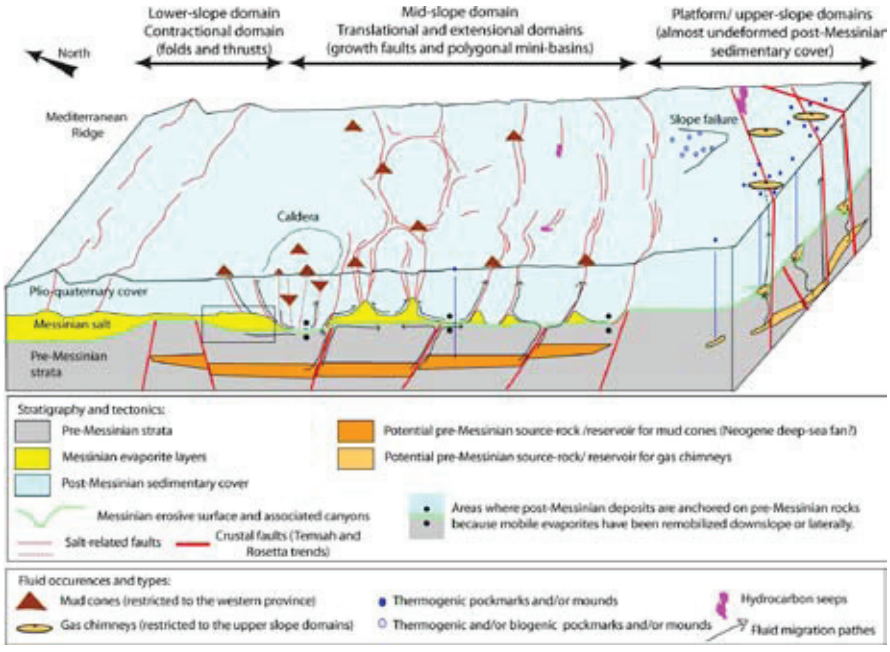

Fig. 3-6: Block diagram summarizing the most common settings of fluid escape structures at the NDSF (Loncke et al., 2004).

4 First case study (manuscript I):

Gas bubble emission from submarine hydrocarbon seeps at the Makran continental margin, offshore Pakistan

Miriam Römer*, Heiko Sahling, Thomas Pape, Volkhard Spieß, Gerhard Bohrmann

MARUM – Center for Marine Environmental Sciences and Department of Geosciences, University of Bremen, Klagenfurter Str., 28359 Bremen, Germany

* Corresponding author. Tel.: +49 (0) 421 218 65059; fax: +49 (0) 421 218 65099.
E-mail address: mroemer@marum.de

Submitted to Journal of Geophysical Research – Oceans
(4 July 2011)

4.1 Abstract

Evidence for twelve sites with gas bubble emissions causing hydroacoustic anomalies in 18 kHz echosounder records ('flares') were obtained at the convergent Makran continental margin. The hydroacoustic anomalies released from hydrocarbon seeps at water depths between 575 and 2870 m disappeared in the water column. Dives with the remotely operated vehicle 'Quest 4000m' revealed that several individual bubble emissions contributed to a hydroacoustic anomaly. Analyzed gas samples suggest that bubbles were mainly composed of methane of microbial origin. Bubble size distributions and rise velocities were determined and the volume flux was estimated by counting the emitted bubbles and using their average volume. We found that a low volume flux (Flare 1 at 575 mbsl: 90 mL min^{-1}) caused a weak hydroacoustic anomaly in the echosounder record whereas high volume fluxes (Flare 2 at 1027 mbsl: 1880 mL min^{-1}; Flare 5-Area C at 2870 mbsl: 760 mL min^{-1}) caused strong anomalies. The total flux of methane bubbles in the study area may be estimated multiplying the average flux of methane causing a strong hydroacoustic anomaly in the echosounder record with the number of recorded strong anomalies. The order-of-magnitude estimate further considers the temporal variability of some of the flares, assumes a constant flux over time, and allows a large range of uncertainty inherent to the method. Our results on the fate of bubbles and the order-of-magnitude estimation suggest that all of the ~40 $\pm$ 25 x 10^6 mol methane emitted per year from emissions within the gas hydrate stability zone remain in the ocean interior.

Keywords: Fluid seepage, gas flare, gas hydrate, methane, Makran accretionary wedge, bubble size distribution

4.2 Indroduction

Gas bubbles emanating from the sea floor into the water column have been observed at numerous sites around the world ocean margins from continental shelf to abyssal depths. They occur in a wide variety of geological settings related to a range of processes, e.g. tectonically active continental margins (Heeschen et al., 2005), thick sediment sequences at fan deposits (Artemov et al., 2007; Naudts et al., 2006), salt tectonics (Leifer et al., 2003), naturally leaking oil reservoirs (Bruening et al., 2010; Hornafius et al., 1999; MacDonald et al., 2004), hydrothermal circulation through sediments (Merewether et al., 1985; Zonenshayn et al., 1987), and destabilizing submarine permafrost due to global warming (Shakova et al., 2010). Most studies on bubble emissions were conducted at shallow water depths as these sites are often vigorously emanating methane, are comparatively easy to access, and contribute to the atmospheric methane inventory (Hornafius et al., 1999; Hovland et al., 1993; Judd, 2004; Kvenvolden et al., 2005; Schmale et al., 2005; Shakova et al., 2010). In contrast, detailed investigations of deep-water bubble emissions are rare. While numerous studies reported indirect evidence for gas bubble release into the water column based on echosounder records (Artemov et al., 2007; Bruening et al., 2010; Heeschen et al., 2005; Leifer et al., 2003; Merewether et al., 1985; Naudts et al., 2006; Zonenshayn et al., 1987) only four publications provide results from visual seafloor inspections at individual gas bubble emission sites. The flux of bubble-forming methane was reported for Hydrate Ridge at the Cascadia convergent margin (Torres et al., 2002), site GC 185 in the Gulf of Mexico (Leifer et al., 2003), Håkon Mosby mud volcano in the Norwegian Sea (Sauter et al., 2006) and Vodyanitskii mud volcano in the Black Sea (Sahling et al., 2009). This limited number of studies and the fact that site-specific emission varied by two orders of magnitude (Torres et al., 2002; Sahling et al., 2009) illustrates the need for additional flux estimations to better evaluate the significance of this frequently reported methane transport process.

Open questions remain regarding the quantity and fate of free methane that is emitted from deep-water seepage sites into the water column. By use of echosounder it was shown that bubbles emitted from sites at water depths several hundred meters below sealevel (mbsl) usually dissolve in the water column (Greinert et al., 2006; Heeschen et al., 2003; McGinnis et al., 2006; Merewether et al., 1985; Sahling et al., 2009; Sauter et al., 2006; Schmale et al., 2005; Zonenshayn et al., 1987). However, for a seepage site at a water depth of about 550 mbsl in the Gulf of Mexico, bubbles could be traced by echosounder throughout the water column to shallow water depths (De Beukelaer et al., 2003). Recent investigations at that site showed that the coating with oil concurrently seeping from the seafloor probably enhances the lifetime of gas bubbles and may be responsible for enhanced methane concentrations at the sea surface (Solomon et al., 2009). Thus, the presence or absence of an oil coating significantly influences the bubble lifetime. In the absence of oil, the main parameters controlling the fate of bubbles in the water column are water depth, initial bubble size, as well as temperature, salinity and methane concentration of the ambient water (Leifer et al., 2002). In addition, at shallow water bubble-induced upwelling may lead to enhanced methane transportation through the water column (Leifer et al., 2006; Sauter et al., 2006). Furthermore, for gas emissions situated within the gas hydrate stability zone (GHSZ), bubble dissolution is hindered during ascent due to the formation of a hydrate rim (Rehder et al., 2002).

The important question whether or not methane from submarine gas emissions reaches the atmosphere has been addressed by several models that quantitatively describe the fate of bubbles rising through the water column (Artemov et al., 2007; McGinnis et al., 2006; Solomon et al., 2009). The model of McGinnis et al. (2006), which is available as GUI (Greinert et al., 2009) describes, among other aspects, the gas exchange processes of a single bubble by considering bubble shrinking rates (Rehder et al., 2002) and was successfully

applied in the Black Sea, where the predicted bubble rising height matched the results from echosounder observations (McGinnis et al., 2006). The model takes into account some of the above mentioned factors, such as initial bubble size and initital rising speed, but does not consider bubble induced upwelling (Leifer et al., 2006; Sauter et al., 2006). In addition, new parameters on the dissolution kinetics of bubbles inside and outside the GHSZ became recently available (Rehder et al., 2009). Therefore, additional field data are needed to validate the single bubble model and to help refining it in order to better understand the fate of methane in the ocean.

The Makran continental margin (MCM) is the submarine part of an accretionary wedge formed due the subduction of the Arabian Plate under the Eurasian Plate. The wedge is considered as one of the most extensive worldwide (Clift and Vannucchi, 2004), as it extends about 1000 km from W to E and 400-500 km from N to S (Fig. 4-1). Fluid escape from the sea floor is a common phenomenon in accretionary subduction zones and has been reported for numerous areas (Le Pichon et al., 1992; Westbrook and Reston, 2002) including the MCM (Von Rad et al., 1996, 2000).

A recent multidisciplinary research campaign at the MCM conducted during R/V Meteor cruises 74 Legs 2 and 3 in 2007 revealed abundant evidence for gas bubble emission from sites spanning the upper shelf to the abyssal plain. As described in an accompanying study (Brüning et al., concomitant paper), a systematic search for seeps was carried out in a 50 km wide area that was almost completely mapped by swath echosounder and TOBI sidescan sonar (Fig. 4-2) in concert with seismic profiling, sediment echosounder surveys, and visual seafloor observations. In total 18 seep sites where identified including twelve sites with evidence for gas emissions (Brüning et al., concomitant paper). Some of the seeps and gas emissions were associated to anticlines that may act as traps for ascending hydrocarbons (Ding et al., 2010). In addition, gas was emitted from sediments located in the oxygen minimum zone, where it had been observed before (Von Rad et al., 1996, 2000).

This study concentrates on deep-water gas bubble emissions at the MCM. The 18 kHz signal of the single beam Parasound echosounder was employed in order to study the bubble emissions that show up as hydroacoustic anomalies (so-called flares) in the water column. Dives with the remotely-operated vehicle (ROV) 'QUEST 4000m' at the seafloor confirmed the presence of gas emissions and allowed to describe the emissions in detail. Gas samples were taken and its molecular composition analysed. One objective of the present study is to provide data such as bubble size distribution and rising speeds, and volume fluxes as basis for developing a better understanding of the significance of naturally driven hydrocarbon gas emissions. A further objective was to elucidate the fate of methane in the water column, which was studied in a combination of seafloor observations at bubble emissions with de-tailed surveys with echosounder.

4.3 Study area

The continuous subduction of the Arabian under the Eurasian Plate since Late Cretatecous times caused the formation of the Makran accretional wedge off Iran and Pakistan (De Jong, 1982). The average actual convergence rate is about 4 cm yr^{-1}, while the rate increases from western to eastern Makran (DeMets et al., 1990). The Murray Ridge is the south-eastern limit of the Arabian Plate, it is considered to be a divergent plate boundary with very low spreading rates (Gordon and DeMets, 1989). The northeastern part of the Arabian Sea has been defined as the Omara Microplate, which is separated from the Arabian Plate by a strike-slip fault named "Sonne" (Fig.4-1). The deformation front of the accretionary wedge is actually situated approximately 150 km seaward from the coastline and trends almost perpendicular to the convergence direction (Byrne et al., 1992). A remarkably thick sediment pile of up to 7 km enters the subduction zone. Approximately the upper 4 km of the incoming sediment section deposited on the subducted plate becomes offscraped and incorporated in the accretionary wedge, while the lower portion of about 3 km thickness is underthrusted and at least partly, later underplated further towards the hinterland (Kopp et al., 2000; Platt et al., 1985). This causes considerable uplift of about 1.5 mm yr^{-1} (White, 1983) and the seaward migration of the shoreline (Kopp et al., 2000; Platt et al., 1985). The morphology of the continental margin segment covering our study area is shown in Figure 4-2. The marine part of the Makran accretionary wedge consists of a narrow shelf, a steep upper continental slope, a considerably flat mid-slope terrace, and a lower slope (Kukowski et al., 2001). The latter is built by sequences of frontally accreted imbricated thrust slices which are morphologically expressed as long, narrow and steep accretionary ridges separated by ponde slope basins. Canyons cut through the mid slope terrace and the lower slope. The Sonne Canyon is discussed as part of the prolongation of the strike-slip fault (Sonne fault) marking the limit between the Ormara micro plate and the Arabian Plate (Kukowski et al., 2000).

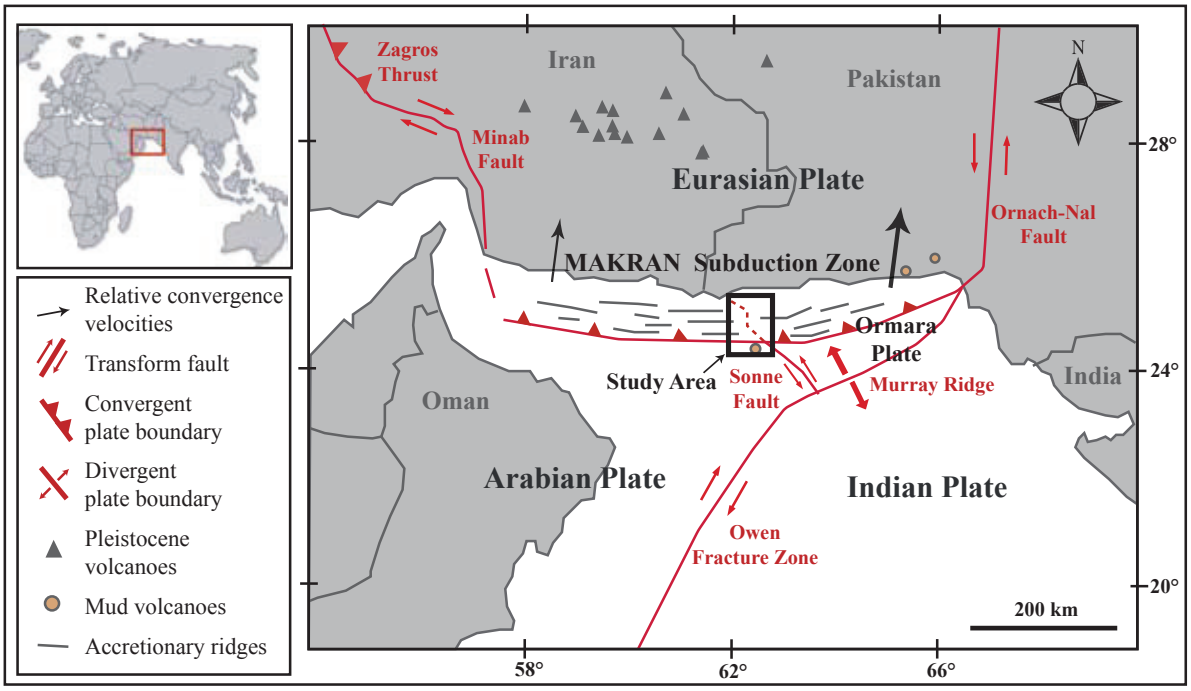

Fig.4-1: Tectonic map of the Makran subduction zone, which is formed by the collision of the Arabian with the Eurasian Plate. The subduction zone is bordered to the east by the Minab Fault and to the west by the Ornach-Nal Fault. Modified after Kukowski et al. (2001) and Grando et al. (2007).

The first evidences for high concentrations of gas in sediments at the Makran continental margin (MCM) were obtained during seismic investigations as so-called "bright spots". These were found at sites of incipient deformation on the abyssal plain, such as Nascent Ridge, and in the cores of folded sediment sequences (White, 1977). Seismic studies further indicated a bottom simulating reflector (BSR), which marks the lower boundary of the gas hydrate stability zone (GHSZ), occurring approximately 500-800 m below the seafloor throughout the continental slope (Minshull and White, 1989). First direct evidence for fluid seepage was obtained in the 1990's by discovering of typical seep-associated features, such as methane anomalies in the water column, seep-related authigenic carbonate precipitation, and chemosynthetic clams (von Rad et al., 1996, 2000). Despite the findings of seeps, their occurrence at depths within the in GHSZ was spatially very limited, which lead to the hypothesis that gas hydrates may act as cap rock preventing the seepage of methane through the sediments (Delisle and Berner, 2002; von Rad et al., 2000). The hypothesis was fostered by the observation of abundant evidence for gas emissions above the upper limit of the GHSZ at about 850 mbsl. It was speculated that at that depths, methane-rich fluids may escape that have been channeled at the base of the GHSZ in the sediments from deeper sections. While this is one possible scenario, von Rad et al. (2000) already noticed the interaction between methane seepage and the existence of a pronounced oxygen minimum zone (OMZ) at water depths between 100 and 1100 mbsl. Methane production may be enhanced in the sediments due to the fact that a lack in oxygen prevents aerobic respiration within the OMZ, which leads to high amounts of organic matter that is available for fermentative processes producing methane. This process could explain the numerous small gas emissions that were found at the respective depths. In turn, methane emissions may contribute to the depletion of oxygen enhancing the OMZ.

In addition to the seeps at the continental slope (von Rad et al., 1996, 2000), mud volcanoes have been described at the shelf close to the coast (Desile, 2002), on land (Ellouz-Zimmermann, 2008), as well as seaward of the first accretionary ridge (Wiedicke et al., 2001). However, the mud volcanoes on the abyssal plain appear inactive (Brüning et al., concomitant paper; Wiedicke et al., 2001).

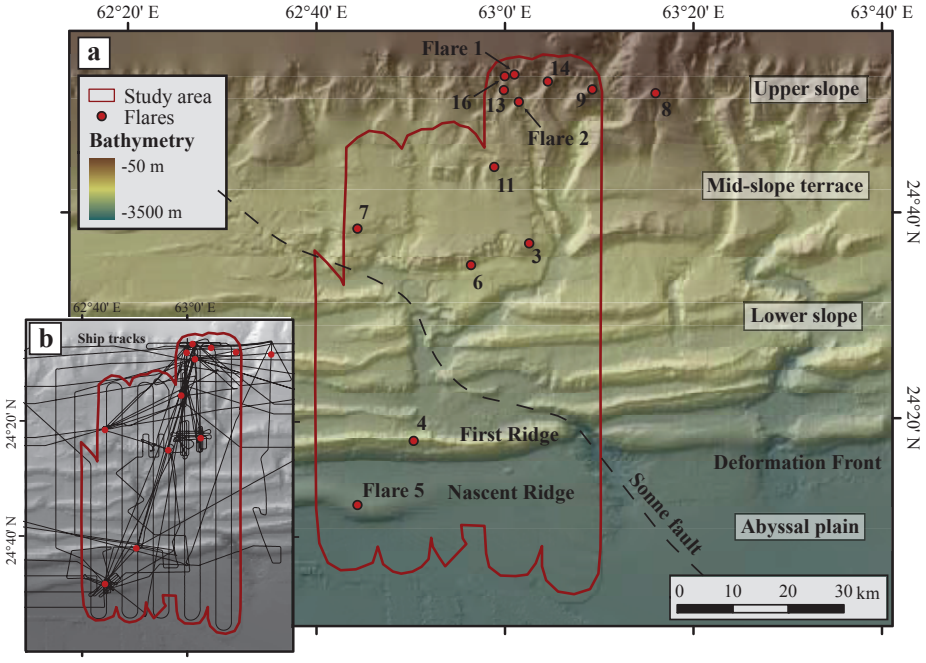

Fig. 4-2: Shaded bathymetric map of the Makran continental margin (MCM) from about 400 m (light colour) to 3000 mbsl (dark colour) water depth. The area encircled by a red line marks the outline of the study area where a systematic search for seeps was carried out using deep towed sidescan sonar (Brüning et al., concomitant paper). Red circles denote the locations where one or more flares were found. (a) Gas emissions were studied in detail at the seafloor by remotely operated vehicle (ROV) 'QUEST at Flare 1, 2, and 5. (b) Shiptrack of R/V Meteor Cruise 74 Leg 2 & 3 illustrating the intensive survey efforts in the study area.

4.4 Methods

4.4.1 Water column investigations

Data used in this study were obtained during R/V Meteor Cruise M74 Legs 2 and 3 in October-November 2007. The ships parametric sediment echosounder system (PARASOUND) operating with a primary frequency of 18 kHz provided a parametric (difference) frequency of ~4 kHz for sub-surface imaging. The primary frequency of 18 kHz allowed recording of hydroacoustic anomalies in the water column caused by gas bubbles (commonly termed flares) as described by Nikolovska et al. (2008). Depending on the overall objectives of the cruise, the single pulse mode was selected as transmission sequence. In this mode, which is preferentially used for flare imaging, only one pulse at a time is present in the water column. In the pulse train mode, used for sub-seafloor imaging, a burst of up to 16 separate pulses is sent out followed by the reception period for multiple echoes, which enhances the horizontal resolution especially in the deep-sea. A consequence of the pulse train mode is that the acoustic image is affected by uneven spatial sampling. The nominal transducer opening angle (4°) corresponds to a footprint size of about 7% of the water depth. The software ATLAS PARASTORE was used for online data processing and plotting. The program SeNT (developed by H. Keil, University of Bremen) was employed for basic data processing and plotting. PARASOUND data as well as metadata are stored and made accessible through the PANGAEA data base (http://doi.pangaea.de).

4.4.2 Seafloor inspections of seepage sites and gas volume flux calculations

The deep water remotely operated vehicle (ROV) MARUM-'QUEST 4000m' was deployed for 18 dives during the M74/3 Cruise. Underwater navigation was achieved using the shipboard IXSEA Posidonia ultra short baseline system (USBL) with an accuracy of 5-10 m. For detecting gas emissions the water column was scanned horizontally for backscatter signals caused by bubbles with the Kongsberg 675 kHz Type 1071 forward looking scanning sonar head mounted on the ROV as described by Nikolovska et al. (2008). Three cameras were used to record video sequences. For close-up videos, a near-bottom mounted broadcast quality 3CCD HDTV video camera was used (Inside Zeus). The spatial resolution is 2.2 MegaPixel at 59.94 Hz interlaced.

Calculations of bubble sizes, bubble emission frequency, and rise velocities were done by analyzing video recordings frame by frame using the software program Adobe Premiere Pro. Individual frames were exported to the program ImageJ (developed by Wayne Rasband, National Institutes of Health, Bethesda, MD; available at http://rsbweb.nih.gov/ij/) for bubble size analyses. Only those bubbles that rose in the same focal plane as an instrument of known size were analyzed. The major (a) and minor axis (b) were measured and the volume was calculated by assuming a rotational ellipsoid with the equivalent spherical radius (r_e) (Equation 4-1).

$$r_e = (a^2 b)^{1/3} \qquad \text{(Eq. 4-1)}$$

The volume flux was calculated in milliliter (ml) per minute (min) by multiplying the average bubble volume with the frequency of emitted bubbles. Because the volume of a bubble is proportional to the third power of r_e, the error in estimating r_e is considered to be the major source of uncertainty in the volume flux estimate. We therefore allow a range of uncertainty for our volume flux estimation by using the standard deviation of r_e, in analogy to earlier studies (Sahling et al., 2009; Sauter et al., 2006).

The volume flux was converted to mass flux (mol CH_4 per minute or year) for comparison with published data. As methane behaves different to an ideal gas, the ideal gas law has to be complemented by the compressibility factor Z (Equation 4-2).

$$PV = nRTZ \qquad \text{(Eq. 4-2)}$$

P is pressure (Pa), V is volume (mL), n is the amount of substance (mol), R is the ideal gas constant (8.314472 J/K mol), and T is temperature (K). The compressibility factor Z can be calculated by solution of a modificated reduced form of the Van

der Waals equation using the critical parameters of temperature and pressure (calculated values for Z are: (a) 0.87 in 575 mbsl with T=285.65 K, (b) 0.77 in 1020 mbsl and T=282.15 K, (c) 0.96 in 2870 mbsl and T=275.15 K).

4.4.3 Molecular and stable carbon isotopic analysis of emitted gas

The molecular composition of venting gas collected close to the seafloor with the pressure tight Gas Bubble Sampler (GBS) (Pape et al., 2010) was analyzed on board using a gas chromatograph (GC; Agilent). Low-molecular-weight hydrocarbons (C_1–C_5) were separated, detected, and quantified with a capillary column connected to a flame ionization detector. The analytical error estimated by multiple injections of commercial hydrocarbon standards was <2.0% for each signal. Stable carbon isotope signatures ($^{13}C/^{12}C$) of methane were measured by GC–isotope ratio mass spectrometry using a Trace GC Ultra connected via GC IsoLink and ConFlo IV interface to a MAT 253 isotope mass spectrometer (Thermo Fisher Scientific). The reproducibility of stable carbon isotope determinations is estimated at ±0.2‰.

4.5 Results

4.5.1 Hydroacoustic investigations

Within the study area (Fig. 4-2), twelve sites with indications for active bubble emissions were found between 575 and 2870 mbsl. Gas bubbles rising through the water column were recorded as acoustic anomalies (flares) with the 18 kHz echosounder. A compilation of representative echographs of all flares is summarized in Table 4-1 and shown in Figure 4-3. Several significant results can be drawn from Figure 4-3:

(1) At each site, at least one hydroacoustic anomaly occurs but in some instances even more. The terms "Flare 1", "Flare 2" etc. are used to assign sites with gas emissions irrespective of the number of individual flares at one site.

(2) Several gas bubble streams released at water depths exceeding 900 mbsl (i.e. within the GHSZ) can be traced hundreds of meters through the water column. Generally, observed flare heights have to be regarded as minimum heights, as the flare position in relation to the vessel could not be specified precisely and only if the gas emission is located exactly in the echosounder beam, the maximum height can be recorded. However, in the water column above Flare 5 (at 2870 mbsl) bubbles can be traced vertically about 2000 m, which, to the best of our knowledge, is the highest flare ever observed. But close to the upper limit of the GHSZ (~850 mbsl) the hydroaocustic anomalies vanish, indicating that the bubbles either become too small or completely dissolve in the water column.

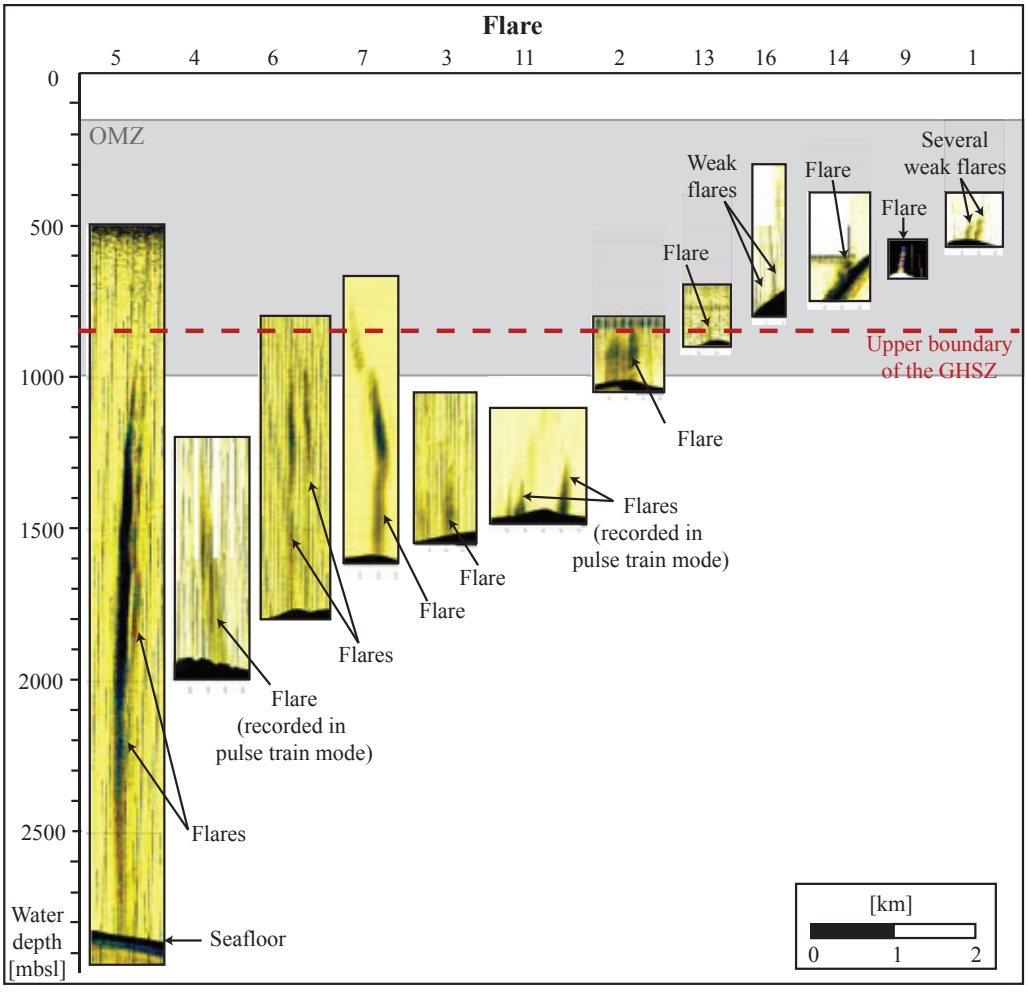

Fig. 4-3 : Summary of echographs recorded by 18 kHz echosounder of all gas emission sites found in the study area. The flares are located in different water depths and the respective echograms were plotted accordingly. The vertical extent of the oxygen minimum zone (OMZ) and the upper limit of the gas hydrate stability zone (GHSZ) are indicated. Flares were recorded with varying echosounder settings, ship speeds and survey efforts, which leads to differences in the quality of plotting the flares.

(3) The intensities of most hydroacoustic anomalies recorded by echosounder at water depths exceeding ~850 mbsl (i.e. within the GHSZ) appear stronger than those emitted at shallower water depths. Although the backscatter intensity depends also on the position of the flare within the echosounder beam, most flares were crossed various times and we are confident, that strong gas emissions were recorded at least ones as an intense flare. Flares above four of the seven seep sites within the GHSZ (Flare 2, 5, 6, and 7) were intensive and the rising bubbles could be followed to about 850 mbsl. Furthermore, the hydroacoustic anomalies at Flare 11 were likely also intensive, but as it was recorded using the echosounder pulse train modus (see chapter 4.3.1), its shape differs from that of other flares recorded in single pulse modus and accordingly, the bubble rising heights could not be determined. Flare 3 and 4 were the only hydroacoustic anomalies in deeper water that appeared weak. In summary, five of the seven deep-water emission sites are classified as strong (Flare 2, 5, 6, 7, and 11) comprising a total of 9 individual hydroacoustic anomalies. In contrast to the deep water (>850 m) flares, the general appearance of those at shallower water (<850 m) appear weaker, i.e. the reflection intensities are generally weaker, individual reflections within the flare can be seen, and the maximal rising height is less.

Table 4-1: Summary of the location and the characteristics of gas emissions in the study area. As flares were recorded with varying echosounder settings, ship speeds and survey efforts, the quality of the echosounder recording for the purpose of flare imaging was either good (+) or bad (-).

Site	Location		Water depth	Quality of echosounder recording	Number of hydroacoustic anomalies	Max. height hydroacoustic anomaly	Relative intensity hydroacoustic anomaly	Dive number of ROV QUEST 4000m	ROV observation at seafloor
	Latitude (°N)	Longitude (°E)	[m]			[m]			
Flare 1	24°53.64'	63°01.45'	575	+	several	270	weak	183, 184	6 sites with bubble streams
Flare 9	24°52.17'	63°09.25'	660	+	1	80	weak	-	-
Flare 14	24°52.74'	63°04.66'	750	-	1	-	weak	-	-
Flare 16	24°53.49'	63°00.51'	750	+	1	150	weak	-	-
Flare 13	24°51.87'	63°59.86'	910	+	1	50	weak	-	-
Flare 2	24°50.80'	63°01.44'	1027	+	1	340	strong	180, 181, 188, 189, 193	10 sites with gas emissions
Flare 11	24°44.52'	63°58.71'	1475	-	2	-	strong	194	1 site found, not video documented
Flare 3	24°37.23'	63°02.55'	1543	-	1	250	weak	190	Gas emission no found
Flare 7	24°38.58'	62°44.34'	1650	+	1	850	strong	182, 185, 191	5 sites with bubble streams
Flare 6	24°34.89'	62°56.32'	1806	+	2	900	strong	186	Gas emission no found
Flare 4	24°17.91'	62°50.25'	1955	-	1	-	weak	195	Gas emission no found
Flare 5	24°11.77'	62°44.38'	2870	+	3	2000	strong	179, 187, 192	4 sites with gas emissions

4.5.2 Regional examples

Flare 1

Flare 1 is located at about 575 mbsl within the Oxygen Minimum Zone (OMZ) on a crest of a NE–SW trending ridge at the upper slope (Fig. 4-4a). Several individual flares, generally weak in intensity and well separated, have been recorded during 18 kHz echosounder surveys in this area with heights between 40 and 270 m (Fig. 4-5). We picked those positions from the echograms where the hydroacoustic anomalies occurred close to the seafloor (Fig 4-5). All of these anomalies are plotted along the ship track (Fig. 4-4a) illustrating that bubble emissions occur in an area of about 200 m in diameter. In addition, bubble emissions occur as well outside this area but were only sporadically recorded. Within the 200 m wide area, the gas emissions aligned in Figure 4-4a were continuously active over the eight days observation periods albeit with varying intensity. Varying gas bubble emission fluxes from this site is suggested by varying flare patterns with regard to flare heights, shape, reflection intensity, and number of individual lines of higher reflectivity observed during echosounder surveys. However, also methodical produced changing geometric parameters may have a part in the variability displayed in the echograms.

Dives with the ROV in the area assigned as Flare 1 revealed the existence of 18 individual seepage sites along the dive track as documented by patches of microbial mats (Fig. 4-6a). At six of these mat patches (Fig. 4-4b) we observed bubbles rising from the central parts. We hypothesize that gas emission at all of the 18 observed microbial mat patches generally occurs, but may be intermittent and, thus, not observed for all microbial mat sites during ROV inspection.

At individual emission sites, the bubbles rose as continuous or transient single streams, with up to three streams (Fig. 4-6). Bubbles were of circular to elliptical shape and oscillated considerably during ascent. As the flare site is located above the GHSZ, gas bubbles should not be covered by hydrate skins, which is in agreement with the observation that accumulated bubbles form one gas phase in

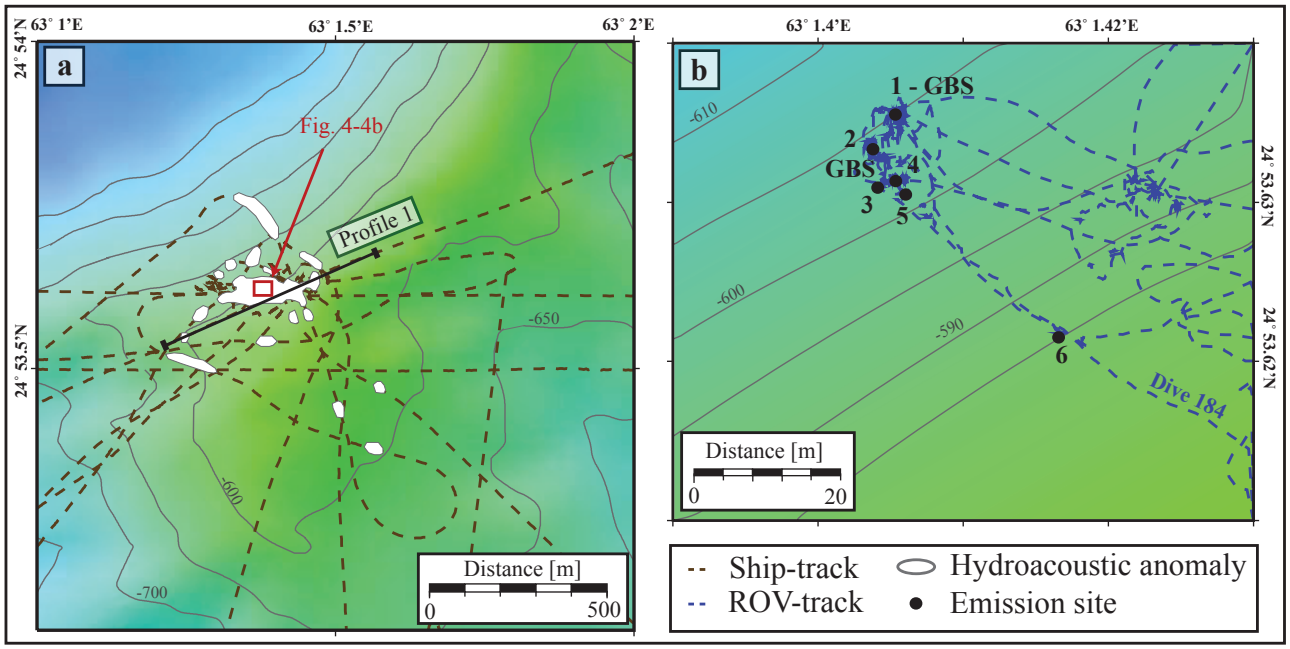

Fig.4-4: (a) Bathymetric map in the area around Flare 1 with the ship-track and hydroacoustic anomalies in the water column. (b) Detailed map of the seep area with the six emission sites found during two ROV dives.

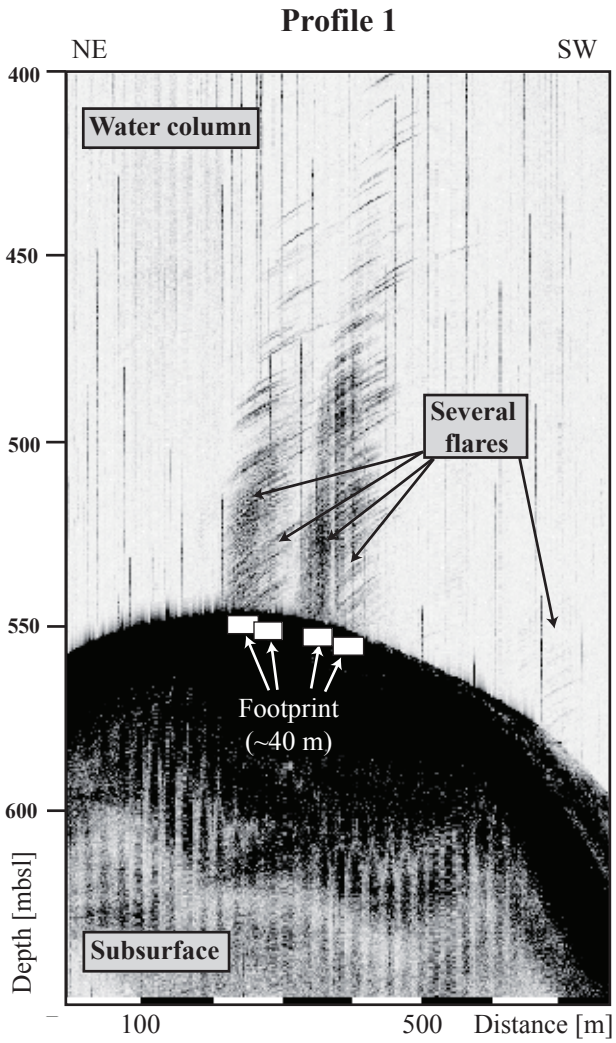

Fig. 4-5: Echogram recorded during crossing the gas emissions at Flare 1. Rising gas bub-bles cause hydroacoustic anomalies (flares) in the water column. See Fig. 4a for location of the profile.

the GBS funnel (Fig. 4-6b).

From the ROV videos the average equivalent spherical radius at emission site 1 within Flare 1 was estimated to be 0.281 ± 0.053 cm (n = 119) (see table 4.2 and chapter 4.4.3). Theses numbers correspond to mean bubble volumes of 0.103 ± 0.055 mL. During an observation period of about four minutes, on average about 1.4 bubbles were emitted per second from this particular site, which corresponds to a flux of 8.65 mL min^{-1}. Assuming that the average bubble size measured at emission site 1 is representative for the six emission sites discovered in the area of Flare 1 (Fig. 4-4b), the total bubble flux was estimated by counting the number of emitted bubbles at each site ranging between 0.003 and 7.4 bubbles per second (Table 4-2). The total emission from all six emission sites was ~90 ml min^{-1}. Assuming that the gas entirely consists of methane, this value corresponds to a methane flux of 0.25 ± 0.13 mol CH_4 min^{-1} (Table 4-2).

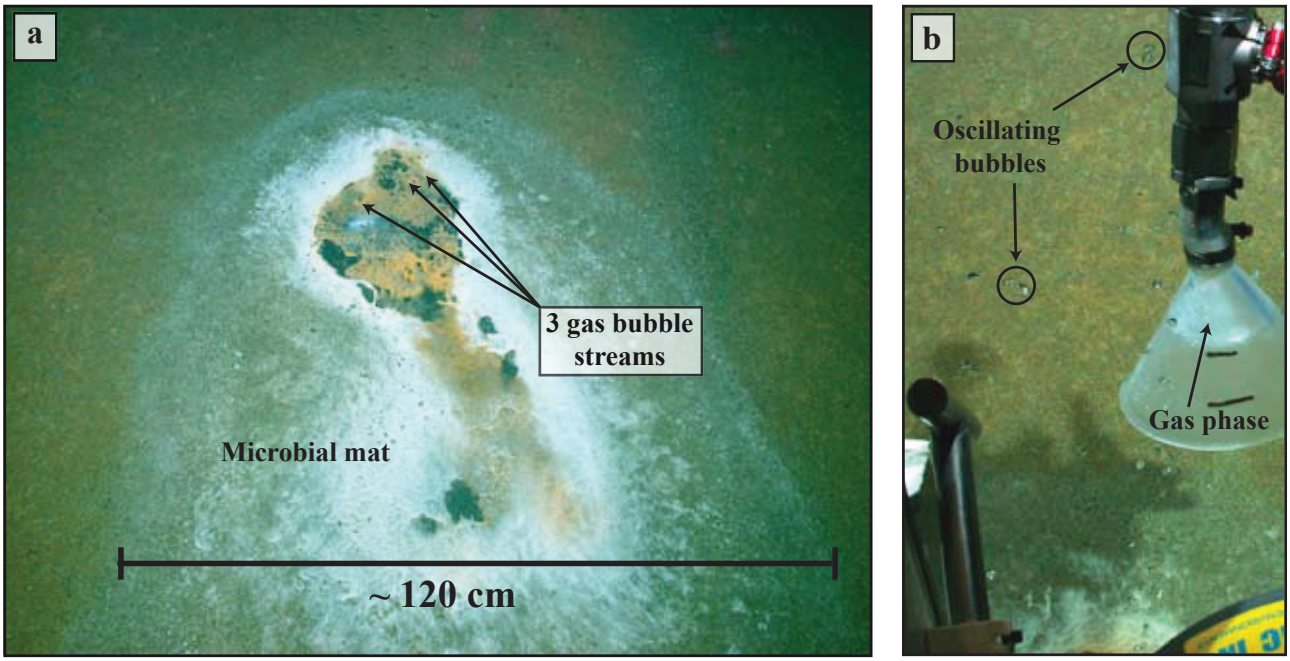

Fig. 4-6: Still images of bubble emissions in the area of Flare 1 taken during ROV dive 184. (a) Three bubble streams escape from emission site 2 from the sediment which is covered by a microbial mat. (b) Observation of oscillating bubbles. The gas sampled in the funnel of the Gas Bubble Sampler showed no evidence for hydrate formation. (Images copyright of MARUM University of Bremen).

Table 4-2: Estimation of the methane flux at the three sites Flare 1, 2, and 5 – Area C where detailed seafloor observations were conducted with the ROV 'QUEST 4000m' in the study area at the MCM.

Site	Emission site no.	Bubble emission frequency [bubbles/s]	Bubble radius r_e [cm]	SD	n	Volume flux [ml/min]	SD	Methane flux [mol CH_4/min]	SD
Flare 1	1	1.4	0.28	0.05	119	8.65	4.62	0.02416	0.01290
	2	7.4				45.73	24.42	0.12772	0.06820
	3	4.8				29.66	15.84	0.08284	0.04424
	4	0.6				3.71	1.98	0.01036	0.00553
	5	0.0				0.03	0.02	0.00009	0.00005
	6	0.0				0.02	0.01	0.00005	0.00003
	Total	**14.2**	**0.28**	**0.05**	**119**	**87.81**	**46.89**	**0.25**	**0.13**
Flare 2	1	65.0	0.35	0.08	90	830.70	760.50	4.71	4.31
	2	6.3				45.45	2.33	0.26	0.01
	3	25.0	0.22	0.03	43	65.40	25.50	0.37	0.14
	4	-							
	5	55.6	0.22	0.03	207	156.79	73.39	0.89	0.42
	6	9.9	0.23	0.06	217	36.98	31.61	0.21	0.18
	7	27.5				199.98	10.24	1.13	0.06
	8	15.0				109.08	5.59	0.62	0.03
	9	-							
	10	56.0	0.26	0.04	47	265.44	134.80	1.50	0.76
	Total	**260.3**	**0.307**	**0.11**	**604**	**1709.82**	**1043.95**	**9.68**	**5.91**
Flare 5	1a	147.3	0.238	0.09	413	287.63	168.63	3.76	2.21
Area C	1b	15.2				64.84	1.73	0.85	0.02
	2	52.4	0.273	0.06	508	313.46	267.24	4.10	3.50
	3	14.7				62.71	1.68	0.82	0.02
	Total	**229.6**	**0.257**	**0.08**	**921**	**728.64**	**439.28**	**9.53**	**5.75**

Flare 2

Flare 2 is located below the OMZ at 1024 to 1040 mbsl close to the crest of a N-S trending ridge (Fig. 4-2). Comprehensive echosounder surveys documented a widespread occurrence of flares (Fig. 4-7a) with heights spanning from 110 to 400 (on average ~180 m) at this ridge (Fig. 4-8). Flares are characterized by clouds of high acoustic backscatter (Figs. 4-3 and 4-8) that, in contrast to those recorded at Flare 1 (Fig. 4-5) for instance, lack any internal structure. We relate the absence of noticable internal structures in pronounced flares to the emission of large amounts of bubbles into the water column, which can not be resolved by our hydroacoustic method.

During four ROV dives performed to locate all bubble emission sites within the Flare 2 area, ten linearly arranged emission sites were found over a distance of 275 m (Fig. 4-7b). Because we systematically searched for the bubble streams we are confident that we found almost all currently active emission sites.

Gas bubbles emanate through chemosynthetic communities typically associated with cold seeps such as mats of sulphide oxidizing filamentous bacteria (Fig. 4-9b) or vesicomyid clams co-occurring with ampharetid polychaets (Fig. 4-9c). At nine of the ten sites two or more bubble streams occur. Four sites show vigorous bubble escape, sometimes in pulses, from several orifices creating numerous bubble streams over a wider area.

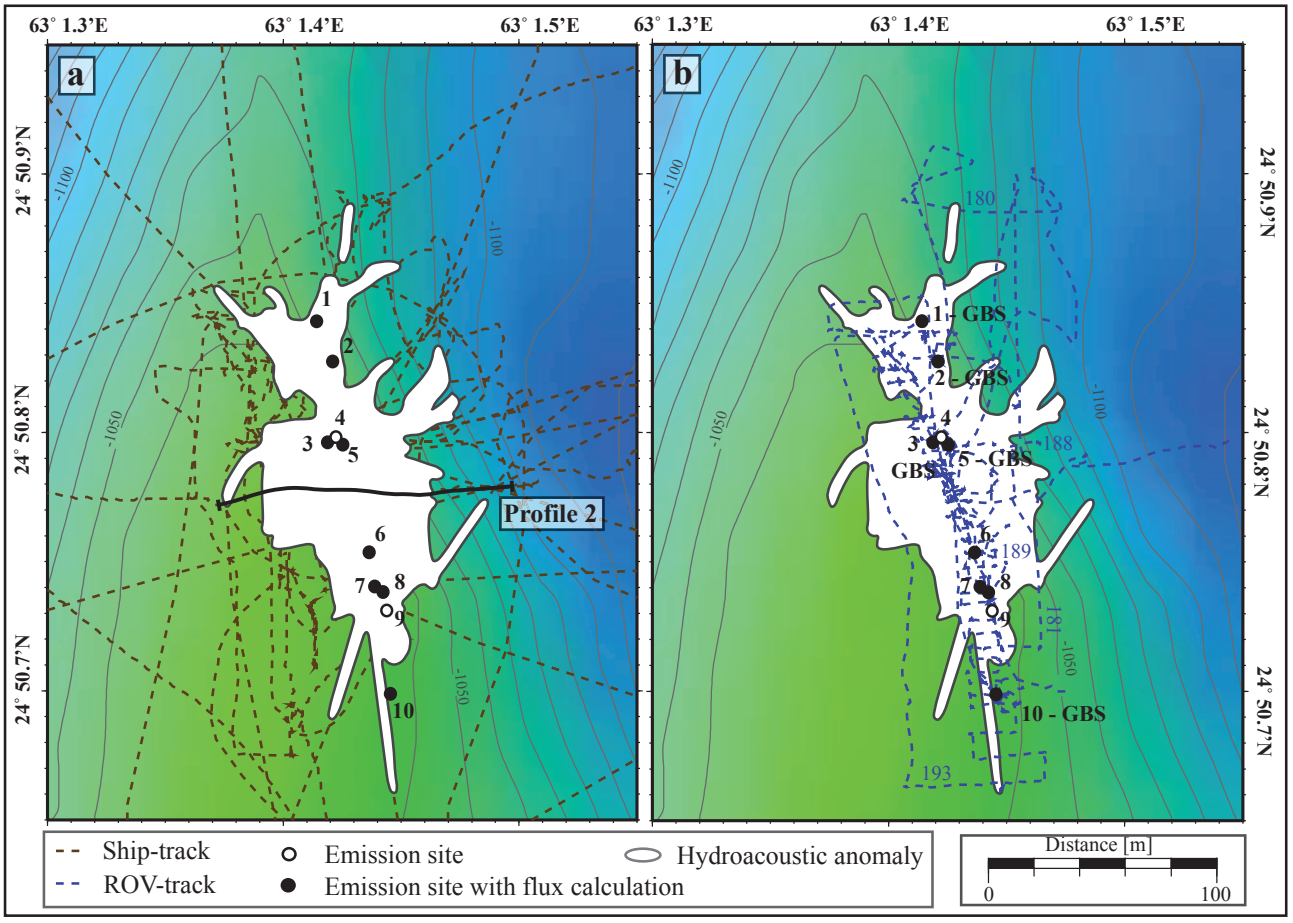

Fig. 4-7: (a) Bathymetric map of the area around Flare 2 depicting the ship-track and the recorded hydroacoustic anomalies in the water column. The black line (Profile 2) marks the profile shown in Figure 4-8. (b) ROV dive tracks at Flare 2 with the location of gas emissions observed at the seafloor. The ten emissions are linearly orientated.

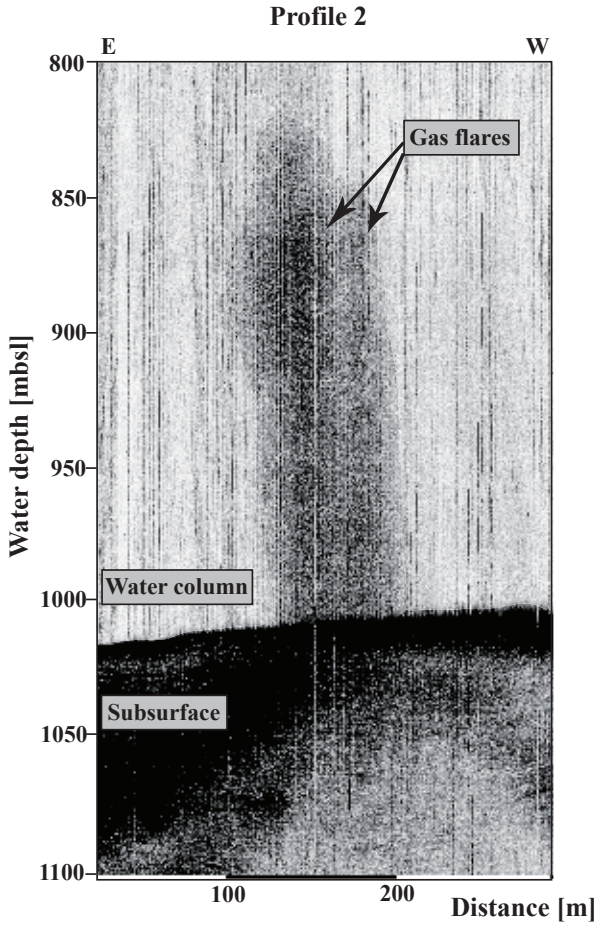

Fig. 4-8: Echogram crossing the gas emissions at Flare 2. The hydroacoustic anomaly is approximately 200 m high and probably composed by two flares that occur close to each other.

Connected to the diverse characters of the emission sites, bubble shapes vary from relatively small circular to large elliptical geometries. Sometimes bubble oscillation, with the tendency of increasing oscillation with increasing bubble sizes, led to blurred bubbles in the video sequences. Hydrate skin formation should occur around bubbles, as Flare 2 is located within the GHSZ. However, immediate hydrate formation was not observed for undisturbed bubbles rising through the water column a few decimeters above the emission site, but occurred unambiguously when bubbles were collected in the GBS funnel (Fig. 4-9a). Based on our observation it looked as if a hydrate rim formed instantaneously once the bubble had been caught in the funnel.

For eight of the ten emission sites discovered within this area, it was possible to estimate the bubble emission rate, whereas two emission sites remained out of consideration due to insufficient video documentation. However, judged from the quick passing by with the ROV, the two uninvestigated sites appeared to be quantitatively minor. For the eight emission sites analyzed bubble emission frequencies were 6 to 65 bubbles per second (Table 4-2). Observation time at each emission site was typically a few minutes. There was no apparent change in bubble flux during these observation periods. At four emission sites the average equivalent spherical radii were estimated and subsequently used to calculate the bubble flux (Table 4-2). On average, the radii were 0.307 ± 0.114 cm (n = 604), corresponding to average bubble volumes of 0.121 ± 0.006 ml. These values were used to quantify the bubble flux at the four sites for which bubble emission frequencies could be established. A total bubble flux of about 1.7 Litre per minute is estimated for the eight emission sites, which – assuming the gas being 100% methane - corresponds to 9.7 ± 5.9 mol CH_4 per minute for the entire Flare 2 area.

In general, there is a good agreement between the intensity of hydroacoustic anomalies in the water column and the bubble emission rate at a specific site as investigated during ROV dives. The emission sites are all located in the center of the wide acoustic anomaly (Fig. 4-7).

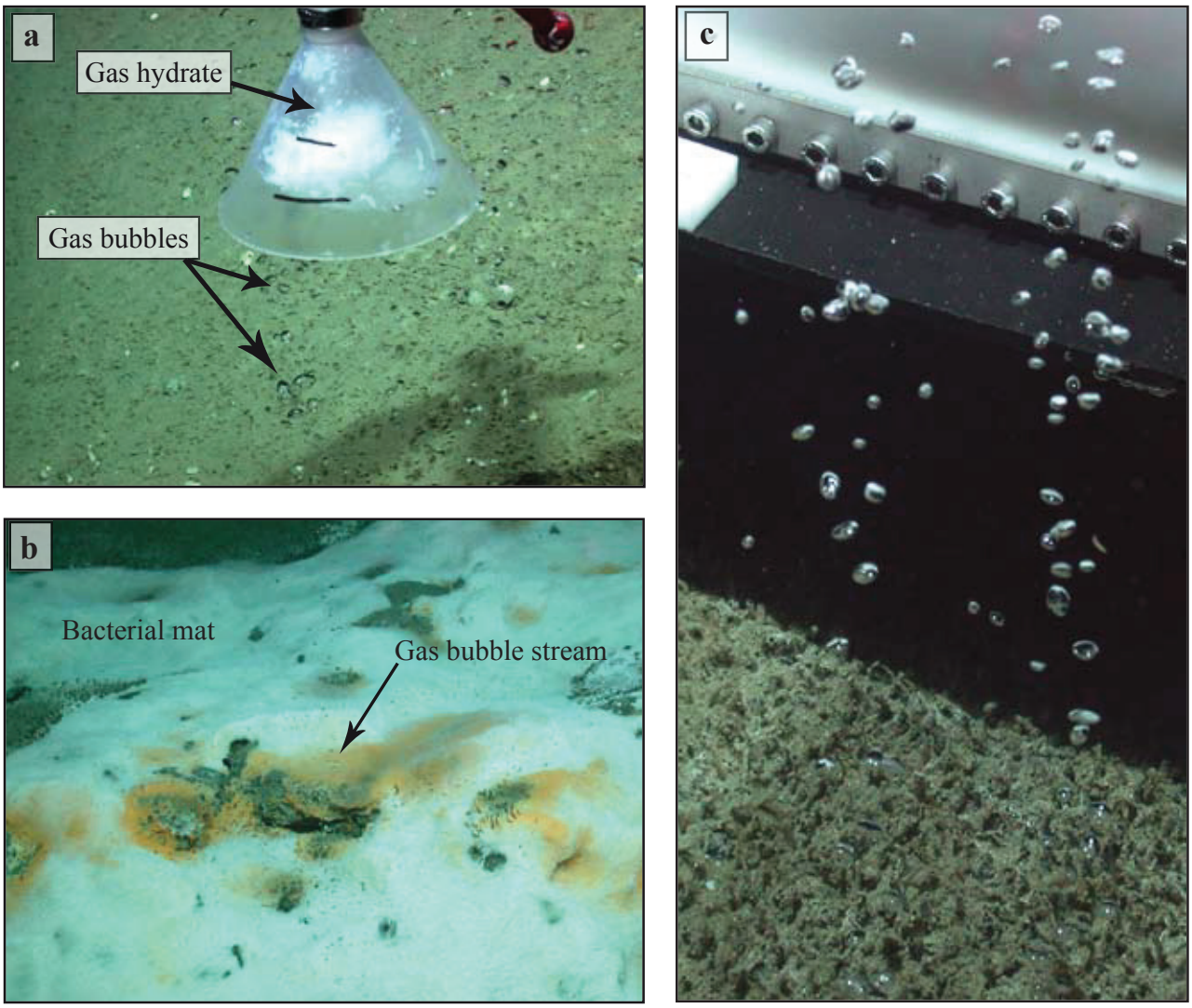

Fig. 4-9: Still images taken during ROV dives 180 (a), 181 (b) and 189 (c) in the area of Flare 2. (a) Gas bubbles were collected with the inverted funnel of the Gas Bubble Sampler at emission site 2. A gas hydrate coating was instantaneously formed around the bubbles when coming into contact with solids. (b) Bubbles emanate in pulses through a thick mat of sulphide oxidizing filamentous bacteria covering the sea floor at emission site 6. (c) Two gas bubble streams discharged at emission site 5. The sea floor is inhabited by ampharetid polychaets. (Images copy-right of MARUM University of Bremen)

Flare 5

Flare 5 is the deepest seep site (2870 mbsl) found during M74 at the MCM located on top of the so-called Nascent Ridge, which is the southernmost new developing up-doming ridge structure (Figs. 4-2 and 4-10). Three up to 2000 m high flares were observed using the 18 kHz echosounder (Figs. 4-3 and 4-11). The nearly vertical orientation of the flares suggests that bubbles rise remarkably straight upward through the water column being almost unaffected by horizontal water currents. However, the high acoustic backscatter within the flare is not as uniform and continuous as observed at Flare 2 (Fig. 4-8) but vary with depth, which we interpret to result from the movement of the bubble stream into and out of the echosounder beam as the bubbles did not rise absolutely straight up but were drifted horizontally. Because high backscatter intensities were not observed close to the seafloor exact determinations of the flare source region was hampered during our limited hydroacoustic surveys. Despite this uncertainty in locating the flare position, it became apparent that at least three individual sets of emissions named gas flare area 5A, 5B and 5C exist (Figs. 4-10 a and b). In general, flares of all three areas are strong in intensity and show, with few exceptions, no internal structures (Fig. 4-11, Profile 5a). Gas emissions from area 5C were continuous as indicated by a flare that could be recorded during all of the six echosounder surveys conducted within eight days. At the other two sites with gas emissions activity varied over time, as i.e. in gas flare area 5A only two of four crossings confirmed a flare and in area 5B flares were observed during three of the four transects.

During three ROV dives, four distinct gas emission sites were found at the seafloor (Fig. 4-10b). Their exact positions agree well with the assigned source regions of flare areas 5A and 5C considering the results from echosounder surveys. In general, the sediments were only scarcely inhabited by chemosynthetic communities such as pogonophoran tubeworms (Polychaeta: Siboglinidae) or scattered living vesicomyid clams (Fig. 4-12), whereas carbonate crusts were virtually absent.

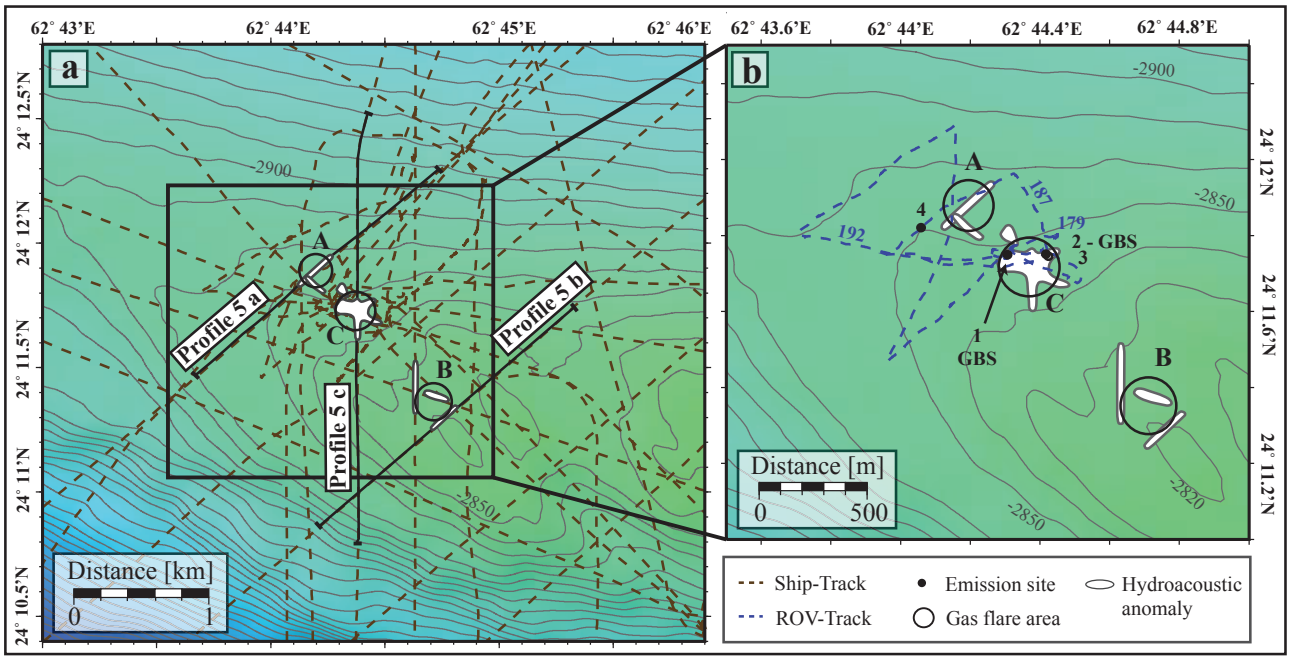

Fig. 5-10: (a) Bathymetric map in the area around Flare 5. Three areas with hydroacoustic anomalies can be distinguished (signified by A, B, and C). (b) Detailed map with ROV dive tracks. Four emission sites have been found and documented.

From each emission site numerous bubble streams emitted. At one site, bubbles percolated intensively through the sediments; no distinct orifices or openings in the sediments could be detected. Gas hydrate skin formation was observed during bubble collection with the GBS funnel (Fig. 4-12b), which is expected as this site is well located within the GHSZ. Bubble sizes varied between individual emission sites. For instance, at emission site 1 a bubble stream of relatively small bubbles was observed in only few centimeters distance to a stream of larger bubbles (Fig. 4-12a). Based on a rough estimation the difference in radius between the streams is about one millimetre or less. The stream of small and almost circular bubbles rose straight upward, whereas the larger bubbles were more elliptical in shape and oscillated during their ascent. In contrast to bubbles emitted at Flare 1 we noticed that the bubbles at the much deeper Flare 5 did not show as strong deformations in shape, which might be an effect of pressure or hydrate rim formation.

The area 5C including emissions 1-3 had been the focus during three ROV dives. With respect to the seafloor coverage (Fig. 4-10b) we are confident that almost all bubble emission sites were found. Bubble size analyses performed at two of these bubble emissions revealed average equivalent spherical radii of 0.257 ± 0.077 cm (n = 921) (Tab.

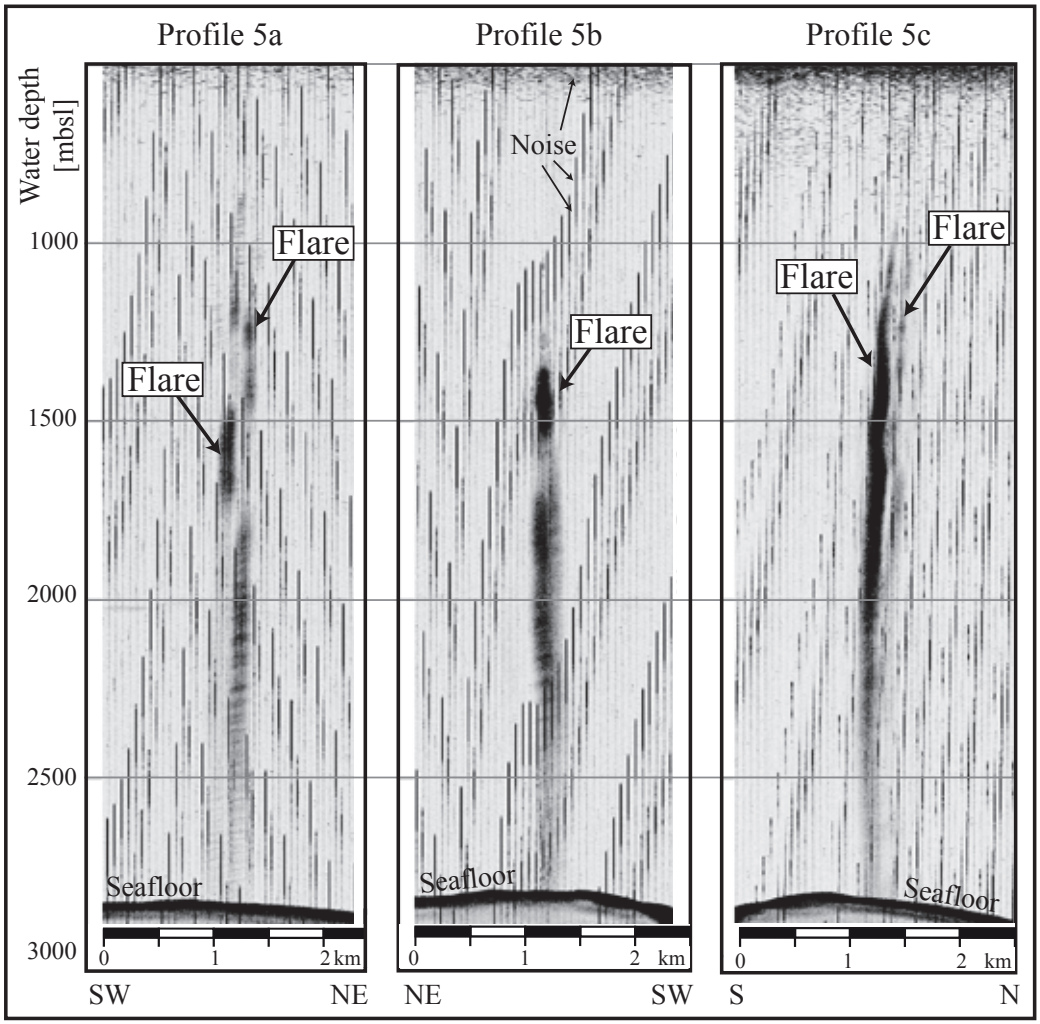

Fig.4-11: Three echograms illustrating the very intense and high flares found at Flare 5.

4-2) corresponding to an average bubble volume of 0.071 ± 0.002 mL. The bubble emission frequency varied considerably between the emission sites with 15 to 150 bubbles per second. In total, 230 bubbles emanate per second from area 5C into the water column (Table 4-2). This results in a volume flux of 729 ± 439 mL min^{-1} or, assuming the gas to consist of pure methane, a methane flux of 9.5 ± 5.8 mol CH_4 min^{-1}.

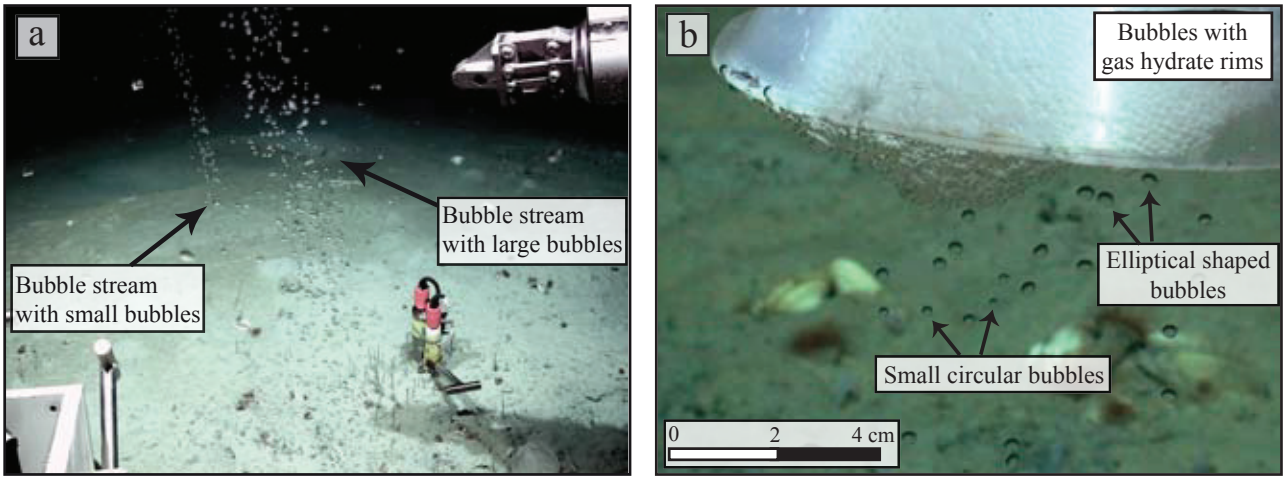

Fig. 4-12: Still images taken during ROV dives 179 (a) and 192 (b) in the area of Flare 5. (a) A photography of the intense emission site 1 with two bubble streams of different bubbles size distributions. (b) A close-up view of bubbles shortly before accumulating in the funnel where they instantaneously obtain a whitish hydrate coating. (Images copyright of MARUM University of Bremen)

4.5.3 Bubble size distribution and rise velocity

The bubble size distribution was measured at eight individual bubble emission sites sourcing Flares 1, 2, and 5 (Table 4-2). In general, the combination of all results shows a Gaussian shaped bubble size distribution with a mean radius of 0.28 cm and a std.-dev. of 0.094 cm (n = 1644; Fig. 4-13a). The variations in all bubble sizes between the seep sites are small (Fig. 4-13b - d). Due to the limited number of measurements, the results were not used for statistical analyses of differences between the seep sites. The data of all bubble sizes that served as base in this study are available as electronic supplement. The rise velocity was estimated for 154 bubbles within the size range of 0.7 – 6.5 mm at Flare 1, 2, 5, 7, and 15. Flare 1, 2, 5, and 7 are positioned within the central study area (Fig. 4-2) while Flare 15 is located about 40 nautical miles east of that. The rise velocity ranged between 10 and 30 cm per second.

4.5.4 Molecular hydrocarbon composition and stable carbon isotopic ratio of methane

Light hydrocarbons in vent gas collected with the GBS at Flares 1, 2, and 5 were strongly dominated by methane (> 99.94 mol-% of C_1– C_5), followed by much smaller amounts of ethane (< 0.03 mol-%) and propane (< 0.01 mol-%; Table 4-3). C_4- and C_5-hydrocarbon derivatives were only found in traces (< 0.01 mol-%) in samples from Flare 2 and Flare 5. For all sites investigated, the C_1/C_{2+} values ranged between 2,756 and 4,078. $\delta^{13}C$ values of methane in vent gas collected with the GBS from Flares 1 and 2 ranged from –68.5 to –68.9‰, whereas those for Flare 5 were about –65.2‰.

Table 4-3: Average molecular compositions of hydrocarbons (in mol-%Σ(C_1–C_5)) in gas samples collected with the Gas Bubble Sampler (GBS) from hydrocarbon seeps on the Makran accretionary wedge.

Flare	CH_4	C_2H_6	C_3H_8	*i*-C_4H_{10}	*n*-C_4H_{10}	unident. C_5-deriv. I	unident. C_5-deriv. II	C_1/C_{2+}	# of samples
1	99.975	0.022	0.003	n.d.	n.d.	n.d.	n.d.	4,029	2
2	99.975	0.015	0.003	0.002	0.002	0.002	n.d.	4,078	3
5	99.944	0.014	0.006	0.005	0.002	0.008	0.002	2,756	1

unident. C_5-deriv. = unidentified C_5-derivative; n.d. = not detected; $C_1/C_{2+} = C_1/(C_2 – C_5)$

4.6 Discussion

4.6.1 Flare characteristics revealed from Parasound 18 kHz echosounder recordings

In the following we discuss the Parasound echosounder performance for gas bubble-induced hydroacoustic anomalies in the water column considering the detailed insight into the bubble stream characteristics obtained by remotely operated vehicle (ROV)-based video documentation. A flare in the echosounder record always originated from several distinct gas bubble emissions from the seafloor. Regularly, several emissions occurred within areas that were smaller than the echosounder footprint size. In case of Flare 1 located at 550 mbsl, the footprint size is about 40 m. Consequently, the five gas emissions (numbered 1-5) occurring within an area of less than 15 m (Fig. 4-4) can not be resolved and, thus, emissions from all five sites contributed to the recorded flare. Considering the numbers of bubbles released from the seafloor, the number of bubbles required to cause the echosounder signal in the water column depicted in Figure 4-5 may be determined. At these five emission sites the total bubble emission frequency was 14 per second (Table 4-2). Assuming a bubble rise velocity of about 20 cm s^{-1} (Fig. 4-14), about 70 bubbles were present in a one meter thick water interval and caused the hydroacoustic anomalies (Fig. 4-5). In comparison, the flare recorded in area 5C (emission sites 1-3, Table 4-2) was created by about 220 bubbles released per second from the seafloor, which amounts to more than 1000 bubbles in a one meter water interval. This difference might explain why some flares appeared weak (Flare 1; Fig. 4-5) whereas other appear strong (Flare 5; Fig. 4-11).

4.6.2 Origin of gas

The strong prevalence of methane (C_1/C_{2+} > ca. 2,750) along with $\delta^{13}C\text{-}CH_4$ values < –65.2‰ indicate a sourcing of light hydrocarbons expelled at Flares 1, 2, and 5 predominantly by microbial organic matter degradation (Bernard et al., 1976). Moreover, individual C_4- and C_5-hydrocarbons which are commonly attributed to thermogenic input (Claypool and Kvenvolden, 1983; Schoell, 1980) were virtually absent in gas expelled at Flare 1. Based on these gas chemical characteristics a significant admixture of thermogenic hydrocarbons is not evident for our sample set. This assumption is corroborated by our ROV-based observations which did not show the presence of oil neither as droplets at the seafloor nor as skins enveloping gas bubbles.

4.6.3 Bubble size distribution

Bubble size distributions of natural bubble emissions have been intensely studied at a shallow water seep site (~<100 mbsl) (Leifer and Boles, 2005; Leifer and Culling, 2010; Leifer et al., 2010). In contrast, only four measurements are available for deep water seep sites (Leifer and MacDonald, 2003; Sahling et al., 2009). In this study, additional data are given for eight individual bubble emissions from three sites (Flare 1, 2, and 5) located between 575 and 2870 mbsl (Table 4-2). The bubble size distribution at all emission sites investigated in this study is remarkably uniform (Fig. 4-13). It follows a Gaussian distribution, with one narrow peak (2.8 ± 0.94 mm, n=1644). Emissions with Gaussian type narrow bubble size distribution have previously been termed minor bubble plumes (Leifer and Boles, 2005; Leifer and Culling, 2010). In contrast, major plumes with generally order of magnitude higher fluxes are characterized by much broader bubble size distributions. Important characteristic of minor plumes are that bubble sizes are independent from the gas flux and that increasing gas flux leads to increasing bubble numbers (Leifer and Boles, 2005; Leifer and Culling, 2010). At major bubble plumes an increase in gas flux leads to an increase in bubble dimensions and subsequently, to much broader bubble size distribution patterns.

In line with the definition by Leifer and Boles (2005) and Leifer and Culling (2010) the following deep-water bubble emissions may be classified as minor plumes: all gas emissions at the MCM, the "steady plume" at GC185 in 550 mbsl in the Gulf of Mexico (Leifer and MacDonald, 2003), and the emission at Vodyanitskii mud volcano in 2070 mbsl (Sahling

et al., 2009). These sites are charcterized by one narrow Gaussian type bubble size distribution with bubble radii ranging between ~0.5 and 7 mm and median or peak values around 2.7 mm (range: 2.6 – 2.8 mm) (Leifer and MacDonald, 2003; Sahling et al., 2009; this study). The pulsing plume described by Leifer et al. (2003) at GC185 is somehow unusual as bubbles were released from an overhanging mouth that collected bubbles causing the pulsating release. Probably as a consequence of this peculiar emission, a broad bubble size distribution was produced. A broad bubble size distribution is also characteristic for oily bubbles, as observed at GC185 but also at shallow water emission sites (Leifer and Culling, 2010; Leifer and MacDonald, 2003). The fact that bubble size distributions at the eight emissions at the MCM are narrow indicates that no significant amounts of oil are emitted together with the gas. This is in agreement with geochemical studies of the collected gases that did not show any evidence of significant contribution of higher hydrocarbons (see chapter 5.2).

In general, the narrow bubble size distributions and average bubble radii between 2.6 and 2.8 mm of all deep water minor plumes reported so far are remarkably uniform. To our knowledge, the sediments of all deep-water bubble emission sites fueling minor plumes are soft and muddy, which strongly suggests that this is one of the key factors controlling the bubble size distribution. It may be speculated that the upward movement of bubbles through fractures in muddy sediments as described by Boudreau et al. (2005) somehow leads to the narrow size distribution. This is a somehow surprising result, as we observed the bubbles to escape from a variety of seafloor structures and coverage including cracks, carbonates, mussel beds, microbial mats or sediments devoid of any organisms. Apparently, these surface structures did not influence the bubble size distribution.

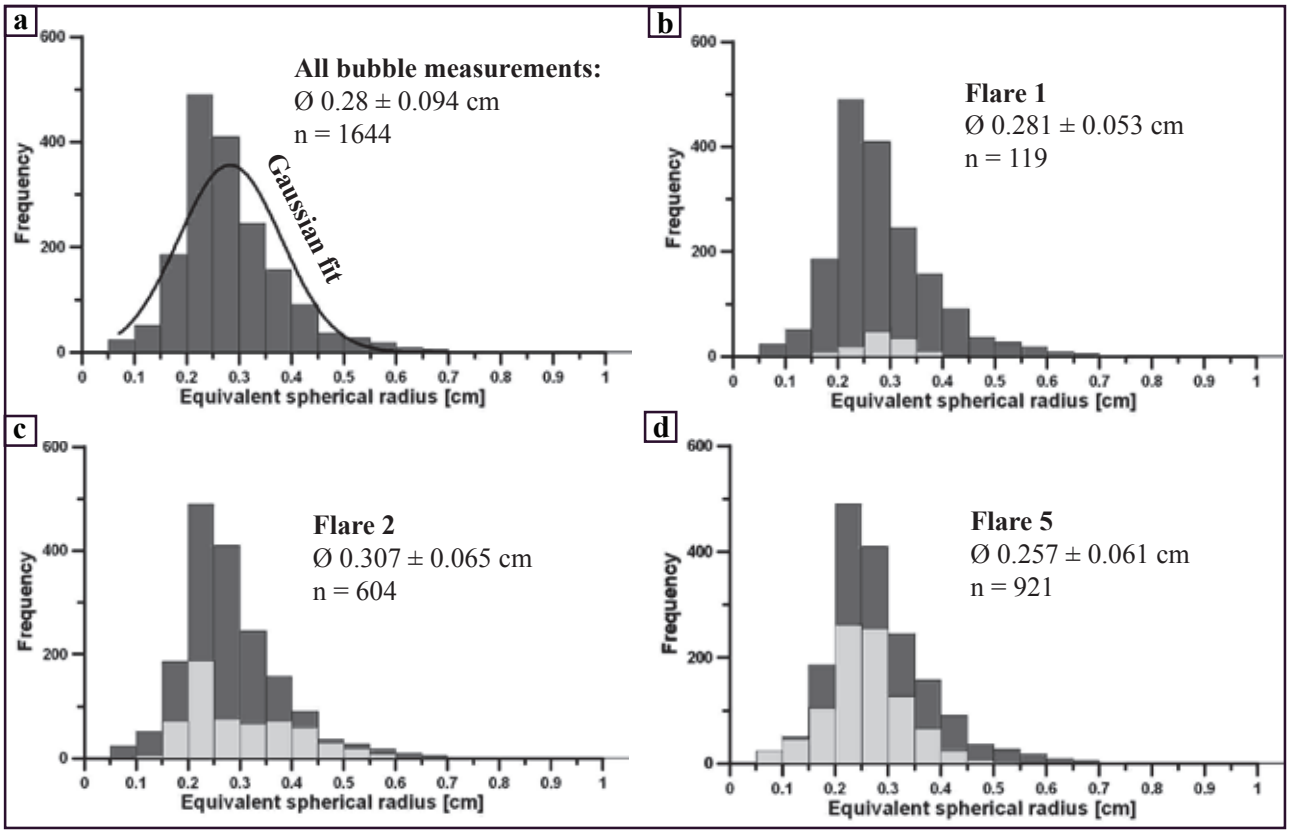

Fig. 4-13: Bubble size distributions of emanating bubbles (a) all measurements and (b-d) measurements differentiated between the four sites.

4.6.4 Bubble rise velocities

A bubble rises due to the buoyancy force and rapidly reaches its terminal velocity as a balance between buoyancy and drag force (Leifer et al., 1995). The bubble rise velocity depends, among other factors, on its size. In general, rise velocities for "clean" bubbles (i.e. unaffected by surfactants) increase with bubble radius up to a size of approximately 0.7 mm (Leifer et al., 1995) (Fig. 4-14). With increasing size, bubbles tend to oscillate and internal deformations causing wakes appear (Leifer and Judd, 2002). Bubbles with radii exceeding 0.7 mm do not only show oscillations in shape but also in path, both leading to decreases in the rising speed. Still larger bubbles are influenced by stronger wake instabilities and have higher modal oscillations. Perpendicular oscillations decrease therefore and the rising speed become faster again (Leifer et al., 1995). In contrast, the presence of surfactants ('dirty bubbles') strongly reduces the rise velocity of bubbles with radii exceeding ~0.6 mm (Fig. 4-14) due to reduction of the interfacial mobility, which is called the Maragoni effect (Patro et al., 2001). Natural examples of surfactants in and on bubbles are primary organic matter, e.g. polysaccharides, proteins, and lipid substances (Leifer and Patro, 2002), or ionic compounds like NaCl (Patro et al., 2001).

McGinnis et al. (2006) used in their model a correlation between the equivalent spherical radius and rising speed of single bubbles, which falls into the field delineated by the curves developed for clean and dirty bubbles (Clift et al., 1978) (Fig. 4-14). Our data generally follow their correlation despite considerable scattering. Moreover, the gas bubbles in our study area may be considered as dirty, because our data do not follow the pronounced local peak in rise velocity for small ~0.6 mm radii clean bubbles.

There are several factors that need to be further considered modifying the rising speed in natural systems. However, the significance of the factors for our data set is difficult to discuss as the mechanisms counteract each other. On the one hand, a considerable increase of the rise velocity could be caused by upwelling effects when high fluxes in a plume or strongly pulsing emissions accelerate the surrounding water (Leifer and MacDonald, 2003). An upwelling flow could decrease the time for

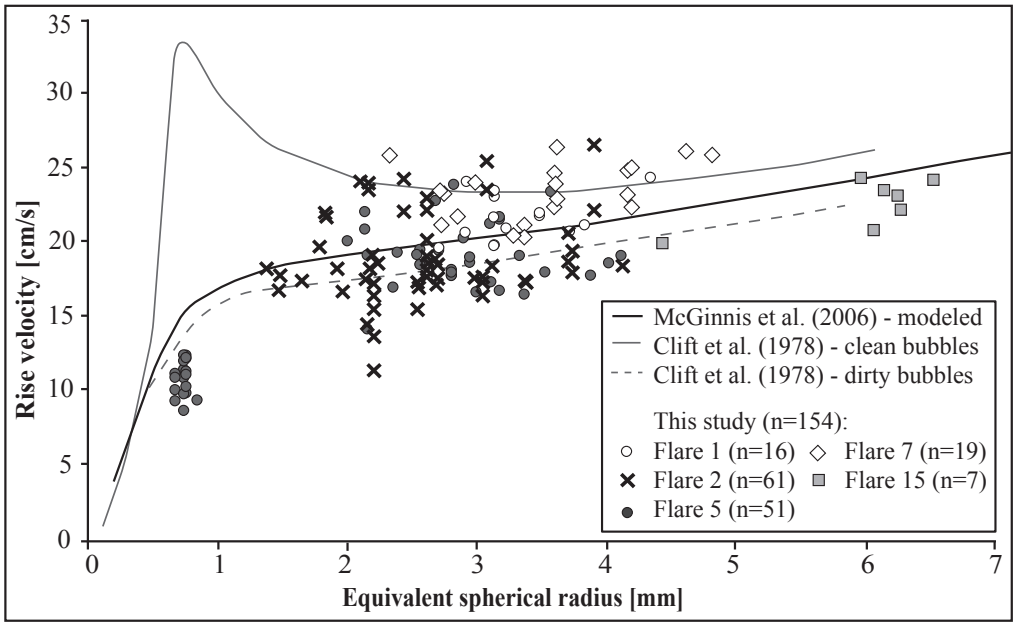

Fig.4-14: Diagram of the rise velocity plotted against the bubble size. The symbols are the measurements from the MCM of this study. The curves are modeled or fitted relations taken from the literature (Clift et al., 1978; McGinnis et al., 2006).

bubbles to reach the mixed layer or even the sea surface (Leifer et al., 2004). This phenomenon has been observed first at seeps in the Santa Barbara Channel at 20 – 70 mbsl by inducing dye into the bubble streams (Leifer et al., 2000). Leifer and MacDonald (2003) calculated upwelling flows for bubble streams in the Gulf of Mexico in 550 m deep seeps of up to 20 cm s^{-1}. The fact that most of the bubbles in our study rose faster than predicted by the model of Clift et al. (1978) for dirty bubbles may indicate that an upwelling flow exists. However, we found no direct evidence for an upwelling flow such as moving suspended particles in the water around bubble streams that would have visualized any significant upwelling flow. It should be noted here, that the model by McGinnis et al. (2006) does not consider any upwelling flow.

On the other hand, the bubble rise velocity may be reduced by the presence of oil or gas hydrate at the gas-water interface. As mentioned before, there is no evidence for the presence of oil escaping from the seafloor at our study sites. In contrast, an influence of gas hydrate may occur. Those small bubbles (~0.7 mm radii) emitted from the seafloor at the deepest sites (Flare 5 at 2870 mbsl) have likely formed a hydrate rim and have considerably lower rise velocities than predicted by the model (Fig. 4-14). The assumption of reduced rise velocities caused by hydrate skins may be corroborated by the observation of significantly higher rise velocities of hydrate-free bubbles emitted at 575 mbsl at Flare 1 which is clearly located above the GHSZ. The bubble ascent at that site was much faster than predicted by the empirical relations proposed by McGinnis et al. (2006), which somehow accounts for the effect of hydrates.

4.6.5 Fate of gas bubbles

The fate of a methane bubble emitted from a submarine seepage site depends primary on its initial radius, the water depth, it's rise velocity, the aqueous methane concentration, the presence of upwelling flows, as well as the presence of surface active substances (Leifer and Patro, 2002; Leifer and Judd, 2002). The balance between these processes determines if and at which rate a methane bubble dissolves. Because the bubble is highly supersaturated in methane with respect to the surrounding sea water, the gas rapidly diffuses out of the bubble due to the concentration difference. In the opposite direction dissolved air (i.e. nitrogen and oxygen) enters the bubble. Furthermore, expansion occurs due to the decreasing hydrostatic pressure as the bubble rises (Leifer and Judd, 2002; Leifer et al., 2000). In general, the bubble size is critical to predict the fate of gas, as larger bubbles transport more methane and a greater fraction of their initial methane to shallower depths than their smaller counterparts (McGinnis et al., 2006).

The fate of bubbles can be analyzed by hydroacoustic means using the 18 kHz signal of the single beam Parasound echosounder, because in addition to localization of bubble emission sites at the seafloor, it is also suitable to follow the bubbles rising within the water column. Applying this technique it was revealed in previous studies that bubbles can rise more than 1300 m through the water column within the GHSZ (Greinert et al., 2006) because they are preserved from complete dissolution by a hydrate rim (Rehder et al., 2002). However, as soon as the bubbles reach the upper limit of the GHSZ, they rapidly dissolve (Greinert et al., 2006; Heeschen et al., 2003). This behavior was also observed offshore Pakistan (Fig. 4-3). Five flares were well imaged by echosounder in the deep-water of which four showed bubbles rising close to or even shortly above the GHSZ. These also include the highest flare ever reported, rising about 2000 m from the seafloor at 2870 mbsl (Fig. 4-3).

We compared the maximal bubble rising heights for those three flare sites presented in the regional examples with results obtained by the single bubble dissolution model (SiBu-GUI) (Greinert and McGinnis, 2009), which is used to calculate bubble rising heights based on the initial bubble size, the molecular gas composition as well as water temperature, salinity, and dissolved gas concentrations. So far the model was applied for

cold seep environments in the anoxic Black Sea (Greinert et al., 2006; McGinnis et al., 2006) and for anoxic hypolimnon of Lake Kinneret (Ostrovsky et al., 2008). The rising height of the average bubble size as well as the maximum bubble size was calculated for each flare (Table 4-4). The used input data can be found in the supplement.

The model results match our observations with the Parasound echosounder for Flare 2 located at a depth of 1020 mbsl: the highest flare observed was 340 m, which corresponds to the model results, revealing rising heights between 200 to 460 m for bubbles of average and maximal sizes, respectively (Table 4-4). However, the model does not match the observed flare heights at Flares 1 and 5, which are the deepest and shallowest sites, respectively, investigated in this study. The largest discrepancy was found for the highest flare (2000 m), for which a maximal height of 1250 m was predicted by the model for the largest bubbles that we observed. A possible explanation for this discrepancy could be the insufficient parameterization of the bubble-water gas exchange, which is hampered due to gas hydrate coatings (Rehder et al., 2009). This process, however, does not explain the observed discrepancy between the actual flare height at Flare 1 (270 m) and modelled bubble rising heights (85 and 50 m for maximal and average bubble sizes, respectively), as this site is located above the GHSZ. At Flare 1 we observed slightly higher bubble rising speeds than those proposed by the model (Fig. 4-14), which could account for some differences. Bubble oil coating, which was shown to affect bubble lifetime (Solomon et al., 2009) might be exluded for Flare 1, as neither oil-staining of the sediment nor uprise of oily bubbles was observed. In addition, the molecular composition of gas collected at the emission site of Flare 1 did not hint to any admixture of non-methane hydrocarbons, which are commonly attributed to thermogenic organic matter decay. Moreover, a non-Gaussian type of the bubble size distribution which previously was related to oil coatings (Leifer and MacDonald, 2003) was not observed (Fig. 4-13). It is beyond the scope of this study to discuss in greater detail the model that we generally regard as a very useful tool for describing bubble behaviour in the water column. The measured parameters presented in this study may help refining any bubble dissolution model.

Despite the uncertainties of the model, it supports our results from hydroacoustic measurements that gas bubbles emitted at water depths >575 mbsl do not reach the mixed surface layer, which is at maximum 120 m thick during winter-monsoon periods (Madhupratap et al., 1996, Wiggert et al., 2005). In addition, it should be stressed that due to gas exchange processes the bubble rising height does not correspond to the height to which methane is transported in the water column. Due to exchange processes almost all of the initial methane of a bubble is lost to the water column before the bubble finally dissolves (McGinnis et al., 2006). Hence, we conclude that the bubble streams investigated in 2007 are very unlikely to have contributed to the atmospheric methane inventory.

Table 4-4: Comparison of recorded bubble rising heights by echosounder and dissolution depth modelled with SiBu-Gui (Greinert et al., 2009).

Site	Water depth [m]	Maximum flare height [m]	Measured bubble diameter [mm]	Rising height modeled [m]	Difference of rising heights [m]
Flare 1	575	270	Max.= 8.4	85	185
			Ø = 5.6	**50**	**220**
Flare 2	1020	340	Max.= 20.4	460	-220
			Ø = 6.14	**200**	**140**
Flare 5	2870	2000	Max.= 12.8	1250	750
			Ø = 5.1	**370**	**1630**

4.6.6 Gas bubble flux

Calculations of bubble emissions on the basis of bubble emission frequencies and average bubble size as carried out in this study have already been performed for other deep-water seepage sites (Leifer and MacDonald, 2003, Sahling et al., 2009). A major uncertainty in estimating the gas volume flux is the exact determination of the bubble radius (r_e) because the volume of a bubble is proportional to r_e^3. This error is accounted for in this study by considering the standard deviation of r_e (Table 4-2) in analogy to earlier studies (Sahling et al., 2009; Sauter et al., 2006). Compared to the uncertainty introduced by determining r_e, we regard all other sources of errors as minor for gas volume flux calculations and do not consider them further. It should be noted however, that our estimates are conservative, as they are based on those bubbles that have been identified visually. It is very likely that additional bubbles emanating from the seepage site remained undetected during the ROV surveys. In addition, our flux estimates are snapshots in time obtained during ROV observation periods ranging from a few minutes to hours. So far, little is known about the temporal variability of the emissions at the MCM although several hydroacoustic anomalies in the water column were repeatedly recorded by echosounder in the course of a day and at different days while a few others had not (namely areas A and B at Flare 5). It is known from gas emissions situated at other tectonic settings that the flux may change on various timescales (Boles et al., 2001; Leifer and Boles, 2005; Leifer et al., 2004; Linke et al., 2010; Naudts et al., 2010; Quigley et al., 1999; Torres et al., 2002). Despite the uncertainties in flux calculations, we converted the calculated fluxes to methane masses emitted per year in order to enable comparison with published data (Table 4-5).

Our results suggest that those emissions that create strong flares in the echosounder records (Fig. 4-3, Table 4-1) largely contribute to the total methane emission at the MCM whereas those emissions generating weak flares are less significant. The methane flux from Flare 1 causing a weak hydroacoustic anomaly is about an order of magnitude lower than the flux estimated for each of the two sites with strong flares (Flares 2 or 5) recorded by echosounder (Table 4-5). Assuming that the ROV-based methane fluxes obtained in this study are representative for all emissions, dozens of gas emissions causing weak flares would be needed in order to significantly add to the methane emission by the strong flares found at five sites (Flare 2, 5, 6, 7, and 11) in the study area. This is unlikely since we found only seven weak flares despite intensive survey efforts in the entire survey area. As a consequence, in the following we concentrate the further discussion on emission sites characterized by strong hydroacoustic anomalies in the echosounder.

As we were able to quantify the emission of gaseous methane at two sites causing strong hydroacoustic anomalies in the echosounder record, we may estimate the total flux of bubbles in the study area. This is based on the assumption, that each of the observed strong hydroacoustic anomalies was caused by gas emissions similar to those at Flare 2 and in area C of Flare 5, respectively, with values of about $5.05 \pm 3.17 \times 10^6$ mol yr^{-1} (Tab. 4-5). In summary, eight strong hydroacoustic anomalies were recorded: At each of Flare 2 and 7 one hydroacoustic anomaly was found, whereas two hydroacoustic anomalies were recorded at Flares 6 and 11. Three hydroacoustic anomalies were recorded at Flare 5 but we may consider only two, due to the fact that gas emissions were found at two of these sites only half of the time (during 5 out of 8 crossings with the ship). As a result, about $40 \pm 25 \times 10^6$ mol yr^{-1} methane escaping as gas bubbles is calculated.

Our estimate of gas bubble emissions that cause a strong hydroacoustic anomaly (Flare 2, gas flare area 5C) falls into the range of values reported from other areas in the deep sea (Tab. 4-4). The flux is in the same order of magnitude as the one strong gas emission observed at Håkon Mosby mud volcano (Sauter et al., 2006). It is interesting to note that, despite the considerable high methane flux, all of our observed emissions fall into the category "minor

plumes" (Leifer and Boles, 2005; Leifer and Culling, 2010). The definition by Leifer and Boles (2005) and Leifer and Culling (2010) is based on the bubble size distribution and was introduced for the most vigorous gas emissions observed at Coal Oil Point in shallow water (Tab. 4-5).

Based on our order of magnitude estimation at the MCM and published values we may calculate the methane gas bubble emission at deep-sea accretionary convergent margin settings on a global scale. Beside the MCM, the methane flux was estimated by Heeschen et al. (2005) for an entire ~24 km broad margin segment at the continental margin offshore Oregon (including Hydrate Ridge). The margin offshore Oregon is comparable to the MCM with regard to the facts that abundant bubble emissions were found (Collier et al., 2005; Heeschen et al., 2003; 2005; Suess et al., 2001), that the bubbles are mainly composed of methane (Torres et al., 2002), and that the bubbles dissolve close to the upper limit of the GHSZ (Heeschen et al., 2003). By measuring the water column methane inventory along with the hydrographic regime Heeschen et al. (2005) calculated the methane flux into the water column below the upper limit of the GHSZ with values of 15 000 mol h^{-1} corresponding to 130 x 10^6 mol yr^{-1}. In order to compare the values from offshore Oregon with those obtained in our study, we may recalculate the methane flux to one kilometre length of continental margin as common denominator. In doing so, we overcome the problem of how to account for different continental margin dimensions and study area sizes. The value for the bubble flux from sources at the slope at the MCM (~50 km) was 0.8 ± 0.5 x 10^6 mol yr^{-1} km^{-1} and that at the Cascadia Margin (~24 km) about 5.4 x 10^6 mol yr^{-1} km^{-1}. If we assume that these values are representative for convergent continental margins with accretionary prisms, we may extrapolate them to the entire 24,500 km long global network (Clift and Vannucchi, 2004), which results in values of 20 - 130 x 10^9 mol yr^{-1}. These values are rather small when compared to, e.g., those strong bubble emissions at Coal Oil Point (Tab. 4-4). In addition, the results by Heeschen et al. (2005) and our own study indicate that all of the methane that is emitted from hydrocarbon seeps at depth within the GHSZ remains in the ocean interior.

Table 4-5: Compilation of gas bubble fluxes at several sites on continental margins.

Location	Water depth	Methane flux		Reference
	[m]	[ml min^{-1}]	[×10^6 mol yr^{-1}]	
Makran - Flare 1	575	88	0.13 (± 0.06)	this study
Makran - Flare 2	1020	1881	5.6 (± 3.36)	this study
Makran - Flare 5 Area C	2870	765	5.26 (± 3.0)	this study
Vodianitsky mud volcano (Black Sea)	2070	152	0.9 (0.4-1.3)	Sahling et al., 2009
GC185 (Gulf of Mexico) - steady stream	525 - 550	213	0.238	Leifer and MacDonald, 2003
GC185 (Gulf of Mexico) - steady, oily, and pulsing stream	525 - 550		1.97	Leifer and MacDonald, 2003
Håkon Mosby mud volcano - one emission	1250 - 1270	1800	6.3 (2.5-11.4)	Sauter et al., 2006
Håkon Mosby mud volcano - all three emissions	1250 - 1270		~19	Sauter et al., 2006
Hydrate Ridge - Northern Summit	600 - 800		21.9	Torres et al., 2002
Tommeliten field, North Sea	65 - 75		1.5	Schneider von Deimling, 2011
UK Block 15/25, North Sea	167		1.1	Hovland and Judd, 1992
Coal Oil Point	60		1825 (± 274)	Hornafius et al., 1999

4.7 Summery and conclusion

A multi-disciplinary approach including hydroacoustic surveys of the water column and underlying sediment in combination with detailed ROV-based visual inspection of the seafloor led to the systematic discovery of 18 hydrocarbon seep sites in the 50 km wide study area at the Makran continental margin (Brüning et al., concomitant paper). At twelve of these sites, gas bubbles emitted from the seafloor caused hydroacoustic anomalies (flares) in the 18 kHz echosounder. As observed during ROV dives, several individual gas bubble emission sites at the seafloor fueled a hydroacoustic anomaly. Close-to-seafloor quantifications of gas emissions at three sites in conjunction with echosunder records in the water column clearly demonstrated that low bubble volume fluxes cause weak hydroacoustic anomalies whereas high fluxes cause strong flares. At the MCM, the emitted gas is mainly composed of methane predominantly of microbial origin. Measured bubble size distributions at eight emission sites are remarkably similar to bubble size distributions at two other deep-water sites reported in previous studies. This suggests that the deep-water bubble size distribution is nearly constant. This has important consequences, because it is known that flux calculations based on results from echosounder surveys as well as the fate of bubbles in the water column largely depend on the initial bubble sizes. In contrast to previous studies, we found that bubbles can persist much longer in the water column and rise to shallow water depths. However, in agreement with earlier observations all of the observed methane bubbles still dissolve within the water column and do not pass the hydrosphere-atmosphere boundary.

4.8 Acknowledgment

We greatly appreciate the shipboard support from the master and crew of R/V METEOR and the scientific-technical operating team of ROV 'QUEST 4000m' (MARUM) for their professional assistance. We would like to thank Hans-Jürgen Hohnberg for constructing the Gas Bubble Sampler and Hanno Keil for providing the software SeNT for hydroacoustic analyses. This work was funded through the DFG-Research/Excellence Cluster "The Ocean in the Earth System".

4.9 References

Artemov, Y.G., V.N. Egorov, G.G. Polikarpov, and S.B., Gulin (2007), Methane emission to the hydro-and atmosphere by gas bubble streams in the Dnieper Paleo-delta, Black Sea, Mar.Ecol. J., 3, 3-25.

Bernard, B.B., J.M. Brooks, W.M. Sackett (1976), Natural gas seepage in the Gulf of Mexico, Earth Planet. Sci. Lett., 31(1), 48-54.

Boles, J.R., J.F. Clark, I. Leifer, and L. Washburn (2001), Temporal variation in natural methane seep rate due to tides, Coal Oil Point area, California, J. Geophys. Res., 106(C11): 27077-27086.

Boudreau, B.P., C. Algar, B.D. Johnson, I. Croudace, A. Reed, Y. Furukawa, K.M. Dorgan, P.A. Jumars, and A.S. Grader (2005), Bubble growth and rise in soft sediments, Geology, 33, 517-520.

Brüning, M., T. Le Bas, B. Murton, H. Sahling, F. Ding, V. Spiess, and G. Bohrmann (in prep.), Abundant evidence for hydrocarbon seepage at the Makran continental margin offshore Pakistan. J. Geophys. Res.

Brüning, M., H. Sahling, I.R. MacDonald, F. Ding, and G. Bohrmann (2010), Origin, distribution, and alteration of asphalts at Chapopote Knoll, Southern Gulf of Mexico, Mar. Pet. Geol., 27, 1093-1106.

Byrne, D.E., L.R. Sykes, and D.M. Davis (1992), Great thrust earthquakes and aseismic slip along the plate boundary of the Makran Subduction Zone, J. Geophys. Res., 97(B1), 449-478.

Claypool, G.E., and K.A. Kvenvolden (1983), Methane and other hydrocarbon gases in marine sediment, Annual Review of Earth and Planetary Sciences, 11(1), 299-327.

Clift, R., J.R. Grace, and M.E. Weber (1978), Bubble, drops, and particles. Academic Press, New York.

Clift, P., and P. Vannucchi (2004), Controls on tectonic accretion versus erosion in subduction zones: Implications for the origin and recycling of the continental crust, Rev. Geophys., 42: RG2001, doi:10.1029/2003RG000127.

Collier, R.W. and M.D. Lilley (2005), Composition of shelf methane seeps on the Cascadia Continental Margin, Geophys. Res. Lett., 32(L06609).

De Beukelaer, S.M., I.R. MacDonald, N.L. Guinnasso, and J.A. Murray (2003), Distinct side-scan sonar, RADARSAT SAR, and acoustic profiler signatures of gas and oil seeps on the Gulf of Mexico slope, Geo-Mar. Lett., 23(3), 177-186.

De Jong, K.A. (1982). Tectonics of the Persian Gulf, Gulf of Oman, and southern Pakistan region, in The Ocean Basins and Margins Vol. 6: The Indian Ocean, edited by A.E.M. Nairn and F.G. Staehli, pp. 315–351, Plenum, New York.

Delisle, G., and U. Berner (2002), Gas hydrates acting as cap rock to fluid discharge in the Macran accretionary prism?, in The tectonic and climatic evolution of the Arabian Sea edited by P.D. Clift, D. Kroon, C. Gaedicke and J. Craig, pp. 137-146, The Geological Society of London, London.

Delisle, G., U. von Rad, H. Andruleit, C. von Daniels, A. Tabrez, and A. Inam (2002), Active mud volcanoes on- and offshore eastern Makran, Pakistan. Int. J. Earth Sci., 91, 93-110.

DeMets, C., R. G. Gordon, D. F. Argus, and S. Stein (1990), Current plate motions. Geophys. J. Int., 101(2), 425-478.

Ding, F., V. Spiess, N. Fekete, B. Murton, M. Brüning, and G. Bohrmann (2010), Interaction between accretionary thrust faulting and slope sedimentation at the frontal Makran accretionary prism and its implications for hydrocarbon fluid seepage, J. Geophys. Res., 115, B08106

Duan, Z., N. Møller, and J.H. Weare (1992), An equation of state for the CH4-CO2-H2O system: I. Pure systems from 0 to 1000°C and 0 to 8000 bar, Geochim. Cosmochim. Acta, 56, 2605-2617.

Ellouz-Zimmermann, N., A. Battani, E. Deville, A. Prinzhofer, and J. Ferrand (2008), Impact of coeval tectonic and sedimentary-driven tectonics on the development of overpressure cells, on the sealing, and fluid migration - Petroleum potential and environmental risks of the Makran Accretionary Prism in Pakistan, Himalayan Journal of Scienes, 5(7), 50-51.

Gordon, R. and C. DeMets, (1989), Present day motion at the Owen Fracture Zone and Dalrymple Trough in the Arabian Sea, J. Geophys. Res., 94, 5560–5570.

Grando, G. and K. McClay, (2007), Morphotectonics

domains and structural styles in the Makran accretionary prism, offshore Iran, Sediment. Geol., 196, 157-179.

Greinert, J., Y. Artemov, V. Egorov, M. De Batist, and D.F. McGinnis (2006), 1300-m-high rising bubbles from mud volcanoes at 2080m in the Black Sea: Hydroacoustic characteristics and temporal variability, Earth Planet. Sci. Lett., 244, 1-15.

Greinert, J. and D.F. McGinnis (2009), Single bubble dissolution model - The graphical user interface SiBu-GUI, Environmental Modelling & Software, 24, 1012-1013.

Heeschen, K., A. Tréhu, R. W. Collier, E. Suess, and G. Rehder (2003), Distribution and height of methane bubble plumes on the Cascadia Margin characterized by acoustic imaging, Geophys. Res. Lett., 30(12), 1643.

Heeschen, K. U., R. W. Collier, M. A. DeAngelis, E. Suess, G. Rehder, P. Linke, and G. P. Klinkhammer (2005), Methane sources, distributions, and fluxes from cold vent sites at Hydrate Ridge, Cascadia Margin, Global Biogeochem. Cycles, 19, GB2016

Hornafius, J. S., D. Quigley, and B. P. Luyendyk (1999), The world's most spectacular marine hydrocarbon seeps (Coal Oil Point, Santa Barbara Channel, California): Quantification of emissions, J. Geophys. Res., 104(C9), 20703-20711.

Hovland, M., A. Judd, and R. A. Burke Jr. (1993), The global flux of methane from shallow submarine sediments, Chemosphere, 26(1-4), 559-578.

Judd, A. G. (2004), Natural seabed gas seeps as sources of atmosheric methane, Environ. Geol., 46, 988-996.

Kopp, C., J. Fruehn, E. R. Flueh, C. Reichert, N. Kukowski, J. Bialas, and D. Klaeschen (2000), Structure of the Makran subduction zone from wide-angle and reflection seismic data, Tectonophysics, 329, 171-191.

Kukowski, N., T. Schillhorn, E. R. Flueh, and K. Huhn (2000), Newly identified strike-slip plate boundary in the northeastern Arabian Sea, Geology, 28(4), 355-359.

Kukowski, N., T. Schillhorn, K. Huhn, U. von Rad, S. Husen, and E. R. Flueh (2001), Morphotectonics and mechanics of the central Makran accretionary wedge off Pakistan, Mar. Geol., 173, 1-19.

Kvenvolden, K. A., and B. W. Rogers (2005), Gaia's breath - global methane exhalations, Mar. Pet. Geol., 22, 579-590.

Leifer, I., W. E. Asher, and P. J. Farley (1995), A validation study of bubble mediated air-sea gas transfer modeling for trace gases, paper presented at The third international symposium on air-water gas transfer, Aeon Verlag, Heidelberg University.

Leifer, I., J. F. Clark, and R. F. Chen (2000), Modifications of the local environment by natural marine hydrocarbon seeps, Geophys. Res. Lett., 27, 3711-3714.

Leifer, I., and A. G. Judd (2002), Oceanic methane layers: the hydrocarbon seep bubble deposition hypothesis, Terra Nova, 14, 417-424.

Leifer, I., and R. K. Patro (2002), The bubble mechanism for methane transport from the shallow sea bed to the surface: A review and sensitivity study, Cont. Shelf Res., 22, 2409-2428.

Leifer, I., and I. R. MacDonald (2003), Dynamics of gas flux from shallow gas hydrate deposits: interaction between oily hydrate bubbles and the oceanic environment, Earth Planet. Sci. Lett., 210, 411-424.

Leifer, I., J. R. Boles, B. P. Luyendyk, and J. F. Clark (2004), Transient discharges from marine hydrocarbon seeps: spatial and temporal variability, Environ. Geol., 46, 1038-1052.

Leifer, I., and J. Boles (2005), Turbine tent measurments of marine hydrocarbon seeps on subhourly timescales, J. Geophys. Res., 110.

Leifer, I., B. P. Luyendyk, J. Boles, and J. F. Clark (2006), Natural marine seepage blowout: Contribution to atmospheric methane, Global Biogeochem. Cycles, 20, GB3008, doi:10.1029/2005GB002668.

Leifer, I., and D. Culling (2010), Formation of seep bubble plumes in the Coal Oil Point seep field, Geo-Mar. Lett., 30(3), 339-353.

Le Pichon, X., K. Kobayashi, and Kaiko-Nankai Scientific C. (1992), Fluid venting activity within the eastern Nankai trough accretionary wedge: A summary of the 1989 Kaiko-Nankai results, Earth Planet. Sci. Lett., 109, 303-318.

Linke, P., S. Sommer, L. Rovelli, and D.-F. McGinnis (2010), Physical limitations of dissolved methane fluxes: The role of bottom-boundary layer processes, Mar. Geol., 272(1-4), 209-222.

Madhupratap, M., S.P. Kumar, P.M.A. Bhattathiri, M.D. Kumar, S. Raghukumar, K.K.C. Nair, N. Ramaiah (1996), Mechanism of the biological response to winter cooling in the northeastern Arabian Sea, Nature, 384(6609), 549-552.

McGinnis, D. F., J. Greinert, Y. Artemov, S. E. Beaubien, and A. Wüest (2006), Fate of rising methane bubbles in stratified waters: How much methane reaches the atmosphere?, J. Geophys. Res., 111(CO9007).

Merewether, R., M. S. Olsson, and P. Lonsdale (1985), Acoustically detected hydrocarbon plumes rising from 2-km depths in Guaymas Basin, Gulf of California, J. Geophys. Res., 90(B4), 3075-3085.

Minshull, T. A., and R. White (1989), Sediment compaction and fluid migration in the Makran accretionary prism, J. Geophys. Res., 94(B6), 7387-7402.

Naudts, L., J. Greinert, Y. Artemov, P. Staelens, J. Poort, P. Van Rensbergen, and M. De Batist (2006), Geological and morphological setting of 2778 methane seeps in the Dnepr paleo-delta, northwestern Black Sea, Mar. Geol., 227, 177-199.

Naudts, L., J. Greinert, J. Poort, J. Belza, E. Vangampelaere, D. Boone, P. Linke, J.-P. Henriet, and M. De Batist (2010), Active venting sites on the gas-hydrate-bearing Hikurangi Margin, off New Zealand: Diffusive- versus bubble-released methane, Mar. Geol., 272(1-4), 233-250.

Nikolovska, A., H. Sahling, and G. Bohrmann (2008), Hydroacoustic methodology for detection, localization, and quantification of gas bubbles rising from the seafloor at gas seeps from the Black Sea, Geochem. Geophys. Geosyst., 9, Q10010, doi:10.1029/2008GC002118

Ostrovsky, I., D. F. McGinnis, L. Lapidus, and W. Eckert (2008), Quantifying gas ebullition with echosounder: the role of methane transport by bubbles in a medium-sized lake, Limnol. Oceanogr. Methods, 6, 105-118.

Pape, T., A. Bahr, J. Rethemeyer, J. D. Kessler, H. Sahling, K.-U. Hinrichs, S. A. Klapp, W. S. Reeburgh, and G. Bohrmann (2010), Molecular and isotopic partitioning of low-molecular-weight hydrocarbons during migration and gas hydrate precipitation in deposits of a high-flux seepage site, Chem. Geol., 269, 350-363.

Patro, R., I. Leifer, and P. Bowyer (2001), Better bubble process modeling: Improved bubble hydrodynamics parameterization, AGU Monograph, 127, 315-320.

Platt, J. P., J. K. Leggett, J. Young, H. Raza, and A. S. (1985), Large-scale sediment underplating in the Makran accretionary prism, southwest Pakistan, Geology, 13, 507-511.

Quigley, D.C., J.S. Hornafius, B.P. Luyendyk, R.D. Francis, J. Clark, L. Washburn (1999), Decrease in natural marine hydrocarbon seepage near Coal Oil Point, California, associated with offshore oil production, Geology, 27, 1047-1050.

Rehder, G., P. W. Brewer, E. T. Peltzer, and G. Friederich (2002), Enhanced lifetime of methane bubble streams within the deep ocean, Geophys. Res. Lett., 29(15),1731, 10.1029/2001GL013966.

Rehder, G., I. Leifer, P. G. Brewer, G. Friederich, and E. T. Peltzer (2009), Controls on methane bubble dissolution inside and outside the hydrate stability field from open ocean field experiments and numerical modeling, Mar. Chem., 114, 19-30.

Sahling, H., G. Bohrmann, Y. G. Artemov, A. Bahr, M. Brüning, S. A. Klapp, I. Klaucke, E. Kozlova, A. Nikolovska, T. Pape, A. Reitz, and K. Wallmann (2009), Vodyanitskii mud volcano, Sorokin trough, Black Sea: Geological characterization and quantification of gas bubble streams, Mar. Pet. Geol., 26(9), 1799-1811.

Sauter, E. J., S. I. Muyakshin, J.-L. Charlou, M. Schlüter, A. Boetius, K. Jerosch, E. Damm, J.-P. Foucher, and M. Klages (2006), Methane discharge from a deep-sea submarine mud volcano into the upper water column by gas hydrate-coated methane bubbles, Earth Planet. Sci. Lett., 243, 354-365.

Schmale, O., J. Greinert, and G. Rehder (2005), Methane emission from high-intensity marine gas geeps in the Black Sea into the atmoshere,

Geophys. Res. Lett., 32.

Schoell, M. (1980), The hydrogen and carbon isotopic composition of methane from natural gases of various origins, Geochim. Cosmochim. Acta, 44, 649-661.

Shakova, N., I. Semiletov, A. Salyuk, V. Yusupov, D. Kosmach, and Ö. Gustafsson (2010), Extensive methane venting to the atmosphere from sediments of the east Siberian Arctic shelf, Science, 327, 1246-1250.

Solomon, E. A., M. Kastner, I. R. MacDonald, and I. Leifer (2009), Considerable methane fluxes to the atmosphere from hydrocarbon seeps in the Gulf of Mexico, Nat. Geosci., 2, 561-565.

Suess, E., M. E. Torres, G. Bohrmann, R. W. Collier, D. Rickert, C. Goldfinger, P. Linke, A. Heuser, H. Sahling, K. Heeschen, C. Jung, K. Nakamura, J. Greinert, O. Pfannkuche, A. Trehu, G. Klinkhammer, M. J. Whiticar, A. Eisenhauer, B. Teichert, and M. Elvert (2001), Sea floor methane hydrates at Hydrate Ridge, Cascadia Margin, in Natural gas hydrates: Occurrence, distribution, and detection, edited by C. Paull, American Geophysical Union.

Torres, M. E., J. McManus, D. Hammond, M. A. d. Angelis, K. U. Heeschen, S. L. Colbert, M. D. Tryon, K. M. Brown, and E. Suess (2002), Fluid and chemical fluxes in and out of sediments hosting methane hydrate deposits on Hydrate Ridge, OR, I: Hydrological provinces, Earth Planet. Sci. Lett., 201, 525-540.

von Rad, U., H. Rösch, U. Berner, M. Geyh, V. Marchig, and H. Schulz (1996), Authigenic carbonates derived from oxidized methane vented from the Makran accretionary prism off Pakistan, Mar. Geol., 136, 55-77.

von Rad, U., U. Berner, G. Delisle, H. Doose-Rolinski, N. Fechner, P. Linke, A. Lückge, H. A. Roeser, R. Schmaljohann, M. Wiedicke, and S. S. Parties (2000), Gas and fluid venting at the Makran accretionary wedge off Pakistan, Geo-Mar. Lett., 20, 10-19.

Westbrook, G. K., and T. J. Reston (2002), The accretionary complex of the Mediterranean Ridge: tectonics, fluid flow and the formation of brine lakes - an introduction to the special issue of Marine Geology, Mar. Geol., 186, 1-8.

White, R. S. (1977), Seismic bright spots in the Gulf of Oman, Earth Planet. Sci. Lett., 37, 29-37.

White, R. S., and K. E. Louden (1983), The Makran continental margin: structure of a thickly sedimented convergent plate boundary, Bull. Am. Assoc. Pet. Geol., 34, 499-518.

Wiedicke, M., S. Neben, and V. Spiess (2001), Mud volcanoes at the front of the Makran accretionary complex, Pakistan, Mar. Geol., 172, 57-73.

Wiggert, J.D., R.R. Hood, K. Banse, and J.C. Kindle (2005), Monsoon-driven biogeochemical processes in the Arabian Sea. Progress In Oceanography, 65(2-4), 176-213.

Zonenshayn, L. P., I. O. Murdmaa, B. V. Baranov, A. P. Kuznetsov, V. S. Kuzin, M. I. Kuz'min, G. P. Avdeyko, P. A. Stunzhas, V. N. Lukashin, M. S. Barash, G. M. Valyashko, and L. L. Demina (1987), An underwater gas source in the Sea of Okhotsk west of Paramushir island, Oceanology, 27(5), 598-602.

5 Second case study (manuscript II):

Geological control and quantity of gas bubbles emanating from a high-flux seep area in the Back Sea - The Kerch seep area

Miriam Römer[1*], Heiko Sahling[1], Thomas Pape[1], André Bahr[2], Thomas Feseker[1], Paul Wintersteller[1], Gerhard Bohrmann[1]

[1] MARUM – Center for Marine Environmental Sciences and Department of Geosciences, University of Bremen, Klagenfurter Str., 28359 Bremen, Germany
[2] Institute of Geosciences, Goethe-University Frankfurt, 60438 Frankfurt am Main, Germany

* Corresponding author: Tel +49(0)421 218 65059 Fax +49(0)421 218 65099
E-mail: mroemer@marum.de

Submitted to Marine Geology
(22 September 2011)

5.1 Abstract

During three ship expeditions between the years 2007 and 2011, we investigated gas bubble emissions at the Don-Kuban paleo-fan offshore Ukraine. More than 500 bubble-induced water column anomalies (flares) were found at the seafloor located above the gas hydrate stability zone (GHSZ) at ~700 m water depth. However, the main focus of the study was a newly discovered hydrocarbon seep named "Kerch seep area" at about 890 m water depth well within the GHSZ. At the Kerch seep area several flares were distributed over an area of approximately 1×1 km. Repeated hydroacoustic surveys conducted over four years suggested that gas discharge varied spatially and temporally within the Kerch seep area but that the number of flares remained rather constant. Selected sites at the seafloor were surveyed by remotely operated vehicle (ROV) in order to quantify the gas emissions by visually estimating the bubble emission frequency and size of the bubbles. Analyses of gas samples revealed that the bubbles consist mainly of methane of predominantly microbial origin. A rough estimate of the methane flux combining visual quantifications with hydroacoustic surveys resulted that between 2.2 and 87 $\times$ 10^6 mol CH_4 yr^{-1} was emitted at the Kerch seep area. Bubbles could be traced by echosounder to the shallowest water depth of 350 m suggesting that all of the released methane remains in the water column. While gas hydrate formation in sediments within the GHSZ generally impedes bubble emission at the seafloor, in situ temperature measurements at the Kerch seep area indicate localized thermal anomalies likely caused by fluid flow. These thermal anomalies reduce the thickness of the GHSZ in the region of the Kerch seep area from about 110 m to only a few meters allowing gas bubbles to ascent through the sediments. We interpret locally up-domed sediments ('mounds') on ultra-high resolution maps produced by an autonomous underwater vehicle (AUV) as a result of hydrate deposition at shallow depths. Part of the gas bubbles ascending from greater depths are forced to migrate horizontally through the sediments which leads to gas escape at the rims of the mounds.

Keywords: cold seep, gas flares, methane flux, gas bubble quantification, gas hydrate stability zone, gas hydrate sealing

5.2 Introduction

Hydrocarbon seepage has been described from several areas in the Black Sea focusing either on the continental shelf and upper slope or on the deep basins whereas seeps at the middle slope at intermediate water depths have gained considerable less attention. For instance, well-known from a multitude of studies are the gas emissions at the broad Dnepr and Danube paleo-fan at the north-western Black Sea margin (Artemov et al., 2007; Lüdmann et al., 2004; Luth et al., 1998; Michaelis et al., 2002; Naudts et al., 2009; Naudts et al., 2008; Naudts et al., 2006; Poort et al., 2007; Popescu et al., 2007). A thorough hydroacoustic survey identified more than two thousands gas emissions at the continental shelf and upper slope (Naudts et al., 2006). In addition, hydrocarbon seepage also occurs at mud volcanoes in the deep Black Sea basins, where warm fluids and mud are transported from greater sediment depth to the seafloor. Several submarine mud volcanoes occur in the Sorokin Trough (Bohrmann et al., 2003; Krastel et al., 2003; Sahling et al., 2009) where they evolved from diapiric zones in a compressional regime (Wagner-Friedrichs, 2007). In contrast to these aforementioned studies hydrocarbon seeps at intermediate water depths are rarely described in the scientific literature. An exception is the Batumi seep area at about 840 m water depth on the continental slope offshore Georgia, which has been found to host active high-flux gas emissions (Haeckel et al., 2008; Klaucke et al., 2006; Nikolovska et al., 2008; Pape et al., 2011; Pape et al., 2010). This seep site lacks significant relief and does not involve material transport from depth (Klaucke et al., 2006) but shows intense gas bubble ebullition activity (Nikolovska et al., 2008).

Gas hydrates form in sediments of the Black Sea below water depth of ~700 m (Pape et al., 2011), when sufficient methane is available. Such hydrates are an important factor controlling the presence and intensity of gas ebullition into the water column as they provide an effective seal for any gas ascending from below. For example, Naudts et al. (2006) observed that the abundant gas emission in the Dnepr paleo-fan are restricted to water depths less than ~700 m, which corresponds to the upper boundary of the gas hydrate stability zone (GHSZ) in the Black Sea water body. Free gas typically accumulates at the base of the GHSZ (BGHSZ). When this gas ascents into the GHSZ it is trapped as hydrates (Hovland, 2002; White, 1979). Nevertheless, the gas hydrate seal may be leaking under certain instances, for example, bubble emissions occur in areas located within the GHSZ such as mud volcanoes in the Sorokin Trough or at Batumi seep area offshore Georgia. At Dvurechenskii mud volcano warm, saline fluids ascend from greater depth resulting in sediment temperatures above the GHSZ (Bohrmann et al., 2003), which explains the migration of gas bubbles through the sediments into the water column (Greinert et al., 2006). In contrast, the mechanisms promoting free gas migration through the GHSZ in the Batumi seep area is yet unknown (Klaucke et al., 2006). This hydrocarbon seep is considered as a gas-driven system with only little advection of pore water (Haeckel et al., 2008). Vigorous gas emissions (Nikolovska et al., 2008) and gas hydrate deposits just below the seafloor (Pape et al., 2010; 2011) characterize this site located at 840 m water depth well within the GHSZ.

The Black Sea is the world's largest anoxic basin with an estimated amount of 6×10^{12} mol yr^{-1} dissolved methane in the water body (Reeburgh et al., 1991). In general, sediments of 10 to 19 km in thickness (Tugolesov et al., 1985) partially containing high organic matter content provide the potential substrates for methane generation. From radiocarbon-based calculations it was proposed that the methane flux from seeps and decomposing gas hydrates into the Black Sea accounts for 0.23 – 0.35 $\times 10^{12}$ mol CH_4 yr^{-1} (Kessler et al., 2006). So far our knowledge about methane sources from the seafloor is limited and quantifications of methane emissions from distinct seepage sites are rare. For example, the amount of emitted methane was quantified at two mud volcanoes in the Sorokin Trough: at Vodyanitski mud volcano methane is emitted as bubbles with

values of about 0.9×10^6 mol CH_4 yr^{-1} (Sahling et al., 2009) and at Dvurechenski mud volcano methane is emitted dissolved with advecting pore water with values between 1.9 and 13.0×10^6 mol CH_4 yr^{-1} as estimated by two different methods (Lichtschlag et al., 2010; Wallmann et al., 2006). As only about 65 mud volcanoes have been discovered in the Black Sea up to now (Kruglyakova et al., 2002), their contribution to the Black Sea methane budget appears negligible. In contrast to this, Artemov et al. (2007) reported for an area at the Dnepr paleo-fan comprising 387.1 km^2 at water depths between 60 and 825 m the existence of about 2200 individual bubble emissions using hydroacoustics. For this area, the authors calculated a methane flux of about 7.5×10^8 mol yr^{-1}, which is significant with respect to the overall Black Sea methane content. However, as this is the only published value for bubble emissions at a Black Sea shelf and upper slope area, additional quantifications of methane escape from bubble emission areas are required to evaluate their impact on the Black Sea methane budget.

In addition, the fate of gas bubbles in the water column is of interest with respect to the question whether or not the potent greenhouse gas methane released from the sediment into the hydrosphere reaches the atmosphere. The destiny of a gas bubble depends primarily on the water depth of the gas release, its initial radius and rising velocity, the aqueous methane concentration, as well as the presence of upwelling flows, and surface active substances (Leifer and Judd, 2002; Leifer and Patro, 2002). The bubble size is crucial for the fate of the gas contained, as larger bubbles transport more methane and potentially a greater fraction of the initial methane amount to shallow water depth compared to their smaller counterparts (MacDonald et al., 2002). In general, a bubble expands in the course of ascent due to decrease in hydrostatic pressure (Leifer et al., 2000; Leifer and Judd, 2002). At the same time, gas exchange between the gas bubble and the ambient water might take place resulting in a rapid decrease of the methane portion inside the bubble. This process is hampered within the GHSZ where gas hydrate rims form around methane bubbles (Maini and Bishnoi, 1981), hence, preventing them from rapid dissolution until they pass the upper limit of the GHSZ (Rehder et al., 2002). Based on the literature, almost all of the methane from seeps remains in the Black Sea water body. Basin-wide modeling suggests that less than 1.5% of the methane escaping the Black Sea seafloor reach the atmosphere (Reeburgh et al., 1991). Even methane fluxes fueled by bubble emissions on the shallow shelf at the Dnepr paleo-fan seem to be retarded within the ocean water, and spots with elevated methane concentrations were only recorded above a seep area shallower than 100 m, whereas high-intensity seep sites in deeper waters do not affect the surface water methane concentration (Schmale et al., 2005). This observation was confirmed by Artemov et al. (2007) using a bubble dissolution model showing that only 1.9% of the methane transported as gas bubbles emanating at the Dnepr paleo-fan reach the air-water boundary in gas phase.

In this study, we focus on a hydrocarbon seepage area in water depths between ~150 and 1200 m at the Don-Kuban paleo-fan south-west of the Kerch Strait. Earlier studies report on the existence of gas emissions in this area (Egorov et al., 2003; Starostenko et al., 2010), but a thorough investigation of this region has not been performed so far. We visited that area during three cruises within four years and investigated the distribution of gas emissions by means of hydroacoustic methods. The focus of this study was laid on a newly discovered gas emission area, called the Kerch seep area, located at about 890 m water depth. Our results give new insights into a specific type of hydrocarbon seep site that is not related to mud volcanic activity but provides gas migration through the GHSZ. Detailed investigation lead to a better understanding of these morphologically inconspicuous deep-water seep sites. High-resolution bathymetry data obtained by autonomous underwater vehicle (AUV), sediment coring and temperature measurements allowed to propose a fluid migration model for the processes

5.3 Regional setting

controlling gas escape from this area which might help to understand its geological and morphological evolution.

The Black Sea is a marginal ocean with maximum water depth of 2.2 km, which is separated by the Mid-Black Sea High (Andrusov and Archangelsky Ridge) into the Western and the Eastern basin (Fig. 5-1A). The basins are underlain by oceanic or thinned continental crust with a sediment cover of 10-19 km in thickness (Tugolesov et al., 1985). The Black Sea is interpreted as a back-arc basin which evolved during late Cretaceous times (Nikishin et al., 2003), as the Tethys was subducted northwards under the volcanic arc of the Balkanides and Pontenides. The compressional environment results from the collision between the Arabian, Anatolian, and the Eurasian Plates. Stress field observations show that the Black Sea region is still in a dominantly compressional environment (Reilinger et al., 1997). The tectonic evolution of the basin is nevertheless characterized by alternations of extensional and compressional phases (Fig. 5-1A) and by different stages of subsidence (Nikishin et al., 2003).

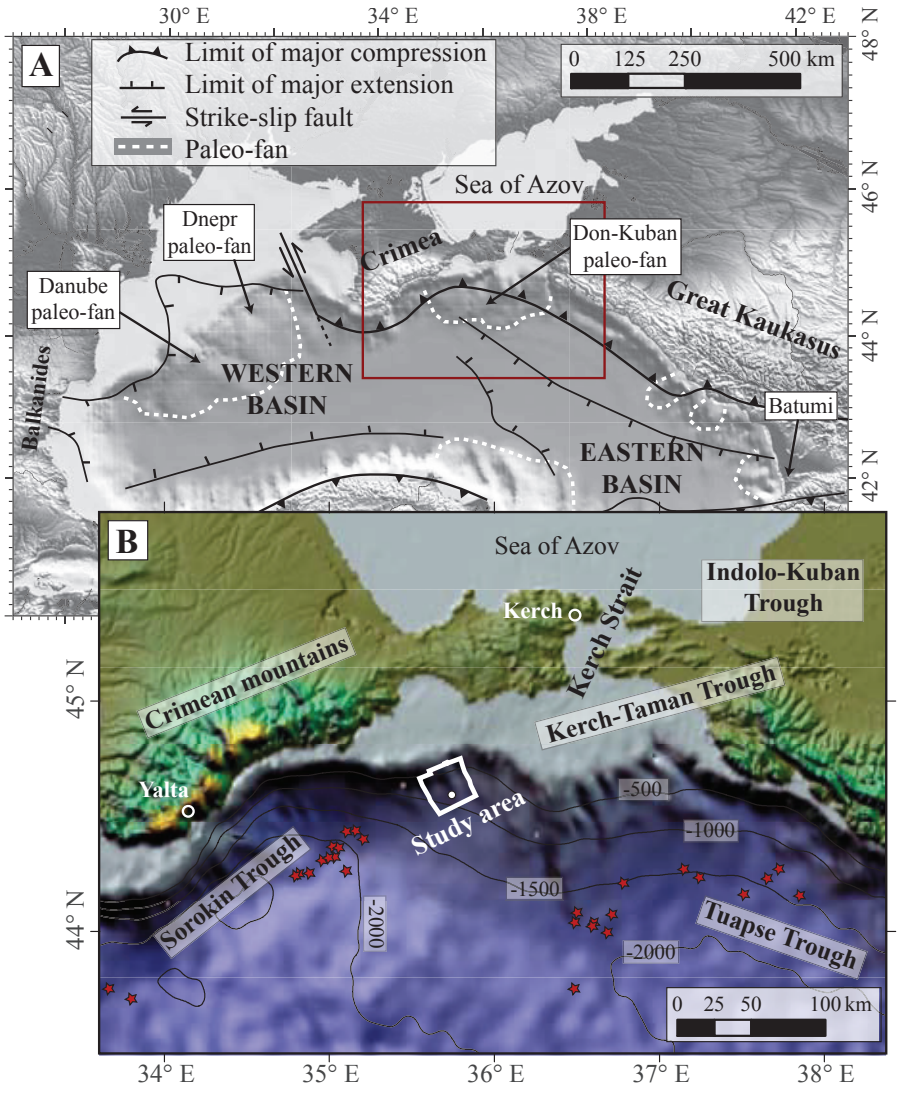

Fig. 5-1: A) Morphologic map of the Black Sea from GEBCO´s gridded bathymetric data sets (http://www.gebco.net/) with main tectonic features after Robinson et al. (1996) and extensions of paleo-fan systems (Vassilev and Dimitrov, 2002). B) Morphological structures south of the Kerch Strait. Red stars mark positions of mud volcanoes (Meisner et al., 2009).

Due to high freshwater supply from numerous rivers (e.g. Danube, Dnepr, Dnister, Don), surface waters have low salinities (17-18 psu) while deep waters are more saline (~22.5 psu) resulting from the inflow of highly saline Mediterranean waters via the Bosphorus. As a result of the salinity differences, a persistently stratified water column is present with only weak vertical mixing, causing permanent anoxic conditions below approximately 150 m (Özsoy and Ünlüata, 1997).

The Kerch Strait is the connection between the Black Sea and the Sea of Azov. The study area is located south-west of the Kerch Strait and east of the Crimean margin (Fig. 5-1B). The margin consists of a wide shallow shelf, which is characterized by the influence of suspended matter derived from the Sea of Azov through the Kerch Strait (Oaie et al., 2005). Furthermore, the large fan south of the Kerch Strait represents the paleo-delta of the Don and Kuban rivers (Barg, 2007; Starostenko et al., 2010). Shale diapirs have been described in the Kerch-Taman Trough that are associated with folds of Oligocene-Miocene age and have probably undergone compaction processes since then (Meisner et al., 2009).

In other paleo-deltas in the Black Sea, formed for instance at the mouths of the Danube and Dnepr, the deposition of organic-rich sediments and the subsequent microbial degradation has led to the formation of shallow gas in the subbottom and also prolific gas seepage into the water column (Naudts et al., 2006). Gas saturated sediments and gas releases have been reported also for the Don-Kuban paleo-fan (Egorov et al., 2003; Starostenko et al., 2010).

5.4 Material and methods

5.4.1 Hydroacoustic methods

During three cruises to the Don-Kuban paleo-fan (R/V METEOR cruises M72/3 in 2007, M84/2 in 2011, and R/V MARIA S. MERIAN cruise MSM15/2 in 2010) several hydroacoustic techniques were used in order to detect and localize gas emissions. For bathymetric and backscatter mapping the swath echosounder Kongsberg Simrad EM 120 with a frequency of 12 kHz (during M72/3 and MSM15/2), Kongsberg Simrad EM 122 also with a frequency of 12 kHz (during M84/2), and Kongsberg Simrad EM710 operating between 70 kHz and 100 kHz (during M84/2) were used. Raw data were processed with CARIS 7.0 HIPS and SIPS and MB-system software (Caress and Chayes, 1996). The grids produced were visualized with the public domain program GMT (Generic Mapping Tool; Wessel and Smith, 1991) and with ESRI Arcmap 10.0 in combination with additional data (e.g. sampling positions, track lines, locations of temperature measurements) for map export. For the detection of gas emissions, the Kongsberg Simrad EM122 and EM710 were used as these systems allow recording the water column data which can be displayed and edited with IVS FLEDERMAUS 7.2 using the 3D-Midwater tool.

The ship-mounted single beam parametric echosounder PARASOUND was used for shallow subbottom and water-column imaging during all three cruises. The primary high frequencies of 18 kHz (M72/3 and M84/2) or 19 kHz (MSM15/2) enable to focus on the observation of the water column. The system settings were optimized for bubble detection (Nikolovska et al., 2008). The transducer opening angle is 4°, resulting in a footprint size of about 7% of the water depth. The secondary low frequency of about 4 kHz was used for subbottom observations. The software ATLAS PARASTORE was applied for online processing. In addition, a simple post-processing was conducted with the program SeNT (developed by H. Keil, University of Bremen) using the PS3 data and final plots were created. PARASOUND data as well as metadata can be found in the PANGAEA data base (Hhttp://doi.pangaea.deH).

During MSM15/2, two dives with MARUM´s

autonomous underwater vehicle (AUV) 'SEAL 5000' were conducted at Kerch-Flare in order to achieve high-resolution swath multibeam data. The AUV was build by the company International Submarine Engineering and is nearly 5.75 m long, with 0.73 m diameter, and a weight of 1.35 tons. Navigation was realized by the PHINS inertial unit from the company IXSEA combining a motion reference unit and an inertial navigation system. In addition, a Doppler velocity log (300 kHz) was used. The ultra short baseline system POSIDONIA was used to independently trace the AUV position. For mission planning and tracking the MIMOSA software package was utilized, developed and provided by IFREMER. The AUV steers about 40 m above the seafloor in order to achieve the best performance of the onboard mounted RESON 7125B multibeam (operating with 400 kHz). Profile line distance was about 60 m, cruising speed about 3 knots. The recorded multibeam data were processed with CARIS 7.0 HIPS and SIPS producing maps with a final resolution of 0.5 m grid cell size.

5.4.2 ROV operations

Three dives (dives 164, 165 and 171) with the deep-water remotely operated vehicle (ROV) 'MARUM Quest 4000m' were conducted at Kerch-Flare during cruise MSM15/2 for seafloor inspections, gas bubble flux evaluation, and gas sampling. GPS-based positioning was performed using the shipboard IXSEA Posidonia ultra short base line (USBL) positioning system. Performance of the USBL system reached an absolute accuracy of 5–10 m in a water depth of ~890 m. For the detection of gas emissions and documentation of short-term variations the ROV was flying 20 m above the seafloor while scanning the water column for backscatter signals caused by bubbles with the Kongsberg 675 kHz Type 1071 horizontally looking scanning sonar head as described by Nikolovska et al. (2008). Sonar records have been recorded and processed with Kongsberg MS1000 and ImageJ (developed by W. Rasband, National Institutes of Health, Bethesda, MD; available at Hhttp://rsbweb.nih.gov/ij/H).

The ROV is equipped with two color-zoom cameras in order to gain an overview and a near bottom mounted broadcast standard 3CCD HDTV zoom video camera for close up video recording. Spatial resolution of this camera is 2.2 Mega-Pixel at 59.94 Hz interlaced. The video material was used for getting a general overview of seafloor structures and for detailed gas bubble recording of the emission sites. For quality improvement of single bubble analysis, a black colored imaging plate handled by the ROV manipulator was used by placing it just behind a gas bubble stream. Due to the plain-colored background and an attached rule for scaling, bubble streams could be recorded in high quality.

Evaluations of bubble sizes and numbers have been conducted with the video recordings by using the Adobe Premiere Pro CS 3.0 program for replaying the videos and counting rising bubbles frame by frame. Frames were exported to the ImageJ program for bubble size analyses. The major and minor axes were measured and the volume was calculated by assuming a rotational ellipsoid with an equivalent spherical radius (Leifer and Patro, 2002). Bubble fluxes (in mL min^{-1}) were calculated considering average bubble volume and amount of bubbles rising through the water column. The volume flux was converted to gas flux (in mol CH_4 min^{-1}) assuming that the gas entirely consists of methane and considering the methane compressibility as described in Römer et al. (submitted).

5.4.3 Samples and analyses

Gravity cores were taken for sedimentological description and the recovery of gas hydrates. During MSM15/2 gravity corer stations were deployed with a 6 m core barrel equipped with soft plastic hose inside to enable rapid access to gas hydrate pieces. During M84/2 the gravity cores were equipped with PVC-liners. In all cases, sediment description and sampling were done immediately after recovery.

Hydrate-bound gas was prepared from intact hydrate pieces according to the method described in Pape et al. (2010). Gas Bubble Samplers (GBS),

operated by the ROV manipulators, were used for pressure sampling of the gas emanating from the seafloor (Pape et al., 2010). Aliquots of hydrate-bound gas and vent gas from the GBS were analyzed onboard immediately upon recovery for their molecular composition (C_1 to C_6, hydrocarbons, Ar, O_2, N_2, CO_2). For this, a two-channel 6890N (Agilent Technologies) gas chromatograph equipped with a capillary column connected to a Flame Ionisation Detector and a stainless steel column packed with a mole sieve coupled to a Thermal Conductivity Detector was used (Pape et al., 2010). The coefficient of variation determined for the analytical procedure was lower than 2%.

Stable hydrogen and carbon isotope ratios ($^2H/^1H$; $^{13}C/^{12}C$) of methane in vent gas and hydrate-bound gas were determined by GC–isotope ratio mass spectrometry (GC–IRMS) on additional gas aliquots in the home lab at the MARUM in Bremen. For this, a Trace GC Ultra-GC IsoLink connected to a MAT 253 isotope ratio mass spectrometer via a ConFlo IV interface (all components Thermo Fisher Scientific Inc.) was used. For separation of methane, a CARBOXEN-1006 PLOT capillary column (Supelco Inc.) was used. All samples were injected at room temperature. Chromatography and reproducibility were checked daily using commercial methane standards (Air Liquide GmbH, Germany).

Considering the molecular gas composition determined during MSM15/2 and CTD-derived bottom water temperature and salinity profiles gained during M72/3, the local phase diagram for gas hydrate was calculated with the HWHYD program (Masoudi and Tohidi, 2005). For modeling the bubble fate and the bubble methane contents, the single bubble dissolution model developed by McGinnis et al. (2006) and provided as SiBu-GUI by Greinert and McGinnis (2009) was used. This model allows for calculating the methane fraction within gas bubbles rising through the water column and the bubble dissolution depth.

5.4.4 In situ sediment temperature measurements

In situ temperature measurements from shallow sediment depths were obtained using an ROV-operated temperature probe during MSM15/2 in 2010. Manufactured by RBR Ltd. in Canada, the so-called T-stick consists of a Delrin rod with 8 sensors spaced at an interval of 6.6 cm, which is connected to a standard data logger (Feseker et al., 2009). Prior to the cruise, the probe had been calibrated to a precision of 0.002 K. Attached to a handle piece, the instrument was inserted vertically into the sediment with the manipulator arm of an ROV. For each measurement, the probe remained in the sediment for 5 to 10 minutes. Temperature readings were recorded continuously at an interval of 5 seconds while the ROV was in the water. Equilibrium sediment temperatures were calculated by extrapolation from the temperature time series recorded while the probe was in the sediment (Villinger & Davis, 1987).

Measurements at greater sediment depths were conducted during M84/2 and MSM15/2 using autonomous miniaturized temperature loggers (MTLs), manufactured by ANTARES Datensystem GmbH in Germany. The loggers were mounted on outriggers that were attached to the barrel of a gravity corer. The spacing between the MTLs varied between 125 and 130 cm. As the MTLs had not been calibrated prior to the cruise, the offset between individual sensors was corrected using a period of time when the gravity corer was hanging in deep water. The resulting relative precision of the measurements is around 0.002 K. At each station, the gravity corer remained in the sediment for between 5 and 10 minutes after penetration to allow for the sensors to adjust to ambient sediment temperature. Equilibrium temperatures were calculated by extrapolation from the recorded time series in the same way as for the ROV-operated probe.

5.5 Results

5.5.1 Seafloor morphology and backscatter

The study area located southwest of the Kerch Strait at the Don-Kuban paleo-fan (Fig. 5-1A) was surveyed intensely along the entire margin from water depths between 150 and 1200 m (Fig. 5-2). The ship-based swath bathymetry shows several roughly N-S trending ridges separated by deeply incised valleys. The Kerch seep area is located at a water depth of ~890 m below sealevel (mbsl) on a crest of a NW-SE trending ridge. High-resolution micro-bathymetric data acquired during AUV dives at the Kerch seep area revealed the occurrence of numerous escarpments (vertical offsets of up to 2.5 m) along the ridge flanks perpendicular to the slope (Fig. 5-3A). We interpret these escarpments as the surface expressions of gravitational sliding or creeping of sediments. The most prominent features visible in the high-resolution bathymetric map are two elliptical-shaped mound structures of different sizes. The larger structure is elevated up to 10 m relative to the surrounding area. Small fractures perpendicular to the above mentioned escarpments in the central part of the elevation (Fig. 5-3A) may indicate that sediments have been domed up. The smaller structure has a radius of about 120 m and is elevated by only a few meters.

Both mound structures are characterized by high backscatter in the ship-mounted multibeam data (Fig. 5-3B). The backscatter image illustrates that the larger mound expands further to the east beyond the coverage of the AUV-based bathymetry. Its total extension is about 1.7 km in E-W and 0.6 km in N-S direction (Fig. 5-3B). From the high-resolution map of the AUV a circular structure becomes apparent at the south-western rim of the small mound, which might be attributed to slumping events (Fig. 5-3A and 5-6A).

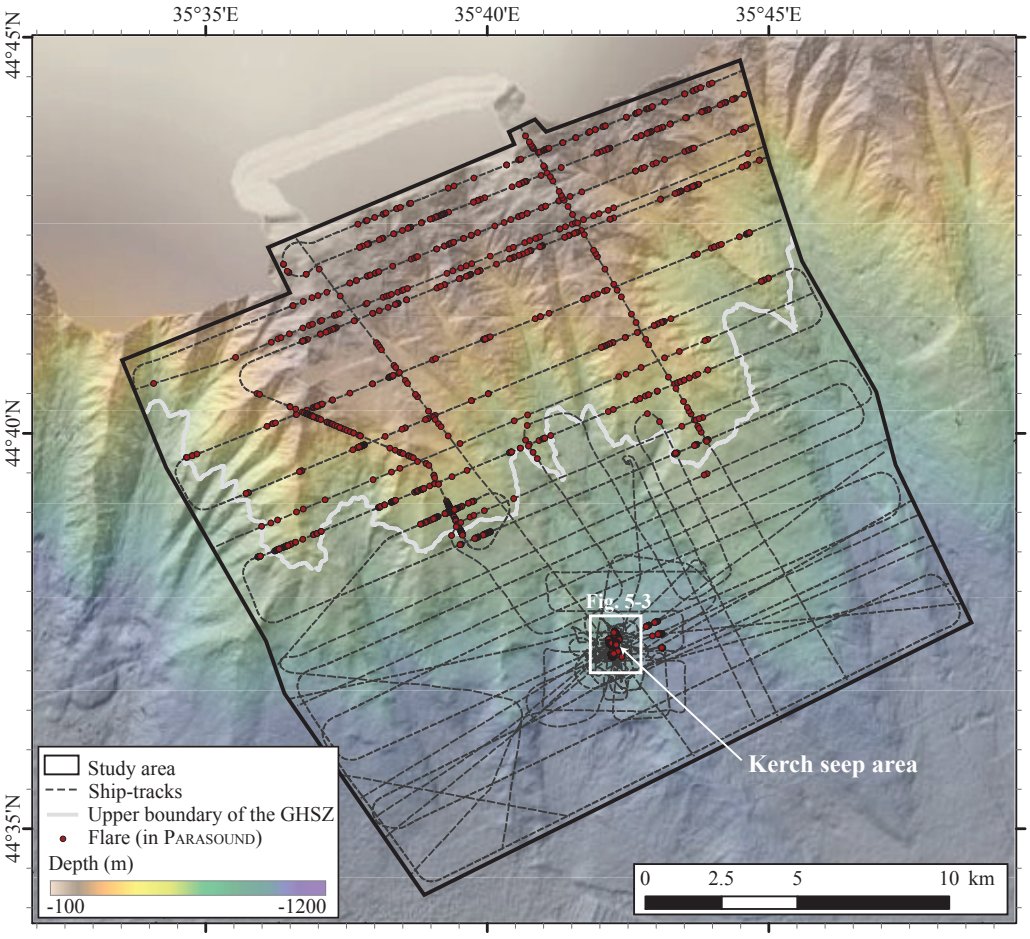

Fig. 5-2: Ship-based swath bathymetry map of the study area at the Don-Kuban paleo-fan. About 600 hydroacoustic anomalies (flares) indicative for ascending gas bubbles were detected in the water column during three cruises conducted within four years. Most of the flares were located in waters shallower than 700 mbsl. This depth marks the upper limit of the gas hydrate stability zone (GHSZ).

5.5.2 Hydroacoustic anomalies in the water column

The general distribution of bubble emissions at the Don-Kuban paleo-fan was studied using the 18-19 kHz signal of the single beam PARASOUND echosounder during three cruises. In total, 597 hydroacoustic anomalies in the water column (commonly termed flares) were detected in the 430 km^2 area at depths between 160 and 980 m (Fig. 5-2). They are preferentially located at the flanks and on the crests of the numerous ridges along the margin. More than 97% of the flares are located above the upper limit of the gas hydrate stability zone (GHSZ) in water depths shallower than 700 mbsl. Only 17 flares, including the flares in the Kerch seep area, were detected in deeper waters.

The existence of the Kerch seep area as a gas emission area located within the GHSZ was first indicated to us by colleagues from the Institute of the Biology of the Southern Sea (IBSS) in Sevastopol, Ukraine (Y. Artemov, pers comm.). The Kerch seep area comprises several hydroacoustic anomalies in the water column, which in part are very strong in intensity. Such anomalies were detected repeatedly with PARASOUND and the ship-mounted multibeam systems EM122 and EM710 during three cruises. A 3D-image of eight flares is shown in Fig. 5-4A, which were detected during the survey conducted 25th March, 2011. Flares 1, 6, and 7 are relatively weak in intensity and dissolve at water depths between 690 and 700 mbsl. In contrast, Flare 2 and 8 appear very strong in intensity and are about 540 and 450 m in height, dissolving at water depths between 350 and 460 mbsl, respectively. Flares 3, 4, and 5 are also relatively intense but are characterized by intermediate rising heights (260 – 290 m).

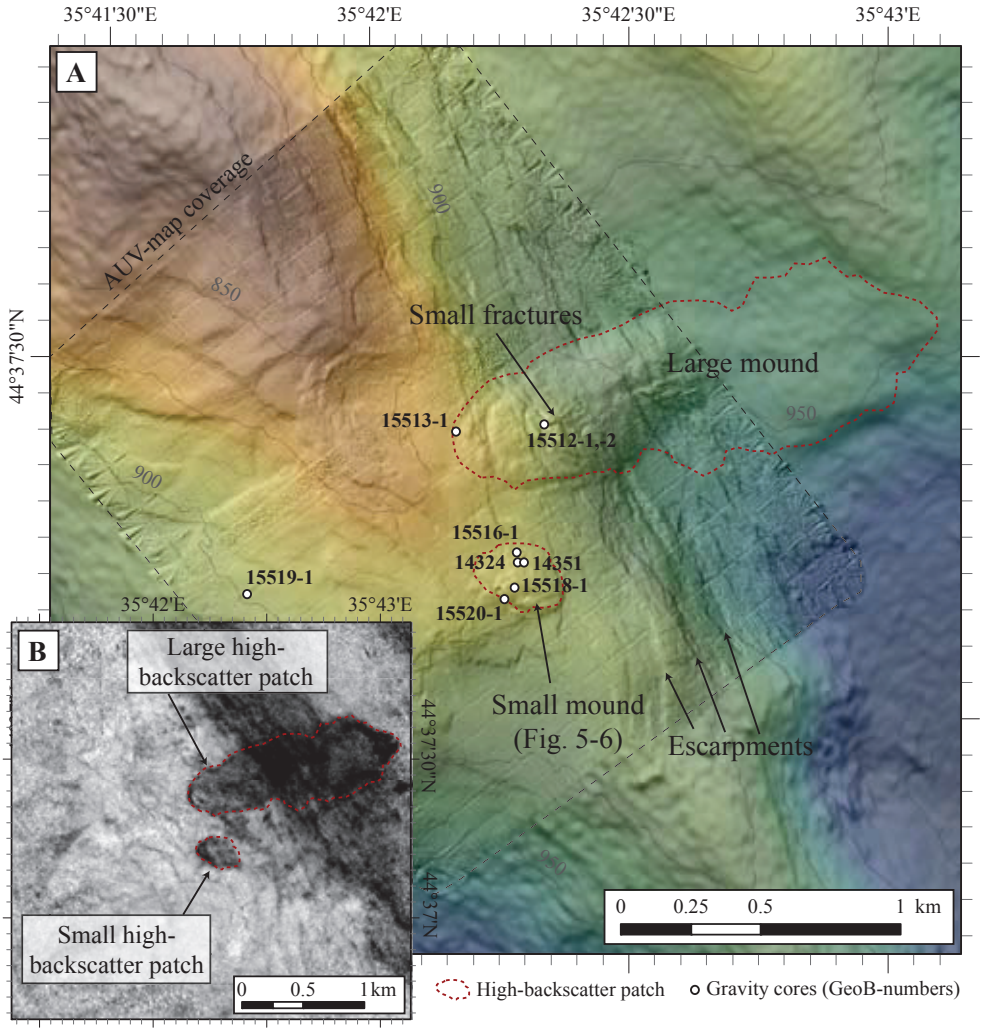

Fig. 5-3: A) High-resolution bathymetric map of the Kerch seep area combining results from AUV- and ship-based swath echosounders. The approximate extents of the mounds as well the gravity corer sampling locations are indicated. B) Ship-based swath echosounder backscatter map of the same area showing two high-backscatter anomalies (dark color) that coincide with the elevated structures visible in the bathymetric map (Fig. 5-3A).

The appearance of flares caused by rising gas bubbles, recorded with the 19 kHz signal during a single beam PARASOUND echosounder profile running from N to S is depicted in Fig. 5-4C. Flares 4 and 5 were crossed near the center of emission and appear strong while Flare 2 was crossed marginally resulting in a weak water column anomaly. The flares are slightly deflected in the water column, probably as a consequence of horizontal water currents. As a result, the upper part of Flare 2 appears in the profile, demonstrating that bubbles of this flare rise up to almost 350 mbsl.

The 4 kHz signal of PARASOUND (Fig. 5-4C) further shows columnar zones in the sediments characterized by blanking and reaching up to about 20 m below the seafloor (mbsf). The horizontal extent of the blanking zones matches the extents of the mounds as revealed from high-resolution

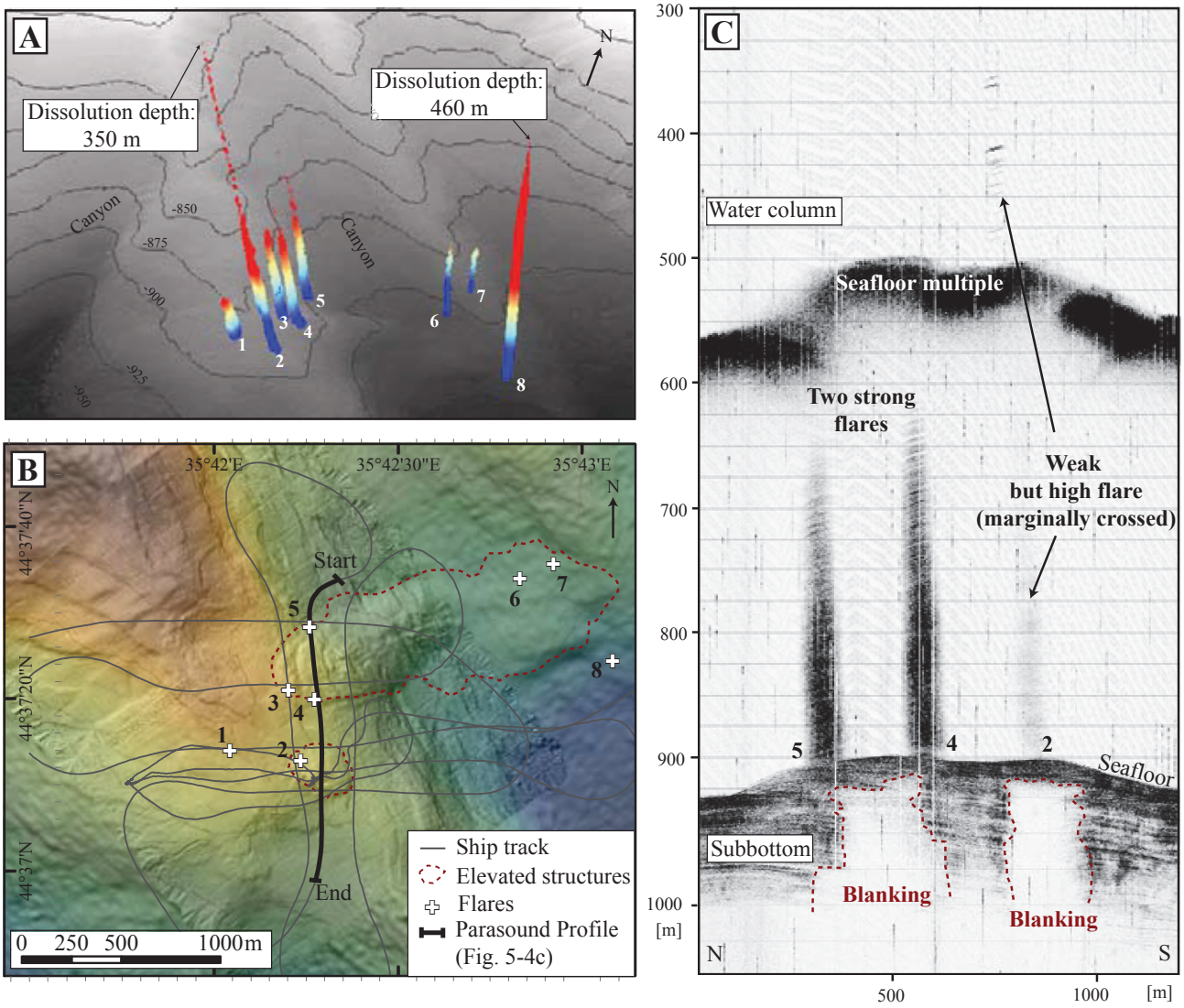

Fig. 5-4: A) 3D-image illustrating gas emissions at the Kerch seep area using the ship-based multibeam system. On the 25th of March 2011 (M84/2) eight flares were observed. B) The ship-track and the flares recorded on the 25th of March 2011 plotted on the AUV- and ship-based swath bathymetry map. The extents of mounds are outlined. Flares were primarily located close to the rims of the mounds. C) Composite PARASOUND echogram recorded while crossing the Kerch seep area. The image shows the 18 kHz signal above the seafloor and the 4 kHz signal below the seafloor. The location of the profile is depicted in Fig. 5-4B.

bathymetry and the high reflectivity patches in the backscatter map (Figs. 5-3A and B), suggesting a generic relationship. The gas emission sites are generally located close to the rims of the mounds (Fig. 5-4B) corresponding to the rims of the sub-surface blanking zones (Fig. 5-4C).

We studied the temporal and spatial variability of gas emission sites in a dedicated area of the Kerch seep area that comprises the small mound and the western part of the large mound (but not the eastern part of the large mound). We compare data from surveys conducted in 2007, 2010, and 2011 and at different days during individual cruises. Fig. 5-5A summarizes the positions of all flare areas (open circles), which are areas where at least one time a hydroacoustic anomaly was observed during all surveys. Due to the footprint size of the echosounder at this water depth, the flare areas were estimated using the corresponding diameter of ~60 m. This compilation shows that gas emission sites tend to cluster at the northern rim of the small mound and at the western rim of the large mound. As we used two different methods for flare detection in different years, we selected the following way of dis-playing the spatial and temporal variability of gas emissions during individual surveys. In Figs. 5B-F those flare areas with active bubble emission are marked by red-filled circles. Black-filled circles mark inactive flare areas, which are locations that were covered during the respective survey but did not show any evidence for bubble emission at that time. Open circles indicate those flare areas that have not been surveyed and for which we have, therefore, no information about their activity. The latter category (open circles) has relevance for the surveys in 2007 and 2010 (Figs. 5-5B – D) using the

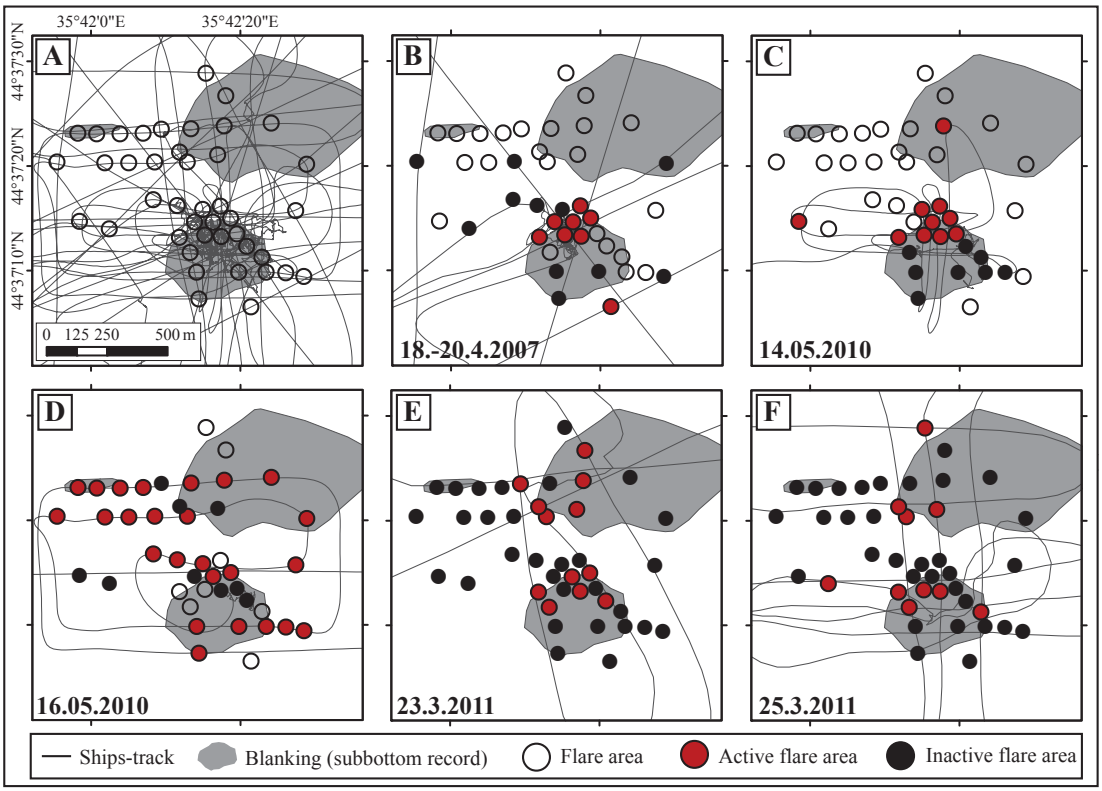

Fig. 5-5: A) Distribution of all 42 flare areas detected within the Kerch seep area with all ship-tracks. The grey shaded areas indicate the extent of acoustic blanking (Fig. 5-4 C) corresponding approximately to the extent of the mounds (Fig. 5-4B). B) to F) The flare activity during five different time periods. The number of active bubble emissions (red-filled circles) compared to the number of inactive bubble emissions at surveyed flare areas (black-filled circles) is more or less the same, which suggests that bubble emissions vary mainly spatially.

single beam Parasound echosounder that can only record flares situated directly beneath the ship. During the surveys in 2011 (Figs. 5-5E and F) we used the multibeam echosounder for flare detection providing coverage of the entire area. In summary, the five surveys (Figs. 5-5B – F) revealed that gas bubbles were always emitted from both structures during the periods of observations, suggesting a continuous gas discharge. Furthermore, results from each of the individual surveys show that gas bubbles are released from two main areas, of which one is located at the northern rim of the small mound and the other is situated at the western rim of the larger mound. Finally, the surveys illustrate that, despite spatial variability of individual bubble emissions, the total number of sites actively emitting gas is fairly constant between the surveys. Between 24 and 74% of the surveyed sites had been active during each of the five surveys with an average value of about 47%.

5.5.3 Visual seafloor observations

In order to document seafloor features, sample gas bubbles, and perform temperature measurements, three ROV dives were conducted at and around the small mound at the Kerch seep area (Fig. 5-6A). The seafloor in that area was generally flat and smooth lacking striking morphological structures. Within an area of about 150 × 200 m covered by the ROV tracks, nine bubble emission sites (BES) characterized by slightly darker sediment than the surrounding were found (Figs. 5-6B). Within those areas the seafloor was perforated by numer-ous small holes with diameters of about 1 to 4 cm (Figs. 5-7A and B). As observed frequently bubble escape takes place from these orifices (Fig. 5-7D). In addition to the holes, features that look like bubble-induced sediment ejection were observed (Fig. 5-7C): The central bright-colored parts are probably exposed coccolith-rich sediment layers that are surrounded by darker sediments, which we interpret as relocated material. These features probably result from

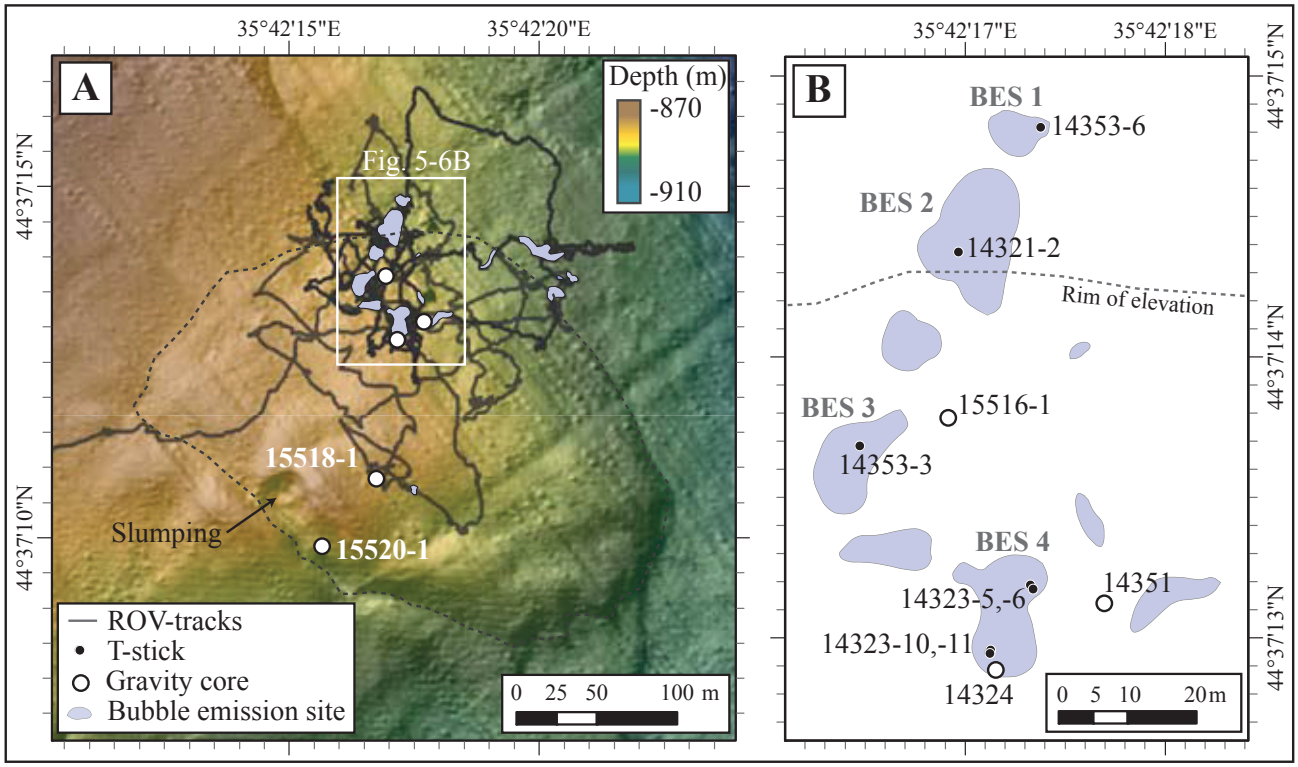

Fig. 5-6: A) ROV dive tracks plotted on the high-resolution bathymetric map compiled from AUV swath echosounder data at the smaller mound in the southern part of the study area. B) Close up of the bubble emission sites at the small mound at the Kerch seep area and sampling stations. Bubble emission sites with gas bubble streams are labeled BES 1 to BES 4.

bubble escape as well. In general, we regard holes or bubble-induced sediment ejection as a result of relatively recent bubble emission and mapped their extent (gray shading in Figs. 5-6A and B).

During the ROV dives, bubble escape was observed at four of the mapped bubble emission sites at the small mound, which were labeled BES 1 to BES 4 (Fig. 5-6B). According to the ROV observations the bubble emission sites are distributed over an area of about 100 × 150 m. This area with observed bubble emission sites is only a small part of the entire area where the results of hydroacoustics suggest gas emissions (Fig. 5-5). Roughly, the area mapped by ROV corresponds to approximately two of the flare areas indicated in Figure 5-5.

Each of the four actively degassing bubble emission sites has an approximate extent of 50 to 230 m^2 and they are irregular in shape (Fig. 5-6B). At times, the bubble escape was very strong in form of numerous intense gas bubble streams (observed at BES 4 during ROV-dive 265), whereas in some cases only few single bubble trains (BES 2 and 3) occurred.

The Kerch seep area is located within the GHSZ, which is confirmed by the observation of gas hydrate formation when bubbles were trapped in the reversely mounted funnel attached to the GBS (Fig. 5-7E). However, some parts of the accumulated gas remained in the gaseous phase, a phenomenon that is not further discussed as it is beyond the scope of the study.

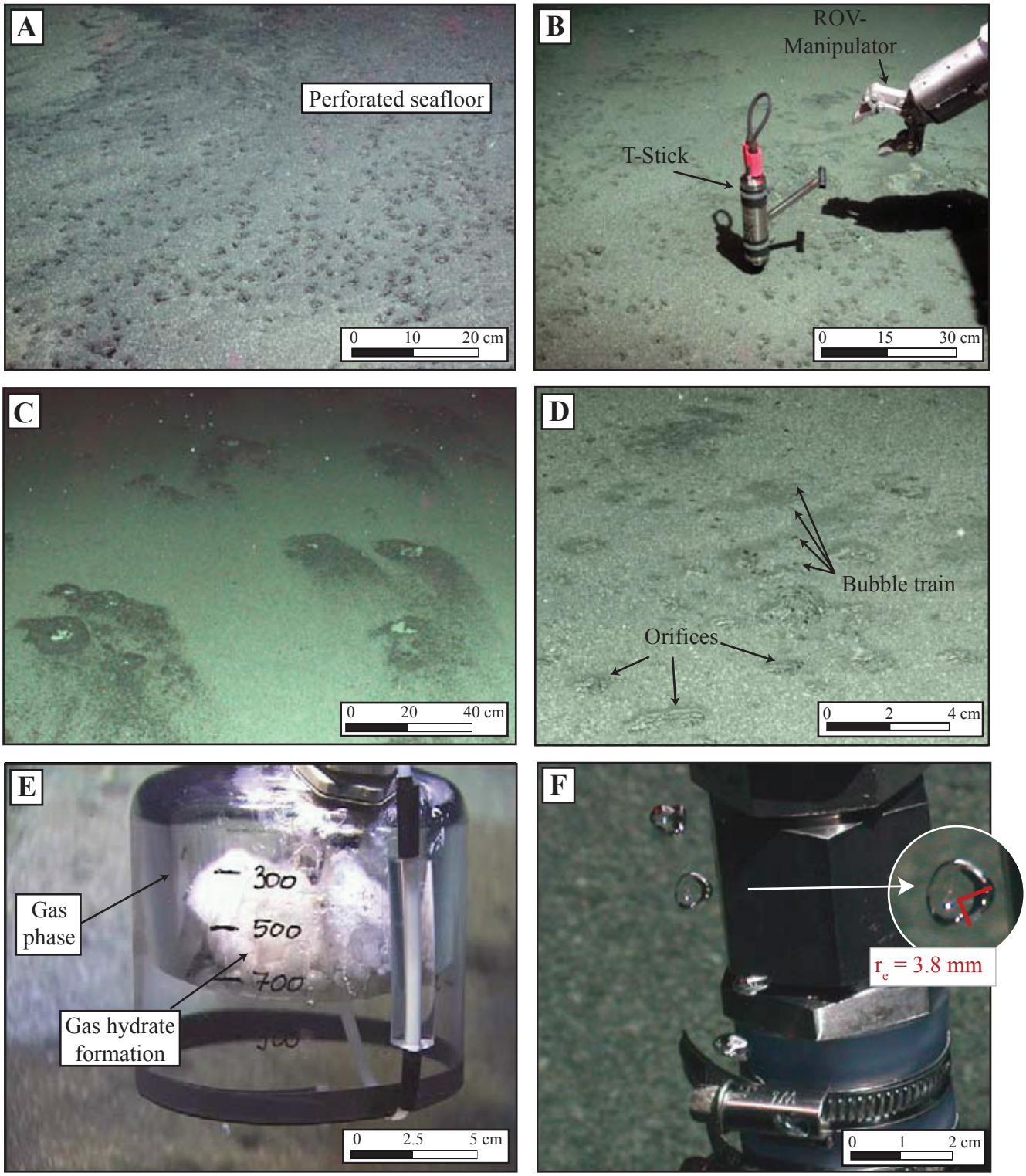

Fig. 5-7: Seafloor images taken with the still camera or frame grabs of the high-definition video camera mounted on ROV 'MARUM Quest 4000m' illustrating the appearance of bubble emission sites and sampling at the Kerch seep area (All images courtesy of MARUM). A) The darker colored sediments are perforated by numerous bubble escape orifices. B) A temperature measurement performed within a bubble emission site using the T-stick handled by the ROV manipulator (GeoB 14323-10). C) Seafloor features very likely also related to gas bubble escape. D) A gas bubble stream emanating from the seafloor. Bubble escape formed orifices of 1 – 4 cm in diameter resulting in the typical perforated seafloor. E) Gas bubbles are collected in a funnel during sampling using the gas bubble sampler (GBS) and the formation of gas hydrates was observed. F) Rising gas bubbles were counted and measured (r_e: bubble equivalent spherical radius) to calculate the gas flux.

5.5.4 Quantification of gas emissions

Visual observations of four bubble emission sites (BES 1 – 4) provide a rough estimate of the gas amount transferred into the water column. For each bubble emission site, the gas bubble streams were documented in detail by high-definition video records and analyzed for the frequency at which bubbles escape from the seafloor and the bubble size (Table 5-1). The observed gas bubble streams emitted between less than 1 and more than 60 bubbles per second, demonstrating the high variability between sites. The bubbles had an average equivalent spherical radius (r_e) of 2.89 ± 0.52 mm (n = 750). The bubble size distribution followed a Gaussian normal distribution with the radii ranging between 1.5 and 5.1 cm. The bubble volumes were calculated assuming a horizontally elliptical shape of the visually analyzed bubbles after determination of the major and minor axis (Fig. 5-7F). The resulting average bubble volume was 0.108 mL for a single bubble and the overall bubble volumes ranged between 0.012 – 0.512 mL. At BES 1 three gas bubble streams existed permanently during the observation time (~25 min). At the most intense gas bubble stream bubbles were emitted continuously at a frequency of 14 bubbles per second. More than 100 bubbles were analyzed and their average radius was 2.76 mm. Consequently, from this bubble stream about 1.20 mL s^{-1} equaling 0.36 mol CH_4 min^{-1} emanated into the water column, assuming the gas being entirely methane (see section 5.4.7). The other two gas bubble streams were not quantified but as they were clearly weaker, we assume that they did not contribute significantly to the methane flux from BES 1.

Four gas bubble streams occurred at BES 2 and existed during the entire observation time (~64 min). At each gas bubble stream bubbles escaped the seafloor with a very low bubble frequency ranging between 1 and 3 bubbles per second. The average bubble radius was 2.67 mm (n = 150). For the entire BES 2, the gas flux accounted for about 0.46 mL s^{-1} correspond-ing to 0.13 mol CH_4 min^{-1}.

At BES 3, two gas bubble streams were documented for 23 min. At one of the gas bubble streams about 3.4 bubbles escaped per second during 460 seconds observation time. The average bubble radius was 3.17 mm (n = 123) and the resulting gas volume flux

Table 5-1: Quantification of the four bubble emission sites (BES 1 to BES 4; for location see Fig. 5-6B) observed during three ROV dives. BES 4 emits far the most amount of methane.

BES	Gas bubble stream	Counting time	Bubble frequency (1 s^{-1})			Bubble equivalent spherical radius (mm)					Bubble volume (ml)		Gas flux (ml min^{-1})		Gas flux (mol min^{-1})	
#	#	s	Ø	min	max	n	Ø	SD	min	max	Ø	SD	Ø	SD	Ø	SD
1	1	60	14	12	15.6	103	2.8	0.3	2.3	3.4	0.09	0.02	73.58	19.74	0.36	0.1
	Total												**73.58**	**19.74**	**0.36**	**0.1**
2	1+2	220	2.9	2	3.6	151	2.7	0.4	1.7	3.6	0.08	0.03	14.45	5.98	0.07	0.03
	3	210	1.6	1.6	1.7								8.07	3.34	0.04	0.02
	4	170	1	0.8	1.4								5.15	2.13	0.03	0.01
	Total												**27.67**	**11.46**	**0.13**	**0.06**
3	1	460	3.4	2.6	4.6	123	3.2	0.6	1.6	4.1	0.14	0.06	29.19	12.24	0.14	0.06
	Total												**58.38**	**24.49**	**0.28**	**0.12**
4	1	10	56.8	52	62	168	3	0.5	1.8	4.1	0.11	0.06	387.5	188.8	1.89	0.92
	2	90	14.3	13.4	16.4	43	2.6	0.4	1.5	3.3	0.08	0.03	65.21	29.17	0.32	0.14
	3	36	29.4	22	34	162	3	0.6	1.9	5.1	0.12	0.08	212.45	140.58	1.03	0.68
	Total												**3325.8**	**1792.8**	**16.18**	**8.73**
Total													**3485.4**	**1848.4**	**16.96**	**9**

Ø = average; n = number; min = minimal; max = maximal; SD = standard diviation

was 0.97 mL s^{-1} corresponding to a methane flux of 0.28 mol min^{-1}. The second gas bubble stream was not quantified, but a short monitoring by the ROV suggested a similar intensity.

BES 4 was the most intense degassing bubble emission site discovered at the Kerch seep area. It was monitored continuously with the ROV-mounted horizontally looking sonar for about 65 minutes. A sonar screenshot is shown as an example in Fig. 8A. Besides sonar imaging, we documented BES 4 with video recordings in which the gas bubble streams were clearly seen (Fig. 5-8B). Within the area of about 2.9 × 2.3 m, 15 intense gas bubble streams were observed of which 13 existed permanently during the entire observation time. An intense gas bubble stream (number 10, Fig. 5-8A) was inactive for the initial 25 minutes but became stable in activity for the remaining time of observation. Another gas bubble stream (number 4, Fig. 5-8A) was more variable in intensity and showed a dormant phase for three minutes. In addition to the 15 intense gas bubble streams, several weaker anomalies of high backscatter appeared in the sonar record with high spatial and temporal variability representing short bubble pulses.

Three of the 15 gas bubble streams were randomly chosen in order to quantify their gas flux. Out of the three, the most intense gas bubble stream had a bubble frequency of 56.8 bubbles per second and the average bubble radius was 2.95 mm (n = 168). The second most active gas bubble stream was less intense with 14.3 bubbles per second, which had an average radius of 2.59 mm (n = 43). The third gas bubble stream showed a bubble frequency of 29.4 bubbles per second and the 162 bubbles analyzed had an average radius of 2.98 mm. Considering that the three quantified gas bubble streams represented approximately one fifth of the total 15 gas bubble streams occurring at BES 4, we roughly estimate the methane flux at about 58.0 mL s^{-1} or 16.18 mol min^{-1} during the ~94 min of visual observation.

Results from ROV-dive observations (video material and records by the horizontally looking sonar) revealed varying activities in time for the four BES. Therefore, the gas flux was calculated for every observation period (Table 5-2), i.e. for the three dives at three different days (14 May 2010, 16 May 2010, and 27 May 2010) using the site-specific flux

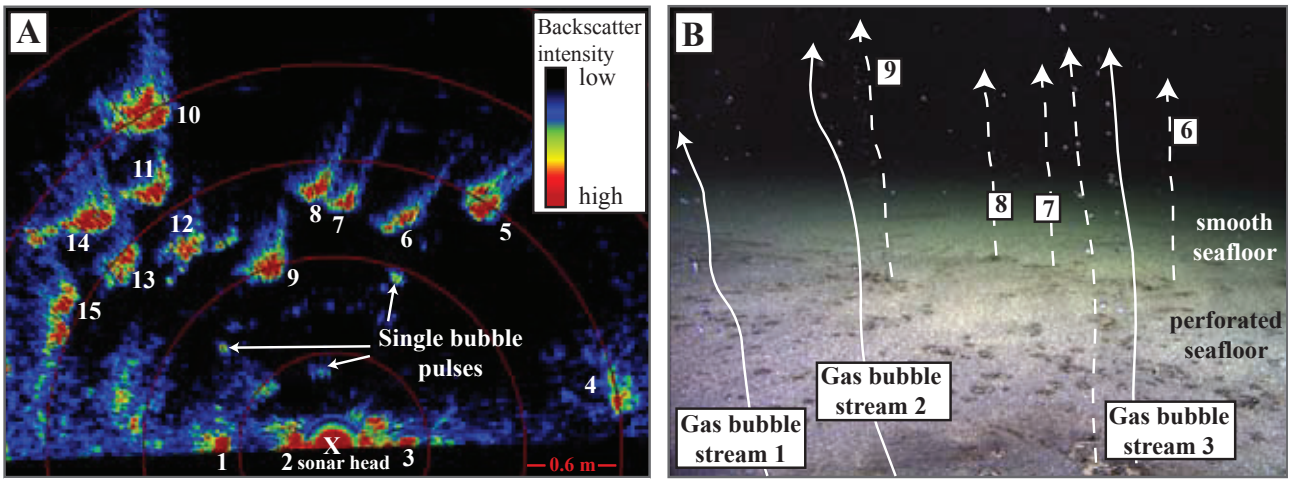

Fig. 5-8: ROV Quest observations at the bubble emission sites BES 4. A) Screenshot of the horizontally looking sonar recorded 15 backscatter anomalies which represent single gas bubble streams. B) Seafloor picture taken at the same time as the sonar record by the high-definition video camera illustrating the gas bubble streams emanating from the seabed that correspond to the anomalies visible in the screenshot of the sonar (Fig. 5-8A). White-colored arrows illustrate the bubble streams that are clearly seen in the video sequence but difficult to trace on the frame grab. Arrows with continuous lines mark the bubble streams which flux was quantified and gas sampled.

for each BES (Table 5-1). On 14 May, only BES 2 and BES 3 were active and jointly emitted 0.42 mol CH_4 min^{-1}. On 16 May BES 1 was not passed during the dive but bubble emission activity was proven for BES 2, 3, and 4. As BES 4 was the most active of the observed bubble emission sites, gas emission on 16 May was the strongest with 16.60 mol min^{-1}. On 27 May gas emissions from BES 1 and 3 were observed and a total flux of 0.64 mol CH_4 min^{-1} is calculated.

Table 5-2: Variability of the methane fluxes (in mol min^{-1}) of the four emission sites as observed during three ROV dives. The total flux at each day gives an impression about the range of fluxes.

Area	14 May 2010	16 May 2010	27 May 2010
BES 1	0	-	0.36
BES 2	0.14	0.14	0
BES 3	0.28	0.28	0.28
BES 4	0	16.18	0
Total	**0.42**	**16.6**	**0.64**

5.5.5 Gas hydrates and authigenic carbonates

A gravity corer (GeoB 15519-1) taken several hundred meters away from the Kerch seep area recovered sediments with the typical Black Sea late glacial to Holocene stratigraphy (Fig. 5-9), which has been classified into three main lithological units (Ross and Degens, 1974): Unit I (coccolith ooze) and Unit II (sapropel) had been deposited during the marine stage of the Black Sea during the mid-late Holocene, and Unit III represents Late Pleistocene-Early Holocene lacustrine mud.

The seven gravity corer taken in the Kerch seep area during M84/2 (Fig. 5-3A) revealed the presence of gas hydrates and authigenic carbonates in the area of the mound structures. Hydrates and carbonates were distributed in a characteristic pattern with indications for massive hydrates and carbonates at the summits of the mounds and small platy pieces of hydrates at their rims. The two gravity corer taken at the summit of the large mound (GeoB 15512-1, -2)

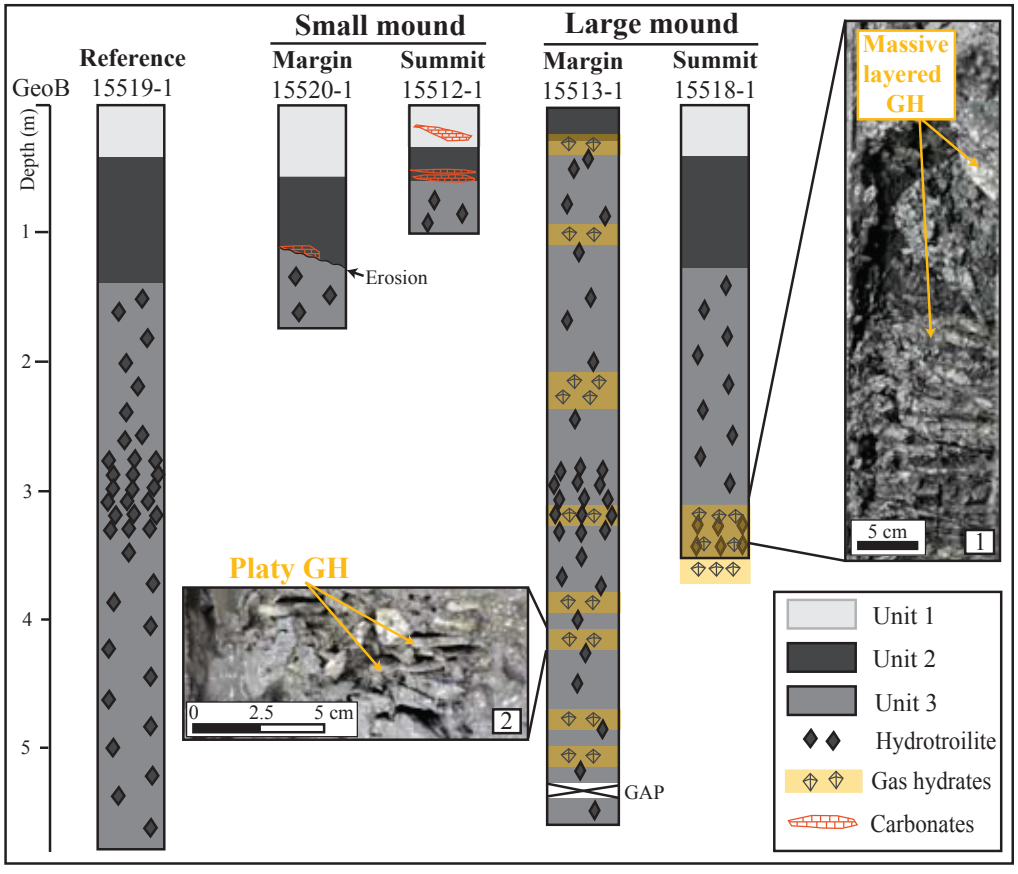

Fig. 5-9: Lithological descriptions of five gravity corer retrieved during M84/2. Several cores contained gas hydrates, either in massive layers at the base of the core (photo 1) or in form of small platy chips distributed in several thin horizontal layers (photo 2). The cores taken at the small mound were relatively short in length and contained carbonate precipitates.

were relatively short (140 and 170 cm, respectively) and recovered gas-rich sediments but no macroscopically visible gas hydrates (GeoB 15512-1 in Fig. 5-9). Sediments belonging to Unit I and II were present in varying thicknesses and contained carbonate precipitates. The core retrieved from the summit of the smaller mound (GeoB 15518-1) was longer and contained gas hydrates in the lowermost part (ca. 320 cm to 375 cmbsf), partly in massive layers (Photo 1 in Fig. 5-9). In contrast to the cores from the summit of the larger mound, carbonate precipitates were not observed. Two cores obtained from marginal sites of each mound (GeoB 15513-1, 15516-1) yielded much higher recoveries than the cores from the summits and contained hydrates in high abundances (15513-1 in Fig. 5-9). The hydrates occurred in layers parallel to the sediment bedding, with the hydrate layers being a few cm thick and consisting of small platy chips (Photo 2 in Fig. 5-9). These hydrates occurred from the base of the sapropel (Unit II) throughout the entire Unit III down to the base of the cores. Carbonate cementation was not observed for those cores.

In addition to the above mentioned gravity corer from the rim of the mounds, another corer taken at the southern rim of the small mound (GeoB 15520-1, recovery: 163 cm) was likely affected by a small-scale sliding process, as Unit II and III were separated by an oblique erosive boundary and carbonate cementation occurred along this boundary (Fig. 5-9). On deck the core was strongly degassing but gas hydrates were not retrieved.

5.5.6 Temperature gradients in the sediments

In situ temperature measurements at shallow sediment depths were conducted using the ROV-operated T-stick at seven stations in the Kerch seep area. In addition, the gravity corer equipped with MTLs was deployed at eight stations in order to obtain measurements from greater sediment depths. The positions of the measurements during the ROV dives and the stations where the gravity corer was deployed are shown in Fig. 5-3A and 5-6B, respectively.

All of the sediment temperature profiles obtained with the gravity corer show a nearly linear increase of temperature with depths (Fig. 5-10). The corresponding temperature gradients range between 0.023 and 0.086 °C m^{-1} (Table 5-3).

Table 5-3: Positions of gravity cores equipped with temperature probes (GC-T) and T-sticks deployed at the Kerch seep area during MSM15/2 and M84/2 and calculated temperature gradients.

Sample code (GeoB)	Sampling tool	Cruise	Location	T-gradient (°C m-1)
14321-2	T-Stick	MSM15-2	44°37.239'N 35°42.282'E	n.a.
14323-5	T-Stick	MSM15-2	44°37.220'N 35°42.288'E	0.14
14323-6	T-Stick	MSM15-2	44°37.219'N 35°42.288'E	0.2
14323-10	T-Stick	MSM15-2	44°37.216'N 35°42.285'E	0.17
14323-11	T-Stick	MSM15-2	44°37.216'N 35°42.285'E	0.054
14353-3	T-Stick	MSM15-2	44°37.223'N 35°42.279'E	0.62
14353-6	T-Stick	MSM15-2	44°37.247'N 35°42.289'E	n.a.
14324	GC-T	MSM15-2	44°37.221' N 35°42.302' E	0.061
14351	GC-T	MSM15-2	44°37.219' N 35°42.295' E	0.086
15512-1	GC-T	M84-2	44°37.420' N 35°42.359' E	0.031
15512-2	GC	M84-2	44°37.419' N 35°42.359' E	Without t-probes
15513-1	GC-T	M84-2	44°37.386' N 35°42.164' E	0.028
15516-1	GC-T	M84-2	44°37.230' N 35°42.282' E	0.049
15518-1	GC-T	M84-2	44°37.182' N 35°42.279' E	0.059
15519-1	GC-T	M84-2	44°37.171' N 35°41.763' E	0.023
15520-1	GC-T	M84-2	44°37.166' N 35°42.261' E	0.045

n.a. = not analyzed

In contrast, the ROV-operated T-stick revealed remarkably high temperature anomalies at or very close to sites of bubble emission (Fig. 5-10). The maximum temperature measured at a sediment depth of about 0.5 m was about 0.3 °C higher than the bottom water (~8.95 °C). Some of the shallow temperature profiles are nearly linear while others zigzag significantly (e.g. GeoB 14353-6), illustrating the highly dynamic temperature system influenced by bubble flow. Despite the fact that these are non-steady state systems, we calculated the temperature gradients (Table 5-3) for the purpose of illustrating the distribution of thermal anomalies related to the seafloor structures in the Kerch seep area (Fig. 5-11).

A temperature gradient of 0.023 °C m^{-1} measured at the reference station of the gravity corer is considered as background value. Similarly low gradients were observed at two other gravity corer stations (GeoB 15512-1, 15513-1), both located at the large mound but remote from bubble emissions. The gravity corer stations located close to bubble emission sites at the small mound showed elevated temperature gradients (Fig. 5-11) ranging between 0.04 and 0.1 °C m^{-1} (GeoB 15520-1, 15516-1, 15518-1, 14324 and 14351). In the course of the three ROV-

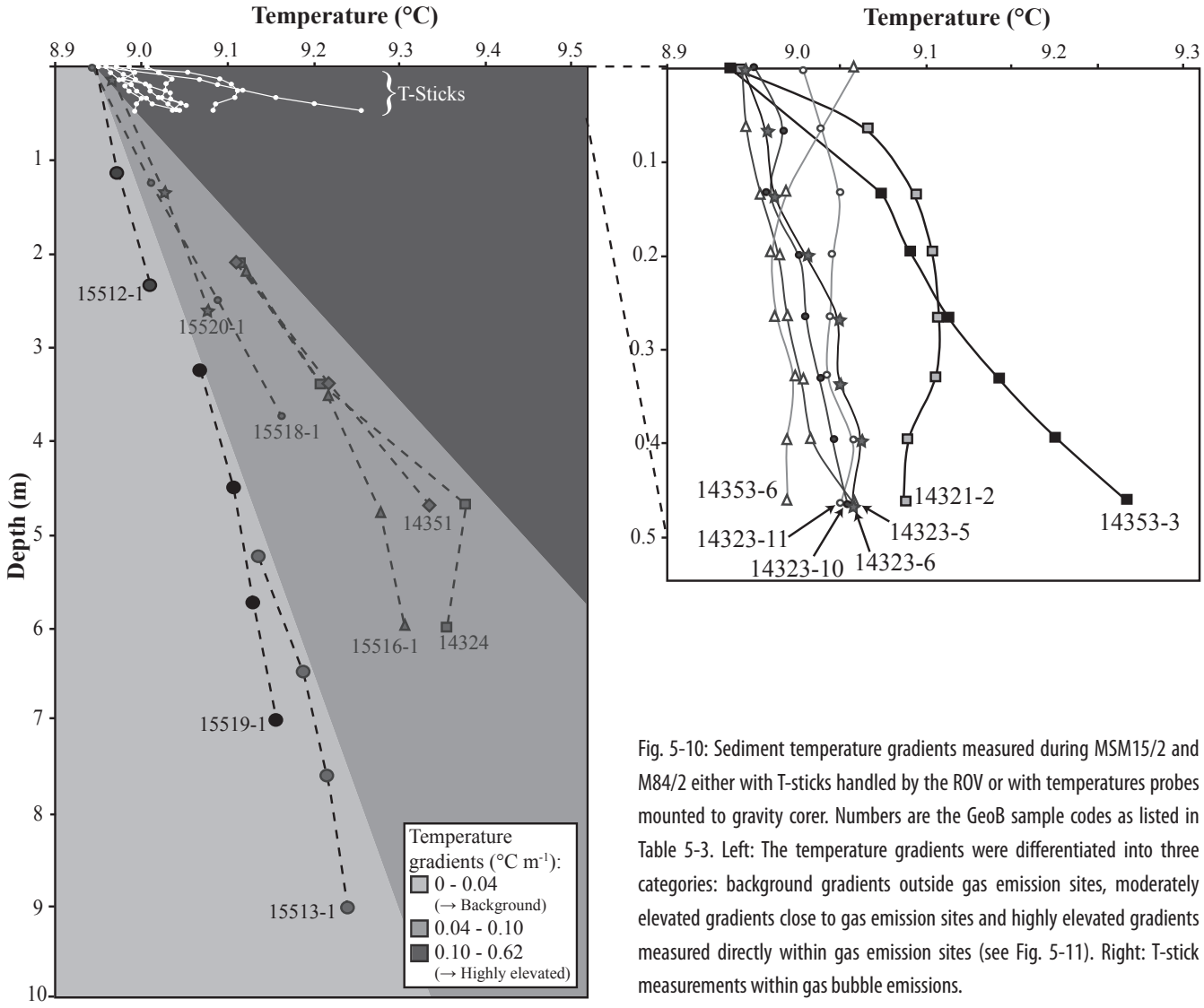

Fig. 5-10: Sediment temperature gradients measured during MSM15/2 and M84/2 either with T-sticks handled by the ROV or with temperatures probes mounted to gravity corer. Numbers are the GeoB sample codes as listed in Table 5-3. Left: The temperature gradients were differentiated into three categories: background gradients outside gas emission sites, moderately elevated gradients close to gas emission sites and highly elevated gradients measured directly within gas emission sites (see Fig. 5-11). Right: T-stick measurements within gas bubble emissions.

dives conducted in the northern part of the small mound, shallow sediment temperature profiles could be measured directly within the orifices created by bubble emission (as illustrated in Fig. 5-7B). With the two exceptions where the profiles were significantly disturbed, the shallow sediment temperature profiles showed elevated temperature gradients over 0.05 °C m^{-1}. One of the measurements was associated with a very high temperature gradient of around 0.62 °C m^{-1} (GeoB 14353-3). Another measurement (GeoB 14321-2) revealed a convex profile with a temperature increase of 0.16 °C within the upper 0.3 m of the sediment.

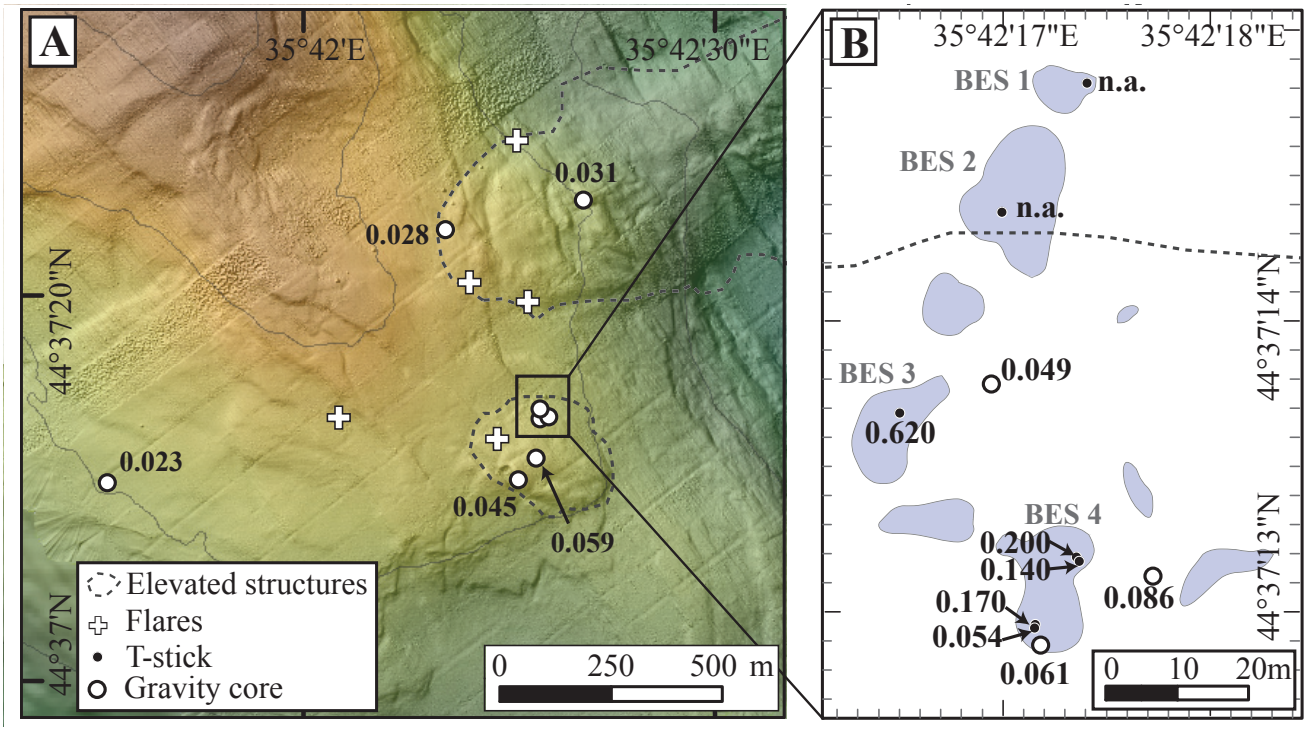

Fig. 5-11: Temperature measurement locations and values of temperature gradients (in °C m^{-1}) as given in Table 5-3 at the Kerch seep area. A) Overview map and B) detailed measurements at the bubble emission sites (BES). The strongest temperature anomalies were recorded by T-stick directly in sediments percolated by bubbles. Station numbers see Figs. 5-3 and 5-6.

5.5.7 Gas composition

The vent gas samples collected with the GBS at four stations within the Kerch seep area were strongly dominated by methane (99.259 mol-% of C_1–C_5 and CO_2), followed by carbon dioxide (0.532 – 0.703 mol-%), ethane (0.028 – 0.032 mol-%) and propane (0.005 mol-%; data not shown). Iso-butane and n-butane were only found in traces (0.004 and 0.002 mol-%, respectively). The mean molecular hydrocarbon ratio (C_1/C_{2+}) of vent gas was 2,372 gas (n = 5; Table 5-4), whereas that of hydrate-bound gas was 2,472 (n = 4). Likewise the stable carbon isotopic composition of methane in both gas types differed only slightly with average δ^{13}C-CH_4 values of –66.6 (‰ V-PDB; Table 5-4) for vent gas and –67.8 (‰ V-PDB) for hydrate-bound gas. The molecular and stable carbon isotopic composition of hydrocarbons and methane, respectively, from all sampling site within the Kerch seep area were quite similar and seem to be independent from the sample locations.

Table 5-4: Molecular composition of light hydrocarbons (expressed as $C_1/C_{2+} = C_1/(C_2 – C_5)$) as well as stable carbon and hydrogen isotopic ratios of methane in vent gas and hydrate-bound gas sampled at the Kerch seep area during cruises MSM15/2 and M84/2.

Sample code (GeoB)	Sampling Tool	Gas Type	C_1/C_{2+}	δ^{13}C-CH_4	δ^2H-CH_4
				[‰ V-PDB]	[‰ SMOW]
14321-1	GBS	Vent gas	2447	–66.3	n.a.
14323-3	GBS	Vent gas	2249	–66.7	n.a.
14323-4	GBS	Vent gas	2330	–66.6	n.a.
		mean	**2342**	**–66.5**	
15513-1	GC	Hydrate-bound gas	2878	–68.4	n.a.
15516-1	GC	Hydrate-bound gas	2424	–67.5	–248.2
15518	GC	Hydrate-bound gas	2498	–66.9	–247.9
14324-2	GC	Hydrate-bound gas	2087	–68.4	n.a.
		mean	**2472**	**–67.8**	**–248.1**

GBS = Gas Bubble Sampler (vent gas); GC = Gravity corer (hydrate-bound gas)

n.a. = not analyzed

5.6 Discussion

5.6.1 Origin of gas

The prevalence of methane (C_1/C_{2+} ca. 2,100 to 2,900; Table 5-4) in light hydrocarbons and its significant depletion in ^{13}C ($\delta^{13}C\text{-}CH_4$ = –68.4 to –66.3‰ V-PDB), indicates that methane in vent and hydrate-bound gas samples taken at the Kerch seep area predominantly originates from microbial methanogenesis (Bernard et al., 1976). Moreover, individual C_4- and C_5-hydrocarbons which are commonly attributed to thermogenic input (Claypool and Kvenvolden, 1983; Schoell, 1980) were virtually absent. Based on these molecular and stable isotopic characteristics, a significant admixture of thermogenic hydrocarbons is not evident for our sample set. In addition, from the δ^2H vs. $\delta^{13}C$-relationship of methane in two selected hydrate-bound gas samples (GeoB 15516-1 and 15518-1, Table 5-4), microbial carbonate reduction as the principal methane formation pathway in the subsurface at the Kerch seep area may be inferred (Whiticar, 1999).

The similarity in molecular compositions of light hydrocarbons and stable carbon isotopic compositions of methane as observed for all gas samples, suggests sourcing from the same gas reservoir for the bubble sites.

5.6.2 Gas hydrate sealing and the exception at the Kerch seep area

The spatial distribution of hydroacoustic anomalies in the study area at the Don-Kuban paleo-fan (Fig. 5-2) strongly indicates gas hydrate sealing, which has previously been described for gas-enriched sites at the Dnepr and Danube paleo-fans (Naudts et al., 2009; Popescu et al., 2007) and for sites on continental margins outside the Black Sea (Paull et al., 1995; Schmuck and Paull, 1993; von Rad et al., 2000). Upward migrating methane is trapped within the GHSZ as it forms hydrates. As illustrated in Fig. 5-12, this mechanism hinders methane from seafloor emission into the water column. A general gas-enrichment of the sediments in the study area is proven by the presence of numerous bubble emissions above the GHSZ in waters shallower than ~700 mbsl.

The gas emissions at the Kerch seep area are a prominent exception, as intensive gas bubble escapes from the seafloor occur within the GHSZ. Considering the molecular gas composition and bottom water salinity, the upper boundary of the GHSZ for sI hydrates (the hydrate structure sI is assumed from the present gas composition) at the Kerch seep area was calculated to be positioned at about 702 mbsl (Fig. 5-13A). With respect to its position at 890 mbsl, a sediment temperature increase by more than 2.1°C would be required to shift the local thermodynamic conditions at the Kerch seep area out of the sI hydrate stability field.

Assuming a geothermal gradient of 23°C km^{-1} the regional base of the GHSZ (BGHSZ) at the Kerch seep area can be estimated at about 1045 mbsl (i.e. 155 mbsf; Fig. 5-13A). However, considering small-scale thermal anomalies increasing the temperature gradients locally to about 620°C km^{-1}, the local BGHSZ would be positioned at much shallower depth at about 895 mbsl (i.e. 5 mbsf; Fig. 5-13B). Temperature anomalies may be related to upward fluid flow driven by compaction of folded Miocene shale sequences, which are known from the Kerch-Taman Trough (Meisner et al., 2009). As a consequence of the flattened BGHSZ, methane bubbles can migrate locally through the sediments,

forming gas hydrates close to the seafloor while a portion of the gas might happen to escape into the water column (Fig. 5-12).

A similar mechanism albeit at a different scale has been described by Wood et al. (2002) using high-resolution seismic sections at the Cascadia margin. The authors propose that local perturbations of the BGHSZ, attributed to the advection of warm fluids, lead to methane seepage at the seafloor. The perturbations in the seismic sections are about 50 m in diameter. In our study we directly measured the thermal anomalies at the seafloor with the T-stick operated by the ROV. The results show, that the width of the thermal anomalies at the Kerch seep area are very small as they are limited to the bubble emission sites only a few meters across. We assume that the thermal anomalies are sufficient to allow gas bubbles to ascent through the GHSZ in order to form shallow hydrate deposits as well as to escape from the sediments into the water column. This is in contrast to other mechanisms that have been proposed, such as the limited availability of water for hydrate formation (Clennell et al., 1999; Ginsburg et al., 1997) or high pore water salinity (Haeckel et al., 2004; Liu and Flemings, 2006; Torres et al., 2004).

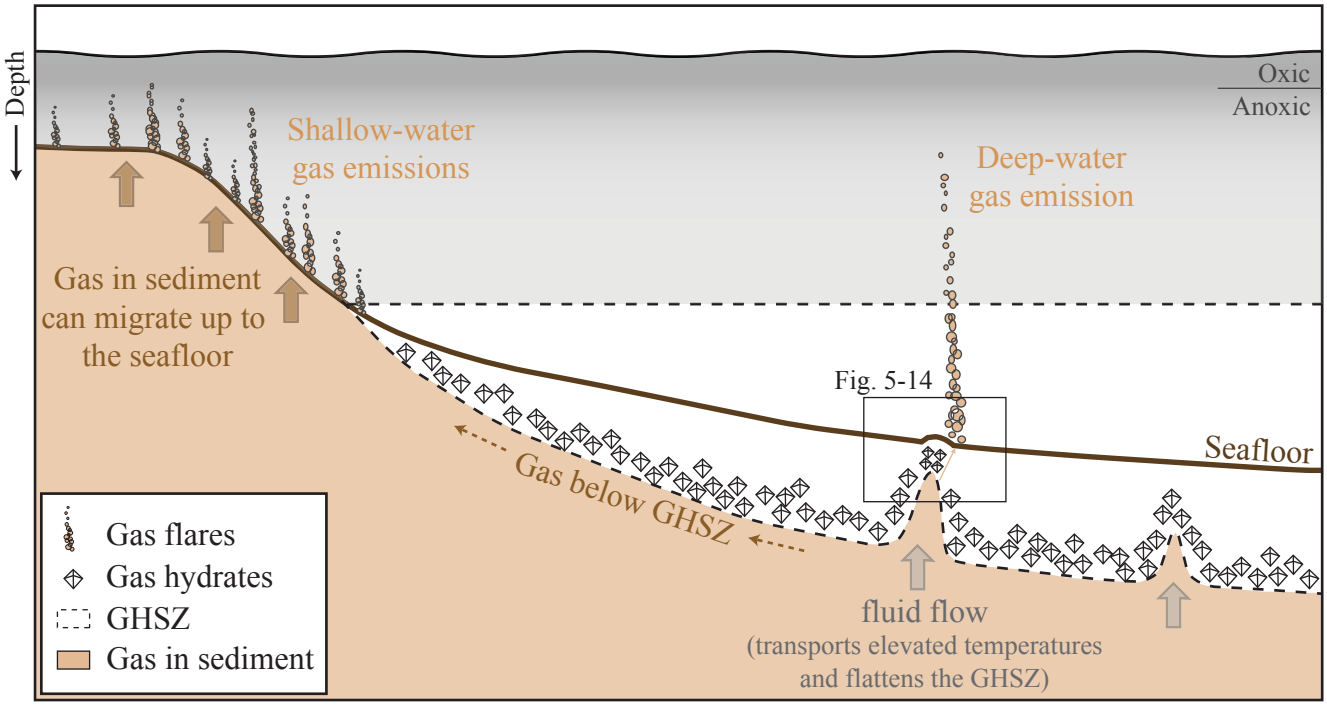

Fig. 5-12: Model of the gas migration through the sediments into the water column along the slope of the Don-Kuban paleo-fan. Gas in the sediments at the shelf and upper slope migrates up to the seafloor and escapes at numerous sites into the water column. In contrast, gas at the lower slope within the gas hydrate stability zone (GHSZ) is trapped in gas hydrates. Free gas only occurs below the base of the GHSZ. Due to elevated temperatures transported by ascent of warm fluids from below, the GHSZ is flattened underneath specific sites, like at the Kerch seep area, where gas can rise up towards the seafloor and eventually into the water column.

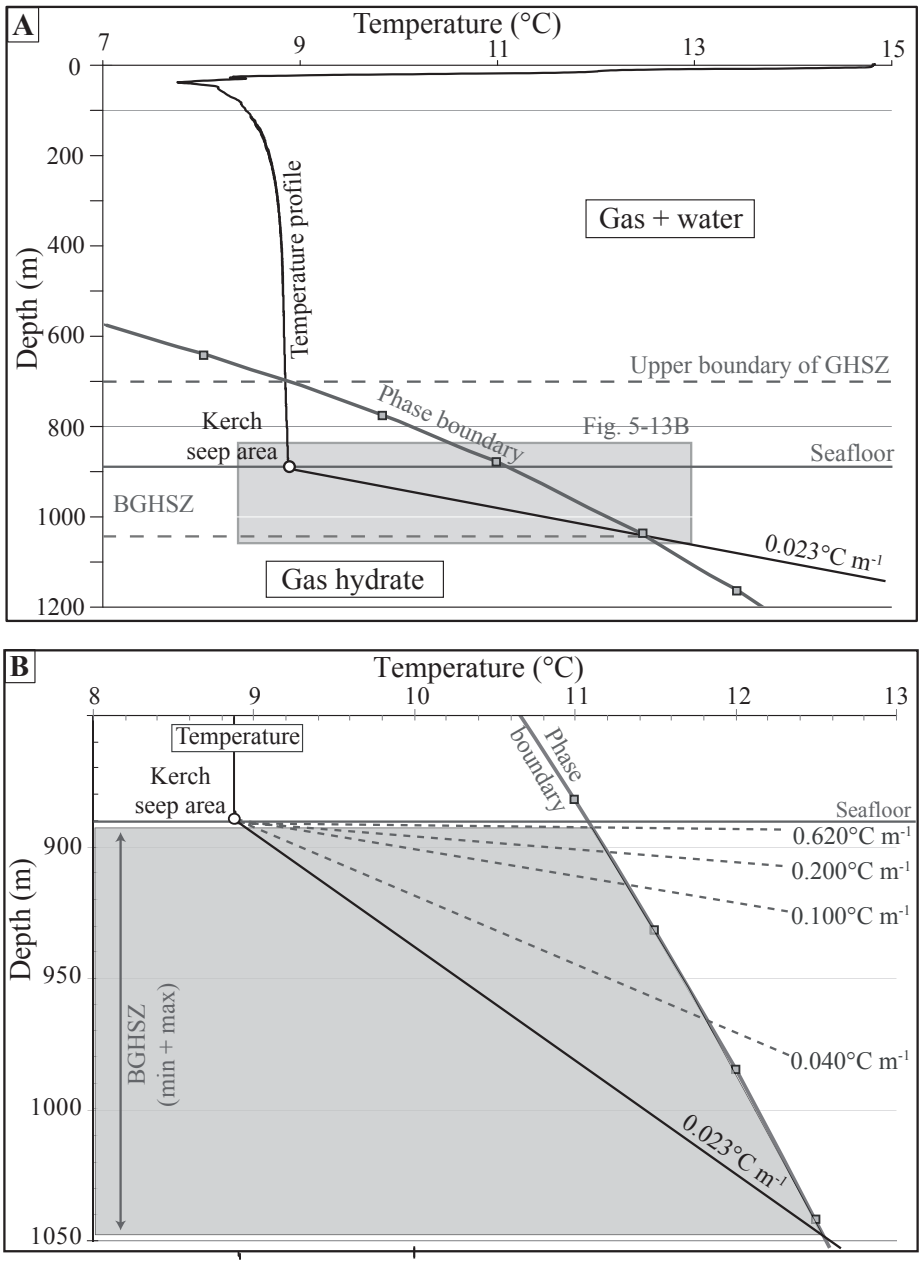

Fig. 5-13: A) Phase diagram for sI gas hydrates calculated using the HWHYD software (Masoudi and Tohidi, 2005) at the Kerch seep area. The temperature profile of the water column was achieved by a ROV-mounted CTD record and for the subsurface a temperature gradient of 0.023°C m^{-1} was assumed. B) Close-up of the subsurface area with additional subbottom temperature gradients as measured at the Kerch seep area (Fig. 5-10). The highly elevated temperature gradients result in the flattening of the BGHSZ up to only a few meters below the seafloor.

5.6.3 Gas hydrate formation at the Kerch seep area

We propose a simplified model of hydrocarbon seepage-related processes and the formation of gas hydrates at the Kerch seep area (Fig. 5-14) integrating all of the hydroacoustic data, seafloor observations, and sampling. Small-scale thermal anomalies due to localized fluid flow allow free gas from below the base of the regional gas hydrate stability zone (~155 mbsf) to ascent through the sediments. At shallow sediment depths, part of the gas is sequestered as gas hydrates. Massive hydrate can form at these shallow deposits because the pressure increase due to clathrate formation can exceed the overburden effective stress of the sediment particles, resulting in an updoming of the overlaying sediments (Torres et al., 2004). In analogy to Hydrate Ridge, where shallow massive hydrate deposits were found in the upper ~20 m of sediments (Torres et al., 2004), we assume a similar thickness for hydrates at the Kerch seep area. At present, the mounds at the Kerch seep area are elevated by up to about 10 meters and the relocation height was probably sufficient to initiate small-scale slumping events at the flanks of the mounds.

Under constant gas supply the gas hydrates get denser and, consequently, a massive layer exists, which prevents free gas from rising towards upper strata. As a consequence, gas is forced to migrate horizontally towards the rims of the massive gas hydrate layer beneath the mound margins, where it can ascent and escape into the water column. The majority of intense flares were recorded at the margins of the mounds (Figs. 5-4B and C). A fraction of the gas, however, may migrate further into the horizontally layered sediments where fresh platy gas hydrates are formed parallel to the sediment bedding (Fig. 5-9). Smaller gas portions may also migrate in transient bubble pulses through small fractures within the mounds, which might have been created during its uplift mainly in the central area (Fig. 5-3A). Methane is constantly released from the shallow hydrate deposits towards the sediment-seawater interface due to

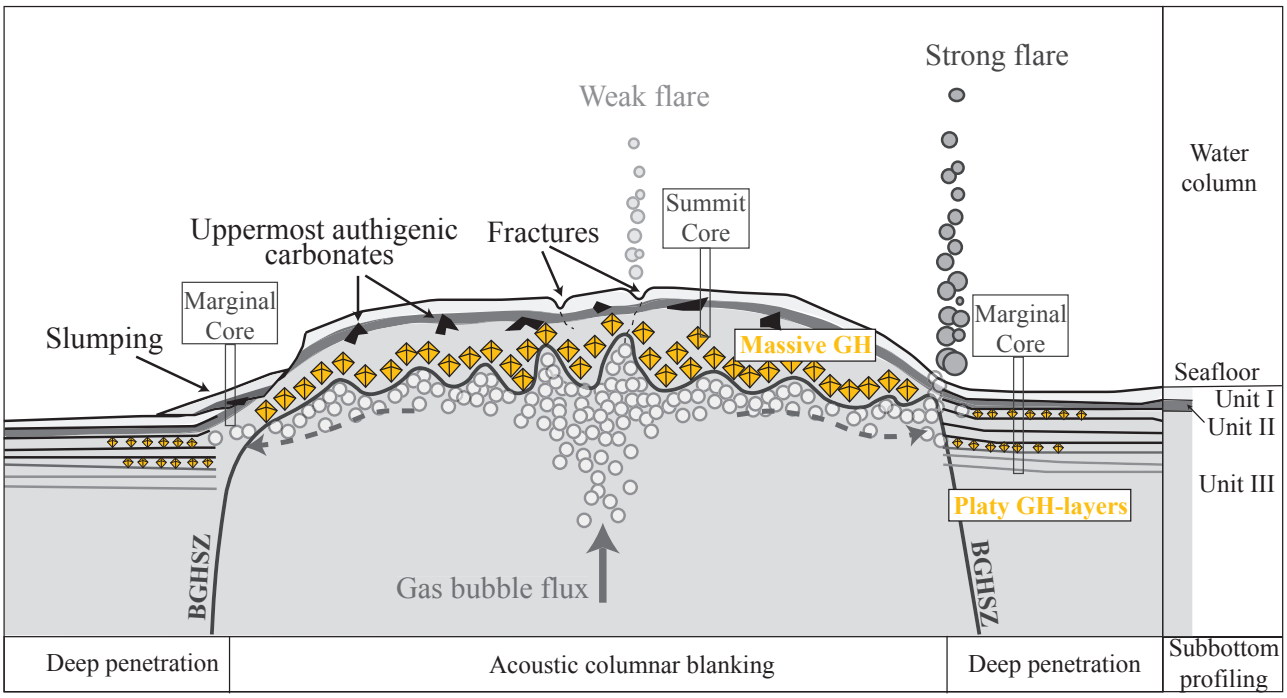

Fig. 5-14: Schematic cross section through a mound structure at the Kerch seep area (not to scale) integrating results from hydroacoustic and morphological observations as well as sediment coring. Gas hydrates form massive layers in shallow depths below the seafloor, forcing free gas to migrate horizontally to the margins where it can escape into the water column.

the concentration difference. Anaerobic oxidation of methane in the sediments leads to formation of authigenic carbonates over time (Ritger et al., 1987). Modeling has shown that cm-sized crusts similar to those found at the summit of the small mound (GeoB 15512-1 in Fig. 5-9) can form in time scales of a few hundred years (Luff et al., 2004).

In backscatter maps produced from multibeam echosounder data, areas with high reflectivity often indicate seep influenced areas due to shallow gas, gas hydrate or carbonate occurrences (Klaucke et al., 2006; Naudts et al., 2008; Orange et al., 2002). The backscatter map of the Kerch seep area (Fig. 5-3B) compiled from multibeam data shows two pronounced high reflectivity anomalies and at both, gravity coring substantiated the presence of shallow gas hydrates and/or carbonates, which most probably result in the high reflectivity.

6.6.4 Quantification of gas discharge at the Kerch seep area

The Kerch seep area is a gas emission area located well within the GHSZ. In order to compare the significance of this type of hydrocarbon seepage with those above the GHSZ as well as mud volcanoes in the deep basin, we conduct an order of magnitude estimation of the total methane flux. First of all, we mapped all of the areas within the Kerch seep area where evidence for bubble emissions was found during all of the hydroacoustic surveys (Fig. 5-5A) resulting in 42 flare areas. The estimated flare areas have a certain size (~60 m) owing to the footprint size of the echosounder and each flare area may comprise one or more individual bubble emission sites. In a second step, we were concerned about the variability of the bubble emissions within the Kerch seep area in time and space that is why we analyzed repeated surveys conducted in three different years and at two different days in 2011 (Figs. 5B – F). While the results show variability both in space in time, the total number of gas emissions at a given survey was comparable, i.e. gas bubbles were emitted at 24 to 74% of the surveyed flare areas during the five surveys with an average of 47%. Consequently, we assume that bubble emission is active at about 20 flare areas (47% of 42 flare areas) at any given time.

We concentrated the ROV surveys in a region that has about the size of two flare areas defined by hydroacoustic methods (Fig. 5-6A). During the dives we conducted an extensive search for bubble emissions using the ROV-mounted horizontally looking sonar as described by Nikolovska et al. (2008) as well as seafloor transects finding in total four sites with bubble emission (BES 1–4, Fig. 5-6B) as well as seafloor structures indicative for recent bubble emissions at additional sites (Figs. 5-7A and C). The seafloor observation is in line with the hydroacoustic surveys indicating changing patterns of bubble emissions in space and time. Therefore, we were not surprised to observe during the three ROV-dives that bubble emissions varied day by day with bubbles being emitted at one site during each of the dives (BES 3) while the others turned on and off (Table 5-2). To account for this variability, we estimated the methane flux day by

day. We deliberately use the wide range of values that span an order of magnitude to allow for a large uncertainty of the study. However, it should be noted that in general we used conservative estimates of the methane flux, for example, during almost all of the dives we observed additional bubble streams that were considered as minor and where therefore not quantified. In the final step, we assume that the methane flux per day as observed by ROV represents the flux in two of the 20 flare areas defined by hydroacoustic methods resulting in a total flux for the Kerch seep area of 4 to 166 mol min^{-1} (or 2 to 87 $\times$ 10^6 mol yr^{-1}).

Comparison of our results with those gained by methane bubble quantifications at other locations demonstrates that the Kerch seep area in general is a prominent gas seepage area. Published methane fluxes for individual bubble emission areas range from very low, such as the Vodyanitski mud volcano in the Black Sea (0.9 $\times$ 10^6 mol yr^{-1}, Sahling et al., 2009), GC 185 in the Gulf of Mexico (0.24 $\times$ 10^6 mol yr^{-1}, Leifer and MacDonald, 2003), and at some sites at the Makran continental margin (0.13 $\times$ 10^6 mol yr^{-1}, Römer et al., submitted) to high such as the Håkon Mosby mud volcano (6.3 $\times$ 10^6 mol yr^{-1}, Sauter et al., 2006) and other sites at the Makran continental margin (5.6 $\times$ 10^6 mol yr^{-1}, Römer et al., submitted). The upper estimate for methane emissions from the Kerch seep area proposed in this study is 87 $\times$ 10^6 mol yr^{-1} which clearly indicates the significance of this bubble emission area.

5.6.5 The fate of methane discharged at the Kerch seep area

Direct observation of gas bubbles in the water column using hydroacoustic methods suggest that bubbles dissolve within the anoxic water column, whose upper limit is about 100 – 150 mbsl. The highest flares that we observed at the Kerch seep area disappear in depths of 350 to 460 mbsl in the echosounder signal (Fig. 5-4A). This strongly suggests that the bubbles dissolve completely as has been proposed by several authors before (Artemov et al., 2007; Greinert et al., 2006; Sahling et al., 2009). However, it can not been ruled out that the disappearance of the flare in the echosounder is a methodological bias, for example the result of bubbles moving out of the echosounder beam or change in their size such that they become acoustically invisible at the chosen echosounder settings. For that reason, we call upon an independent method to study the fate of methane in the water column using the single bubble dissolution model SiBu-GUI (Greinert and McGinnis, 2009; McGinnis et al., 2006). Considering the physico-chemical parameters determined at the Kerch seep area and a bubble diameter between 3 and 10 mm (Table 5-1), the model predicts a complete dissolution at depths of 650 and 540 mbsl, respectively. Even more important, the model predicts that almost all of the methane that was originally in the bubble upon release at the seafloor (Table 5-4) dissolved into the water column well before the bubble itself dissolved. In conclusion, we consider that all of the methane that is emitted to the water column at the Kerch seep area remains in the anoxic water body of the Black Sea.

5.6.6 Significance of the Kerch seep area for the Black Sea methane budget

Using a geochemical box model, the basin wide methane flux from seeps and dissociating gas hydrates into the water column of the Black Sea was estimated by Kessler at al. (2006) at 0.23 – 0.35 × 10^{12} mol yr^{-1}, and confirmed by results from a recent model (0.29 × 10^{12} mol yr^{-1}; Schmale et al., 2011). This high methane flux can not be balanced by the methane sources that are known at present. For example, the overall methane flux from all deep-water mud volcanoes only account for 10^{8} – 10^{9} mol yr^{-1} considering the published fluxes for individual mud volcanoes between 0.9 × 10^{6} mol yr^{-1} and 13 × 10^{6} mol yr^{-1} (Lichtschlag et al., 2010; Sahling et al., 2009; Wallmann et al., 2006) and a total number of about 100 mud volcanoes in the Black Sea (including ~65 summarized by Kruglyakova et al. (2002) plus yet undiscovered ones). However, every new discovery adds to the list of hydrocarbon seeps in the Black Sea and in this sense, our finding of the Kerch seep area represents a so far underestimated type of gas emission, which has to be considered in methane budget calculations. One of the difficulties in detecting gas emissions such as the Kerch seep area is that they lack significant seabed morphology, thus, ship-based multibeam bathymetry is not sufficient for detection. It requires either high-resolution backscatter maps of the seafloor, in which gas hydrate deposits or carbonates show up as high-backscatter anomalies (Fig. 5-3B) or surveys of the water column for bubble-induced flares with echosounder (Figs. 5-4A and C). So far, the Batumi seep area offshore Georgia is the only other gas emission area within the GHSZ similar to the Kerch seep area that has been described in detail (Klaucke et al., 2005, 2006; Nikolovska et al., 2008; Pape et al. 2010, 2011) but several indications for additional sites exist that have not been studied in detail yet. In all of the publications focusing on gas emissions at the shelf and upper continental slope there are reports of a few sites at intermediate depth within the GHSZ (Artemov et al., 2007; Egorov et al., 2003; Naudts et al., 2006; Popescu et al., 2007). In addition, our own unpublished results indicate numerous gas emissions within the GHSZ at the Turkish continental margin. Given the vast unexplored middle slope of the continental margin surrounding the Black Sea we believe that hundreds of these gas emissions exist, which could contribute to the total methane flux at least as much as the deep-water mud volcanoes (10^{8} – 10^{9} mol yr^{-1}) but likely even more.

Although not the focus of this present study, it is worth mentioning that more than 500 gas emissions occur above the GHSZ in our study area at the Don-Kuban paleo-fan as illustrated in Figure 5-2. The density of gas emissions is comparable to those at the Dnepr paleo-fan (Naudts et al., 2006) suggesting that this is another yet unquantified source region for methane. So far, the flux of these mostly shallow gas emissions (down to 832 mbsl) has been estimated only on the Dnepr paleo-delta using quantitative hydroacoustic methods (Artemov et al., 2007) indicating that about 7.47 × 10^{8} mol yr^{-1} from 2200 gas emission sites are emitted in an 387.1 km^{2} area of the seafloor. Further quantitative studies are needed to better constrain the methane flux from the continental shelf and slope.

5.7 Conclusion

This study represents novel data from an intensive methane emission area that adds to the list of known hydrocarbon seeps in the Black Sea. The sediments at the Don-Kuban paleo-fan are generally enriched in methane predominantly of microbial origin. In the shelf and shallow slope areas the gas migrates through the sediment and escapes from numerous gas bubble sites into the water column. At intermediate slope depths situated within the GHSZ, uprising methane is generally trapped in sedimentary gas hydrates. However, at few sites, such as the Kerch seep area at 890 m water depth, free gas is expelled from the seafloor despite its location well within the GHSZ. In this area the temperature gradient is locally strongly increased most likely due to ascending warm fluids from deeper sediment sequences. As a consequence, the base of the GHSZ is locally shifted upwards to only a few meters below the seafloor. Therefore, free gas can migrate through the GHSZ through small fractures or weakening zones to the seafloor and further into the water column. The locally flattened base of the GHSZ leads additionally to the formation of gas hydrates in the shallow sediments at the Kerch seep area. At sites where free gas and gas hydrates accumulate, the overlying sediments might be pushed upwards leading to the formation of seafloor mounds. With time the gas hydrates form a massive layer and any additional uprising gas gets accumulated underneath the massive gas hydrate layer and migrates horizontally to the rim of the structures, where it eventually escapes into the water column. Another part of the gas migrates into the surrounding sediments forming thin platy hydrates along permeable horizons. Continuous hydrate formation lets the elevated structure grow into the periphery.

Due to its inconspicuous morphology the discovery of this type of deep-sea seep sites is problematic. This is probably the reason why deep-water seepage in the Black Sea was previously thought to be almost exclusively associated with mud volcanism. Exceptions, such as the Batumi seep area offshore Georgia, and the Kerch seep area investigated in this study, are characterized by slight morphological expressions which are best discernible from high-resolution bathymetric maps. The fact that gas hydrates and carbonates are precipitated in the seep-influenced sediments at the Kerch seep area facilitates the discovery of this type of cold seeps. Hydroacoustic anomalies in the water column initially indicate seafloor gas bubble escape while subsequent multibeam backscatter information helps to confirm the presence of a pronounced seep area and its spatial distribution.

Individual gas emission sites at the Kerch seep area are spread over an area of about 1×1 km. They are very variable in gas emission activity within scales from hours to days, as gas pathways are opened and closed frequently. However, during our monitoring campaigns performed within four years, the overall gas flux remained more or less stable. The mass of methane annually emanating from the Kerch seep area is slightly higher than reported gas fluxes from deep-water mud volcanoes in the Black Sea. Nevertheless, similar to previous studies, our observations clearly demonstrate that all methane discharged remains within the water column due to aqueous dissolution and does not enter the seasurface-atmosphere boundary.

5.8 Acknowledgments

We greatly appreciate the shipboard support from the master and crew of the research vessels METEOR and MARIA S. MERIAN as well as the professional assistance of the scientific and technical operating teams of the ROV 'MARUM Quest 4000m' and AUV 'Seal'. Furthermore, we thank Christian dos Santos Ferreira for the processing of the bathymetric data. T. Malakhova is acknowledged for conducting the stable isotope analysis of methane. This work was funded through DFG-Research Center / Excellence Cluster "The Ocean in the Earth System".

5.9 References

Artemov, Y.G., Egorov, V.N., Polikarpov, G.G. and Gulin, S.B., 2007. Methane emission to the hydro- and atmosphere by gas bubble streams in the Dnieper Paleo-delta, the Black Sea. Marine Ecological Journal, 6: 5-26.

Barg, I., 2007. Age and origin of the Kerch Strait and the Sea of Azov. Doklady Earth Sciences, 412(1): 17-18.

Bernard, B.B., Brooks, J.M. and Sackett, W.M., 1976. Natural gas seepage in the Gulf of Mexico. Earth and Planetary Science Letters, 31(1): 48-54.

Bohrmann, G., Ivanov, M., Foucher, J.P., Spiess, V., Bialas, J., Greinert, J., Weinrebe, W., Abegg, F., Aloisi, G., Artemov, Y., Blinova, V., Drews, M., Heidersdorf, F., Krabbenhöft, A., Klaucke, I., Krastel, S., Leder, T., Polikarpov, I., Saburova, M., Schmale, O., Seifert, R., Volkonskaya, A. and Zillmer, M., 2003. Mud volcanoes and gas hydrates in the Black Sea: new data from Dvurechenskii and Odessa mud volcanoes. Geo-Marine Letters, 23(3): 239-249.

Caress, D.W. and Chayes, D.N., 1996. Improved processing of Hydrosweep DS multibeam data on the R/V Maurice Ewing. Marine Geophysical Research, 18(6): 631-650.

Claypool, G.E. and Kvenvolden, K.A., 1983. Methane and other Hydrocarbon Gases in Marine Sediment. Annual Review of Earth and Planetary Sciences, 11(1): 299-327.

Clennell, M.B., Hovland, M., Booth, J.S., Henry, P. and Winters, W.J., 1999. Formation of natural gas hydrates in marine sediments 1. Conceptual model of gas hydrate growth conditioned by host sediment properties. Journal of Geophysical Research, 104(B10): 22985-23003.

Egorov, V.N., Polikarpov, G.G., Giulin, S.B., Artemov, Y.G., Stokozov, N.A. and Kostova, S.K., 2003. Modern conception about forming-casting and ecological role of methane gas seeps from bottom of the Black Sea. Marine Ecological Journal, 2(3): 5-26. (in Russian)

Feseker, T., Pape T., Wallmann K., Klapp S. A., Schmidt-Schierhorn F., and Bohrmann G., 2009. The thermal structure of the Dvurechenskii mud volcano and its implications for gas hydrate stability and eruption

dynamics. Marine and Petroleum Geology, 26(9): 1812-1823.

Ginsburg, G.D. and Soloviev, V.A., 1997. Methane migration within the submarine gas-hydrate stability zone under deep-water conditions. Marine Geology, 137: 49-57.

Greinert, J., Artemov, Y., Egorov, V., De Batist, M. and McGinnis, D., 2006. 1300-m-high rising bubbles from mud volcanoes at 2028m in the Black Sea: Hydroacoustic characteristics and temporal variability. Earth and Planetary Science Letters, 244: 1-15.

Greinert, J. and McGinnis, D.F., 2009. Single bubble dissolution model - The graphical user interface SiBu-GUI. Environmental Modelling & Software, 24: 1012-1013.

Haeckel, M., Suess, E., Wallmann, K. and Rickert, D., 2004. Rising methane gas bubbles form massive hydrate layers at the seafloor. Geochimica et Cosmochimica Acta, 68(21): 4335-4345.

Haeckel, M., Reitz, A., Klaucke, I. and Sahling, H., 2008. Methane budget of a large gas hydrate province offshore Georgia, Black Sea, 6th International Conference on Gas Hydrates, Vancouver, British Columbia, Canada.

Hovland, M., 2002. On the self-sealing nature of marine seeps. Continental Shelf Research, 22(16): 2387-2394.

Kessler, J.D., Reeburgh, W.S., Southon, J., Seifert, R., Michaelis, W. and Tyler, S.C., 2006. Basin-wide estimates of the input of methane from seeps and clathrates to the Black Sea. Earth and Planetary Science Letters, 243(3-4): 366-375.

Klaucke, I., Sahling, H., Bürk, D., Weinrebe, W. and Bohrmann, G., 2005. Mapping deep-water gas emissions with sidescan sonar. EOS Transactions, 86(38): 341-346.

Klaucke, I., Sahling, H., Weinrebe, W., Blinova, V., Bürk, D., Lursmanashvili, N. and Bohrmann, G., 2006. Acoustic investigation of cold seeps offshore Georgia, eastern Black Sea. Marine Geology, 231(1-4): 51-67.

Krastel, S., Spiess, V., Ivanov, M., Weinrebe, W., Bohrmann, G., Shashkin, P. and Heidersdorf, F., 2003. Acoustic investigations of mud volcanoes in the Sorokin Trough, Black Sea. Geo-Marine Letters, 23(3): 230-238.

Kruglyakova, R., Gubanov, Y., Kruglyakov, V. and Prokoptsev, G., 2002. Assessment of technogenic and natural hydrocarbon supply into the Black Sea and seabed sediments. Continental Shelf Research, 22(16): 2395-2407.

Leifer, I., Clark, J.F. and Chen, R.F., 2000. Modifications of the Local Environment by Natural Marine Hydrocarbon Seeps. Geophysical Research Letters, 27(22): 3711-3714.

Leifer, I. and Judd, A.G., 2002. Oceanic methane layers: the hydrocarbon seep bubble deposition hypothesis. Terra Nova, 14(6): 417-424.

Leifer, I. and MacDonald, I., 2003. Dynamics of the gas flux from shallow gas hydrate deposits: interaction between oily hydrate bubbles and the oceanic environment. Earth and Planetary Science Letters, 210(3-4): 411-424.

Leifer, I. and Patro, R.K., 2002. The bubble mechanism for methane transport from the shallow sea bed to the surface: A review and sensitivity study. Continental Shelf Research, 22(16): 2409-2428.

Lichtschlag, A., Felden, J., Wenzhöfer, F., Schubotz, F., Ertefai, T.F., Boetius, A. and de Beer, D., 2010. Methane and sulfide fluxes in permanent anoxia: In situ studies at the Dvurechenskii mud volcano (Sorokin Trough, Black Sea). Geochimica et Cosmochimica Acta, 74: 5002-5018.

Liu, X. and Flemings, P.B., 2006. Passing gas through the gas hydrate stability zone at southern Hydrate Ridge, offshore Oregon. Earth and Planetary Science Letters, 241: 211-226.

Lüdmann, T., Wong, H.K., Konerding, P., Zillmer, M., Petersen, J. and Flüh, E., 2004. Heat flow and quantity of methane deduced from a gas hydrate field in the vicinity of the Dnieper Canyon, northwestern Black Sea. Geo-Marine Letters, 24(3): 182-193.

Luff, R., Wallmann, K. and Aloisi, G., 2004. Numerical modeling of carbonate crust formation at cold vent sites: Significance for fluid and methane budgets and chemosynthetic biological communities.

Earth and Planetary Science Letters, 221: 337-353.
Luth, U., Luth, C. and Thiel, H., 1998. MEGASEEBS - Methane Gas Seep Explorations in the Black Sea. Ber Zentrum Meeres- und Klimaforsch, Univ Hamburg, 14: 133.
MacDonald, I.R., I., L., Sassen, R., Stine, P., Mitchell, R. and Guinasso Jr., N., 2002. Transfer of hydrocarbons from natural seeps to the water column and atmosphere. Geofluids, 2(2): 95-107.
Maini, B.B. and Bishnoi, P.R., 1981. Experimental investigation of hydrate formation behaviour of a natural gas bubble in a simulated deep sea environment. Chemical Engineering Science, 36(1): 183-189.
Masoudi, R. and Tohidi, B., 2005. Estimating the hydrate stability zone in the presence of salts and/or organic inhibitors using water partial pressure. Journal of Petroleum Science and Engineering, 46(1-2): 23-36.
McGinnis, D.F., Greinert, J., Artemov, Y., Beaubien, S.E. and Wüest, A., 2006. Fate of rising methane bubbles in stratified waters: How much methane reaches the atmosphere. Journal of Geophysical Research, 111 (C09007).
Meisner, A., Krylov, O. and Nemcok, M., 2009. Development and structural architecture of the Eastern Black Sea. The Leading Edge, 28(9): 1046-1055.
Michaelis, W., Seifert, R., Neuhaus, K., Treude, T., Thiel, V., Blumenberg, M., Knittel, K., Gieseke, A., Peterknecht, K., Pape, T., Boetius, A., Amann, R., Jorgensen, B.B., Widdel, F., Peckmann, J., Pimenov, N.V. and Gulin, M.B., 2002. Microbial reefs in the Black Sea fueled by anaerobic oxidation of methane. Science, 297: 1013-1015.
Naudts, L., De Batist, M., Greinert, J. and Artemov, Y., 2009. Geo- and hydro-acoustic manifestations of shallow gas and gas seeps in the Dnepr paleodelta, northwestern Black Sea. The Leading Edge, 28(9): 1030-1040.
Naudts, L., Greinert, J., Artemov, Y., Beaubien, S.E., Borowski, C. and Batist, M.D., 2008. Anomalous sea-floor backscatter patterns in methane venting areas, Dnepr paleo-delta, NW Black Sea. Marine Geology, 251(3-4): 253-267.
Naudts, L., Greinert, J., Artemov, Y., Staelens, P., Poort, J., Van Rensbergen, P. and De Batist, M., 2006. Geological and morphological setting of 2778 methane seeps in the Dnepr paleo-delta, northwestern Black Sea. Marine Geology, 227: 177-199.
Nikishin, A.M., Korotaev, M.V., Ershov, A.V. and Brunet, M.-F., 2003. The Black Sea basin: tectonic history and Neogene-Quaternary rapid subsidence modelling. Sedimentary Geology, 156(1-4): 149-168.
Nikolovska, A., Sahling, H. and Bohrmann, G., 2008. Hydroacoustic methodology for detection, localization, and quantification of gas bubbles rising from the seafloor at gas seeps from the Black Sea. Geochemistry, Geophysics, Geosystems, 9 (Q10010).
Oaie, G., Secrieru, D. and Shimus, K., 2005. Black Sea Basin: Sediment types and distribution, sedimentation processes. Geo-Eco-Marina, 9-10: 21-30.
Orange, D.L., Yun, J., Maher, N., Barry, J. and Greene, G., 2002. Tracking California seafloor seeps with bathymetry, backscatter and ROVs. Continental Shelf Research, 22(16): 2273-2290.
Özsoy, E. and Ünlüata, Ü., 1997. Oceanography of the Black Sea: a review of some recent results. Earth-Science Reviews, 42: 231-272.
Pape, T., Bahr, A., Klapp, S.A., Abegg, F. and Bohrmann, G., 2011. High-intensity gas seepage causes rafting of shallow gas hydrates in the southeastern Black Sea. Earth and Planetary Science Letters, 307(1-2): 35-46.
Pape, T., Bahr, A., Rethemeyer, J., Kessler, J.D., Sahling, H., Hinrichs, K.-U., Klapp, S.A., Reeburgh, W.S. and Bohrmann, G., 2010. Molecular and isotopic partitioning of low-molecular-weight hydrocarbons during migration and gas hydrate precipitation in deposits of a high-flux seepage site. Chemical Geology, 269: 350-363.
Paull, C.K., Ussler, W.I., Borowski, W.S. and Spiess, F.N., 1995. Methane-rich plumes on the Carolina continental rise: Associations with gas hydrates.

Geology, 23(1): 89-92.

Poort, J., Kutas, R.I., Klerkx, J., Beaubien, S.E., Lombardi, S., Dimitrov, L., Vassilev, A. and Naudts, L., 2007. Strong heat flow variability in an active shallow gas environment, Dnepr palaeo-delta, Black Sea. Geo-Marine Letters, 27: 185-195.

Popescu, I., Lericolais, G., Panin, N., De Batist, M. and Gillet, H., 2007. Seismic expression of gas and gas hydrates across the western Black Sea. Geo-Marine Letters, 27: 173-183.

Reeburgh, W.S., Ward, B.B., Whalen, S.C., Sandbeck, K.A., Kilpatrick, K.A. and Kerkhof, L.J., 1991. Black Sea methane geochemistry. Deep-Sea Research I, 38: 1,189-1,210.

Rehder, G., Brewer, P.W., Peltzer, E.T. and Friedrich, G., 2002. Enhanced lifetime of methane bubble streams within the deep ocean. Geophysical Research Letters, 29(15): 1731-1734.

Reilinger, R.E., McClusky, S.C., Oral, M.B., King, R.W., Toksoz, M.N., Barka, A.A., Kinik, I., Lenk, O. and Sanli, I., 1997. Global Positioning System measurements of present-day crustal movements in the Arabia-Africa-Eurasia plate collision zone. Journal of Geophysical Research, 102(B5): 9983-9999.

Ritger, S., Carson, B. and Suess, E., 1987. Methane-derived authigenic carbonates formed by subduction-induced pore-water expulsion along the Oregon/Washington margin. Geological Society of America Bulletin, 98: 147-156.

Robinson, A.G., Rudat, J.H., Banks, C.J. and Wiles, R.L.F., 1996. Petroleum geology of the Black Sea. Marine and Petroleum Geology, 13(2): 195-223.

Römer, M., Sahling, H., Pape, T., Spiess, V. and Bohrmann, G., submitted. Gas bubble emission from submarine hydrocarbon seeps at the Makran continental margin (offshore Pakistan). Journal of Geophysical Reseach.

Ross, D.A. and Degens, E.T., 1974. Recent sediments of Black Sea. In: E.T. Degens and D.A. Ross (Editors), The Black Sea - Geology, chemistry, and biology. American Association of Petroleum Geologists, pp. 183-199.

Sahling, H., Bohrmann, G., Artemov, Y.G., Bahr, A., Brüning, M., Klapp, S.A., Klaucke, I., Kozlova, E., Nikolovska, A., Pape, T., Reitz, A. and Wallmann, K., 2009. Vodyanitskii mud volcano, Sorokin trough, Black Sea: Geological characterization and quantification of gas bubble streams. Marine and Petroleum Geology, 26(9): 1799-1811.

Sauter, E.J., Muyakshin, S.I., Charlou, J.-L., Schlüter, M., Boetius, A., Jerosch, K., Damm, E., Foucher, J.-P. and Klages, M., 2006. Methane discharge from a deep-sea submarine mud volcano into the upper water column by gas hydrate-coated methane bubbles. Earth and Planetary Science Letters, 243: 354-365.

Schmale, O., Greinert, J. and Rehder, G., 2005. Methane emission from high-intensity marine gas geeps in the Black Sea into the atmoshere. Geophysical Research Letters, 32 (L07609).

Schmale, O., Haeckel, M. and McGinnis, D.F., 2011. Response of the Black Sea methane budget to massive short-term submarine inputs of methane. Biogeosciences, 8: 911-918.

Schmuck, E.A. and Paull, C.K., 1993. Evidence for gas accumulation associated with diapirism and gas hydrates at the head of the Cape Fear Slide. Geo-Marine Letters, 13(3): 145-152.

Schoell, M., 1980. The hydrogen and carbon isotopic composition of methane from natural gases of various origins. Geochimica et Cosmochimica Acta, 44(5): 649-661.

Starostenko, V.I., Rusakov, O.M., Shnyukov, E.F., Kobolev, V.P. and Kutas, R.I., 2010. Methane in the northern Black Sea: characterization of its geomorphological and geological environments. Geological Society, London, Special Publications, 340(1): 57-75.

Torres, M.E., Wallmann, K., Tréhu, A.M., Bohrmann, G., Borowski, W.S. and Tomaru, H., 2004. Gas hydrate growth, methane transport, and chloride enrichment at the southern summit of Hydrate Ridge, Cascadia margin off Oregon. Earth and Planetary Science Letters, 226(1-2): 225-241.

Tugolesov, D.A., Gorshkov, A.S., Meysner, L.B., Soloviov, V.V., Khakhalev, E.M., Akilova, Y.V., Akentieva, G.P., Gabidulina, T.I., Kolomeytseva, S.A., Kochneva, T.Y., Pereturina, I.G. and Plashihina, I.N.,

1985. Tectonics of the Mesozoic Sediments of the Black Sea Basin, Moscow.

Vassilev, A. and Dimitrov, L., 2002. Spatial and quantity evaluation of the Black Sea gas hydrates. Russian Geology and Geophysics, 43(7): 637-649.

Villinger, H., and Davis, E. E., 1987. A New Reduction Algorithm for Marine Heat Flow Measurements. Journal of Geophysical Research, 92(B12): 12846-12856.

von Rad, U., Berner, U., Delisle, G., Doose-Rolinski, H., Fechner, N., Linke, P., Lückge, A., Roeser, H.A., Schmaljohann, R., Wiedicke, M. and Parties, S.S., 2000. Gas and fluid venting at the Makran accretionary wedge off Pakistan. Geo-Marine Letters, 20: 10-19.

Wagner-Friedrichs, M., 2007. Seafloor seepage in the Black Sea: Mud volcanoes, seeps and diapiric structures imaged by acoustic methods. PhD Thesis, University of Bremen, Bremen, 154 pp.

Wallmann, K., Drews, M., Aloisi, G. and Bohrmann, G., 2006. Methane discharge into the Black Sea and the global ocean via fluid flow through submarine mud volcanoes. Earth and Planetary Science Letters, 248(1-2): 545-560.

Wessel, P. and Smith, W.H.F., 1991. Free software helps map and display data. Eos Transactions AGU, 72(41): 441.

White, R.S., 1979. Gas hydrate layers trapping free gas in the Gulf of Oman. Earth and Planetary Science Letters, 42: 114-120.

Whiticar, M.J., 1999. Carbon and hydrogen isotope systematics of bacterial formation and oxidation of methane. Chemical Geology, 161: 291-314.

Wood, W.T., Gettrust, J.F., Chapman, N.R., Spence, G.D. and Hyndman, R.D., 2002. Decreased stability of methane hydrates in marine sediments owing to phase-boundary roughness. Nature, 420(6916): 656-660.

6 Third case study (manuscript III):

Gas bubble flux connected to carbonate slabs in the Central Province at the Nile Deep Sea Fan (Eastern Mediterranean Sea)

Miriam Römer[1*], Heiko Sahling[1], Thomas Pape[1], Christian dos Santos Ferreira[1], Antje Boetius[1,2], Frank Wenzhöfer[1,2], Gerhard Bohrmann[1]

[1] MARUM – Center for Marine Environmental Sciences and Department of Geosciences, University of Bremen, Klagenfurter Str., 28359 Bremen, Germany
[2] Max Planck Institute for Marine Microbiology, Celsiusstr. 1, 28359 Bremen, and Alfred Wegener Institute for Polar and Marine Research in the Helmholtz Association, 27515 Bremerhaven, Germany

[*] Corresponding author: Phone +49(0)421 218 65059 Fax +49(0)421 218 65099
E-mail: mroemer@marum.de

to be submitted to Marine and Petroleum Geology

6.1 Abstract

Carbonate slabs close to the seafloor are manifestations of sustained fluid seepage. The distributions of such carbonate slabs can be evaluated by using backscatter anomalies in multibeam data. During a high resolution ship-based multibeam survey covering 325 km^2 seafloor area in the Central Province of the Nile Deep Sea Fan (NDSF) we identified more than 150 high-backscatter anomalies at water depths between 1500 and 1800 m. These high-backscatter anomalies are typically tens to hundreds meters in diameter. Visual seafloor inspections of three areas characterized by such anomalies confirmed the presence of carbonate pavement. Systematic PARASOUND echosounder surveys of the water column showed intense hydroacoustic anomalies (flares) indicative for gas bubble streams above 8% of all the carbonate slabs (high-backscatter anomalies) discovered. The echosounder records indicate that flares disappear due to gas dissolution at depths corresponding to the upper limit of the gas hydrate stability zone located at about 1350 m water depth. For quantification of gas bubble emissions, autonomous underwater vehicle (AUV)-based multibeam data localizing individual bubble streams were combined with results from seafloor investigations by a remotely operated vehicle (ROV) at distinct emission sites. For a selected carbonate slab (C-1), fluxes between 0.32 and 1.3 x 10^6 mol methane per year were calculated. Ultra-high resolution maps obtained from AUV-based multibeam surveys showed that the carbonate slabs project from the very smooth surrounding seafloor by several decimeters up to two meters in the central part. Calculations of volumes and respective amounts of carbonate-bound carbon in the slabs revealed that C-1 is composed of at least 327 x 10^6 mol carbon. Taking into account published ages of a carbonate crust and the quantitative values obtained in our study we conclude that the flux of methane transported as gas bubbles is significantly higher than the amount of methane-bound carbon that is oxidized microbially and precipitated as carbonates.

Keywords: methane flux, gas flares, cold seeps, authigenic carbonates, high-backscatter anomalies, Eastern Mediterranean Sea, autonomous underwater vehicle

6.2 Introduction

Numerous seafloor structures related to fluid seepage including mud volcanoes, brine lakes, carbonate slabs, pockmarks, and mounds are known from the Nile Deep Sea Fan (NDSF) (e.g. Loncke et al. 2004; Loncke et al. 2006; Dupré et al. 2007; Gontharet et al. 2007; Bayon et al. 2009b; Dupré et al. 2010). This study concentrates on carbonate slabs occurring in the Central Province of the NDSF (Fig. 6-1), which have gained considerable less attention compared to the spectacular mud volcanoes such as Cheops, North Alex, Osiris, Isis, or Amon (e.g. Dupré et al. 2008; Feseker et al. 2009; Huguen et al. 2009; Dupré et al. 2010; Feseker et al. 2010). Fluid-related structures are particular abundant in the Central Province of the NDSF between 1500 and 2500 m water depth where sediments are completely destabilized through gravitational processes (Loncke et al. 2004; Bayon et al. 2009b).

In general, areas of high seafloor backscatter imaged with multibeam systems have been interpreted as manifestation of fluid seepage, as in various places at the NDSF submersible investigations have demonstrated that the high backscatter areas are characterized by the presence of methane-derived authigenic carbonates (Loncke et al. 2004; Zitter et al. 2005; Dupré et al. 2010). The carbonates often form pavements covering the seafloor several tens to hundreds of meters in diameter. Due to the fact that almost all of the high backscatter is related to authigenic carbonates the term carbonate slab (instead of high-backscatter anomaly) is used in the following.

Two sub-regions at the Central Province of the NDSF are differentiated – the lower slope and the middle slope (Loncke et al. 2004; Bayon et al. 2009b). The lower slope is characterized by slope parallel ridges and troughs caused by a deformed sedimentary cover overlaying debris flows. Fractured carbonates exposed at the top of the ridges have been interpreted as relicts of fossil seep sites next to pockmarks, which are the sites of present methane seepage (Bayon et al. 2009b). At the lower slope numerous of such seep manifestations have been documented considering multibeam backscatter characteristics (Loncke et al. 2004). The middle slope is morphologically smooth with seafloor parallel debris flows below a smooth seabed. Due to the occurrence of high backscatter areas in much lower density, it was concluded that seepage at the middle slope is less common if compared to the lower slope (Loncke et al. 2004; Bayon et al. 2009b). However, deep-towed sidescan sonar surveys in two selected areas revealed that high backscatter is also widespread on the lower middle slope (Dupré et al. 2008; Bayon et al. 2009b; see Figure 6-2a).

Prior to our study, a submersible dive confirmed that carbonate-paved areas cause the high backscatter and pieces of carbonate crusts were recovered (Gontharet et al. 2007; Bayon et al. 2009a). Isotopic analyses (Gontharet et al. 2007) and biomarker (Gontharet et al. 2009) have shown that the carbonates have formed as a consequence of the anaerobic oxidation of methane (AOM) converting microbial methane from the deeper subsurface. U-Th dating of a 5.5 cm thick crust has substantiated that the crusts have been growing downward, with the oldest (uppermost) parts of the crust being ~5000 years in age (Bayon et al. 2009a).

Gas bubble emissions associated to the carbonate slabs in our study area has already been inferred from acoustic anomalies in the water column previously recognized by deep-towed sidescan sonar imaging (Dupré et al. 2010; see also Fig. 6-2a). These findings stimulated our study as we were interested to quantify the amount of methane emanating into the water column through gas bubbles. Quantifications of seafloor bubble emissions into deep waters are still rare, but the quantity of bubble emission at other areas worldwide suggests site-specific fluxes in the range of several million mol of methane per year (Hornafius et al. 1999; Torres et al. 2002; Leifer and MacDonald 2003; Heeschen et al. 2005; Sauter et al. 2006; Artemov et al. 2007; Sahling et al. 2009; Römer et al. submitted-a; Römer et al. submitted-b). In addition, we were interested to investigate the fate of the gas bubbles in the water column, and if they could transport the potent greenhouse gas methane from the sediment into the upper

hydrosphere and, eventually into the atmosphere.
In this study, we mapped the distribution of high-backscatter anomalies within a seafloor area of 325 km^2 at the lower middle slope of the Central Province on the NDSF. High-resolution ship-based multibeam echosounder data revealed the presence of more than 150 subcircular high-backscatter anomalies, and TV-sled surveys confirmed the presence of carbonate slabs at the seafloor. In order to record evidence for gas bubbles in the water column commonly termed 'flares' and to study the fate of gas bubbles in the water column, a systematic PARASOUND echosounder survey was conducted. In addition, we systematically surveyed the carbonate slabs in order to quantitatively estimate at how many gas emissions occur. Selected bubble emission sites were studied in detail using a remotely operated vehicle (ROV). An order of magnitude estimation of the gas flux was conducted by combining data from autonomous underwater vehicle (AUV) flare mapping and ROV-based video documentation of selected gas bubble streams. AUV-based multibeam maps were further used to quantify the amount of carbonate stored at the seafloor. The overarching goal of this study was, to unravel the significance of gas bubble emission associated to carbonate slabs in the Central Province at the NDSF.

6.3 Study area

The Nile Deep Sea Fan (NDSF) is a thick sedimentary wedge in the Eastern Mediterranean Sea (Fig. 6-1). The sedimentary sequence formed since the late Miocene (Salem 1976) and is mainly composed of terrigeneous sediments delivered from the Nile River. Nowadays, two main fluviatil transport pathways exist: the Rosetta branch in the western part and the Damietta branch in the eastern part of the continental platform (Loncke et al. 2009). At the foot of the deltaic platform a capacious deep-sea fan formed.
The interaction of salt tectonics and various sediment deposition and relocation processes, such as turbidites, slumps or debris flows, mainly controlled the morphology of the NDSF (Gaullier et al. 2000; Mascle et al. 2000; Loncke et al. 2002; Loncke et al. 2006). For instance, salt-related tectonic deformations are caused by the gravity of overburden sediments overlying the large quantities of evaporates precipitated during the Messinian salinity crisis (Hsu et al. 1977; Ryan 1978). Gravity-induced gliding of salt and sliding of sediment loading have also induced the formation of extensions at the shelf and upper slope and compression at the deeper slope and the abyssal plain (Gaullier et al. 2000; Loncke et al. 2002; Loncke et al. 2004).

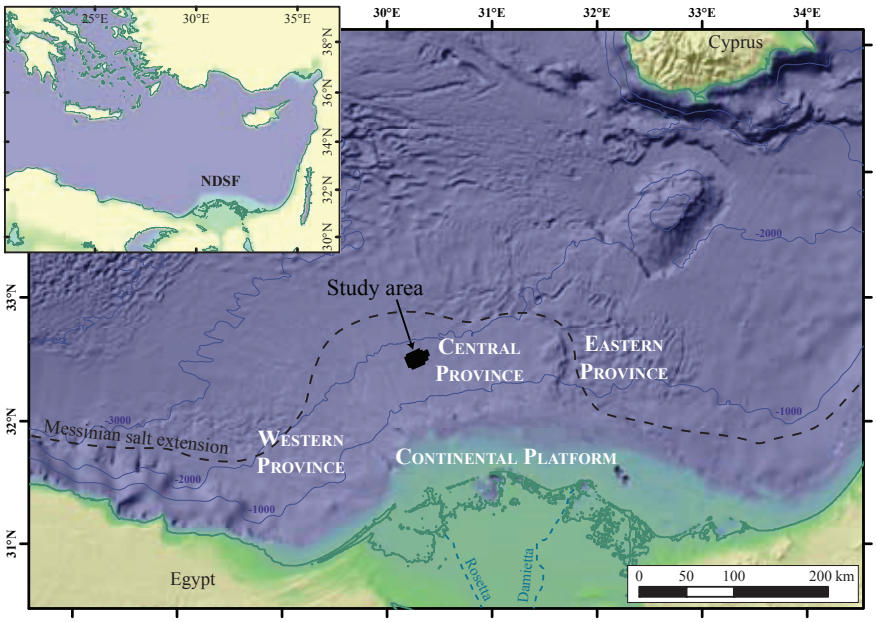

Fig.6-1: Shaded bathymetry of the Nile Deep Sea Fan (NDSF), and the Egyptian continental platform from a compilation of GEBCO-data and ship-based swath echosounder data of several cruises (Courtesy of IFREMER). The fan is divided into the Western, Central, and Eastern Provinces according to their morphological characteristics (Loncke et al., 2004). The study area is located landwards to the southern limit of Messinian salt extension depicted by the dashed line (Loncke et al. 2009).

6.4 Methods

6.4.1 Hydroacoustics

During R/V MARIA S. MERIAN cruises MSM13/3 and 13/4 in 2009, several integrated hydroacoustic techniques were used in order to detect and localize seep areas. For bathymetric and backscatter mapping, a multibeam echosounder (MBES) Kongsberg EM 120 with a frequency of 120 kHz was used. Raw data were processed with the MB-system software (Caress and Chayes 1996). The produced grids were visualized with ESRI Arcmap 10.0 for map export.

The shallow subbottom was imaged with the ship-mounted single beam parametric echosounder PARASOUND using a secondary low frequency of about 4 kHz. Gas bubbles in the water column were detected as acoustic anomalies (flares) with the primary high frequency of 19 kHz of PARASOUND as described by Nikolovska et al. (2008). The footprint size of the echosounder is about 7% of the water depth. Data were processed online with the ATLAS PARASTORE software. In addition, a simple post-processing was conducted with the program SeNT (H. Keil, University of Bremen) using the PS3 data and final plots were created. Access to PARASOUND data as well as metadata is made available through the PANGAEA data base (http://doi.pangaea.de).

During MSM13/4, MARUM´s autonomous under-water vehicle (AUV) SEAL 5000 was deployed (dive #28) for high-resolution multibeam mapping of the seafloor with RESON 7125B. Operational procedures and data analyses are summarized in Römer et al. (submitted-a). Flares caused by gas bubbles ascending in the water column were detected by checking unprocessed data of the sidescan-like multibeam signal in CARIS 7.0 HIPS AND SIPS.

6.4.2 Seafloor observations and sampling

MARUM's deep-water remotely operated vehicle (ROV) QUEST 4000m was deployed aboard R/V MARIA S. MERIAN during cruise MSM13/3. Absolute GPS-based underwater positioning was performed using the shipboard IXSEA Posidonia ultra short base line (USBL) positioning system. For the detection of gas emissions, the ROV was flying 20 m above the seafloor while scanning the water column for backscatter signals induced by bubbles with the Kongsberg 675 kHz Type 1071 forward looking scanning sonar head as described in Nikolovska et al. (2008).

The ROV was equipped with two color-zoom cameras in order to gain an overview of seafloor features and a near-bottom mounted broadcast-quality 3CCD HDTV zoom video camera for detailed video close up recording. The spatial resolution of this camera is 2.2 Mega-Pixel at 59.94 Hz interlaced. The HDTV video material was used for detailed gas bubble documentation at the emission sites. A black 'imaging plate' with a cm-scale was placed with the ROV manipulator behind the gas bubble streams in order to improve visibility of individual bubbles. The bubble volume fluxes were estimated by determine bubble sizes and frequencies of emitted bubbles from the video recordings with the program Adobe Premiere Pro CS 3.0. Frames were exported to the program ImageJ (W. Rasband, National Institutes of Health, Bethesda, MD; available at http://rsbweb.nih.gov/ij/) for the purpose of bubble size analyses. The major and minor axes were measured and the volume calculated by assuming a rotational ellipsoid with an equivalent spherical radius. Fluxes were calculated in milliliter (mL) per minute (min) using the results of the average bubble volume and the number of bubbles escaping into the water column. The volume flux was converted to gas flux (in mol CH_4 per minute or year) assuming that the gas entirely consists of methane and considering the compressibility of methane (Römer et al. submitted-b).

Gas Bubble Samplers (GBS) operated with the ROV manipulators (Pape et al. 2010a), were used for pressure sampling of the gas venting from

the seafloor at two stations (station 980-1_GBS1: 32°30.061'N, 30°15.615'E and Station 980-1_GBS2: 32°30.064'N, 30°15.617'E). The gas samples were analyzed for their molecular composition by gas chromatography. Light hydrocarbons (C_1 to C_6) were separated, detected, and quantified with a capillary column connected to a Flame Ionization Detector, whereas O_2, N_2, CO_2 were determined using a stainless steel column packed with a mole sieve and coupled to a Thermal Conductivity Detector. The coefficient of variation determined for the analytical procedure was less than 2%.

Gas hydrate phase diagrams were calculated with the hydrate predicting program HWHYD (Centre for Gas Hydrate Research, Heriot-Watt University, U.K.; Masoudi and Tohidi 2005) using the gas compositions of the vent gas samples and salinity data. The distribution of the gas hydrate stability zone (GHSZ) was evaluated considering the gas hydrate phase diagrams and temperature data from CTD records in the working area.

A TV-guided multicorer (TV-MUC) was used to map seep areas at the seafloor. The TV-MUC is equipped with a black-and-white video-data telemetry system and towed at a distance of about 2.5 m above ground allowing visualization of a seafloor area of approximately 2 by 3 m. The Posidonia USBL transponder was employed for accurate positioning.

6.5 Results

6.5.1 General seafloor features

A high-resolution hydroacoustic survey to determine the distribution of carbonate slabs was conducted at the slope of the Central Province of the NDSF (Fig.6-1). The seafloor in the study area comprising 325 km^2 and located at depths between 1500 and 1800 meters below sea level (mbsl) is generally very smooth (Fig. 6-2a). Some of the carbonate slabs became already apparent in the multibeam map because of their positive relief. However, they are much better imaged in the backscatter map as they are characterized by high backscatter signals which clearly distinguishes them from the generally low backscatter of the seafloor in that area (Fig. 6-2c). In total, 163 randomly distributed high-backscatter anomalies that we interpret as carbonate slabs were detected (Fig. 6-2d).

In a selected area, the carbonate slabs were surveyed in detail with the AUV-based multibeam providing high-resolution bathymetric maps (Figs. 6-3a, b, c) as well as backscatter images (Fig. 6-4). Data from the AUV-maps indicate that elevations of the carbonate slabs are in the range 0.4 – 1.8 m (Fig. 6-3b, c), while the results from the ship-based multibeam suggest elevations of ~2 – 5 m. We speculate that the extent of the vertical exaggeration as obtained from the ship-based multibeam system is related to the higher backscatter of the carbonate slabs and to the bottom detection algorithm of the swath echosounder. Figure 6-3b and 6-3c illustrate a blister-like shape of the carbonate slabs with elevated central parts and no discernable relief towards the edges. The central parts of the slabs are characterized by a rougher surface than the surrounding soft sediments and occasionally by fractures of up to ~1 m deep (Fig. 6-3b, c). Adjacent to the carbonate slabs, small mounds (~10 m in diameter and 0.4 to 1 m in height and pockmarks (up to 15 m in diameter and about 1 m deep) were observed (Figs. 6-3a, b). These features did not reveal any backscatter anomalies.

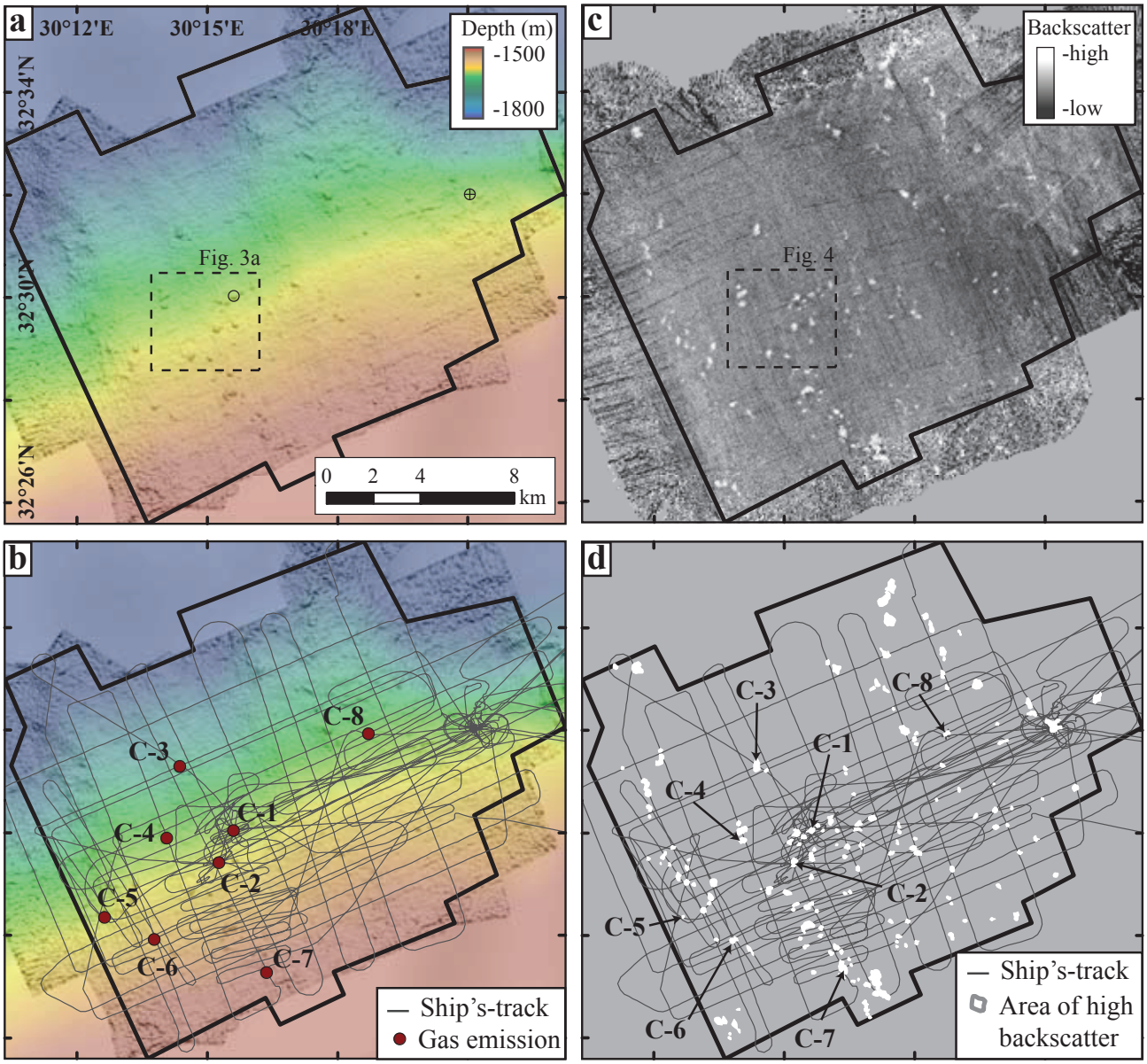

Fig. 6-2 a: Ship-based multibeam echosounder (MBES) bathymetric map of the ~325 km^2 study area in the Central Province at the NDSF and the position of previous studies (+: Bayon et al. 2009b; o: Dupré et al. 2010). The seafloor is generally smooth with the exception of numerous slightly elevated features distributed over the study area. b: Hydroacoustic surveys conducted during MSM13/3 and 13/4 in 2009 revealed eight areas with gas emissions (C-1 to C-8) connected to carbonate slabs. c: The ship-based MBES backscatter map shows 163 high-backscatter anomalies in the study area. d: Illustration of the systematic echosounder surveys. A total of 103 high-backscatter anomalies were crossed in order to search for gas emissions with PARASOUND echosounder. Eight gas emissions were detected during the systematic search and all are related to high-backscatter anomalies.

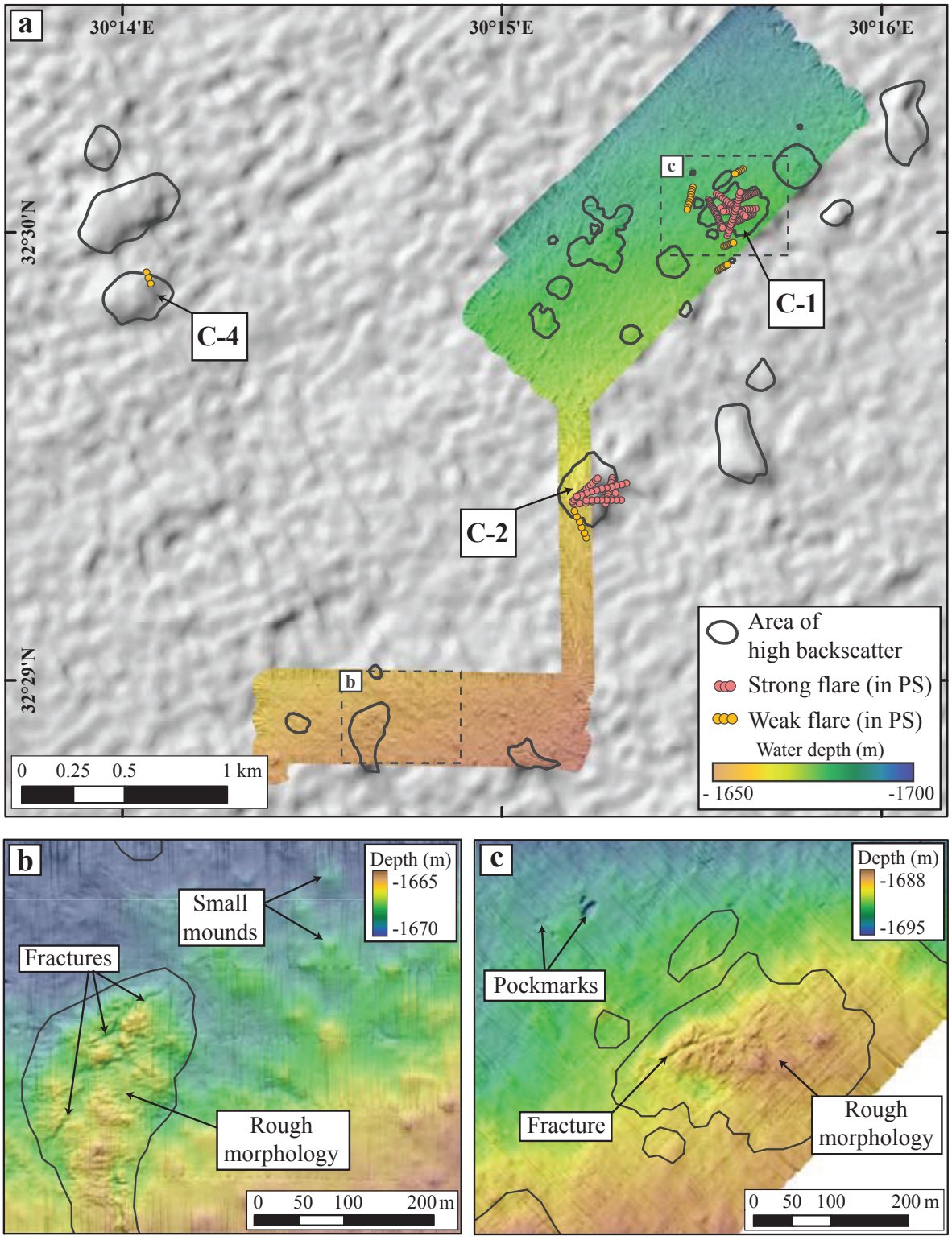

Fig. 6-3 Composite figure of AUV-based multibeam map (color), ship-based multibeam map (gray hill shade), the outline of high-backscatter anomalies (Fig. 6-4), and flare locations detected in PARASOUND records (PS). a: Overview map illustrating the multibeam coverage acquired during AUV dive #28. b: Close-up of the southern part illustrating the rough and fractured morphology of the carbonate slabs characterized by high backscatter as outlined. Mounds lower than 1 meter in height are not associated with backscatter anomalies. c: The carbonate slab C-1 shows a rough seafloor morphology with a readilyrecognizable fracture. Few small pockmarks were detected north-west of C-1. The largest one is about 10 × 15 m in width and ~1.3 m deep.

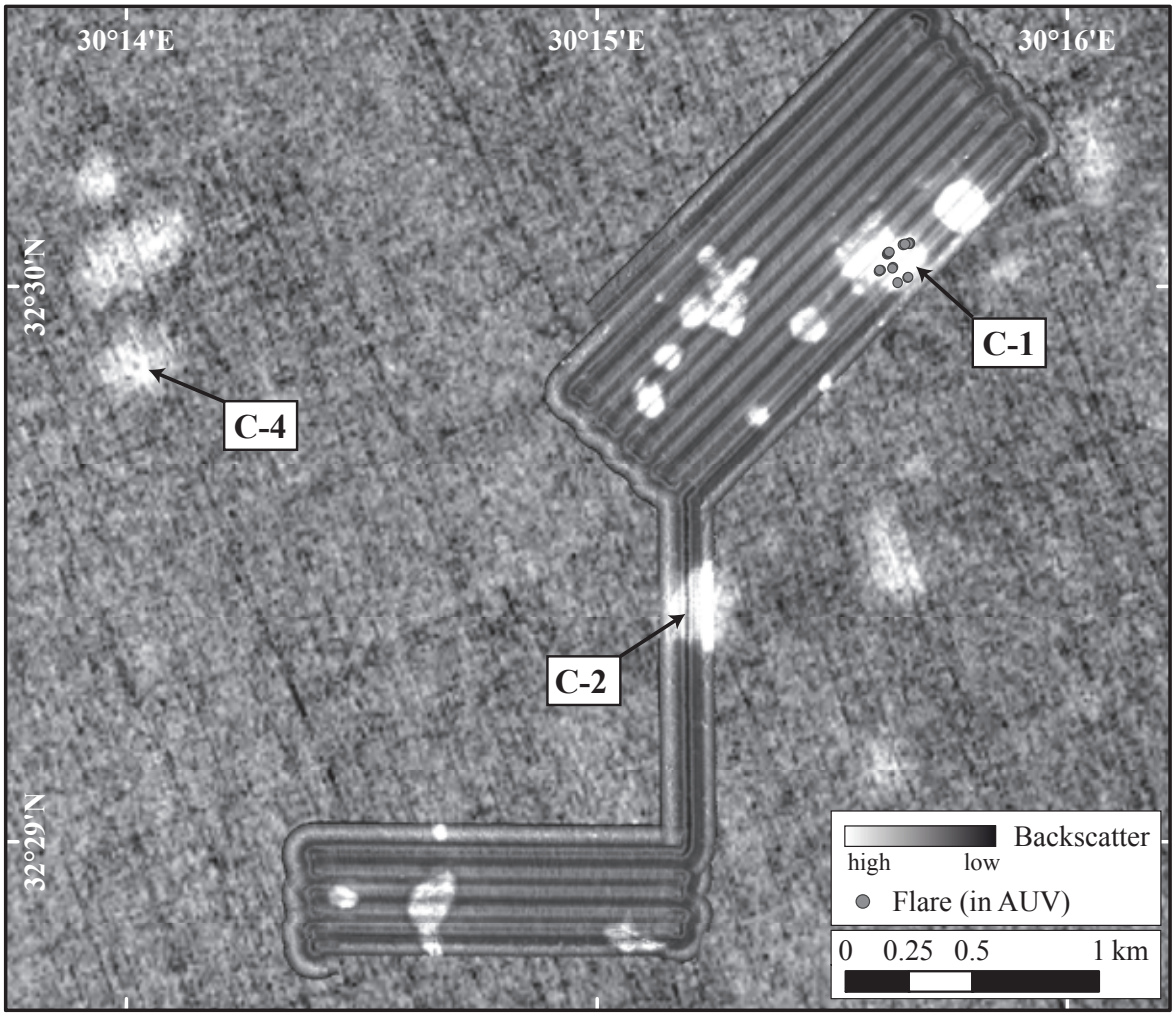

Fig. 6-4: Backscatter image of the central part of the study area compiling the ship-based and AUV-based multibeam backscatter data. Several circular or irregular shaped high-backscatter anomalies are clearly defined. About 20 flares were recorded with the AUV-based multibeam (Fig. 6-6) at carbonate slab C-1 (gray dots).

6.5.2 Acoustic anomalies in the water column and in the subbottom

The ship's PARASOUND system was used to check for hydroacoustic anomalies in the water column (commonly termed flares) caused by ascending gas bubbles. Based on the initial observation that gas emissions occurs through carbonate slabs, we conducted a systematic PARASOUND search by crossing 103 high-backscatter anomalies in the study area with the ship (Fig. 6-2d). The footprint size of the echosounder was about 120 m at the respective water depth, so, there was the great chance to confirm bubble emission by a single survey track in case it occurred during the time of investigation. In total, eight flares have been found at high-backscatter anomalies (numbered C-1 to C-8 in Fig. 6-2b). Accordingly, bubbles emanated from about 8% of the total surveyed carbonate slabs. Remarkably, flares were exclusively found to originate from carbonate slabs indicating that these are the predominant sites of present fluid emission. The typical appearance of flares in PARASOUND echosounder recordings is illustrates Figure 6-5. The gas bubbles rise straight upward, equally to the direction the flares were crossed, suggesting that they are not deflected by horizontal water

currents. Well-pronounced flares with diameters of about 180 m indicate that bubbles are emitted from a spatially confined area at the seafloor. The dense backscatter reflections resulting from gas bubbles in the water column are in sharp contrast to the surrounding seawater lacking any reflections. In the uppermost part of the flares, the backscatter reflections appear less intense, which likely results from bubble reduction and disappearance due to aqueous dissolution. The maximum rising height of the flare-producing bubbles (at C-1) was about 585 m above the seafloor, corresponding to a water depth of 1075 mbsl. All detectable bubbles disappeared at water depths between 1330 and 1470 mbsl, except for flares at C-1 and C-2, of which several reached shallower depths (up to 1075 m). However, as illustrated in Fig. 6-5, the majority of these flares already disappeared at about 1380 mbsl and only single reflections probably caused by single bubbles or groups of bubbles reached shallower water depths. The tops of the flares corresponded well with the upper limit of the gas hydrate stability zone (GHSZ), which was calculated to be located at about 1350 mbsl in that region (Chapter 6.6.1).

The echograms of the PARASOUND record during crossing three carbonate slabs (Fig. 6-5) show that flares originated from small elevations. Furthermore, sub-seafloor reflections were interrupted below the

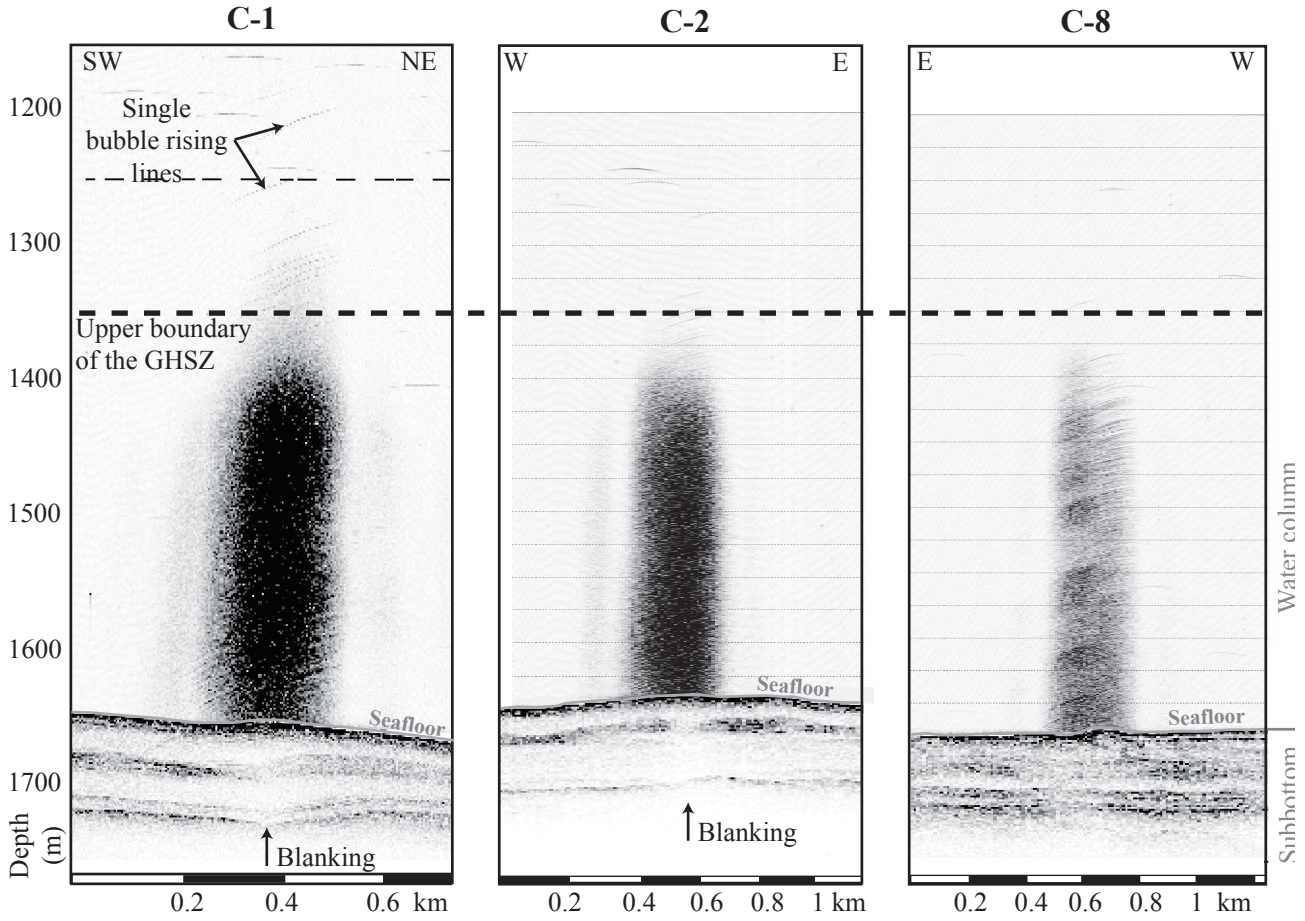

Fig. 6-5: Composite figure showing the secondary low frequency signal below and the primary high frequency signal of PARASOUND echosounder above the seafloor of profiles crossing the carbonate slabs C-1, C-2, and C-8. Blanking in the subbottom is visible in the secondary low frequency signal. At the carbonate slabs the seafloor is locally elevated. Gas emissions are substantiated by pronounced hydroacoustic anomalies in the water column (flares) that are about 300 m in height, with the top narrowing the depth of the upper boundary of the GHSZ at about 1350 mbsl (dashed line). Only few reflections probably caused by single bubbles or small groups of bubbles reached water depths of about 1200 mbsl (C-1).

carbonate slabs. The local blanking might indicate the presence of a narrow conduits through which gas migrates upward through the layered sediment towards the seafloor. However, it can not be ruled out that subbottom blanking at least in part resulted from acoustic energy being absorbed by the dense bubbles in the water column or from a reduced penetration of the signal through the carbonate slabs.

In addition to the use of the PARASOUND echosounder, gas bubbles in the water column were mapped at higher spatial resolution with the AUV-based multibeam system (Fig. 6-6). The sidescan-like signal recorded by the multibeam system showed the backscatter versus distance to the transducers at the AUV. Those hydroacoustic anomalies in the section representing the water column are caused by bubble streams.

Seafloor examinations with the ROV at the seafloor suggested that each of the hydroacoustic anomalies observed in the AUV-based multibeam data corresponded to an individual bubble stream. The coordinates of these bubble emissions were picked from the AUV-based multibeam data by considering the position of the AUV and the horizontal offsets. At C-1 about 20 individual bubble streams (flares in AUV multibeam data) were picked as shown in Figure 6-7. Their locations were mainly confined to sites within the carbonate slab, which is in agreement with the distribution of flares as determined with the PARASOUND echosounder system. The red lines along the ship track in Figure 6-7 depict areas which were characterized by the presence of strong acoustic anomalies ('strong flares') in the water column. Due to the large footprint size of the echosounder of ~120 m, the exact location of the gas emissions could not be resolved. However, because areas of strong flares (detected with PARASOUND) match the origins of flares (AUV) in the center of the carbonate slab, it might be stated that most of the emissions are located centrally.

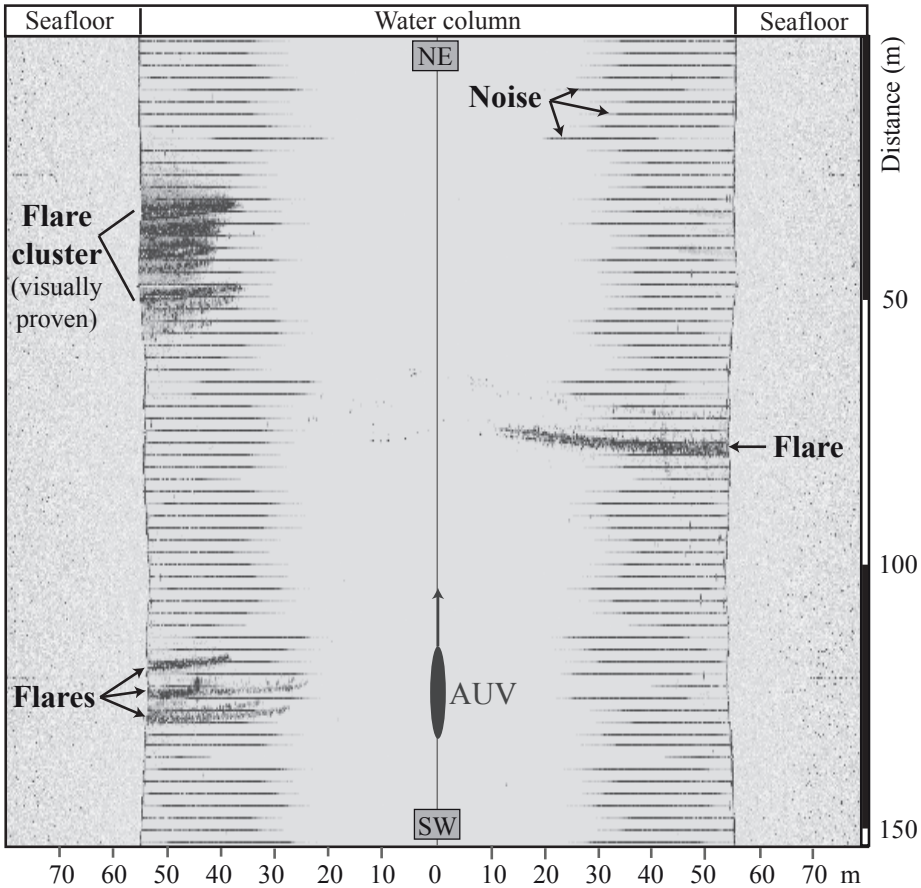

Fig. 6-6: Recording of unprocessed MBES sidescan-like data collected during an AUV dive by crossing carbonate slab C-1 shows several separate flares. Such recordings permit a more precise localization of the gas bubble emissions within C-1 than PARASOUND recordings enable. The x-axis represents the distance below the transducer in the AUV and the y-axis the surveyed distance of the AUV crossing C-1 in a north-eastern direction.

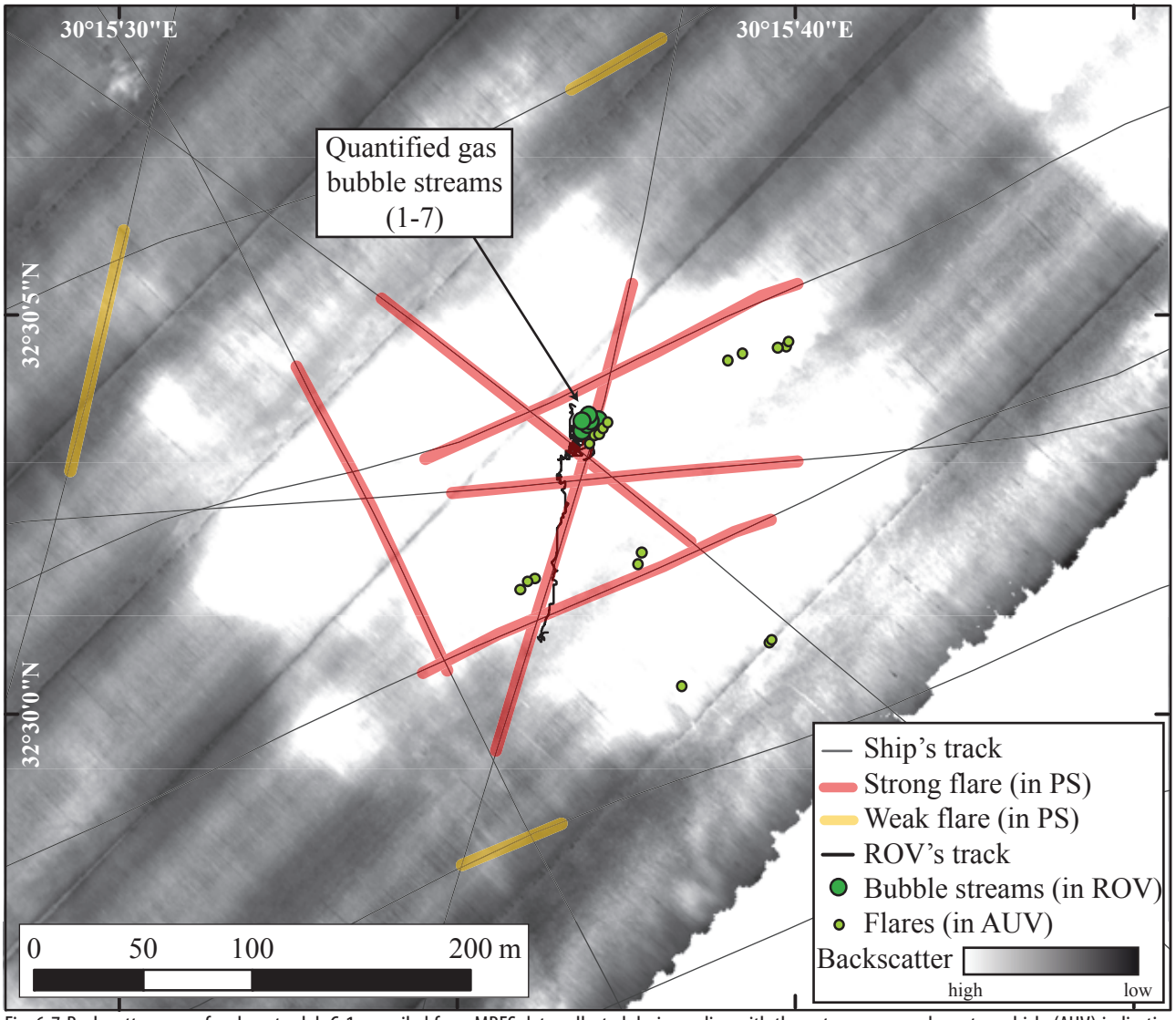

Fig. 6-7: Backscatter map of carbonate slab C-1 compiled from MBES data collected during a dive with the autonomous underwater vehicle (AUV) indicating the extent of the high-backscatter anomaly. Indications of gas emissions from PARASOUND echosounder (PS) coincide with the visually proven bubble streams found in the centre of the carbonate pavement during a dive with a remotely operated vehicle (ROV). Additional gas emissions were detected by analyzing the MBES data of the AUV dive.

6.5.3 Visual seafloor observations at the carbonate slabs

Three TV-MUC stations were carried out at carbonate slabs C-1, C-2, and C-8 in order to map carbonate occurrences at the seafloor. In general, there was a good correlation between the distribution of carbonates exposed at the seafloor and the extent of high backscatter (Fig. 6-8). However, the extent of carbonate paved areas mapped visually was generally smaller than that of the high-backscatter anomalies, suggesting that additional carbonates exist within the sediments. This is in line with the visual observation that the transition from carbonates at the seafloor to the surrounding fine grained sediments was always very gradual. Carbonate crusts at the periphery of the carbonate slabs seem to be increasingly covered by sediments.

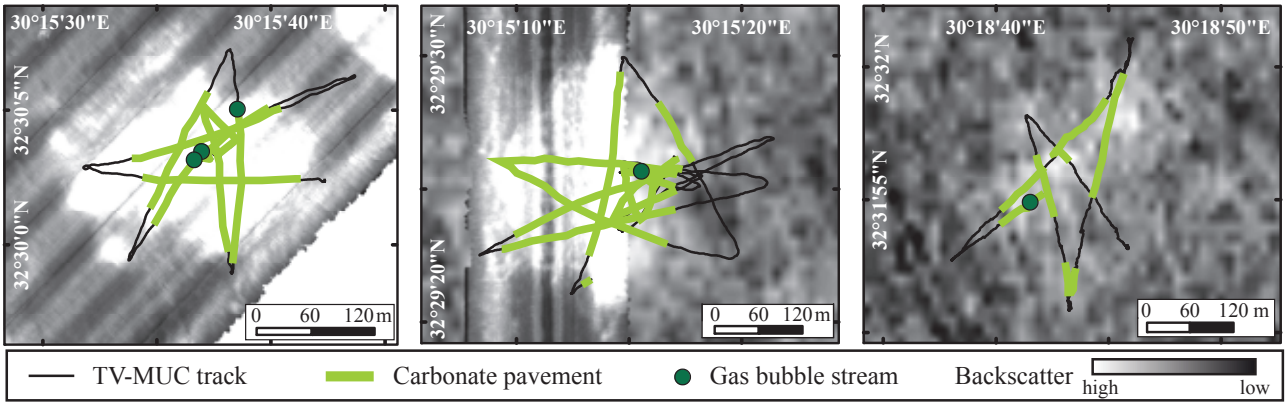

Fig. 6-8: The extent of carbonate slabs (green lines) observed along TV-MUC surveys (black lines) plotted on top of backscatter maps (AUV and ship-based multibeam) at C-1 (left), C-2 (middle), and C-8 (right) illustrating the correlation between the presence of carbonates and high-backscatter anomalies. Gas bubble streams observed during TV-MUC deployments in all three areas emanated in most cases from sites within the carbonate slabs. (TV-MUC stations: #974 (left), #978 (middle), and #1060 (right)).

An ROV dive (# 251) was conducted at carbonate slab C-1 in order to document the seafloor structures and to sample at the seep site (Fig. 6-7). At C-1 almost all of the seafloor was covered by carbonates forming a flat continuous slab (Fig. 6-9a). Fractures some cm deep cross cut the surface of the crust in a reticular pattern. The fractures or cracks are filled with dark-grey in color sediments, which may indicate sulfidic conditions. The surface of the carbonate slab is flat but rugged by cm-sized brownish carbonate excrescents protruding from the plain crust. Only a very thin sediment cover overlaid parts of the carbonate crust. Numerous small bivalve shells were distributed widespread over the carbonate crust. Larger fractures up to one meter deep and uplifted carbonates were observed near the center of the slab (Fig. 6-9b). Living vestimentiferan tubeworms grew in the cavities below the uplifted carbonate crusts, indicating sulfide-rich conditions below.

Seven single gas bubble streams emanating from the seafloor were found within an area of only few meters in diameter at a location that perfectly coincided with the origin of flares as imaged by AUV-based multibeam (Fig. 6-7). Bubbles escaped through small fractures within the carbonate crust. During gas sampling at two gas emission sites with the gas bubble sampler (GBS) for analyses of the gas composition (see chapter 6.5.4), gas hydrate formation covering the gas bubbles occurred (Fig. 6-9c). The formation of hydrate rims surrounding gas bubbles was expected, because the sampling area was located well within the GHSZ. However, such a rim was not directly observed so far when bubbles rise through the water column as images are generally blurred due to in-motion unsharpness. We have been fortunate to observe hydrate skin formation for bubbles that got temporarily adhered to the surface of our black 'imaging plate'. At the initial hydrate formation stage hydrates formed as plates floating on the bubble surface. Continuous collision with other bubbles lead to further gas hydrate crystallization and finally entire gas hydrate coatings evolved (Fig. 6-9d).

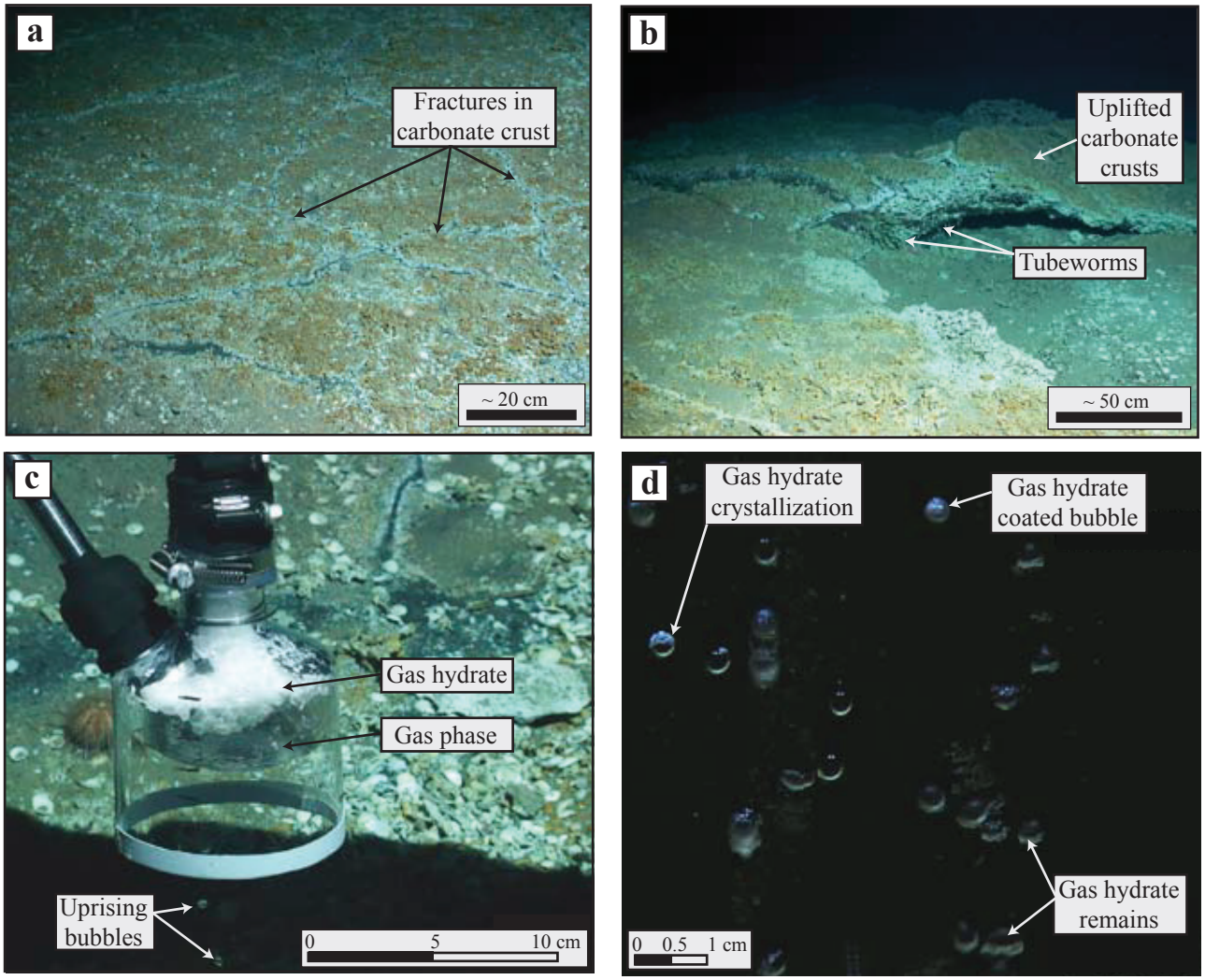

Fig. 6-9: Seafloor pictures taken during ROV dive (#251) at carbonate slab C-1 (Images courtesy of MARUM, Bremen). a: Pavement-like carbonates covering large parts of the seafloor were cut by numerous cm-sized fractures. Numerous bright shells were distributed on the carbonate crust and living sea urchins grazed at the surface. b: Areas of uplifted and broken-apart carbonates more than ~0.5 m in thickness. Vestimentiferan tubeworms rooted below these uplifted carbonates. c: During collection of gas bubbles escaping the seafloor gas hydrate formation was observed in the inverted funnel of the GBS (Station #980-1). d: A portion of the uprising gas bubbles stacked to the black 'imaging plate' used to optimize bubble visibility and showed initial formation of hydrate rims.

6.5.4 Gas composition and the gas hydrate stability limit

Light hydrocarbons in vent gas collected with the GBS at two bubble emission sites at carbonate slab C-1 were strongly dominated by methane (99.977 and 99.975 mol-% of C_1–C_6), followed by ethane (0.0216 and 0.0231 mol-%) and propane (0.0014 and 0.0018 mol-%). iso-butane and n-butane were only found in traces. The mean molecular hydrocarbon ratio (C_1/C_{2+}) exceeded 4,000 in both samples.

Considering the composition of vent gas as well as water column temperature and salinity in this region, the position of the upper limit of the gas hydrate stability zone was estimated at 1350 m water depth.

6.5.5 Visual gas flux estimation

Interpretation of high-definition video recordings of the bubble streams from carbonate slab C-1 allow for an estimation of the flux of gas venting into the water column. By analyzing the bubble emission frequencies and bubble sizes at the seafloor, the volume fluxes of five gas bubble streams were estimated (Table 6-1). Emission frequencies at individual emission sites ranged between 0.2 and 8.3 bubbles per second. At those streams with low emission frequencies (<2 bubbles per second) the bubbles were released in pulses comprising about 20 to 70 bubbles, which were interrupted by dormant phases with bubble emission ceased for several seconds. The mean equivalent spherical radius of the 539 bubbles measured (see Appendix) was 2.75 ± 0.75 mm with the actual bubble diameters ranging between 1.0 mm and 7.7 mm. Average volumes of individual bubbles (assuming a horizontally elliptical shape of the bubbles after measuring the major and minor axis) were 0.126 ± 0.116 mL (Table 6-1). Consequently, the total gas flux calculated for the five bubble streams was 67.91 ± 55.52 mL min^{-1} and, assuming the gas being entirely methane (chapter 6.5.4), the corresponding methane flux was 0.61 ± 0.50 mol min^{-1}.

Table 6-1 Gas flux estimation for gas bubble streams at carbonate patch C-1.

Gas bubble stream	Observation time	Bubble frequency	Numbers of bubbles analyzed	r_e		Gas volume		Gas flux		Methane flux	
	(s)	(1 s^{-1})		(mm)		(mL)		(mL min^{-1})		(mol min^{-1})	
#		Ø	n	Ø	SD	Ø	SD	Ø	SD	Ø	SD
1	2115	8.3	138	1.74	0.2	0.023	0.008	11.4	3.96	0.103	0.036
3	1460	5	131	2.79	0.82	0.11	0.097	33	29.1	0.299	0.263
5	908	1.1	140	3.62	1.08	0.244	0.221	16.1	14.59	0.146	0.132
6	376	0.2	-	2.75	0.75	0.126	0.116	1.13	1.04	0.01	0.009
7	829	0.8	130	2.86	0.91	0.126	0.137	6.27	6.82	0.057	0.062
Total	**5688**	**15.3**	**539**	**2.75**	**0.75**	**0.126**	**0.116**	**67.91**	**55.52**	**0.61**	**0.5**

r_e = bubble equivalent spherical radius; Ø = average; n = number; SD = standard diviation

6.5.6 Extent of seafloor coverage and volumes of carbonate slabs

Based on the visual observations we assume that the positive seafloor morphology mainly results from authigenic carbonate precipitation. Moreover, we may estimate the volume of the carbonate slabs by assigning their extents and heights using the AUV-based multibeam maps. Apparently, this is a minimum estimate that solely accounts for those parts of the slabs protruding from the surrounding seafloor, whereas parts having precipitated within the seafloor are ignored.

The northeastern part of the area mapped during an AUV dive comprised 15 carbonate slabs characterized by seafloor elevations (Fig. 6-3) and high-backscatter anomalies (Fig. 6-4). Beside carbonate slab C-1, further carbonate slabs were present in this area and numbered A-1 to A-7 (Fig. 6-10a; Table 6-2). The dimensions of the elevations within the areas of high-backscatter anomalies were measured as illustrated in Figs. 6-10 b to d. Because most of the elevations have a nearly subcircular extent, their mean radii could be considered for calculations of the seafloor area covered by them. For those carbonate slabs with a pronounced elliptical shape, the average lengths of the major and minor axis were determined. As a result, areas of individual carbonate patches range between 284

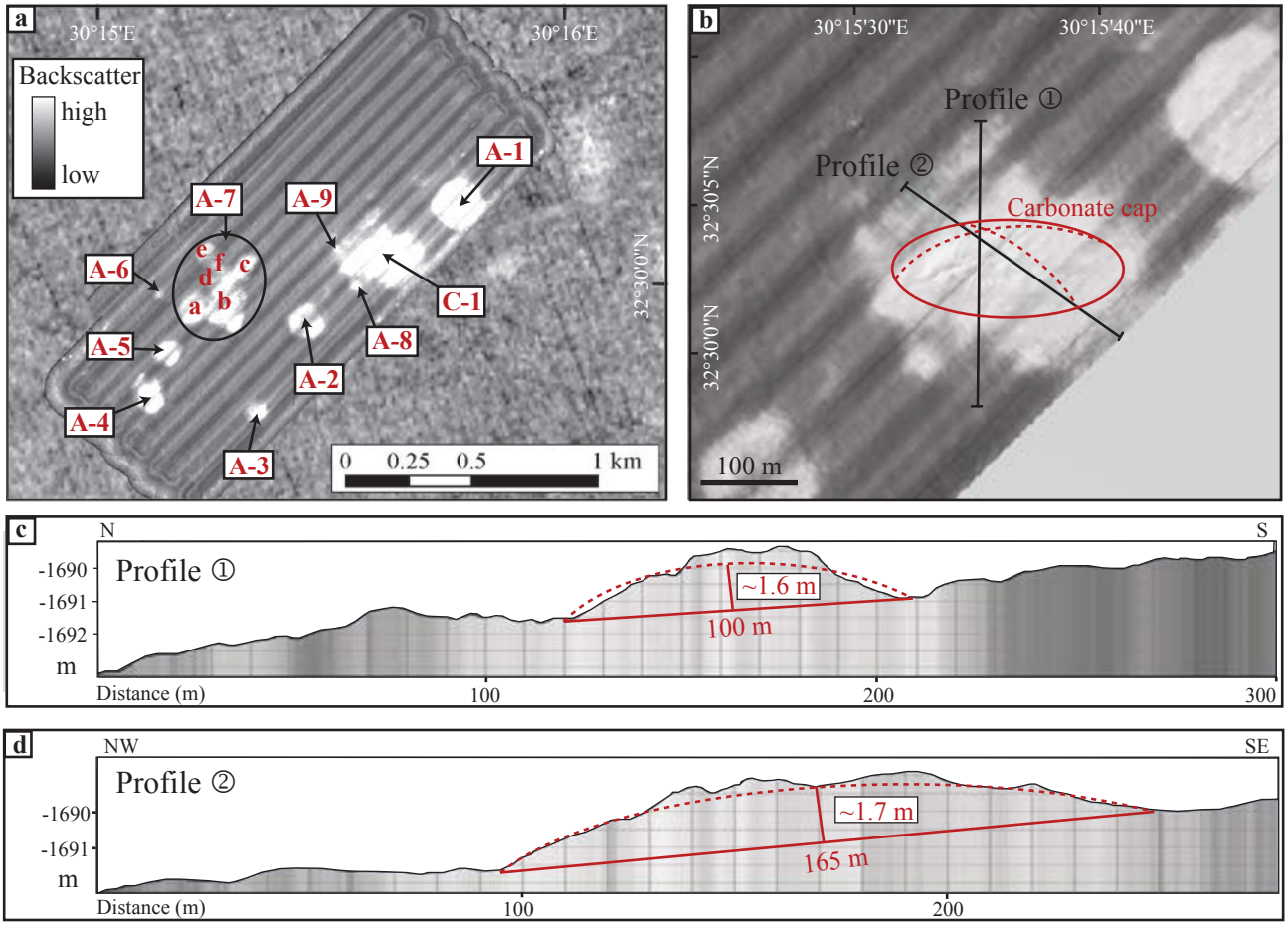

Fig. 6-10 a: Ship and AUV-based backscatter map of the northern part of the area covered during the AUV dive. The dimensions of 15 carbonate slabs were estimated (numbers refer to Table 6-2). b-d: For volume estimates of the 15 carbonate slabs, the AUV-based backscatter map was draped on the bathymetry as exemplified for carbonate slab C-1. c and d: Profiles crossing the carbonate slab as illustrated in Fig. 6-10b. The profiles clearly show the blister –like shape of the feature rising ~1.6 m above the generally smooth and flat seafloor (both with high vertical exaggeration).

and 21,991 m^2 with an average of 5,240 m^2 (Table 6-2). The total area covered by carbonate slabs is about 78,600 m^2, corresponding to ~6.6% of the entire area.

The average heights at the central top of the spherical or elliptical shaped elevations of all carbonate slabs range between 0.4 and 1.8 m. Assuming the shape of a partial sphere or a half ellipsoid, the volumes of individual carbonate slabs range between 50 and 38,272 m^3 (mean 5,970 m^3), whereas the total volume of all slabs is about 89,600 m^3.

Table 6-2 Volume estimation of the carbonate patches distributed in an area of about 1.8 km^2 around C-1 (see Fig. 6-10a) and estimate of the carbon stored within the patches.

Patch	**Size**		**Shape**	**Area**	**Height**	**Volume**	**$CaCO_3$**	**Weight**	**C**
#	a (m)	b (m)		(m^2)	(m)	(m^3)	(m^3)	($\times 10^6$ g)	($\times 10^6$ mol)
C-1	100	280	elliptical	21991	1.6	22724	20452	32723	327
A-1	89	89	spherical	6221	1.3	3890	3501	5601	56
A-2	102	102	spherical	8171	1.2	4904	4414	7062	71
A-3	56	56	spherical	2463	0.9	1109	998	1597	16
A-4	81	109	elliptical	6934	1.4	12482	11234	17974	180
A-5	56	56	spherical	2463	0.6	739	665	1064	11
A-6	28	28	spherical	616	0.5	154	139	222	2
A-7a	68	68	spherical	3632	0.7	1272	1145	1832	18
A-7b	108	188	elliptical	15947	1.8	38272	34445	55112	551
A-7c	66	66	spherical	3421	0.8	1283	1155	1848	18
A-7d	19	19	spherical	284	0.4	50	45	72	1
A-7e	52	52	spherical	2124	0.5	531	478	765	8
A-7f	54	27	elliptical	1145	0.6	840	756	1209	12
A-8	29	50	elliptical	1139	0.4	645	581	929	9
A-9	51	51	spherical	2043	0.7	664	598	956	10
Total				**78593**		**89559**	**80603**	**128964**	**1290**

a = minor diameter; b = major diameter

6.6 Discussion

6.6.1 Methane bubbles emanating at carbonate slab C-1

The carbonate slab C-1 is a typical seafloor manifestation of fluid seepage at the lower middle slope in the Central Province of the Nile Deep Sea Fan (NDSF). Because carbonates exposed at the seafloor at C-1 (Fig. 6-9 a-c) strongly resemble in shape and appearance those methane-related carbonates described before (Bayon et al. 2009a; Bayon et al. 2009b), we suppose that the carbonates in our study area have likewise been formed through the anaerobic oxidation of methane (AOM). Our results (Fig. 6-8) as well as those from earlier studies (Bayon et al. 2009b; Dupré et al. 2010) have shown that the high backscatter in multibeam data results from the presence of carbonates at the seafloor. We propose, therefore, that all of the 163 patches characterized by high-backscatter in our study area (Fig. 6-2) are caused by carbonate slabs at the seafloor. While gas bubble emissions through carbonate slabs have been described before (Dupré et al. 2010), our systematic examinations revealed that gas bubbles were emitted at about 8% of these features during the time of our observations. Acoustic evidence for gas emissions at C-1 are similar to those obtained at other carbonate slabs (Fig. 6-5), therefore, we consider our ROV-based studies at C-1 as representative for all of the eight sites (C-1 to C-8) with evidence for bubble emissions (Fig. 6-2b).

The strong prevalence of methane (C_1/C_{2+} >4,000) in light hydrocarbons of the vent gas samples suggests that methane escaping from carbonate slab C-1 predominantly originates from microbial methanogenesis (Bernard et al. 1976). Additionally, C_4- to C_6-hydrocarbons which are commonly attributed to thermogenic input (Schoell 1980; Claypool and Kvenvolden 1983) were only found in traces. This is different to the composition of gas expelled at the Isis and Amon mud volcanoes in the Eastern Province where methane originates from a mixture from thermogenic and microbial sources (Mastalerz et al. 2007, 2009). Nevertheless, our result suggests that the gas emissions through the carbonate slabs in the Central Province are sourced from shallower sediment depths compared to those at the deep-rooting mud volcanoes in the Eastern Province. This observation corresponds to the interpretation of Bayon et al. (2009b) who suggested a relation of the seeps in the Central Province to sediment destabilization with numerous slumps and slides probably promoting fluid escape from shallow sediment depths.

We may conduct an order-of-magnitude estimation of the gas bubble flux at the carbonate slab C-1 by combining results from the AUV-based multibeam system with the ROV-based seafloor observations. About 20 individual gas bubble emissions were identified in the AUV-based multibeam record (Fig. 6-6), their location is shown in Figure 6-7. During the ROV-dive the locations of gas emission sites as well as the fact that each of the bubble streams caused a flare in the multibeam could be confirmed. Quantification of methane fluxes by use of the videos recorded during the ROV dive at five individual bubble streams yielded in total 0.32×10^6 mol CH_4 yr^{-1}. We consider this as the minimum estimate as this is the flux that we actually observed. We may calculate a maximum value by extrapolating the estimated flux of five bubble streams to the total number of about 20 bubble streams that we found to occur at C-1 resulting in flux of about 1.3×10^6 mol CH_4 yr^{-1}. Of course, this estimation contains large uncertainties, as, for instance, data on the intensity range of all 20 emission sites and the spatial and temporal variability of gas emissions are unavailable, so far.

The flux of methane as bubbles at the carbonate slab C-1 is in the same order-of-magnitude as those inform seep sites in other regions, i.e. Vodyanitski mud volcano in the Black Sea (0.9×10^6 mol CH_4 yr^{-1}; Sahling et al. 2009), Håkon Mosby mud volcano in the Barents Sea (6.3×10^6 mol CH_4 yr^{-1}; Sauter et al. 2006), GC-185 in the Gulf of Mexico (0.2×10^6 mol CH_4 yr^{-1}; Leifer and MacDonald 2003), several gas emission sites at the Makran continental margin (0.1 to 5.6×10^6 mol CH_4 yr^{-1}; Römer et al. submitted-b), or at the Kerch seep area in the Black Sea (2.2 – 87.0 $\times 10^6$ mol CH_4 yr^{-1}; Römer et al. submitted-a). This similarity in the fluxes of methane as gas bubbles for the different seep sites has not necessarily

been expected as they are related to a variety of seep types and connected to different geological settings.

For the eight gas emission sites (C-1 to C-8) discovered in the study area, the hydroacoustic records show that ascending gas bubbles dissolve within the water column between 1075 and 1470 mbsl. This is well below the mixed surface layer in the Eastern Mediterranean Sea (Lascaratos et al. 1993; D'Ortenzio et al. 2005). Hence, hydrocarbon seepage in this area is not relevant for the transport of methane from the seafloor to the upper hydrosphere or even into the atmosphere.

Noticeable is the correlation between the bubble dissolution depth and the upper boundary of the GHSZ. The upper boundary of the GHSZ in this area was calculated to occur at about 1350 mbsl, which is about 200 m deeper than that reported for the Amsterdam mud volcano in the Anaximander Mountain region, Northeastern Mediterranean Sea (Pape et al. 2010b). Differences in the actual extent of the GHSZ at the two sites are most likely due to differences in the gas composition and in other physico-chemical parameters, such as water temperature and salinity, which have been considered for individual hydrate phase calculations and assignments of the hydrate stability field. All flares investigated in this study reached almost the top of the GHSZ, while two flares were even observed at shallower water depths. However, in both cases only faint reflections indicative for single bubbles or groups of bubbles were visible in the Parasound echograms above the upper boundary of the GHSZ, whereas the majority of the bubbles was dissolved already just below the boundary similar to the other flares (Fig. 6-5a). This relation has been observed in other areas, e.g. at the Cascadia margin (Heeschen et al. 2003), at mud volcanoes in the Black Sea (Greinert et al. 2006), and the Makran continental margin (Römer et al. submitted-b). As confirmed by our visual observations (Fig. 6-9d) and supported by the bubble rising heights, gas bubbles rising upwards within the GHSZ are protected from aqueous dissolution by gas hydrate rims. The bubbles rapidly dissolve as soon as the upper limit of the GHSZ is reached.

Considering the physico-chemical parameters at our study area, the single bubble dissolution model SiBu-GUI (McGinnis et al. 2006; Greinert and McGinnis 2009) revealed bubble dissolution depths similar to the results from our hydroacoustic studies. The average equivalent spherical radius determined for bubbles emitted at C-1 was $r_e = 2.75 \pm 0.75$ mm (Table 6-1), and the bubble size ranged between 1.0 and 7.7 mm. The SiBu-GUI modeling results revealed a dissolution depth range of 1590 (bubble size of 1 mm) to 1220 mbsl (bubble size of 7.7 mm). Calculations using the mean bubble size resulted in complete gas dissolution at about 1402 mbsl, which is very close to the dissolution depths observed with the PARASOUND echosounder (~1380 mbsl). Results from the model further indicate that the relatively long lifetime of the bubbles is the result of inhibited gas exchange with the surrounding seawater due to the presence of hydrate rims enveloping the gas bubbles. Calculations for bubbles without hydrate coatings revealed that average-sized bubbles would be completely dissolved at about 1630 mbsl (corresponding to 40 m flare height).

6.6.2 Carbonate slabs

Authigenic methane-derived carbonates can form particular landscapes at hydrocarbon seeps in the global ocean. For example, chemoherm complexes several hundred meters in diameter at the base and several tens of meters in height were described from offshore Oregon (Teichert et al. 2005). The sizes of authigenic carbonate precipitates in sediments at mounds and other seafloor structures offshore Costa Rica and southern Nicaragua ranged from several tens of meters up to about a kilometers in diameter (Han et al. 2004; Sahling et al. 2008b). At pockmarks at the Congo Fan, carbonates occur in nodules in the sediments as well as exposed at the seafloor (Sahling et al. 2008a; Haas et al. 2010) influencing an area of about half a kilometer in diameter. While the lateral extents of these carbonates have been described, to our knowledge, volumes of authigenic carbonates at distinct submarine areas and, hence, estimates of C stored in such carbonates have not been published so far. Such a volume may give an impression on how much methane-derive carbon is sequestered as carbonates at the seafloor.

The generally flat and smooth seafloor in the Central Province allows conducting an order-of-magnitude estimation of the volume of the carbonate slabs using high-resolution AUV-based multibeam maps (Figs. 6-10b-d). We found that the carbonate slabs project above the surrounding seafloor with heights of a few decimeters to a maximum of 1.8 m in the central parts (Table 6-2). It is uncertain which processes affect the carbonate slabs to protrude from the surrounding seafloor, but from the visual observations at the seafloor (e.g. Fig. 6-9b) it appears as if the elevation is entirely composed of carbonates as illustrated in Figure 6-11. Considering their shape, we estimated the volume of that part of the carbonate slab that overtops the seafloor (Table 6-2), which is apparently a minimum estimate as additional carbonates almost certainly occur around and below that part.

The carbonates observed in our study are very similar to those described by Gontharet et al. (2007, 2009) and Bayon et al. (2009a) that were sampled about 10 km east of our main study site (Fig. 6-2). At both sites, the carbonates form flat slabs tens to hundreds of meters in diameters. While we were not able to sample any carbonates, Gontharet et al. (2009) had been successful (sample NL7CC2). By using U-Th data, Bayon et al. (2009a) proposed that the carbonates precipitated within the sediments and that they grow in a downward direction. The carbonate crusts in this area of the NDSF predominantly consist of 83 – 95 wt-% carbonate, paralleled by detritus and minor authigenic phases (barite, gypsum and pyrite; Gontharet et al. 2007). The bulk specific density of carbonate samples described in Bayon et al. (2009a) was 1.6 g cm^{-3}. Considering a fraction of 90% carbonate, a specific density of 1.6 g cm^{-3}, and the estimated volumes of the carbonate slabs (89,600 m^3), we calculate that a total of about 1.29×10^9 mol C is stored in the 15 carbonate slabs in the part of our study area analyzed regarding the carbonate slaps (Table 6-2 and Fig. 6-10a).

The significances of the gas bubble transport process and of the methane sequestration in carbonates at the carbonate slab C-1 are highlighted in Fig. 6-11. An uncertain amount of methane migrates into shallow sediments. A fraction of methane that is dissolved in the pore water is consumed by AOM resulting in the formation of carbonate ions and, eventually, precipitation as carbonate (327×10^6 mol C). Another fraction of the ascending methane vents into the water column (currently about 0.32 to 1.3×10^6 mol C yr^{-1}). If we assume that the amount of methane converted by AOM within the pore waters equals that being released into the water column, the carbonates would have formed within about 200 to 1000 years. However, there is evidence that some parts of the crusts are significantly older (Bayon et al. 2009a). Based on U-Th-dating they estimated that the oldest part of a 5.5 cm thick crust is about 5000 years and that the youngest part has formed recently (given the large error inherent to the dating method). If we assume that carbonate formation takes place since several thousands of years as revealed for a single crust sample from the NDSD (Bayon et al. 2009a), the amounts of methane

consumed by AOM and of carbon sequestered in carbonates is significantly smaller than those amounts of methane and carbon transported by gas bubbles flux from that area.

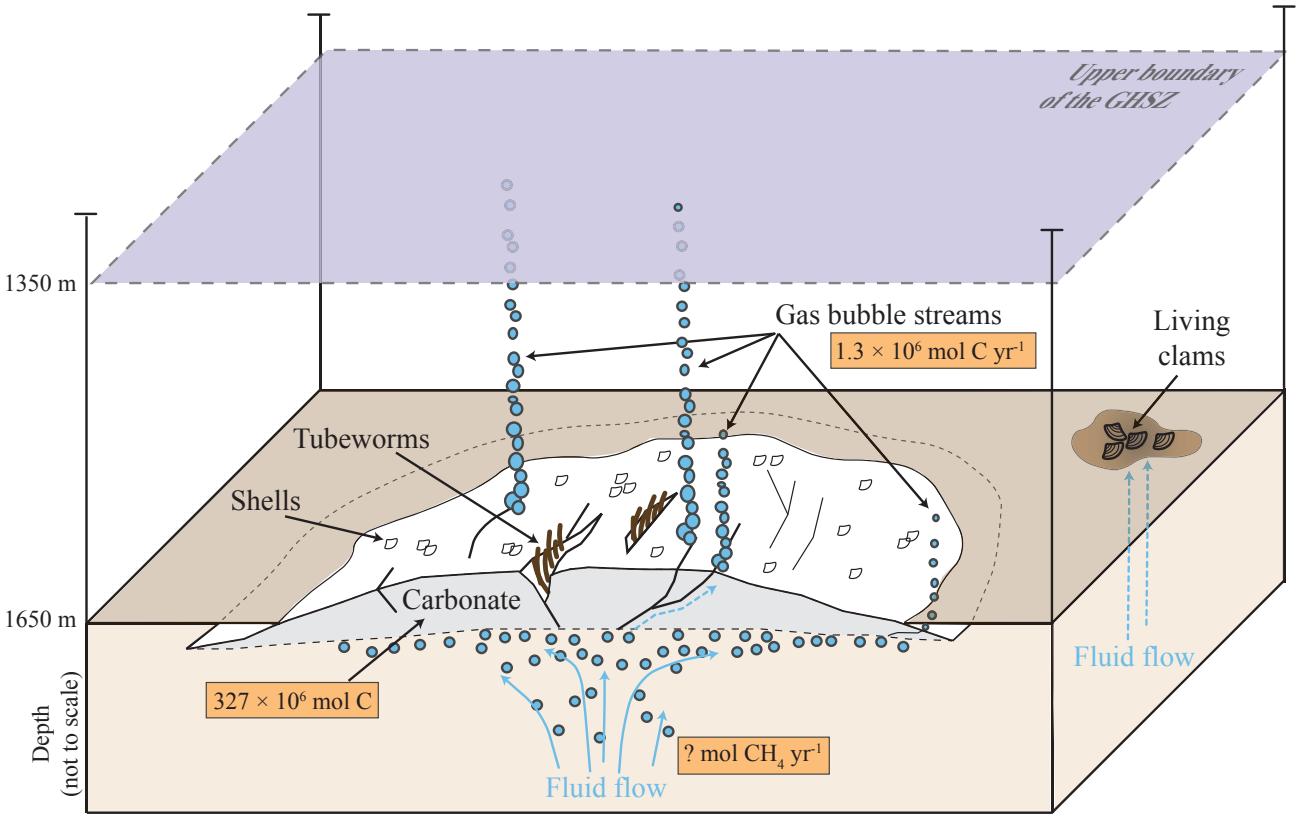

Fig. 6-11: Schematic illustration of a carbonate slab with gas bubble streams migrating through fractures into the water column. Numbers indicate the amount of carbonate-bound carbon as well as the flux of methane as gas bubbles determined for carbonate slab C-1. Gas bubbles rising through the water column finally disappear at about 1350 mbsl, corresponding to the upper boundary of the gas hydrate stability zone (GHSZ).

6.7 Conclusion

Within the study area located in the Central Province at the Nile Deep Sea Fan (NDSF) and comprising about 325 km^2, 163 carbonate slabs on the seafloor were detected by their high reflectivity in multibeam backscatter images. A systematic hydroacoustic survey in 2009 revealed that gas emission occurred from ~8% of the carbonate slabs during the time of observation. The flux of methane bubbles into the water column is in the lower range of values of methane fluxes from other gas emission sites as well as mud volcanoes around the world but generally in the same order-of-magnitude.

While this study concentrated on carbonate slabs at mid-slope depth in the Central Province, previous studies reveal evidence for hundreds if not thousands of additional high-backscatter anomalies on the NDSF. The high-backscatter anomalies certainly have different genesis and occur in regionally different geological settings. However, as shown in our study, rather unspectacular seafloor manifestations such as carbonate slabs should be taken into account when it comes to estimates of methane being transported from the sediments into the hydrosphere. The carbonate slabs in our study area are related to debris flow deposits at the middle slope. This type of geological setting is much larger than our study area suggesting that many additional carbonate slabs and gas emissions exist at least in the Central Province of the NDSF.

6.8 Acknowledements

We greatly appreciate the shipboard support from the master and crew of the research vessel MARIA S. MERIAN as well as the professional assistance of the scientific and technical operating teams of MARUM's ROV QUEST 4000m and AUV SEAL. Inga Golbeck is acknowledged for help with analyzing gas bubbles from video recordings and Paul Wintersteller and Marten Schmager for processing of ship-based bathymetric data. Research financial support was provided by the DFG-Research Center/Excellence Cluster "The Ocean in the Earth System".

6.9 References

Artemov YG, Egorov VN, Polikarpov GG, Gulin SB (2007) Methane emission to the hydro-and atmosphere by gas bubble streams in the Dnieper Paleo-delta, the Black Sea Marine. Ecol J 6:5-26

Bayon G, Henderson GM, Bohn M (2009a) U-Th stratigraphy of a cold seep carbonate crust. Chemical Geology 260:47-56

Bayon G, Loncke L, Dupré S, Caprais JC, Ducassou E, Duperron S, Etoubleau J, Foucher J-P, Fouquet Y, Gontharet S, Henderson GM, Huguen C, Klaucke I, Mascle J, Migeon S, Olu-Le Roy K, Ondréas H, Pierre C, Sibuet M, Stadnitskaia A, Woodside J (2009b) Multi-disciplinary investigation of fluid seepage on an unstable margin: The case of the Central Nile deep sea fan. Marine Geology 261:92-104

Bernard BB, Brooks JM, Sackett WM (1976) Natural gas seepage in the Gulf of Mexico. Earth and Planetary Science Letters 31:48-54

Caress DW, Chayes DN (1996) Improved processing of Hydrosweep DS multibeam data on the R/V Maurice Ewing. Marine Geophysical Research 18:631-650

Claypool GE, Kvenvolden KA (1983) Methane and other Hydrocarbon Gases in Marine Sediment. Annual Review of Earth and Planetary Sciences 11:299-327

D'Ortenzio F, Iudicone D, de Boyer Montegut C, Testor P, Antoine D, Marullo S, Santoleri R, Madec G (2005) Seasonal variability of the mixed layer depth in the Mediterranean Sea as derived from in situ profiles. Geophysical Research Letters 32: L12605

Dupré S, Buffet G, Mascle J, Foucher J-P, Gauger S, Boetius A, Marfia C, Team tAA, Team tQR, Party tBS (2008) High-resolution mapping of large gas emitting mud volcanoes on the Egyptian continental margin (Nile Deep Sea Fan) by AUV surveys. Marine Geophysical Researches 29:275-290

Dupré S, Woodside J, Foucher J-P, de Lange G, Mascle J, Boetius A, Mastalerz V, Stadnitskaia A, Ondréas H, Huguen C, Harmégnies F, Gontharet S, Loncke L, Deville E, Niemann H, Omoregie E, Olu-Le Roy K, Fiala-Medioni A, Dählmann A, Caprais J-C, Prinzhofer A, Sibuet M, Pierre C, Damsté JS (2007) Seafloor geological studies above active gas chimneys off Egypt (Central Nile Deep Sea Fan). Deep Sea Research Part I: Oceanographic Research Papers 54:1146-1172

Dupré S, Woodside J, Klaucke I, Mascle J, Foucher J-P (2010) Widespread active seepage activity on the Nile Deep Sea Fan (offshore Egypt) revealed by high-definition geophysical imagery. Marine Geology 275:1-19

Feseker T, Brown K, Blanchet C, Scholz F, Nuzzo M, Reitz A, Schmidt M, Hensen C (2010) Active mud volcanoes on the upper slope of the western Nile deep-sea fan – first results from the P362/2 cruise of R/V Poseidon. Geo-Marine Letters 30:169-186

Feseker T, Dählmann A, Foucher JP, Harmegnies F (2009) In-situ sediment temperature measurements and geochemical porewater data suggest highly dynamic fluid flow at Isis mud volcano, eastern Mediterranean Sea. Marine Geology 261:128-137

Gaullier V, Mart Y, Bellaiche G, Mascle J, Vendeville BC, Zitter T, Second Leg Prismed IISP (2000) Salt tectonics in and around the Nile deep-sea fan: insights from the PRISMED II cruise. Geological Society, London, Special Publications 174:111-129

Gontharet S, Pierre C, Blanc-Valleron M-M, Rouchy JM, Fouquet Y, Bayon G, Foucher JP, Woodside J, Mascle J, Party TNS (2007) Nature and origin of diagenetic carbonate crusts and concretions from mud volcanoes and pockmarks of the Nile deep-sea fan. Deep-Sea Reseach II 54:1292-1311

Gontharet S, Stadnitskaia A, Bouloubassi I, Pierre C, Damsté JSS (2009) Palaeo methane-seepage history traced by biomarker patterns in a carbonate crust, Nile deep-sea fan (Eastern Mediterranean Sea). Marine Geology 261:105-113

Greinert J, Artemov Y, Egorov V, De Batist M, McGinnis D (2006) 1300-m-high rising bubbles from mud volcanoes at 2080m in the Black Sea: Hydroacoustic characteristics and temporal variability. Earth and Planetary Science Letters 244:1-15

Greinert J, McGinnis DF (2009) Single bubble dissolution model - The graphical user interface SiBu-GUI. Environmental Modelling & Software

24:1012-1013
Haas A, Peckmann J, Elvert M, Sahling H, Bohrmann G (2010) Patterns of carbonate authigenesis at the Kouilou pockmarks on the Congo deep-sea fan. Marine Geology 268:129-136
Han X, Suess E, Sahling H, Wallmann K (2004) Fluid venting activity on the Costa Rica margin: new results from authigenic carbonates. International Journal of Earth Sciences 93:596-611
Heeschen K, Tréhu A, Collier RW, Suess E, Rehder G (2003) Distribution and height of methane bubble plumes on the Cascadia Margin characterized by acoustic imaging. Geophysical Research Letters 30:12,1643
Heeschen KU, Collier RW, DeAngelis MA, Suess E, Rehder G, Linke P, Klinkhammer GP (2005) Methane sources, distributions, and fluxes from cold vent sites at Hydrate Ridge, Cascadia Margin. Global Biogeochemical Cycles 19:GB2016
Hornafius JS, Quigley D, Luyendyk BP (1999) The world's most spectacular marine hydrocarbon seeps(Coal Oil Point, Santa Barbara Channel, California)- Quantification of emissions. Journal of Geophysical Research 104:20,730-720
Hsu KJ, Montadert L, Bernoulli D, Cita MB, Erickson A, Garrison RE, Kidd RB, Melieres F, Muller C, Wright R (1977) History of the Mediterranean salinity crisis. Nature 267:399-403
Huguen C, Foucher JP, Mascle J, Ondréas H, Thouement M, Gontharet S, Stadnitskaia A, Pierre C, Bayon G, Loncke L, Boetius A, Bouloubassi I, de Lange G, Caprais JC, Fouquet Y, Woodside J, Dupré S, Party atNS (2009) Menes caldera, a highly active site of brine seepage in the Eastern Mediterranean sea: „In situ" observations from the nautinil expedition (2003). Marine Geology 261:138-152
Lascaratos A, Williams RG, Tragou E (1993) A Mixed-Layer Study of the Formation of Levantine Intermediate Water. Journal of Geophysical Research 98:14739-14749
Leifer I, Judd AG (2002) Oceanic methane layers: the hydrocarbon seep bubble deposition hypothesis. Terra Nova 14:417-424
Leifer I, MacDonald I (2003) Dynamics of the gas flux from shallow gas hydrate deposits: interaction between oily hydrate bubbles and the oceanic environment. Earth and Planetary Science Letters 210:411-424
Leifer I, Patro RK (2002) The bubble mechanism for methane transport from the shallow sea bed to the surface: A review and sensitivity study. Continental Shelf Research 22:2409-2428
Loncke L, Gaullier V, Bellaiche G, Mascle J (2002) Recent depositional patterns of the Nile deep-sea fan from echo-character mapping. AAPG Bulletin 86:1165-1186
Loncke L, Gaullier V, Droz L, Ducassou E, Migeon S, Mascle J (2009) Multi-scale slope instabilities along the Nile deep-sea fan, Egyptian margin: A general overview. Marine and Petroleum Geology 26:633-646
Loncke L, Gaullier V, Mascle J, Vendeville BC, Camera L (2006) The Nile deep-sea fan: An example of interacting sedimentation, salt tectonics, and inherited subsalt paleotopographic features. Marine and Petroleum Geology 23:297-315
Loncke L, Mascal J, Parties FS (2004) Mud volcanoes, gas chimneys, pockmarks and mounds in the Nile deep-sea fan (Eastern Mediterranean): geophysical evidences. Marine and Petroleum Geology 21:669-689
Maini BB, Bishnoi PR (1981) Experimental investigation of hydrate formation behaviour of a natural gas bubble in a simulated deep sea environment. Chemical Engineering Science 36:183-189
Mascle J, Benkhelil J, Bellaiche G, Zitter T, Woodside J, Loncke L, Party PIS (2000) Marine geologic evidence for a Levantine-Sinai plate, a new piece of the Mediterranean puzzle. Geology 28:779-782
Masoudi R, Tohidi B (2005) Estimating the hydrate stability zone in the presence of salts and/or organic inhibitors using water partial pressure. Journal of Petroleum Science and Engineering 46:23-36
Mastalerz V, de Lange GJ, DÃ¤hlmann A, Feseker T (2007) Active venting at the Isis mud volcano, offshore Egypt: Origin and migration of

hydrocarbons. Chemical Geology 246:87-106
Mastalerz V, de Lange GJ, Dählmann A (2009) Differential aerobic and anaerobic oxidation of hydrocarbon gases discharged at mud volcanoes in the Nile deep-sea fan. Geochimica et Cosmochimica Acta 73:3849-3863
McGinnis DF, Greinert J, Artemov Y, Beaubien SE, Wüest A (2006) Fate of rising methane bubbles in stratified waters: How much methane reaches the atmosphere. Journal of Geophysical Research 111: CO9007
Nikolovska A, Sahling H, Bohrmann G (2008) Hydroacoustic methodology for detection, localization, and quantification of gas bubbles rising from the seafloor at gas seeps from the Black Sea. Geochemistry, Geophysics, Geosystems 9:Q10010
Pape T, Bahr A, Rethemeyer J, Kessler JD, Sahling H, Hinrichs K-U, Klapp SA, Reeburgh WS, Bohrmann G (2010a) Molecular and isotopic partitioning of low-molecular-weight hydrocarbons during migration and gas hydrate precipitation in deposits of a high-flux seepage site. Chemical Geology 269:350-363
Pape T, Kasten S, Zabel M, Bahr A, Abegg F, Hohnberg H-J, Bohrmann G (2010b) Gas hydrates in shallow deposits of the Amsterdam mud volcano, Anaximander Mountains, Northeastern Mediterranean Sea. Geo-Marine Let. 30:187-206
Rehder G, Brewer PW, Peltzer ET, Friedrich G (2002) Enhanced lifetime of methane bubble streams within the deep ocean. Geophysical Research Letters 29:15,1731
Römer M, Sahling H, Pape T, Bahr A, Wintersteller P, Bohrmann G (submitted-a) Geological control and quantity of gas bubbles emanating from a high-flux seep area in the Black Sea - The Kerch-Flare. Marine Geology
Römer M, Sahling H, Pape T, Spiess V, Bohrmann G (submitted-b) Gas bubble emission from submarine hydrocarbon seeps at the Makran continental margin (offshore Pakistan). Journal of Geophysical Reseach
Ryan WBF (1978) Messinian badlands on the southeastern margin of the Mediterranean Sea. Marine Geology 27:349-363
Sahling H, Bohrmann G, Artemov YG, Bahr A, Brüning M, Klapp SA, Klaucke I, Kozlova E, Nikolovska A, Pape T, Reitz A, Wallmann K (2009) Vodyanitskii mud volcano, Sorokin trough, Black Sea: Geological characterization and quantification of gas bubble streams. Marine and Petroleum Geology 26:1799-1811
Sahling H, Bohrmann G, Spiess V, Bialas J, Breitzke M, Ivanov M, Kasten S, Krastel S, Schneider R (2008a) Pockmarks in the Northern Congo Fan area, SW Africa: Complex seafloor features shaped by fluid flow. Marine Geology 249:206-225
Sahling H, Masson DG, Ranero CR, Hühnerbach V, Weinrebe W, Klaucke I, Bürk D, Brückmann W, Suess E (2008b) Fluid seepage at the continental margin offshore Costa Rica and southern Nicaragua. Geochemistry Geophysics Geosystems 9:Q05S05
Salem R (1976) Evolution of Eocene-Miocene sedimentation patterns in parts of northern Egypt. AAPG Bulletin 60:34-64
Sauter EJ, Muyakshin SI, Charlou J-L, Schlüter M, Boetius A, Jerosch K, Damm E, Foucher J-P, Klages M (2006) Methane discharge from a deep-sea submarine mud volcano into the upper water column by gas hydrate-coated methane bubbles. Earth and Planetary Science Letters 243:354-365
Schoell M (1980) The hydrogen and carbon isotopic composition of methane from natural gases of various origins. Geochimica et Cosmochimica Acta 44:649-661
Teichert B, Gussone N, Eisenhauer A, Bohrmann G (2005) Clathrites: Archives of near-seafloor pore-fluid evolution (δ44/40Ca, δ13C, δ18O) in gas hydrate environments. Geology 33:213-216
Torres ME, McManus J, Hammond D, Angelis MAd, Heeschen KU, Colbert SL, Tryon MD, Brown KM, Suess E (2002) Fluid and chemical fluxes in and out of sediments hosting methane hydrate deposits on Hydrate Ridge, OR, I: Hydrological provinces. Earth and Planetary Science Letters 201:525-540
Zitter TAC, Huguen C, Woodside JM (2005) Geology of mud volcanoes in the eastern Mediterranean from combined sidescan sonar and submersible surveys. Deep-Sea Research I 52:457-475

7 Concluding remarks and perspectives

Emissions of gas bubbles are much more common than appreciated so far as illustrated, for instance, in the three areas studied as part of this thesis, where more evidence for gas bubble emissions were found than expected prior to the cruises. The methodology for the detection of gas emissions improved significantly leading to a continuous growing number of findings as reported in the recent literature. Improved techniques for the detection of gas emissions (especially hydroacoustic methods including single beam echosounder, swath echosounder, sidescan sonar) arose within the last years and renewed inspections of areas, where formerly no evidence for gas emissions had been observed, often lead to new discoveries. By using these techniques routinely during research cruises along continental margins a lot more will be learned about the wide variety of gas emissions related to different geological settings.

The three case studies show that gas emissions occur at both types of continental margins: at active margins, like the Makran continental margin, as well as at passive margins, like the paleo-fan system in the Black Sea and the Nile Deep Sea Fan in the Eastern Mediterra-nean. Furthermore, the gas emissions are either widely distributed within the areas (Makran continental margin; Nile Deep Sea Fan) or more intensive than previously considered (Kerch Flare seep area). Although different factors may control the gas migration pathways in the different geological settings, the fact that enough gas is present in the sediments to lead to gas emissions at the seafloor unite the three areas studied here. Furthermore, the source of the gas in all three study areas is biogenic.

The quantification of gas bubble emissions in this thesis significantly enhances the list of reported quantitative methane flux data from a wide variety of geological settings located at continental margins (Table 7-1). Gas emissions at geological structures such as mud volcanoes or individual seep sites range between 0.13×10^6 up to 87×10^6 mol yr^{-1} (Table 7-1). The upper limit with 87×10^6 mol yr^{-1} is very high and was obtained in the study at the Kerch seep area, where the estimation of the flux was connected to large uncertainty. However, the range of values obtained for gas bubble emissions at particular geological structures is similar in the order-of-magnitude as values obtained of fluxes of methane dissolved in advecting porewater (<0.1 $\times 10^6$ up to 14×10^6 mol yr^{-1}). This comparison illustrates that both transport pathways (gas bubble flux and advection of dissolved methane in fluids) need to be considered when estimating the flux of methane from the sediments to the water column.

So far, the estimations of fluxes concentrated on individual geological structures, only very few attempts have been made to quantify fluxes on larger spatial scale. The bubble flux was quantified at larger spatial scale at Coal Oil Point at about 60 m water depth and at Dnepr paleo-fan in an area at 66-832 m water depth using hydroacoustics techniques as central method. These techniques were combined with discrete measurements at the seafloor (Coal Oil Point) or estimation of fluxes based on theoretical considerations of the backscatter target strength caused by the bubbles (Dnepr paleo-fan). The case study at the Makran continental margin at water depth between 300 and 3000 m further increases these large scale estimations by combining hydroacoustics with discrete ROV-based quantifications of bubble streams at the seafloor.

The technique used to quantify gas bubble fluxes by analyses of video material, which was used in this study as well as in prior publications, has been turned out to be an efficient and relatively simply applied method, but provides rather rough estimation of the gas bubble fluxes with large uncertainties. Further improvements like for instance automatization of bubble flux estimation or calibration with sonar systems would probably help to decrease these uncertainties. Nevertheless, it allows an order-of-magnitude estimation and can be used for general comparisons. In addition,

it should be pointed out, that the presented results are based on relatively steady gas bubble emission streams that could be quantified assuming little variations. This is inevitable due to the limited observation time during ROV dives. Evidence for potential short-term violent eruptions or outbursts could only be achieved with long-term monitoring.

Table 7-1: Summary of the methane fluxes published previously and obtained in this study.

Structure	Area	Water depth (m)	Transport pathway to the water column	Flux (10^6 mol CH_4 yr^{-1})	Reference
Flare 1	Makran continental margin	575	gaseous	0.13 (± 0.07)	This study
Flare 2	Makran continental margin	1020	gaseous	5.09 (± 3.31)	This study
Flare 5 Area C	Makran continental margin	2870	gaseous	5.01 (± 3.02)	This study
Vodyanitskii mud volcano	Black Sea	2070	gaseous	0.9 (0.4-1.3)	Sahling et al., 2009
Dvurechenskii mud volcano	Black Sea	2050	dissolved	1.9	Wallmann et al., 2006
				13	Lichtschlag et al., 2010
Kerch seep area	Black Sea	890	gaseous	2.2 - 87	This study
Dnepr paleo-fan	Black Sea	66-832	gaseous	747	Artemov et al., 2007
Håkon Mosby mud volcano	Norwegian Sea	1250	gaseous	6.3 (2.5-11.4)	Sauter et al., 2006
Håkon Mosby mud volcano	Norwegian Sea	1250	dissolved	14	Felden et al., 2010
Carbonate slab C-1	Eastern Mediterranean	1650	gaseous	0.32-1.3	This study
Napoli mud volcano	Eastern Mediterranean	2000	dissolved	0.5-1.3	Wallmann et al., 2006
Milano mud volcano	Eastern Mediterranean	2000	dissolved	0.2-0.7	Wallmann et al., 2006
Kazan mud volcano	Eastern Mediterranean	2000	dissolved	<0.1	Wallmann et al., 2006
Mound culebra	Offshore Costa Rica	1650	dissolved	0.6	Mau et al., 2006
Mound 12	Offshore Costa Rica	1000	dissolved	0.4	Mau et al., 2006
Mound 11	Offshore Costa Rica	1000	dissolved	0.007	Mau et al., 2006
Atalante	Offshore Barbados	5000	dissolved	6.5	Wallmann et al., 2006
Cyclops	Offshore Barbados	5000	dissolved	0.6	Wallmann et al., 2006
GC185	Gulf of Mexico	525 - 550	gaseous	1.97	Leifer and MacDonald, 2003
Hydrate Ridge - Northern Summit	Offshore Oregon	600 - 800	gaseous	21.9	Torres et al., 2002
Tommeliten field	North Sea	65 - 75	gaseous	1.5	Schneider von Deimling et al., 2011
UK Block 15/25	North Sea	167	gaseous	1.1	Hovland and Judd, 1992
Coal Oil Point	Offshore California	60	gaseous	1825 (± 274)	Hornafius et al., 1999

The present knowledge on gas emissions in the ocean is sketch in Figure 7-1. Previous studies as well as the three case studies confirm the widespread bubble flux at tectonically active as well as passive continental margins. Although it was shown that significant amounts of methane are transported as gas bubbles from the sediments to the water column, all three case studies suggest that the gas bubbles dissolve within the water column and that the methane remains in the ocean interior (where it is finally removed by oxidation through microbes). Even though the lifetime of gas bubbles in these deep-water settings is enhanced due to the formation of gas hydrate rims, they rapidly dissolve when reaching the upper boundary of the GHSZ (Fig. 7-1). Hence, the methane emitted at these deep-water gas bubble emission areas does not reach the mixed layer or even the atmosphere and do not contribute to the atmospheric methane inventory. Consequently, the deep-water emissions like those studied in this work do not play a role in climate change. However, as described in the literature and illustrated in Figure 7-1, gas bubble emissions at shallow water depth and emissions of oil-coated bubbles might reach the sea surface and release their residual methane content to the atmosphere. Furthermore, other processes that have been proposed but never observed like gas hydrate rafting could lead to enhanced atmospheric methane input. In light of future global warming, there is the scientific need to pay special attention on shallow water gas emissions: recent evidence for enhanced methane emission due to bottom water warming inducing gas hydrate decomposition has the potential of transporting methane from the seabed to the atmosphere.

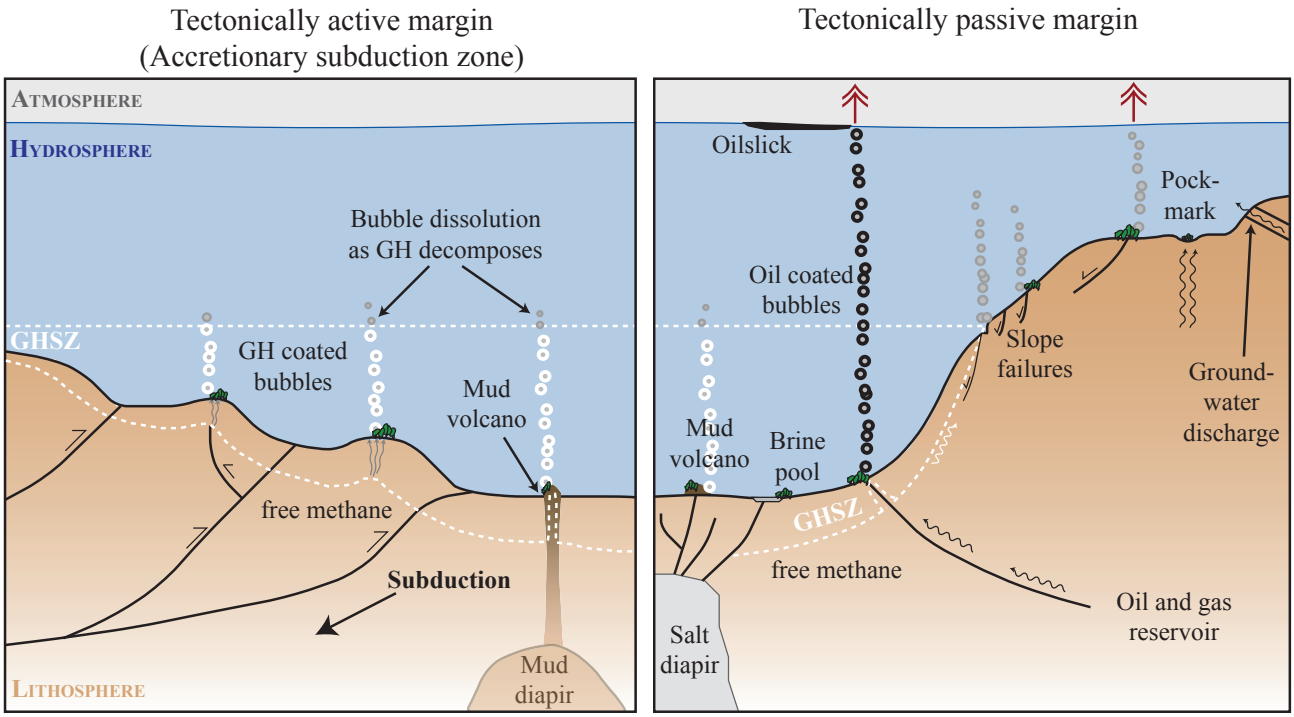

Fig. 7-1: Possible gas emissions at tectonically active (left) and passive (right) continental margins and the different migration pathways. The white dashed like illustrates the GHSZ, where emitting gas bubbles would form hydrate rims preventing them from dissolution. Nevertheless, only very shallow located gas bubble emission or if deeper located only when coated with oil reach the sea surface.

Despite the fact that the transport pathway of methane as gas bubbles from deep-water hydrocarbon seeps may not be relevant for the atmospheric methane inventory, it was shown that the gas bubble migration through the sediments is a significant process in order to understand the manifestation of seepage at the seafloor. For instance, the case study at the Kerch seep area lead to the conclusion that the formation of gas hydrate close to the sediment surface is induced by bubbles rising through sediments. Such shallow hydrate deposits can potentially fuel and stabilize geochemical processes at seeps leading to colonization and growth of abundant chemoautotroph organisms. In conclusion, bubbles rising through the sediments on the one hand by-pass the benthic filter and transport methane into the water column. On the other hand, bubbles may lead to formation of shallow hydrate deposits and thus, provide the basis for unique life of seep biota at the seafloor.

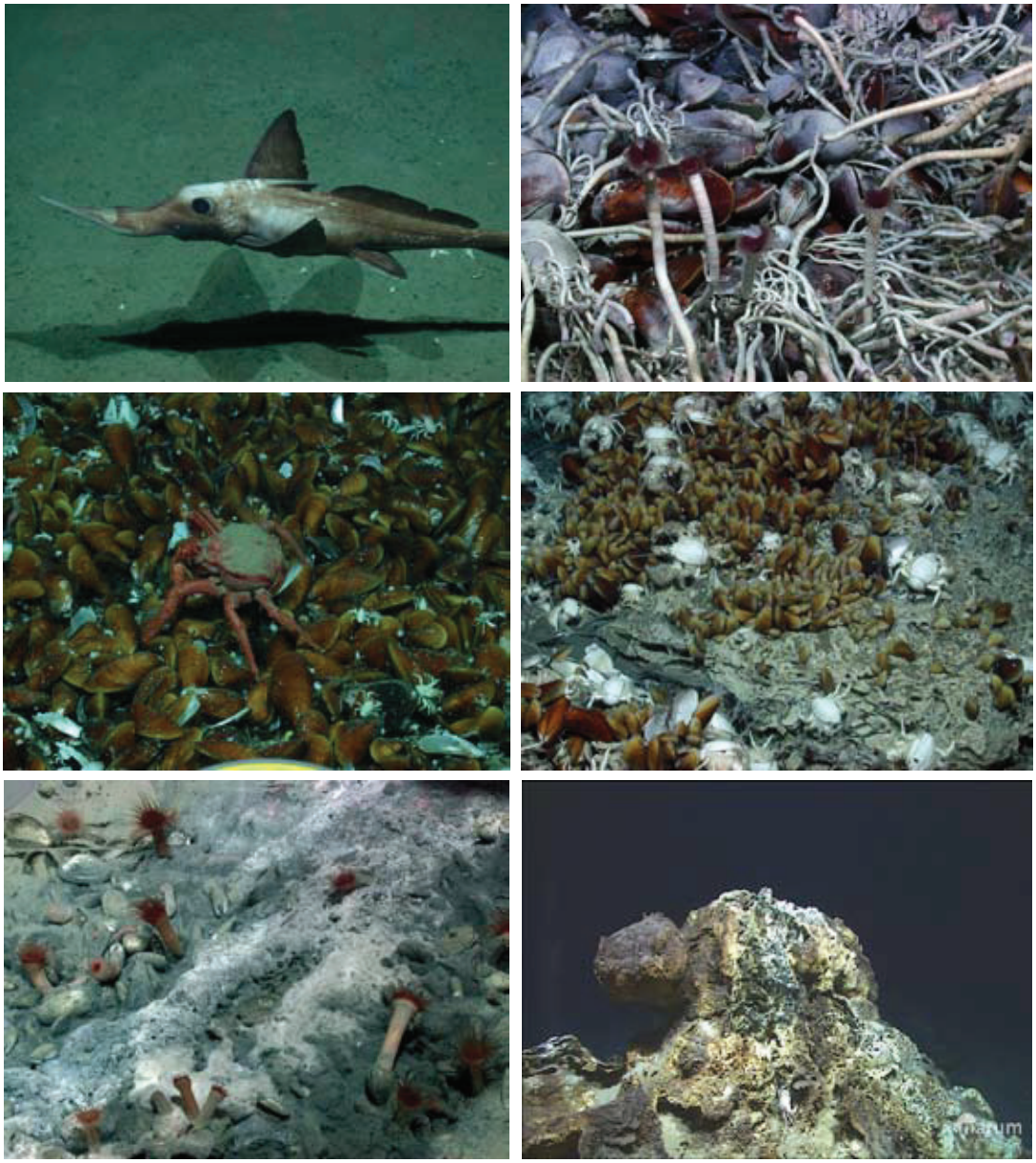

References

Aloisi G, Bouloubassi I, Heijs SK, Pancost RD, Pierre C, Damsté JSS, Gottschal JC, Forney LJ, Rouchy J-M (2002) CH4-consuming microorganisms and the formation of carbonate crusts at cold seeps. Earth and Planetary Science Letters 203:195-203

Aloisi G, Pierre C, Rouchy J-M, Foucher J-P, Woodside J, Party MS (2000) Methane-related authigenic carbonates of eastern Mediterranean Sea mud volcanoes and their possible relation to gas hydrate destabilisation. Earth and Planetary Science Letters 184:321-338

Anderson A, Bryant W (1990) Gassy sediment occurrence and properties: Northern Gulf of Mexico. Geo-Marine Letters 10:209-220-220

Archer D (2007) Methane hydrate stability and anthropogenic climate change. Biogeosciences Discuss. 4:993-1057

Archer D, Buffett B, Brovkin V (2009) Ocean methane hydrates as a slow tipping point in the global carbon cycle. Proceedings of the National Academy of Sciences 106:20596-20601

Artemov YG, Egorov VN, Polikarpov GG, Gulin SB (2007) Methane emission to the hydro-and atmosphere by gas bubble streams in the Dnieper Paleo-delta, the Black Sea Marine. Ecol J 6:5-26

Bahr A, Pape T, Abegg F, Bohrmann G, van Weering T, Ivanov MK (2010) Authigenic carbonates from the eastern Black Sea as an archive for shallow gas hydrate dynamics - Results from the combination of CT imaging with mineralogical and stable isotope analyses. Marine and Petroleum Geology 27:1819-1829

Bahr A, Pape T, Bohrmann G, Mazzini A, Haeckel M, Reitz A, Ivanov M (2009) Authigenic carbonate precipitates from the NE Black Sea: a mineralogical, geochemical, and lipid biomarker study. International Journal of Earth Sciences 98:677-695

Bangs NL, Hornbach MJ, Moore GF, Park JO (2010) Massive methane release triggered by seafloor erosion offshore southwestern Japan. Geology 38:1019-1022

Barg I (2007) Age and origin of the Kerch Strait and the Sea of Azov. Doklady Earth Sciences 412:17-18

Bayon G, Henderson GM, Bohn M (2009a) U-Th stratigraphy of a cold seep carbonate crust. Chemical Geology 260:47-56

Bayon G, Loncke L, Dupré S, Caprais JC, Ducassou E, Duperron S, Etoubleau J, Foucher J-P, Fouquet Y, Gontharet S, Henderson GM, Huguen C, Klaucke I, Mascle J, Migeon S, Olu-Le Roy K, Ondréas H, Pierre C, Sibuet M, Stadnitskaia A, Woodside J (2009b) Multi-disciplinary investigation of fluid seepage on an unstable margin: The case of the Central Nile deep sea fan. Marine Geology 261:92-104

Bernard BB, Brooks JM, Sackett WM (1976) Natural gas seepage in the Gulf of Mexico. Earth and Planetary Science Letters 31:48-54

Berner RA (1980) Early Diagenesis - A Theoretical Approach. Princeton University Press, Princeton

Biastoch A, Treude T, Rüpke LH, Riebesell U, Roth C, Burwicz EB, Park W, Latif M, Böning CW, Madec G, Wallmann K (2011) Rising Arctic Ocean temperatures cause gas hydrate destabilization and ocean acidification. Geophysical Research Letters 38:L08602

Boetius A, Ravenschlag K, Schubert CJ, Rickert D (2000) A marine microbial consortium apparently mediating anaerobic oxidation of methane. Nature 407:623-626

Bohrmann G, Abegg F, Bahr A, Bergenthal M, Brüning M, Brinkmann F, Dentrecolas S, Franke P, Gassner A, Hessler S, Hohnberg H-J, Hüttich D, Illhan T, Klapp S, Kopiske E, Meyer JP, Nikolovska A, Olu-Le Roy K, Pape T, Pollmeyer A, Ratmeyer V, Renken J, Reuter M, Sick E, Suck I, Temel Ö, Trutscheid T, Wladmann C, Wilhelm T, Zarrouk M (2008) Report and preliminary results of R/V Meteor Cruise Report M70/3, Iraklion - Iraklion, 21 November - 8 December 2006. In. Berichte, Fachbereich Geowissenscahften, Universität Bremen, No. 262, Bremen, p 75

Bohrmann G (2007) Report and preliminary results of R/V Meteor cruise report M72/3, Istanbul - Trabzon, 17 March - 23 April, 2007. Marine gas hydrates of the eastern Black Sea. Berichte, Fachbereich Geowissenschaften, Universität Bremen

Bohrmann G (2011a) Report and preliminary results of RV MARIA S. MERIAN Cruise MSM 15/2, Istanbul

(Turkey) - Piraeus (Greece), 10 May - 2 June 2010. Origin and structure of methane, gas hydrates and fluid flows in the Black Sea. Berichte, Fachbereich Geowissenschaften, Universität Bremen

Bohrmann G (2011b) Report and preliminary results of RV METEOR Cruise M84/2, Istanbul Istanbul, 26 February 02 April, 2011. Origin and Distribution of Methane and Methane Hydrates in the Black Sea. Berichte, Fachbereich Geowissenschaften, Universität Bremen

Bohrmann G, Greinert J, Suess E, Torres M (1998) Authigenic carbonates from the Cascadia subduction zone and their relation to gas hydrate stability. Geology 26:647-650

Bohrmann G, Ivanov M, Foucher JP, Spiess V, Bialas J, Greinert J, Weinrebe W, Abegg F, Aloisi G, Artemov Y, Blinova V, Drews M, Heidersdorf F, Krabbenhöft A, Klaucke I, Krastel S, Leder T, Polikarpov I, Saburova M, Schmale O, Seifert R, Volkonskaya A, Zillmer M (2003) Mud volcanoes and gas hydrates in the Black Sea: new data from Dvurechenskii and Odessa mud volcanoes. Geo-Marine Letters 23:239-249

Bohrmann G, Torres M (2006) Gas hydrates in marine sediments. In: Schulz HD, Zabel M (eds) Marine Geochemistry. Springer, pp 481-512

Boles JR, Clark JF, Leifer I, Washburn L (2001) Temporal variation in natural methane seep rate due to tides, Coal Oil Point area, California. J. Geophys. Res 106:27077-27086

Boudreau BP, Algar C, Johnson BD, Croudace I, Reed A, Furukawa Y, Dorgan KM, Jumars PA, Grader AS (2005) Bubble growth and rise in soft sediments. Geology 33:517-520

Brewer PG, Paull C, Peltzer ET, Ussler W, Rehder G, Friederich G (2002) Measurements of the fate of gas hydrates during transit through the ocean water column. Geophysical Research Letters 29

Brüning M, Le Bas T, Murton B, Sahling H, Ding F, Spiess V, Bohrmann G (in prep.) Abundant evidence for hydrocarbon seepage at the Makran continental margin offshore Pakistan. J. Geophys. Res.

Brüning M, Sahling H, MacDonald IR, Ding F, Bohrmann G (2010) Origin, distribution, and alteration of asphalts at Chapopote Knoll, Southern Gulf of Mexico. Marine and Petroleum Geology 27: 1093-1106

Buffett B, Archer D (2004) Global inventory of methane clathrate: sensitivity to changes in the deep ocean. Earth and Planetary Science Letters 227:185-199

Burwicz EB, Rüpke LH, Wallmann K (2011) Estimation of the global amount of submarine gas hydrates formed via microbial methane formation based on numerical reaction-transport modeling and a novel parameterization of Holocene sedimentation. Geochimica et Cosmochimica Acta 75:4562-4576

Byrne DE, Stykes LR, Davis DM (1992) Earthquakes and aseismic slip along the plate boundary of the Makran subduction zone. Journal of Geophysical Research 97:449-478

Campbell KA (2006) Hydrocarbon seep and hydrothermal vent paleoenvironments and paleontology: Past developments and future research directions. Palaeogeography, Palaeoclimatology, Palaeoecology 232:362-407

Caress DW, Chayes DN (1996) Improved processing of Hydrosweep DS multibeam data on the R/V Maurice Ewing. Marine Geophysical Research 18:631-650

Çifçi G, Dondurur D, Ergün M (2003) Deep and shallow structures of large pockmarks in the Turkish shelf, Eastern Black Sea. Geo-Marine Letters 23:311-322

Claypool GE, Kaplan IR (1974) The origin and distribution of methane in marine sediments. In: Kaplan IR (ed) Natural gases in marine sediments, pp 99-139

Claypool GE, Kvenvolden KA (1983) Methane and other Hydrocarbon Gases in Marine Sediment. Annual Review of Earth and Planetary Sciences 11:299-327

Clennell MB, Judd A, Hovland M (2000) Movement and Accumulation of Methane in Marine Sediments: Relation to Gas Hydrate Systems. In: Max MD (ed) Natural Gas Hydrate - in Oceanic and Permafrost Environments. Kluwer Academic

Publishers, Dordrecht (The Netherlands)
Clift P, Vannucchi P (2004) Controls on tectonic accretion versus erosion in subduction zones: implications for the origin and recycling of the continental crust. Review of Geophysics 42
Clift R, Grace JR, Weber ME (1978) Bubble, drops, and particles. Academic Press, New York
Collier JS, Brown CJ (2005) Correlation of sidescan backscatter with grain size distributionof surficial seabed sediments. Marine Geology 214:431-449
D'Ortenzio F, Iudicone D, de Boyer Montegut C, Testor P, Antoine D, Marullo S, Santoleri R, Madec G (2005) Seasonal variability of the mixed layer depth in the Mediterranean Sea as derived from in situ profiles. Geophysical Research Letters 32: L12605
Davy H (1811) On a combination of oxymuriatic gas and oxigen gas. Philosophical Transactions of the Royal Society 101:155
Davy B, Pecher I, Wood R, Carter L, Gohl K (2010) Gas escape features off New Zealand: Evidence of massive release of methane from hydrates. Geophysical Research Letters 37:L21309
De Angelis MA, Baross JA, Lilley MD (1991) Enhanced microbial methane oxidation in water from a deep-sea hydrothermal vent field at simulated in situ hydrostatic pressures. Limnol. Oceanogr. 36:565-570
De Beukelaer SM, MacDonald IR, Guinnasso NL, Murray JA (2003) Distinct side-scan sonar, RADARSAT SAR, and acoustic profiler signitures of gas and oil seeps on the Gulf of Mexico slope. Geo-Marine Letters 23:177-186
De Jong KA (1982) Tectonics of the Persian Gulf, Gulf of Oman, and southern Pakistan region. In: The Ocean Basins and Margins Vol. 6: The Indian Ocean, edited by Nairn AEM and Staehli FG, pp. 315–351, Plenum, New York.
Delisle G (2004) The mud volcanoes of Pakistan. Environmental Geology 46:1024-1029
Delisle G, Berner U (2002) Gas hydrates acting as cap rock to fluid discharge in the Macran accretionary prism? In: Clift PD, Kroon D, Gaedicke C, Craig J (eds) The tectonic and climatic evolution of the Arabian Sea. The Geological Society of London, London, pp 137-146
Delisle G, von Rad U, Andruleit H, von Daniels CH, Tabrez AR, Inam A (2002) Active mud volcanoes on- and offshore eastern Makran, Pakistan. International Journal of Earth Sciences 91:93-110
DeMets C, Gordon RG, Argus DF, Stein S (1990) Current plate motions. Geophys. J. Int. 101(2): 425-478
Dickens GR (2001) The potential volume of oceanic methane hydrates with variable external conditions. Organic Geochemistry 32:1179-1193
Dickens GR (2003) Rethinking the global carbon cycle with a large, dynamic and microbially mediated gas hydrate capacitor. Earth and Planetary Science Letters 213:169-183
Dickens GR (2011) Down the Rabbit Hole: toward appropriate discussion of methane release from gas hydrate systems during the Paleocene-Eocene thermal maximum and other past hyperthermal events. Clim. Past 7:831-846
Dickens GR, O'Neil JR, Rea DK, Owen RM (1995) Dissociation of oceanic methane hydrate as a cause of the carbon isotope excursion at the end of the Paleocene. Paleoceanography 10:965-971
Ding F, Spiess V, Fekete N, Murton B, Brüning M, Bohrmann G (2010) Interaction between accretionary thrust faulting and slope sedimentation at the frontal Markan Accretionary Prism, their resultant shallow sediment structure and some implication for hydrocarbon fluid seepage. Journal of Geophysical Research 115: B08106
Dlugokencky EJ, Nisbet EG, Fisher R, Lowry D (2011) Global atmospheric methane: budget, changes and dangers. Philosophical Transactions of the Royal Society A: Mathematical, Physical and Engineering Sciences 369:2058-2072
Duan Z, Møller N, Weare JH (1992) An equation of state for the CH4-CO2-H2O system: I. Pure systems from 0 to 1000°C and 0 to 8000 bar. Geochemica et Cosmochimica Acta 56:2605-2617
Dubilier N, Bergin C, Lott C (2008) Symbiotic diversity in marine animals: the art of harnessing

chemosynthesis. Nat Rev Micro 6:725-740
Dupré S, Buffet G, Mascle J, Foucher J-P, Gauger S, Boetius A, Marfia C, the AsterX AUV Team, the Quest ROV Team, the BIONIL Scientific Party (2008) High-resolution mapping of large gas emitting mud volcanoes on the Egyptian continental margin (Nile Deep Sea Fan) by AUV surveys. Marine Geophysical Researches 29:275-290
Dupré S, Woodside J, Foucher J-P, de Lange G, Mascle J, Boetius A, Mastalerz V, Stadnitskaia A, Ondréas H, Huguen C, Harmégnies F, Gontharet S, Loncke L, Deville E, Niemann H, Omoregie E, Olu-Le Roy K, Fiala-Medioni A, Dählmann A, Caprais J-C, Prinzhofer A, Sibuet M, Pierre C, Damsté JS (2007) Seafloor geological studies above active gas chimneys off Egypt (Central Nile Deep Sea Fan). Deep Sea Research Part I: Oceanographic Research Papers 54:1146-1172
Dupré S, Woodside J, Klaucke I, Mascle J, Foucher J-P (2010) Widespread active seepage activity on the Nile Deep Sea Fan (offshore Egypt) revealed by high-definition geophysical imagery. Marine Geology 275:1-19
Egorov VN, Polikarpov GG, Giulin SB, Artemov YG, Stokozov NA, Kostova SK (2003) Modern conception about forming-casting and ecological role of methane gas seeps from bottom of the Black Sea. Marine Ecological Journal 2:5-26
Ellouz-Zimmermann N, Battani A, Deville E, Prinzhofer A, Ferrand J (2008) Impact of coeval tectonic and sedimentary-driven tectonics on the development of overpressure cells, on the sealing, and fluid migration - Petroleum potential and environmental risks of the Makran Accretionary Prism in Pakistan. Himalayan Journal of Scienes 5(7): 50-51.
Etiope G, Klusman RW (2002) Geologic emissions of methane to the atmosphere. Chemosphere 49:777-789
Felden J, Wenzhöfer F, Feseker T, Boetius A (2010) Transport and consumption of oxygen and methane in different habitats of the Håkon
Mosby Mud Volcano (HMMV). Limnol. Oceanogr. 55:2366-2380
Feseker T, Brown K, Blanchet C, Scholz F, Nuzzo M, Reitz A, Schmidt M, Hensen C (2010) Active mud volcanoes on the upper slope of the western Nile deep-sea fan – first results from the P362/2 cruise of R/V Poseidon. Geo-Marine Letters 30:169-186
Feseker T, Dählmann A, Foucher JP, Harmegnies F (2009a) In-situ sediment temperature measurements and geochemical porewater data suggest highly dynamic fluid flow at Isis mud volcano, eastern Mediterranean Sea. Marine Geology 261:128-137
Feseker T, Pape T, Wallmann K, Klapp SA, Schmidt-Schierhorn F, Bohrmann G (2009b) The thermal structure of the Dvurechenskii mud volcano and its implications for gas hydrate stability and eruption dynamics. Marine and Petroleum Geology 26:1812-1823
Gaullier V, Mart Y, Bellaiche G, Mascle J, Vendeville BC, Zitter T, Second Leg Prismed IISP (2000) Salt tectonics in and around the Nile deep-sea fan: insights from the PRISMED II cruise. Geological Society, London, Special Publications 174:111-129
Gay A, Lopez M, Berndt C, Séranne M (2007) Geological controls on focused fluid flow associated with seafloor seeps in the Lower Congo Basin. Marine Geology 244:68-92
Gay A, Lopez M, Cochonat P, Séranne M, Levaché D, Sermondadaz G (2006) Isolated seafloor pockmarks linked to BSRs, fluid chimneys, polygonal faults and stacked Oligocene-Miocene turbiditic palaeochannels in the Lower Congo Basin. Marine Geology 226:25-40
Gontharet S, Pierre C, Blanc-Valleron M-M, Rouchy JM, Fouquet Y, Bayon G, Foucher JP, Woodside J, Mascle J, Party TNS (2007) Nature and origin of diagenetic carbonate crusts and concretions from mud volcanoes and pockmarks of the Nile deep-sea fan. Deep-Sea Reseach II 54:1292-1311
Gontharet S, Stadnitskaia A, Bouloubassi I, Pierre C, Damsté JSS (2009) Palaeo methane-seepage history traced by biomarker patterns in a carbonate crust, Nile deep-sea fan (Eastern Mediterranean Sea). Marine Geology 261:105-113
Gordon R, DeMets C (1989) Present day motion at

the Owen Fracture Zone and Dalrymple Trough in the Arabian Sea. J. Geophys. Res. 94: 5560–5570

Grando G, McClay K (2007) Morphotectonics and structural styles in the Macran accretionary prism, offshore Iran. Sedimentary Geology 196:157-179

Granin N, Makarov M, Kucher K, Gnatovsky R (2010) Gas seeps in Lake Baikal – detection, distribution, and implications for water column mixing. Geo-Marine Letters 30:399-409

Greinert J, Artemov Y, Egorov V, De Batist M, McGinnis D (2006) 1300-m-high rising bubbles from mud volcanoes at 2080m in the Black Sea: Hydroacoustic characteristics and temporal variability. Earth and Planetary Science Letters 244:1-15

Greinert J, Bohrmann G, Elvert M (2002) Stromatolithic fabric of authigenic carbonate crusts: result of anaerobic methane oxidation at cold seeps in 4,850 m water depth. International Journal of Earth Sciences 91:698-711

Greinert J, McGinnis DF (2009) Single bubble dissolution model - The graphical user interface SiBu-GUI. Environmental Modelling & Software 24:1012-1013

Haas A, Peckmann J, Elvert M, Sahling H, Bohrmann G (2010) Patterns of carbonate authigenesis at the Kouilou pockmarks on the Congo deep-sea fan. Marine Geology 268:129-136

Haeckel M, Reitz A, Klaucke I, Sahling H (2008) Methane budget of a large gas hydrate province offshore Georgia, Black Sea. In:6th International Conference on Gas Hydrates, Vancouver, British Columbia, Canada

Haeckel M, Suess E, Wallmann K, Rickert D (2004) Rising methane gas bubbles form massive hydrate layers at the seafloor. Geochimica et Cosmochimica Acta 68:4335-4345

Han X, Suess E, Sahling H, Wallmann K (2004) Fluid venting activity on the Costa Rica margin: new results from authigenic carbonates. International Journal of Earth Sciences 93:596-611

Heeschen K, Tréhu A, Collier RW, Suess E, Rehder G (2003) Distribution and height of methane bubble plumes on the Cascadia Margin characterized by acoustic imaging. Geophysical Research Letters 30

Heeschen KU, Collier RW, DeAngelis MA, Suess E, Rehder G, Linke P, Klinkhammer GP (2005) Methane sources, distributions, and fluxes from cold vent sites at Hydrate Ridge, Cascadia Margin. Global Biogeochemical Cycles 19

Hornafius JS, Quigley D, Luyendyk BP (1999) The world's most spectacular marine hydrocarbon seeps(Coal Oil Point, Santa Barbara Channel, California)- Quantification of emissions. Journal of Geophysical Research 104:20,730-720

Hornbach M, Saffer D, Holbrook WS (2004) Critically pressures free-gas reservoirs below gas-hydrate provinces. Nature 427:142-144

Hovland H, Judd AG (1988) Seabed pockmarks and seepages. Graham & Trotman, Oxford

Hovland M (2002) On the self-sealing nature of marine seeps. Continental Shelf Research 22:2387-2394

Hovland M, Judd A, Burke Jr. RA (1993) The global flux of methane from shallow submarine sediments. Chemosphere 26:559-578

Hovland M, Judd AG (1992) The global production of methane from shallow submarine sources. Continental Shelf Research 12:1231-1238

Hsu KJ, Montadert L, Bernoulli D, Cita MB, Erickson A, Garrison RE, Kidd RB, Melieres F, Muller C, Wright R (1977) History of the Mediterranean salinity crisis. Nature 267:399-403

Huguen C, Foucher JP, Mascle J, Ondréas H, Thouement M, Gontharet S, Stadnitskaia A, Pierre C, Bayon G, Loncke L, Boetius A, Bouloubassi I, de Lange G, Caprais JC, Fouquet Y, Woodside J, Dupré S, Party atNS (2009) Menes caldera, a highly active site of brine seepage in the Eastern Mediterranean sea: „In situ" observations from the nautinil expedition (2003). Marine Geology 261:138-152

Hustoft S, Mienert Jr, Bünz S, Nouzé H (2007) High-resolution 3D-seismic data indicate focussed fluid migration pathways above polygonal fault systems of the mid-Norwegian margin. Marine Geology 245:89-106

IPCC report 2007: Climate Change 2007. Cambridge University Press, Cambridge, United Kingdom and New York, NY, USA.

Judd A, Hovland M (2007) Seabed fluid flow. Cambridge University Press, Cambridge

Judd AG (2004) Natural seabed gas seeps as sources of atmosheric methane. Environmental Geology 46:988-996

Katz ME, Pak DK, Dickens GR, Miller KG (1999) The Source and Fate of Massive Carbon Input During the Latest Paleocene Thermal Maximum. Science 286:1531-1533

Kessler JD, Reeburgh WS, Southon J, Seifert R, Michaelis W, Tyler SC (2006) Basin-wide estimates of the input of methane from seeps and clathrates to the Black Sea. Earth and Planetary Science Letters 243:366-375

Kiel S (2009) Global hydrocarbon seep-carbonate precipitation correlates with deep-water temperatures and eustatic sea-level fluctuations since the Late Jurassic. Terra Nova 21:279-284

Klaucke I, Masson DG, Petersen CJ, Weinrebe W, Ranero CR (2008) Multifrequency geoacoustic imaging of fluid escape structures offshore Costa Rica: implications for the quantification of seep processes. Geochemistry Geophysics Geosystems 9

Klaucke I, Sahling H, Weinrebe W, Blinova V, Bürk D, Lursmanashvili N, Bohrmann G (2006) Acoustic investigation of cold seeps offshore Georgia, eastern Black Sea. Marine Geology 231:51-67

Klauda JB, Sandler SI (2005) Global Distribution of Methane Hydrate in Ocean Sediment. Energy & Fuels 19:459-470

Kopf AJ (2002) Significance of mud volcanism. Rev. Geophys 40:1005

Kopp C, Fruehn J, Flueh ER, Reichert C, Kukowski N, Bialas J, LKlaeschen D (2000) Structure of the Makran subduction zone from wide-angle and reflection seismic data. Tectonophysics 329:171-191

Krastel S, Spiess V, Ivanov M, Weinrebe W, Bohrmann G, Shashkin P, Heidersdorf F (2003) Acoustic investigations of mud volcanoes in the Sorokin Trough, Black Sea. Geo-Marine Letters 23:230-238

Kroeger KF, di Primio R, Horsfield B (2011) Atmospheric methane from organic carbon mobilization in sedimentary basins - The sleeping giant? Earth-Science Reviews In Press, Corrected Proof

Kruglyakova R, Gubanov Y, Kruglyakov V, Prokoptsev G (2002) Assessment of technogenic and natural hydrocarbon supply into the Black Sea and seabed sediments. Continental Shelf Research 22:2395-2407

Kukowski N, Schillhorn T, Flueh ER, Huhn K (2000) Newly identified strike-slip plate boundary in the northeastern Arabian Sea. Geology 28:355-359

Kukowski N, Schillhorn T, Huhn K, von Rad U, Husen S, Flueh ER (2001) Morphotectonics and mechanics of the central Makran accretionary wedge off Pakistan. Marine Geology 173:1-19

Kvenvolden KA (1988) Methane hydrate - ″A major reservoir of carbon in the shallow geosphere? Chemical Geology 71:41-51

Kvenvolden KA (1993) Gas hydrates - geological perspective and global change. Rev. Geophys. 31:173-187

Kvenvolden KA (2002) Methane hydrate in the global organic carbon cycle. Terra Nova 14:302-306

Kvenvolden KA, Rogers BW (2005) Gaia's breath--global methane exhalations. Marine and Petroleum Geology 22:579-590

Lascaratos A, Williams RG, Tragou E (1993) A Mixed-Layer Study of the Formation of Levantine Intermediate Water. Journal of Geophysical Research 98:14739-14749

Le Pichon X, Kobayashi K, Crew K-NS (1992) Fluid venting activity within the Eastern Nankai Trough accretionary wedge: A summary of the 1989 Kaiko-Nankai results. Earth and Planetary Science Letters 109:303-318

Leifer I (2010) Characteristics and scaling of bubble plumes from marine hydrocarbon seepage in the Coal Oil Point seep field. J. Geophys. Res. 115: C11014

Leifer I, Asher WE, Farley PJ (1995) A validation study of bubble mediated air-sea gas transfer modeling for trace gases. In: Jähne B, Monahan EC (eds)The third international symposium on air-water gas

transfer, Heidelberg University.Aeon Verlag, pp 269-283

Leifer I, Boles J (2005) Turbine tent measurements of marine hydrocarbon seeps on subhourly timescales. J. Geophys. Res 110

Leifer I, Boles JR, Luyendyk BP, Clark JF (2004) Transient discharges from marine hydrocarbon seeps: spatial and temporal variability. Environmental Geology 46:1038-1052

Leifer I, Clark JF, Chen RF (2000) Modifications of the Local Environment by Natural Marine Hydrocarbon Seeps. Geophysical Research Letters 27:3711-3714

Leifer I, Culling D (2010) Formation of seep bubble plumes in the Coal Oil Point seep field. Geo-Marine Letters 30:339-353

Leifer I, Judd AG (2002) Oceanic methane layers: the hydrocarbon seep bubble deposition hypothesis. Terra Nova 14:417-424

Leifer I, Kamerling M, Luyendyk B, Wilson D (2010) Geologic control of natural marine hydrocarbon seep emissions, Coal Oil Point seep field, California. Geo-Marine Letters 30:331-338

Leifer I, Luyendyk BP, Boles J, Clark JF (2006) Natural marine seepage blowout: Contribution to atmospheric methane. Global Biogeochemical Cycles 20

Leifer I, MacDonald I (2003) Dynamics of the gas flux from shallow gas hydrate deposits: interaction between oily hydrate bubbles and the oceanic environment. Earth and Planetary Science Letters 210:411-424

Leifer I, Patro RK (2002) The bubble mechanism for methane transport from the shallow sea bed to the surface: A review and sensitivity study. Continental Shelf Research 22:2409-2428

Lichtschlag A, Felden J, Wenzhöfer F, Schubotz F, Ertefai TF, Boetius A, de Beer D (2010) Methane and sulfide fluxes in permanent anoxia: In situ studies at the Dvurechenskii mud volcano (Sorokin Trough, Black Sea). Geochimica et Cosmochimica Acta 74:5002-5018

Linke P, Sommer S, Rovelli L, McGinnis D-F (2010) Physical limitations of dissolved methane fluxes: The role of bottom-boundary layer processes. Marine Geology 272:209-222

Liu X, Flemings PB (2006) Passing gas through the hydrate stability zone at southern Hydrate Ridge, offshore Oregon. Earth and Planetary Science Letters 241:211-226

Loncke L, Gaullier V, Bellaiche G, Mascle J (2002) Recent depositional patterns of the Nile deep-sea fan from echo-character mapping. AAPG Bulletin 86:1165-1186

Loncke L, Gaullier V, Droz L, Ducassou E, Migeon S, Mascle J (2009) Multi-scale slope instabilities along the Nile deep-sea fan, Egyptian margin: A general overview. Marine and Petroleum Geology 26:633-646

Loncke L, Gaullier V, Mascle J, Vendeville BC, Camera L (2006) The Nile deep-sea fan: An example of interacting sedimentation, salt tectonics, and inherited subsalt paleotopographic features. Marine and Petroleum Geology 23:297-315

Loncke L, Mascal J, Parties FS (2004) Mud volcanoes, gas chimneys, pockmarks and mounds in the Nile deep-sea fan (Eastern Mediterranean): geophysical evidences. Marine and Petroleum Geology 21:669-689

Lüdmann T, Wong HK, Konerding P, Zillmer M, Petersen J, Flüh E (2004) Heat flow and quantity of methane deduced from a gas hydrate field in the vicinity of the Dnieper Canyon, northwestern Black Sea. Geo-Marine Letters 24:182-193

Luff R, Wallmann K, Aloisi G (2004) Numerical modeling of carbonate crust formation at cold vent sites: significance for fluid and methane budgets and chemosynthetic biological communities. Earth and Planetary Science Letters 221:337-353

Luth U, Luth C, Thiel H (1998) MEGASEEBS - Methane Gas Seep Explorations in the Black Sea. Ber Zentrum Meeres- und Klimaforsch, Univ Hamburg 14:133

Luyendyk B, Kennett J, Clark JF (2005) Hypothesis for increased atmospheric methane input from hydrocarbon seeps on exposed continental shelves during glacial low sea level. Marine and Petroleum Geology 22:591-596

MacDonald IR, I. L, Sassen R, Stine P, Mitchell R, Guinasso Jr. N (2002) Transfer of hydrocarbons

from natural seeps to the water column and atmosphere. Geofluids 2:95-107
Madhupratap M, Kumar SP, Bhattathiri PMA, Kumar MD, Raghukumar S, Nair KKC, Ramaiah N (1996) Mechanism of the biological response to winter cooling in the northeastern Arabian Sea. Nature 384(6609): 549-552
Maini BB, Bishnoi PR (1981) Experimental investigation of hydrate formation behaviour of a natural gas bubble in a simulated deep sea environment. Chemical Engineering Science 36:183-189
Manga M, Brumm M, Rudolph ML (2009) Earthquake triggering of mud volcanoes. Marine and Petroleum Geology 26:1785-1798
Mascle J, Benkhelil J, Bellaiche G, Zitter T, Woodside J, Loncke L, Party PIS (2000) Marine geologic evidence for a Levantine-Sinai plate, a new piece of the Mediterranean puzzle. Geology 28:779-782
Maslin M, Owen M, Betts R, Day S, Dunkley Jones T, Ridgwell A (2010) Gas hydrates: past and future geohazard? Philosophical Transactions of the Royal Society A: Mathematical, Physical and Engineering Sciences 368:2369-2393
Masoudi R, Tohidi B (2005) Estimating the hydrate stability zone in the presence of salts and/or organic inhibitors using water partial pressure. Journal of Petroleum Science and Engineering 46:23-36
Mastalerz V, de Lange GJ, Dählmann A, Feseker T (2007) Active venting at the Isis mud volcano, offshore Egypt: Origin and migration of hydrocarbons. Chemical Geology 246:87-106
Mastalerz V, de Lange GJ, Dählmann A (2009) Differential aerobic and anaerobic oxidation of hydrocarbon gases discharged at mud volcanoes in the Nile deep-sea fan. Science Direct 73:3849-3863
Matthews MD (1996) Migration - a view from the top. In: Schumacher D, Abrams MA (eds) Hydrocarbon migration and its near-surface expression. American Association of Petroleum Geologists Memoir, pp 139-155
Mau S, Sahling H, Rehder G, Suess E, Linke P, Soeding E (2006) Estimates of methane output from mud extrusions at the erosive convergent margin off Costa Rica. Marine Geology 225:129-144
Mazzini A, Ivanov MK, Nermoen A, Bahr A, Bohrmann G, Svensen H, Planke S (2008) Complex plumbing systems in the near subsurface: Geometries of authigenic carbonates from Dolgovskoy Mound (Black Sea) constrained by analogue experiments. Marine and Petroleum Geology 25:457-472
McGinnis DF, Greinert J, Artemov Y, Beaubien SE, Wüest A (2006) Fate of rising methane bubbles in stratified waters: How much methane reaches the atmosphere. Journal of Geophysical Research 111
Meisner A, Krylov O, Nemcok M (2009) Development and structural architecture of the Eastern Black Sea. The Leading Edge 28:1046-1055
Merewether R, Olsson MS, Lonsdale P (1985) Acoustically detected hydrocarbon plumes rising from 2-km depths in Guaymas Basin, Gulf of California. Journal of Geophysical Reseach 90:3075-3085
Michaelis W, Seifert R, Neuhaus K, Treude T, Thiel V, Blumenberg M, Knittel K, Gieseke A, Peterknecht K, Pape T, Boetius A, Amann R, Jorgensen BB, Widdel F, Peckmann J, Pimenov NV, Gulin MB (2002) Microbial reefs in the Black Sea fueled by anaerobic oxidation of methane. Science 297:1013-1015
Milkov AV (2004) Global estimates of hydrate-bound gas in marine sediments: how much is really out there? Earth-Science Reviews 66:183-197
Milkov AV, Dickens GR, Claypool GE, Lee Y-J, Borowski WS, Torres ME, Xu W, Tomaru H, Tréhu AM, Schultheiss P (2004) Co-existance of gas hydrate, free gas, and brine within the regional gas hydrate stability zone at Hydrate Ridge (Oregon margin): evidence from prolonged degassing of a pressurized core. Earth and Planetary Science Letters 222:829-843
Milkov AV, Dzou L (2007) Geochemical evidence of secondary microbial methane from very slight biodegradation of undersaturated oils in a deep hot reservoir. Geology 35:455-458
Minshull TA, White R (1989) Sediment compaction and fluid migration in the Makran accretionary

prism. Journal of Geophysical Research 94:7387-7402

Naehr TH, Rodriguez NM, Bohrmann G, Paull CK, Botz R (2000) Methane-derived authigenic carbonates associated with gas hydrate decomposition and fluid venting above the Blake Ridge Diapir. In: PAull CK, Matsumoto R, Wallace PJ, Dillon WP (eds) Proceedings of the Ocean Drilling Program, Scientific Results, pp 285-300

Naudts L, De Batist M, Greinert J, Artemov Y (2009) Geo- and hydro-acoustic manifestations of shallow gas and gas seeps in the Dnepr paleodelta, northwestern Black Sea. The Leading Edge 28:1030-1040

Naudts L, Greinert J, Artemov Y, Beaubien SE, Borowski C, Batist MD (2008) Anomalous sea-floor backscatter patterns in methane venting areas, Dnepr paleo-delta, NW Black Sea. Marine Geology 251:253-267

Naudts L, Greinert J, Artemov Y, Staelens P, Poort J, Van Rensbergen P, De Batist M (2006) Geological and morphological setting of 2778 methane seeps in the Dnepr paleo-delta, northwestern Black Sea. Marine Geology 227:177-199

Naudts L, Greinert J, Poort J, Belza J, Vangampelaere E, Boone D, Linke P, Henriet J-P, De Batist M (2010) Active venting sites on the gas-hydrate-bearing Hikurangi Margin, off New Zealand: Diffusive- versus bubble-released methane. Marine Geology 272:233-250

Niemann H, Fischer D, Graffe D, Knittel K, Montiel A, Heilmayer O, Nöthen K, Pape T, Kasten S, Bohrmann G, Boetius A, Gutt J (2009) Biogeochemistry of a low-activity cold seep in the Larsen B area, western Weddell Sea, Antarctica. Biogeosciences 6:2383-2395

Nikishin AM, Korotaev MV, Ershov AV, Brunet M-F (2003) The Black Sea basin: tectonic history and Neogene-Quaternary rapid subsidence modelling. Sedimentary Geology 156:149-168

Nikolovska A, Sahling H, Bohrmann G (2008) Hydroacoustic methodology for detection, localization, and quantification of gas bubbles rising from the seafloor at gas seeps from the Black Sea. Geochemistry, Geophysics, Geosystems 9

Nisbet EG, Chappellaz J (2009) Shifting Gear, Quickly. Science 324:477-478

Oaie G, Secrieru D, Shimus K (2005) Black Sea Basin: Sediment types and distribution, sedimentation processes. Geo-Eco-Marina 9-10:21-30

Orange DL, Yun J, Maher N, Barry J, Greene G (2002) Tracking California seafloor seeps with bathymetry, backscatter and ROVs. Continental Shelf Research 22:2273-2290

Ostrovsky I, McGinnis DF, Lapidus L, Eckert W (2008) Quantifying gas ebullition with echosounder: the role of methane transport by bubbles in a medium-sized lake. Limnology and Oceanography: Methods 6:105-118

Özsoy E, Ünlüata Ü (1997) Oceanography of the Black Sea: a review of some recent results. Earth-Sciece Reviews 42:231-272

Pape T, Bahr A, Klapp SA, Abegg F, Bohrmann G (2011a) High-intensity gas seepage causes rafting of shallow gas hydrates in the southeastern Black Sea. Earth and Planetary Science Letters 307:35-46

Pape T, Bahr A, Rethemeyer J, Kessler JD, Sahling H, Hinrichs K-U, Klapp SA, Reeburgh WS, Bohrmann G (2010a) Molecular and isotopic partitioning of low-molecular-weight hydrocarbons during migration and gas hydrate precipitation in deposits of a high-flux seepage site. Chemical Geology 269:350-363

Pape T, Feseker T, Kasten S, Fischer D, Bohrmann G (2011b) Distribution and abundance of gas hydrates in near-surface deposits of the Håkon MosbyMud Volcano, SW Barents Sea. Geochemistry, Geophysics, Geosystems 12: Q09009

Pape T, Kasten S, Zabel M, Bahr A, Abegg F, Hohnberg H-J, Bohrmann G (2010b) Gas hydrates in shallow deposits of the Amsterdam mud volcano, Anaximander Mountains, Northeastern Mediterranean Sea. Geo-Marine Letters 30:187-206

Patro R, Leifer I, Bowyer P (2002) Better Bubble Process Modeling: Improved Bubble Hydrodynamics Parameterization. Geophysical Monograph-American Geophysical Union 127:315-320

Paull CK, Brewer PG, Ussler III W, Peltzer ET, Rehder G, Clague D (2003) An experiment demonstrating that marine slumping is a mechanism to transfer methane from seafloor gas-hydrate deposits into the upper ocean and atmosphere. Geo-Marine Letters 22:198-203

Paull CK, Ussler WI, Borowski WS, Spiess FN (1995) Methane-rich plumes on the Carolina continental rise: Associations with gas hydrates. Geology 23:89-92

Pecher IA (2002) Oceanography: Gas hydrates on the brink. Nature 420:622-623

Platt JP, Leggett JK, Young J, Raza H, S. A (1985) Large-scale sediment underplating in the Makran accretionary prism, southwest Pakistan. Geology 13:507-511

Platt U, Allan W, Lowe D (2004) Hemispheric average Cl atom concentration from 13C/12C ratios in atmospheric methane. Atmospheric Chemistry and Physics 4:2393-2399

Poort J, Kutas RI, Klerkx J, Beaubien SE, Lombardi S, Dimitrov L, Vassilev A, Naudts L (2007) Strong heat flow variability in an active shallow gas environment, Dnepr palaeo-delta, Black Sea. Geo-Mar Letters 27:185-195

Popescu I, Lericolais G, Panin N, De Batist M, Gillet H (2007) Seismic expression of gas and gas hydrates across the western Black Sea. Geo-Mar Letters 27:173-183

Quigley DC, Hornafius JS, Luyendyk BP, Francis RD, Clark J, Washburn L (1999) Decrease in natural marine hydrocarbon seepage near Coal Oil Point, California, associated with offshore oil production. Geology 27: 1047-1050

Reagan MT, Moridis GJ (2009) Large-scale simulation of methane hydrate dissociation along the West Spitsbergen Margin. Geophysical Research Letters 36:L23612

Reeburgh WS (2007) Oceanic methane biogeochemistry. Chemical Reviews 107:486-513

Reeburgh WS, Ward BB, Whalen SC, Sandbeck KA, Kilpatrick KA, Kerkhof LJ (1991) Black Sea methane geochemistry. Deep-Sea Research I 38:1,189-181,210

Rehder G, Brewer PW, Peltzer ET, Friederich G (2002a) Enhanced lifetime of methane bubble streams within the deep ocean. Geophysical Research Letters 29:1731-1734

Rehder G, Brewer PW, Peltzer ET, Friedrich G (2002b) Enhanced lifetime of methane bubble streams within the deep ocean. Geophysical Research Letters 29

Rehder G, Leifer I, Brewer PG, Friederich G, Peltzer ET (2009) Controls on methane bubble dissolution inside and outside the hydrate stability field from open ocean field experiments and numerical modeling. Marine Chemistry 114:19-30

Reilinger RE, McClusky SC, Oral MB, King RW, Toksoz MN, Barka AA, Kinik I, Lenk O, Sanli I (1997) Global Positioning System measurements of present-day crustal movements in the Arabia-Africa-Eurasia plate collision zone. J. Geophys. Res. 102:9983-9999

Rice DD, Claypool GE (1981) Generation, accumulation, and resource potential of biogenic gas. AAPG Bulletin 65:5-25

Ritger S, Carson B, Suess E (1987) Methane-derived authigenic carbonates formed by subduction-induced pore-water expulsion along the Oregon/Washington margin. Geological Society of America Bulletin 98:147-156

Robinson AG, Rudat JH, Banks CJ, Wiles RLF (1996) Petroleum geology of the Black Sea. Marine and Petroleum Geology 13:195-223

Römer M, Sahling H, Pape T, Bahr A, Wintersteller P, Bohrmann G (submitted-a) Geological control and quantity of gas bubbles emanating from a high-flux seep area in the Black Sea - The Kerch-Flare. Marine Geology

Römer M, Sahling H, Pape T, Spiess V, Bohrmann G (submitted-b) Gas bubble emission from submarine hydrocarbon seeps at the Makran continental margin (offshore Pakistan). Journal of Geophysical Reseach

Ross DA, Degens ET (1974) Recent sediments of Black Sea. In: Degens ET, Ross DA (eds) The Black Sea - Geology, chemistry, and biology. American Association of Petroleum Geologists, pp 183-199

Ruppel C, Dickens GR, Castellini DG, Gilhooly W, Lizarralde D (2005) Heat and salt inhibition of gas hydrate formation in the northern Gulf of Mexico. Geophysical Research Letters 32

Ryan WBF (1978) Messinian badlands on the southeastern margin of the Mediterranean Sea. Marine Geology 27:349-363

Sager WW, MacDonald IR, Hou R (2003) Geophysical signatures of mud mounds at hydrocarbon seeps on the Louisiana continental slope, northern Gulf of Mexico. Marine Geology 198:97-132

Sahling H, Bohrmann G, Artemov YG, Bahr A, Brüning M, Klapp SA, Klaucke I, Kozlova E, Nikolovska A, Pape T, Reitz A, Wallmann K (2009) Vodyanitskii mud volcano, Sorokin trough, Black Sea: Geological characterization and quantification of gas bubble streams. Marine and Petroleum Geology 26:1799-1811

Sahling H, Bohrmann G, Spiess V, Bialas J, Breitzke M, Ivanov M, Kasten S, Krastel S, Schneider R (2008a) Pockmarks in the Northern Congo Fan area, SW Africa: Complex seafloor features shaped by fluid flow. Marine Geology 249:206-225

Sahling H, Masson DG, Ranero CR, Hühnerbach V, Weinrebe W, Klaucke I, Bürk D, Brückmann W, Suess E (2008b) Fluid seepage at the continental margin offshore Costa Rica and southern Nicaragua. Geochemistry Geophysics Geosystems 9

Sahling H, Rickert D, Lee RW, Linke P, Suess E (2002) Macrofaunal community structure and sulfide flux at gas hydrate deposits from the Cascadia convergent margin, NE Pacific. Marine Ecology Progress Series 231:121-138

Salem R (1976) Evolution of Eocene-Miocene sedimentation patterns in parts of northern Egypt. AAPG Bulletin 60:34-64

Sauter EJ, Muyakshin SI, Charlou J-L, Schlüter M, Boetius A, Jerosch K, Damm E, Foucher J-P, Klages M (2006) Methane discharge from a deep-sea submarine mud volcano into the upper water column by gas hydrate-coated methane bubbles. Earth and Planetary Science Letters 243:354-365

Schmale O, Greinert J, Rehder G (2005) Methane emission from high-intensity marine gas geeps in the Black Sea into the atmoshere. Geophysical Research Letters 32

Schmale O, Haeckel M, McGinnis DF (2011) Response of the Black Sea methane budget to massive short-term submarine inputs of methane. Biogeosciences Discuss. 7:9117-9136

Schmuck EA, Paull CK (1993) Evidence for gas accumulation associated with diapirism and gas hydrates at the head of the Cape Fear Slide. Geo-Marine Letters 13:145-152

Schneider von Deimling J, Rehder G, Greinert J, McGinnnis DF, Boetius A, Linke P (2011) Quantification of seep-related methane gas emissions at Tommeliten, North Sea. Continental Shelf Research 31:867-878

Schoell M (1980) The hydrogen and carbon isotopic composition of methane from natural gases of various origins. Geochimica et Cosmochimica Acta 44:649-661

Shakova N, Semiletov I, Salyuk A, Yusupov V, Kosmach D, Gustafsson Ö (2010) Extensive methane venting to the atmosphere from sediments of the east Siberian Arctic shelf. Science 327:1246-1250

Shipley TH, Housten MH, Buffler RT, Shaub FJ, McMillen KJ, Ladd JW, Worzel JL (1979) Seismic evidence for widespread possible gas hydrate horizons on continental slopes and rises. Am. Assoc. Petrol. Bull. 63:2204-2213

Sloan EDj (1998) Physical/chemical properties of gas hydrates and application to world margin stability and climatic change. In: Henriet JP, Mienert J (eds) Gas Hydrates: Relevance to World Margin Stability and Climate Change. Geological Society, London, pp 31-50

Smith WHF, Sandwell DT (1997) Global Sea Floor Topography from Satellite Altimetry and Ship Depth Soundings. Science 277:1956-1962

Solomon EA, Kastner M, MacDonald IR, Leifer I (2009) Considerable methane fluxes to the atmosphere from hydrocarbon seeps in the Gulf of Mexico. Nature Geoscience 2:561-565

Sommer S, Pfannkuche O, Linke P, Luff R, Greinert J, Drews M, Gubsch S, Pieper M, Poser M, Viergutz T (2006) Efficiency of the benthic filter: Biological

control of the emission of dissolved methane from sediments containing shallow gas hydrates at Hydrate Ridge. Global Biogeochemical Cycles 20

Spielhagen RF, Werner K, Sørensen SA, Zamelczyk K, Kandiano E, Budeus G, Husum K, Marchitto TM, Hald M (2011) Enhanced Modern Heat Transfer to the Arctic by Warm Atlantic Water. Science 331:450-453

Stadnitskaia A, Ivanov MK, Poludetkina EN, Kreulen R, van Weering TCE (2008) Sources of hydrocarbon gases in mud volcanoes from the Sorokin Trough, NE Black Sea, based on molecular and carbon isotopic compositions. Marine and Petroleum Geology 25:1040-1057

Starostenko VI, Rusakov OM, Shnyukov EF, Kobolev VP, Kutas RI (2010) Methane in the northern Black Sea: characterization of its geomorphological and geological environments. Geological Society, London, Special Publications 340:57-75

Suess E (2010) Marine cold seeps. In: Timmis KN (ed) Handbook of hydrocarbon and lipid microbiology. Springer-Verlag, Berlin Heidelberg, pp 187-203

Suess E, Torres ME, Bohrmann G, Collier RW, Greinert J, Linke P, Rehder G, Trehu A, Wallmann K, Winckler G, Zuleger E (1999) Gas hydrate destabilization: enhanced dewatering, benthic material turnover and large methane plumes at the Cascadia convergent margin. Earth and Planetary Science Letters 170:1-15

Suess E, Torres ME, Borhmann G, Collier RW, Rickert D, Goldfinger C, Linke P, Heuser A, Sahling H, Heeschen K, Jung Cm, Nakamura K, Greinert J, Pfannkuche O, Trehu A, Klinkhammer G, Whitecar M, Eisenhauer A, Techert B, Elvert M (2001) Sea Floor Methane Hydrates at Hydrate Ridge, Cascadia Margin. Natural Gas Hydrates - Occurence, Distribution and Detection (ed. C. K. Paull and W. P. Dillon) Amerikan Geophysical Union:87-99

Teichert B, Gussone N, Eisenhauer A, Bohrmann G (2005a) Clathrites: Archives of near-seafloor pore-fluid evolution (δ44/40Ca, δ13C, δ18O) in gas hydrate environments. Geology 33:213-216

Teichert BMA, Bohrmann G, Suess E (2005b) Chemoherms on Hydrate Ridge: Unique microbially-mediated carboante build-ups growing into the water column. Palaeogeography, Palaeoclimatology, Palaeoecology 227:67-85

Tissot BP, Welte Dh (1984) Petroleum formation and occurrence. Springer-Verlag, Berlin

Torres ME, McManus J, Hammond D, Angelis MAd, Heeschen KU, Colbert SL, Tryon MD, Brown KM, Suess E (2002) Fluid and chemical fluxes in and out of sediments hosting methane hydrate deposits on Hydrate Ridge, OR, I: Hydrological provinces. Earth and Planetary Science Letters 201:525-540

Torres ME, Teichert BMA, Tréhu A, Borowski W, Tomaru H (2004a) Relationship of pore water freshening to accretionary processes in the Cascadia margin: Fluid sources and gas hydrate abundance. Geophysical Research Letters 31

Torres ME, Wallmann K, Tréhu AM, Bohrmann G, Borowski WS, Tomaru H (2004b) Gas hydrate growth, methane transport, and chloride enrichment at the southern summit of Hydrate Ridge, Cascadia margin off Oregon. Earth and Planetary Science Letters 226:225-241

Tréhu AM, Long PE, Torres ME, Bohrmann G, R. RF, Collett TS, Goldberg DS, Milkov AV, Riedel M, Schultheiss P, Bangs NL, Barr SR, Borowski WS, Claypool GE, Delwiche ME, Dickens GR, Gracia E, Guerin G, Holland M, Johnson JE, Lee Y-J, Liu C-S, Su X, Teichert B, Tomaru H, Vanneste M, Watanabe M, Weinberger JL (2004) Three-dimensional distribution of gas hydrate beneath southern Hydrate Ridge: constraints from ODP Leg 204. Earth and Planetary Science Letters 222:845-862

Tryon MD, Brown KM, Torres ME (2002) Fluid and chemical flux in and out of sediments hosting methane hydrate deposits on Hydrate Ridge, OR, II: Hydrological processes. Earth and Planetary Science Letters 201:541-557

Tugolesov DA, Gorshkov AS, Meysner LB, Soloviov VV, Khakhalev EM, Akilova YV, Akentieva GP, Gabidulina TI, Kolomeytseva SA, Kochneva TY, Pereturina IG, Plashihina IN (1985) Tectonics of the Mesozoic Sediments of the Black Sea Basin. In: Nedra, Moscow, p 215

Valentine DL, Blanton DC, Reeburgh WS, Kastner M

(2001) Water column methane oxidation adjacent to an area of active hydrate dissociation, Eel river Basin. Geochimica et Cosmochimica Acta 65:2633-2640

Vandré C, Cramer B, Gerling P, Winsemann J (2007) Natural gas formation in the western Nile delta (Eastern Mediterranean): Thermogenic versus microbial. Organic Geochemistry 38:523-539

Vassilev A, Dimitrov L (2002) Spatial and quantity evaluation of the Black Sea gas hydrates. Russian Geology and Geophysics 43:637-649

Villinger H, Davis EE (1987) A New Reduction Algorithm for Marine Heat Flow Measurements. J. Geophys. Res. 92(B12): 12846-12856.

von Huene R, Scholl DW (1991) Observations at convergent margins concerning sediment subduction, subduction erosion, and the growth of continental crust. Reviews of Geophysics 29:279-316

von Rad U, Berner U, Delisle G, Doose-Rolinski H, Fechner N, Linke P, Lückge A, Roeser HA, Schmaljohann R, Wiedicke M, Parties SS (2000) Gas and fluid venting at the Makran accretionary wedge off Pakistan. Geo-Marine Letters 20:10-19

von Rad U, Rösch H, Berner U, Geyh M, Marchig V, Schulz H (1996) Authigenic carbonates derived from oxidized methane vented from the Makran accretionary prism off Pakistan. Marine Geology 136:55-77

Wagner-Friedrichs M (2007) Seafloor seepage in the Black Sea: Mud volcanoes, seeps and diapiric structures imaged by acoustic methods. In: Fachbereich Geowissenschaften. University of Bremen, Bremen, p 154

Wallmann K, Burwicz E, Ruepke L, Marquardt M, Pinero E, Haeckel M, Hensen C (2011) Constraining the global inventory of methane hydrate in marine sediments. Proceedings of the 7th International Confernce on Gas Hydrates (ICGH 2011)

Wallmann K, Drews M, Aloisi G, Bohrmann G (2006) Methane discharge into the Black Sea and the global ocean via fluid flow through submarine mud volcanoes. Earth and Planetary Science Letters 248:545-560

Wessel P, Smith WHF (1991) Free software helps map and display data. Eos Transactions AGU 72:441

Westbrook GK, Reston TJ (2002) The accretionary complex of the Mediterranean Ridge: tectonics, fluid flow and the formation of brine lakes - an introduction to the special issue of Marine Geology. Marine Geology 186:1-8

Westbrook GK, Thatcher KE, Rohling EJ, Piotrowski AM, Pälike H, Osborne AH, Nisbet EG, Minshull EA, Lanoisellé M, James RH, Hühnerbach V, Green D, Fisher RE, Crocker AJ, Chabert A, Bolton C, Beszczynska-Möller A, Berndt C, Aquilina A (2009) Escape of methane gas from the seabed along the west Spitsbergen continental margin. Geophysical Research Letters 36:L15608

White RS (1977) Seismic bright spots in the Gulf of Oman. Earth and Planetary Science Letters 37:29-37

White RS (1979) Gas hydrate layers trapping free gas in the Gulf of Oman. Earth and Planetary Science Letters 42:114-120

White RS, Louden KE (1983) The Makran continental margin: structure of a thickly sedimented convergent plate boundary. Bulletin of the American Association of Petroleum Geologists 34:499-518

Whiticar MJ (1990) A geochemial perspective of natural gas and atmospheric methane. Organic Geochemistry 16:531-547

Whiticar MJ (1999) Carbon and hydrogen isotope systematics of bacterial formation and oxidation of methane. Chemical Geology 161:291-314

Whiticar MJ, Faber E, Schoell M (1986) Biogenic methane formation in marine and freshwater environments: CO2 reduction vs. Acetate fermentation - Isotope evidence. Geochimica et Cosmochimica Acta 50:693-709

Wiedicke M, Neben S, Spiess V (2001) Mud volcanoes at the front of the Makran accretionary complex, Pakistan. Marine Geology 172:57-73

Wiggert JD, Hood RR, Banse K, Kindle JC (2005) Monsoon-driven biogeochemical processes in the Arabian Sea. Progress In Oceanography 65(2-4): 176-213

Wood WT, Gettrust JF, Chapman NR, Spence GD, Hyndman RD (2002) Decreased stability of methane hydrates in marine sediments owing to phase-boundary roughness. Nature 420:656-660

Wuebbles DJ, Hayhoe K (2002) Atmospheric methane and global change. Earth-Science Reviews 57:177-210

Zhang Y (2003) Methane escape from gas hydrate systems in marine environment, and methan-driven oceanic eruption. Geophysical Research Letters 30:1398-1401

Zitter TAC, Huguen C, Woodside JM (2005) Geology of mud volcanoes in the eastern Mediterranean from combined sidescan sonar and submersible surveys. Deep-Sea Research I 52:457-475

Zonenshayn LP, Murdmaa IO, Baranov BV, Kuznetsov AP, Kuzin VS, Kuz'min MI, Avdeyko GP, Stunzhas PA, Lukashin VN, Barash MS, Valyashko GM, Demina LL (1987) An underwater gas source in the Sea of Okhotsk west of Paramushir island. Oceanology 27:598-602

Danksagung

Die drei vergangenen Jahre waren sehr spannend, lehrreich und eine große Herausforderung für mich, die ich ohne die Unterstützung von einigen ganz besonderen Menschen sicher nicht so hätte abschließen können. Die so abwechslungsreiche Arbeit und besonders die intensiven Zeiten und interdisziplinären wissenschaftlichen Austäusche während der Forschungsfahrten machen diese Phase unvergesslich und so ist mir die Zeit, seit ich in Bremen dieser tollen Arbeit nachgehen darf, wie im Fluge vergangen.

Dass ich überhaupt diese Möglichkeit erhalten habe, diese Arbeit zu machen, ist meinem Betreuer Gerhard Bohrmann zu verdanken, der mich nicht kannte aber trotzdem daran glaubte, dass ich diese Arbeit machen könne und mich einstellte, obwohl ich aus einem ganz anderen wissenschaftlichen Gebiet kam. Und inzwischen weiß ich, dass es einen lernhungrigen jungen Wissenschaftler kaum hätte besser treffen können, als in seiner Arbeitsgruppe zu landen. Gerhard hat mir immer das Gefühl gegeben hinter mir zu stehen und einen wichtigen Beitrag zu leisten. Sein Vertrauen und seine Anerkennung sind nicht zuletzt die Motivation die mich antreibt und mir dazu auch noch den Spaß an der Forschung vermittelt.
Als meinen Zweit-Gutachter möchte ich als nächstes Herrn Prof. Heinrich Villinger dafür danken, dass er sich des Gutachtens angenommen hat und zudem den Eindruck vermittelt hat, er freue sich darauf meine Arbeit zu lesen und zu begutachten.
Des weiteren danke ich dem `MARUM - Center for Marine environmental sciences´, das diese Arbeit finanziert und somit letztendlich erst möglich gemacht hat. Zudem bietet das MARUM ein ideales Umfeld indem unterschiedlichste Bereiche aus dem Feld der marinen Wissenschaften geballt sind und zudem zahlreiche Forschungsmethoden zur Verfügung stehen.

Ohne die Betreuung und Unterstützung von Heiko Sahling wäre diese Arbeit ganz bestimmt nicht zustande gekommen. Es war seine initiale Grundidee und ich kann mich wirklich sehr glücklich schätzen, dass ich daran teilnehmen und von ihm lernen darf. Neben den essentiellen Wissensinhalten hat er mir versucht klar zu machen, was noch alles zum wissenschaftlichen Arbeiten dazu gehört und mich immer wieder ermutigt und bestärkt.
Als weitere sehr große Hilfe für meine Arbeit möchte ich Thomas Pape sehr danken. Thomas nimmt sich immer für einen Zeit, wenn es ihm möglich ist, und leistet mit vielen wichtigen kritischen Diskussionen und Erklärungen einen ganz wichtigen Beitrag zu meinem wissenschaftlichen Verständnis.

Ein sehr großes Dankeschön geht an Raum 1050, denn die Arbeit hätte wohl kaum so viel Spaß gemacht, wären da nicht David und Morten (und seit ein paar Monaten nun auch Tingting) mit mir durch die vielen anstrengenden aber auch fröhlichen Tage gegangen.

Neben der Unterstützung einzelner, ist vor allem der Zusammenhalt innerhalb der Arbeitsgruppe einer der wichtigsten Faktoren, die die gesamte Arbeitsstimmung beeinflussen. In der Arbeitsgruppe Bohrmann wird sich nicht nur gegenseitig unterstützt, die Gruppenzusammenstellung ermöglicht zudem einen konstruktiven und effektiven Austausch. Es ist vor allem dieser Rahmen als Grundvoraussetzung der jeden einzelnen in der Gruppe bestärkt und fördert. Dazu zählen auch nicht zuletzt Angelika und Greta, die uns sozusagen den Rücken freihalten und helfen die Formalitäten in den Griff zu bekommen. Und auch Jan-Hendrik, Yann, Tobias, Jiangong, Michal, Stephan, Markus, Aki , die alle dazu beitragen, dass viel diskutiert und hinterfragt wird. Genauso auch unsere Gäste wie Falin, You-Ren, Tatjana und Alexander, mit denen immer neuer Wind in die Arbeitsgruppe kommt und vor allem immer dazu Anlass gibt, auch mal wieder beisammen zu sitzen und Kuchen zu essen.
Einen großen Dank an Christian und Paul für die vielen schönen grids. Auch die sind eine wichtige Grundlage wo sie doch oftmals noch unsere einzige Informationsquelle vom Meeresgrund in der Tiefsee

darstellen, wo visuelle Eindrücke bislang fehlen.
Außerdem möchte ich gern den fleißigen Studentischen Hilfskräften danken, ohne die es zeitlich wohl nicht schaffbar gewesen wäre, alle Daten auszuwerten und zu bearbeiten. Vor allem Inga und Carmen danke ich für viele viele Stunden Video-Auswertungen und hoffe sehr, es führte nicht dazu, dass die beiden nun kein Sekt mehr trinken können oder Whirlpoole meiden müssen. Auch Marten und Steffi möchte ich danken, für euer großes Engagement beim Prozessieren der hydroakustischen Daten sowohl während der Ausfahrt als auch darauf zurück in Bremen.

Die intensivsten Eindrücke und Lernprozesse hatte ich auf den Ausfahrten und ich möchte mich daher bei vielen Mitstreitern an Bord für diese tollen Erfahrungen bedanken:
Zum einen der Crew von R/V Maria S. Merian und auch der von R/V Meteor. Das erfolgreiche Arbeiten an Bord hängt zu einem enormen Teil an der guten Zusammenarbeit von uns auf der wissenschaftlichen Seite mit den Kapitänen und Crew-Mitgliedern auf den Schiffen ab und ich habe nur positive Erfahrungen bisher in dieser Hinsicht gemacht. Auch den zahlreichen Crew-Mitgliedern des MARUM, die die technischen Großgeräte wie ROV, AUV und MeBo an Bord bedient haben, möchte ich für ihre Motivation und großen Einsatz danken. Dann möchte ich natürlich auch den Fahrtleitern danken; neben Gerhard durfte ich auch mit Antje Boetius und Frank Wenzhöfer auf Ausfahrt gehen und von allen dreien habe ich sehr viel gelernt. Auch den vielen anderen Teilnehmern möchte ich für so viele Bereicherungen und Diskussionen danken, darunter möchte ich Michael Ivanov, Christian Borowski, André Bahr, Tom Feseker, Matthias Haeckel und Elena Piñero ganz besonders hervorheben. Und natürlich meine liebe Petra Pop Ristova, die mir eine große mentale Stütze war und eine gute Freundin geworden ist.

Dann möchte ich noch meiner „Hamburg-Crew“: Janna, Linda und Wisa, danken. Ich freu mich, einen Teil der damaligen Runde immer noch hier zu haben. Und die Pausen, in denen wir unsere Problemchen an denen wir grad tüfteln loswerden, führen so fast immer zu einer raschen Lösung und es kann meist schnell weitergeforscht werden.
Generell danke ich noch all denjenigen, die immer hinter mir standen und mich so gut sie konnten unterstützt haben. Dazu zählen viele ganz liebe Freude wie Beke, Mascha, Mari, Gerti, Annette, Marie, Paul, Stephan, Lutz, Nils und natürlich meine Familie. Ganz besonders meine Eltern und meine Großeltern sind mir eine so wichtige Stütze, weil sie immer an mich glauben und wenn es mal anstrengend ist (wie beispielsweise in den letzten paar Wochen) sich auch stundenlang Zeit nehmen um mir wieder neue Energie einzuflößen.

Name: Miriam Römer Datum : 27.10.2011
Anschrift: Helmstedter Str. 1, 28215 Bremen

Erklärung

Hiermit versichere ich, dass ich

1. die Arbeit ohne unerlaubte fremde Hilfe angefertigt habe,
2. keine anderen als die von mir angegebenen Quellen und Hilfsmittel benutzt habe und
3. die den benutzten Werken wörtlich oder inhaltlich entnommenen Stellen als solche kenntlich gemacht habe.

Bremen, den 27.10.2011

Unterschrift